

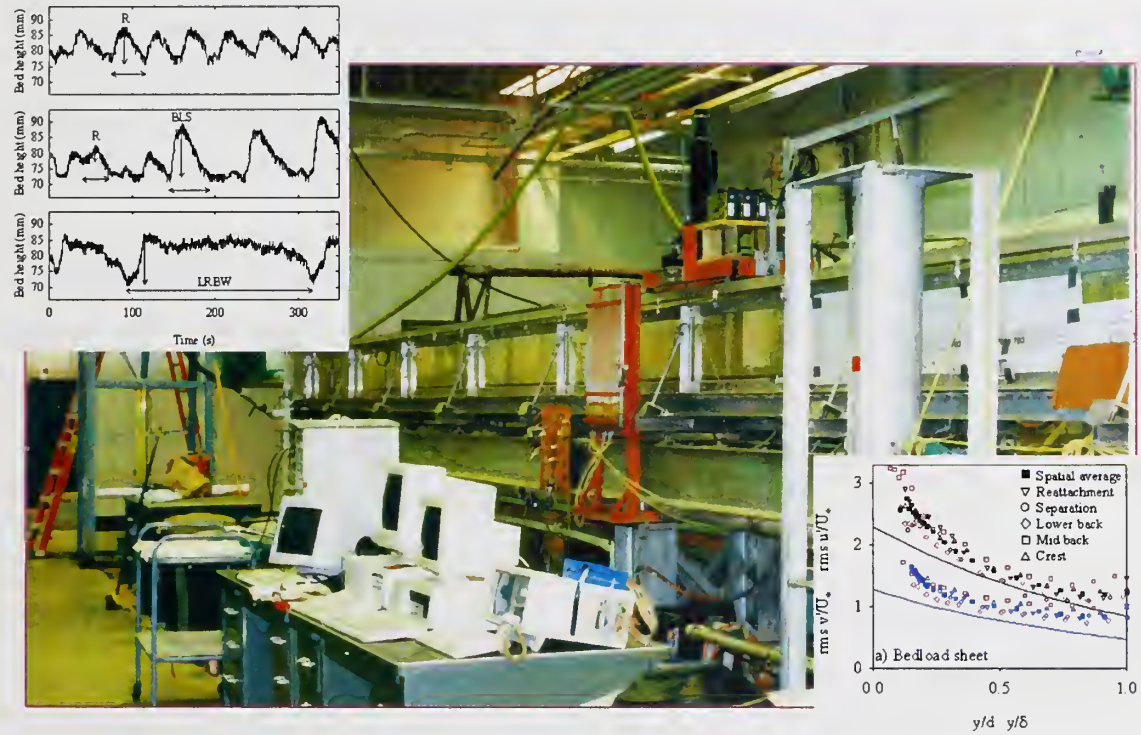
Historic, Archive Document

Do not assume content reflects current scientific knowledge, policies, or practices.



National Sedimentation Laboratory
 Channel and Watershed Processes Research Unit
 Oxford, Mississippi

Flow and bedform dynamics of a
 bimodal sand-gravel mixture



by Joanne K. Horton, Sean J. Bennett, James L. Best
 & Roger A. Kuhnle

Research Report No. 32

September 2002

**United States
Department of
Agriculture**



National Agricultural Library

Acknowledgements

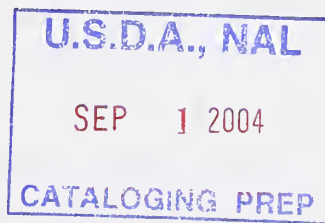
This report represents the completed Ph.D. thesis of Joanne K. Horton, submitted to the school of Earth Sciences, University of Leeds. Here it is reproduced verbatim.

The completion of this study was made possible by the award of NERC Case Grant GT04/97/131/FS. The help and support of academics, friends and family has enabled me to complete nearly four years of challenging, but enjoyable, research, culminating in the production of this thesis. Unfortunately it is not possible to mention all those who have assisted me here.

My laboratory flume experiments would not have been possible without the advice and actions of John Cox and Paul Seay at the National Sedimentation Laboratory, Oxford, Mississippi. Indeed, I am very grateful to all those at the Sedlab who added some light relief from the experimental regime! In particular I would like to thank Anna Curini, Andrea Curini, Daniel Wren, Vince Campbell and Paul Comper.

The analysis of my data at the University of Leeds was greatly assisted by discussions with various people within the School of Earth Science, especially Jurgen Neuberg, Nick Teanby and Michael Bourne. Very welcome interruption from my bedforms was provided by all in the Seddie group, in particular Clare Buckee, Mark Franklin, Clare Davies and Rufus Brunt. I would also like to thank David Deakin, Jane Deakin, Shanta Seereeram, David Moreton, Jenny Underwood, Stefan Fritz, Sue Adair, Tom Manson and many others for various distractions.

Special thanks go to my supervisors Sean Bennett, Jim Best and Roger Kuhnle for their ideas, encouragement and constructive comments on my work. My family have provided the greatest source of support and motivation, for which I am extremely grateful.



Abstract

Little information exists regarding the morphology, texture, dynamics and turbulent flow characteristics associated with bedforms developed in mixed sized sediments, which are ubiquitous in nature. Previous technical limitations associated with measurement resolution and recirculating coarse clasts in flumes have hindered the laboratory investigation of bedforms characteristic of bimodal sediments.

A unique, extensive data set has been compiled from laboratory flume experiments conducted using a bimodal sediment mixture (grain size ranging from 0.177 to 32 mm, $D_{50} = 1.82$ mm) over a range of discharges at two flow depths. Extensive measurements were taken under equilibrium flow conditions to define the sedimentological and hydraulic characteristics of the bedforms generated, including continuous records of bed and water surfaces, laser Doppler anemometer velocity measurements, and fractional and total sediment transport samples. At the end of each run, the sorting patterns of the bed surface were documented by photographs and clay-piston samples, and in two experimental runs, the bed was fixed to facilitate detailed investigation of the turbulent flow field.

For the range of flow depths and discharges investigated, several distinct bedforms were identified as bed shear stress increased: ripples (up to 5 mm high, 0.8 m long), bedload sheets (up to 12 mm high, 1.1 m long) and low-relief bed waves (up to 10-15 mm high (dependent on flow depth), 4.9 m long). Fluctuations in fractional and total sediment transport are linked to bedform migration. The height of the low-relief bedforms scales with the coarsest clasts in transport, with grain roughness dominating form roughness and causing profiles of downstream velocity to deviate from the law-of-the-wall. Calculated values of the von Kármán constant, κ , are thus reduced from a clear water value of 0.41, and, in contrast to previous work, values of Coles' (1956) wake coefficient, Π , are predominantly negative. The present data set is used to validate existing velocity distribution models. Velocity and turbulence parameters vary across and above a bedform due to changes in surface elevation and roughness e.g. turbulent shear layers originate from coarse clasts and bedform crests (demonstrated by profiles and contour maps). The frequency of wake flapping (< 2 Hz) is evaluated by time series analysis. Shear layer flapping causes values of the correlation coefficient to be reduced from the flat-bed boundary layer value of 0.4. Mixing length and kinematic viscosity are greatest over the crest of low-relief bed waves. Across the bedform transition, the degree of spatial variability and magnitude of Reynolds stress, turbulence intensity and production, sediment transport and the vertical extent of quadrant 2 events increases. A conceptual model of bedform development in bimodal mixtures is proposed, incorporating the effects of bedform amalgamation, selective entrainment, and variations in shear stress and surface roughness.

Contents

Title page	i
Acknowledgements	ii
Abstract	iii
Contents	iv
List of figures	viii
List of tables	xv
List of plates	xviii
List of symbols	xix
List of acronyms	xxii
 CHAPTER 1: INTRODUCTION AND REVIEW OF BEDFORMS ASSOCIATED WITH A BIMODAL SAND-GRAVEL MIXTURE	
	1-1
1.1 Interactions between bed morphology, turbulent flow structure and sediment transport	1-1
1.2 Characteristics of bimodal sediments	1-3
1.3 Characteristics of bedforms	1-5
1.3.1 Ripples and dunes	1-5
1.3.2 Bedforms in sediment mixtures	1-9
1.4 Bedform stability fields	1-22
1.5 Aims and structure of thesis	1-24
 CHAPTER 2: EXPERIMENTAL APPARATUS AND PROCEDURE	
	2-1
2.1 Equilibrium flow and experimental program	2-1
2.1.1 Equilibrium conditions and the test section	2-1
2.1.2 Experimental procedure	2-1
2.1.3 Mobile bed experiments	2-1
2.1.4 Fixed bed experiments	2-1
2.2 Laboratory flume facility	2-3
2.2.1 Flume channel	2-4
2.2.2 Water recirculation	2-4

2.2.3 Water discharge – Venturi meter and differential pressure transducer	2-4
2.3 Sediment mixture, recirculating and sampling	2-7
2.3.1 Bulk sediment mixture	2-7
2.3.2 Bedload reirculation and sampling	2-9
2.3.3 Suspended sediment sampling	2-13
2.3.4 Sediment bed surfacee samples – clay piston sampler	2-14
2.4 Measurement devices	2-14
2.4.1 Sediment bed and water surface elevations, and water surfacee slopes – ultrasonic probes	2-14
2.4.2 Motion control system	2-16
2.4.3 Water elevation and surface slope - Point gauges	2-16
2.4.4 Velocity and turbulence measurements –laser Doppler anemometry (LDA)	2-17
2.4.5 Camera and video	2-21
2.4.6 Temperature	2-21
2.5 Comparison of recirculating and sediment feed flumes and field observations	2-21

CHAPTER 3: MORPHOLOGICAL AND TEXTURAL CHARACTERISTICS OF BEDFORMS GENERATED IN A BIMODAL SAND-GRAVEL MIXTURE

3.1 Introduction	3-1
3.2 Data analysis	3-1
3.2.1 Hydraulic conditions	3-1
3.2.2 Sediment bed elevation records	3-2
3.2.3 Transport rates and grain size distributions for bedload, suspended load and the bed surface	3-2
3.3 Results	3-3
3.3.1 Hydraulic conditions	3-3
3.3.2 Bedform classification, morphology and dynamics	3-3
3.3.3 Bedform texture and bedload transport	3-11
3.3.4 Suspended sediment	3-18
3.4 Discussion	3-20
3.4.1 Bedform length and time scales	3-20
3.4.2 Effeet of flow on bedform geometry and texture	3-24
3.4.3 Relation of bedform geometry to bedload and suspended load	3-26
3.4.4 Conceptual model for sediment transport in bimodal mixtures	3-29

3.4.5 Comparison with dunes	3-31
3.5 Conclusions	3-33

CHAPTER 4: MEAN FLOW OVER BEDFORMS DEVELOPED IN A BIMODAL SAND-GRAVEL MIXTURE: EVALUATION OF THE LAW-OF-THE-WALL, VELOCITY DEFECT-WAKE LAW AND VELOCITY DISTRIBUTION MODELS 4-1

4.1 Introduction	4-1
4.2 Data analysis	4-1
4.2.1 Hydraulic conditions – fixed bed	4-1
4.2.2 Sediment bed-elevation records	4-2
4.2.3 Laser Doppler anemometry (LDA) records – flow velocity profiles	4-2
4.3 Results	4-9
4.3.1 Hydraulic conditions – fixed bed	4-9
4.3.2 Mean flow field over a fixed bed	4-10
4.3.3 Boundary shear stress and shear velocity	4-11
4.3.4 Comparison of vertical profiles of time-averaged downstream velocity with the law-of-the-wall and the velocity defect-wake law	4-14
4.4 Discussion	4-18
4.4.1 Boundary shear stress determination	4-18
4.4.2 Spatial variations in time-averaged flow velocities and Reynolds stresses	4-19
4.4.3 Comparison of the mean flow field over bedforms	4-20
4.4.4 Flow resistance	4-23
4.4.5 Comparison of calculated y_0 , k_s , κ , and Π values with previous results	4-28
4.4.6 Comparison of spatially-averaged velocity data with the law-of-the-wall	4-36
4.4.7 Comparison of spatially-averaged velocity data with the velocity defect-wake law	4-40
4.4.8 Comparison of time-averaged velocity with theoretical models	4-42
4.5 Conclusions	4-51

CHAPTER 5: THE TURBULENT FLOW STRUCTURE OVER BIMODAL SAND-GRAVEL BEDFORMS: IMPLICATIONS FOR SEDIMENT TRANSPORT AND BEDFORM DEVELOPMENT 5-1

5.1 Introduction	5-1
5.2 Data analysis	5-2
5.2.1 Turbulence parameters	5-2
5.2.2 Quadrant analysis	5-3
5.2.3 Time series analysis in the frequency domain: spectral analysis	5-4
5.3 Results	5-6
5.3.1 Turbulence intensity and skewness	5-6
5.3.2 Reynolds stress	5-19
5.3.3 Correlation coefficient of Reynolds stress	5-25
5.3.4 Quadrant analysis	5-27
5.3.5 Turbulence production	5-36
5.3.6 Kinematic eddy viscosity	5-41
5.3.7 Mixing length	5-47
5.3.8 Time series analysis in the frequency domain	5-51
5.4 Discussion and conclusions	5-56
5.4.1 Comparison of mobile and fixed beds	5-56
5.4.2 The influence of roughness transitions on the turbulent flow field	5-58
5.4.3 Influence of turbulence on sediment transport	5-59
5.4.4 Comparison of the turbulent flow structure over bedload sheets, low-relief bed waves, ripples and dunes	5-62
5.4.5 Bedform development	5-65

CHAPTER 6: CONCLUSIONS AND OPPORTUNITIES FOR FUTURE RESEARCH

6-1

6.1 Conclusions	6-1
6.1.1 Bedform morphology	6-1
6.1.2 Bedform texture and sediment transport	6-1
6.1.3 Mean flow characteristics	6-2
6.1.4 Flow resistance	6-3
6.1.5 Turbulent flow structure	6-3
6.1.6 Conceptual model of bedform development in a bimodal sand-gravel mix	6-3
6.1.7 Comparison of low-relief bedforms with dunes	6-5
6.2 Opportunities for future research	6-6

APPENDIX I: CONSIDERATION OF ANOMALOUS DATA VALUES FROM ULTRASONIC AND LDA TIME SERIES	I-1
I.1 Ultrasonic probes	I-1
I.2 LDA	I-2

List of figures

Figure 1.1: The interrelationships and feedbacks between bedform development, sediment transport and the turbulent boundary layer structure. After Best (1993). **1-1**

Figure 1.2: A bimodal sediment distribution from the West Solent, UK, with characteristic peaks in the sand and gravel size ranges. From Williams (1990). **1-4**

Figure 1.3: Plot of bedform height against wavelength for ripples and dunes. From Ashley (1990). **1-6**

Figure 1.4: Schematic model of changing flow and turbulence structure across the ripple-dune transition (Bennett and Best, 1995). **1-8**

Figure 1.5: Bed pressure and lift and drag forces acting on hemispheres. After Brayshaw *et al.* (1984). **1-13**

Figure 1.6: Vortex systems associated with an isolated particle. From Best (1996), after Acarlar and Smith (1987a). **1-15**

Figure 1.7: Flow regions associated with the presence of a pebble cluster on the turbulent flow field. From Buffin-Bélanger and Roy (1998). **1-16**

Figure 1.8: Schematic diagram of a bedload sheet observed by Whiting *et al.* (1988) in Duck Creek, Wyoming. **1-16**

Figure 1.9: Temporal variations in total and fractional transport rates. From Iseya and Ikeda (1987) and Whiting *et al.* (1988). **1-18**

Figure 1.10: Schematic model of bedload transport, longitudinal sediment sorting and sediment supply. From Iseya and Ikeda (1987) and Dietrich *et al.* (1989). **1-19**

Figure 1.11: Bedform phase diagrams. From Chiew (1991) and Best (1996). **1-23**

Figure 1.12: The interrelationships and feedbacks between the main components characterised in the experimental flume experiments. 1-25

Figure 2.1: Experimental procedure. 2-2

Figure 2.2: Schematic diagram of the laboratory flume employed. 2-3

Figure 2.3: Manometer. 2-5

Figure 2.4: Calibration of the Venturi meter and differential pressure transducer. 2-5

Figure 2.5: Calibration of the air diaphragm pump. 2-7

Figure 2.6: Bulk sediment mixture used in the present experiments. 2-8

Figure 2.7: Calibration of the accumulation tube. 2-12

Figure 2.8: Distance measurement with ultrasonic probes. 2-15

Figure 2.9: Main components of the LDA measuring system. From Dantec (2000). 2-18

Figure 3.1: Example bed records over a range of flow depths and discharges. 3-4

Figure 3.2: Simultaneous bed records. 3-5

Figure 3.3: Dendrogram for run M. 3-6

Figure 3.4: Example plot of bedform period against height for run M illustrating cluster membership. 3-7

Figure 3.5: Representative grain size distributions for a ripple (a, run I), bedload sheet (b and c, run K and C) and low-relief bed wave (d and e, run M and N) bed configurations. 3-13

Figure 3.6: Textural variations over a low-relief bed wave, run G, series 1. 3-17

Figure 3.7: Suspended sediment transport. 3-18

Figure 3.8: Variations in the height of low-relief bed waves (LRBW) with flow depth.	3-20
Figure 3.9: Secondary flow circulation.	3-21
Figure 3.10: Bedform height versus a) bedform length, b) period and c) migration rate.	3-22
Figure 3.11: Bedload transport as a function of bedform migration rate.	3-23
Figure 3.12: Morphological perturbations of bedforms.	3-24
Figure 3.13: Variations in bedform height, length, period and migration rate with discharge.	3-25
Figure 3.14: Variations in mean grain size of bedload and specific bedform areas with discharge.	3-26
Figure 3.15: Variations in bedload transport rate.	3-27
Figure 3.16: Comparison of bedload and bedform transport rate.	3-29
Figure 3.17: Bedform phase diagram from Best (1996).	3-32
Figure 4.1: Representative examples of the determination of water surface slope over a fixed bed.	4-2
Figure 4.2: Division of the bed height time series into specific bedform regions.	4-2
Figure 4.3: Bed elevation map of the test section dominated by bedload sheets.	4-4
Figure 4.4: Position of velocity and turbulence measurement points over a bedload sheet.	4-4
Figure 4.5: Bed elevation map of the test section containing the region around the crest of a low-relief bed wave.	4-5

Figure 4.6: Position of velocity and turbulence measurement points in the vicinity of the crest of a low-relief bed wave. **4-5**

Figure 4.7: Examples of the projection of Reynolds stress measurements to the bed. **4-7**

Figure 4.8: Contour maps of mean flow over bedload sheets (BLS) and the crestal region of a low-relief bed wave (LRBW). **4-11**

Figure 4.9: Examples of Reynolds shear stress profiles normalised by shear velocity against dimensionless flow depth. **4-12**

Figure 4.10: Examples of the application of the law-of-the-wall and velocity defect-wake law using linear least squares regression. **4-16**

Figure 4.11: Estimates of boundary shear stress with varying flow depth and discharge. **4-19**

Figure 4.12: Spatial variations in time-averaged flow velocities. **4-20**

Figure 4.13: Comparison of selected profiles of normalised downstream and vertical velocity over bedload sheets, low-relief bed waves and dunes (Bennett and Best (1995)). **4-22**

Figure 4.14: The Darcy-Weisbach friction factor and estimations of the form related friction factor. **4-26**

Figure 4.15: Spatially-averaged values of y_0 and k_s over a range of bed shear stresses. **4-29**

Figure 4.16: The distribution of time-averaged y_0 and k_s over a fixed bedload sheet. **4-30**

Figure 4.17: The distribution of time-averaged y_0 and k_s over a fixed low-relief bed wave. **4-31**

Figure 4.18: Cumulative frequency of the wake coefficient and von Kármán's constant. **4-32**

Figure 4.19: Values of κ and Π determined over a range of bed shear stresses. **4-34**

Figure 4.20: Variations in κ and Π over a fixed bedload sheet. **4-35**

Figure 4.21: Variations in κ and H over a fixed low-relief bed wave.**4-35****Figure 4.22:** The law-of-the-wall fitted to the present data and compared with the empirical equations of Kirkgoz (1989).**4-37****Figure 4.23:** The application of the law-of-the-wall to velocity profiles.**4-38****Figure 4.24:** The application of the velocity defect-wake law to velocity profiles over fixed boundaries (Kirkgoz, 1989).**4-41****Figure 4.25:** The velocity defect-wake law for the present data compared with the empirical equation of Kirkgoz (1989) for flow over smooth beds.**4-42****Figure 4.26:** Comparison of the measured and predicted spatially-averaged velocity profile for Run A.**4-44****Figure 4.27:** Comparison of the present data with the model of Wiberg and Smith (1991).**4-46****Figure 4.28:** Subdivision of the flow into specific layers, from Nikora *et al.* (2001).**4-47****Figure 4.29:** Comparison of the measured and predicted downstream velocity distribution from Nikora *et al.* (2001).**4-48****Figure 4.30:** Comparison of the present experimental data with the theoretical spatio-temporally-averaged velocity distribution model of Nikora *et al.* (2001).**4-49****Figure 5.1:** Classification of turbulent events into quadrants.**5-4****Figure 5.2:** Spatial distribution maps of time-averaged velocity moments (bedload sheets).**5-7****Figure 5.3:** Spatial distribution maps of time-averaged velocity moments (low-relief bed waves).**5-9****Figure 5.4:** Spatially-averaged downstream and vertical turbulence intensities, normalised with shear velocity.**5-13**

Figure 5.5: Normalised turbulence intensity against dimensionless flow depth for specific bedform regions. **5-18**

Figure 5.6: Maps of the spatial distribution of Reynolds stress over a) fixed bedload sheet, b) fixed low-relief bed wave. **5-21**

Figure 5.7: Spatially-averaged dimensionless Reynolds stress against normalised flow depth. **5-22**

Figure 5.8: Normalised Reynolds stress against dimensionless flow depth for specific bedform regions. **5-23**

Figure 5.9: Normalised Reynolds stress measurements plotted against dimensionless flow depth - comparison with dunes (Bennett and Best, 1995). **5-23**

Figure 5.10: The correlation coefficient of Reynolds stress, R , plotted against dimensionless flow depth for specific bedform regions. **5-26**

Figure 5.11: The spatially-averaged correlation coefficient of Reynolds stress against dimensionless flow depth. **5-27**

Figure 5.12: Maps of the spatial distribution of the normalised number (%) of quadrant events over fixed bedload sheets. **5-29**

Figure 5.13: Fractional contribution of each quadrant to $-\overline{u'v'}$ over a range of thresholds (bedload sheets) . **5-32**

Figure 5.14: Maps of the spatial distribution of the normalised number (%) of quadrant events over a fixed low-relief bed wave. **5-34**

Figure 5.15: Fractional contribution of each quadrant to $-\overline{u'v'}$ over a range of thresholds (low-relief bed wave). **5-35**

Figure 5.16: Spatially-averaged turbulence generation, T , plotted against normalised flow depth. **5-39**

Figure 5.17: Spatially-averaged turbulence production plotted against depth averaged velocity.

5-40

Figure 5.18: Turbulence production plotted against dimensionless flow depth for specific bedform regions.

5-40

Figure 5.19: Spatially-averaged eddy viscosity, normalised by the product of shear velocity and flow depth, plotted against dimensionless flow depth.

5-42

Figure 5.20: Profiles of dimensionless a) eddy viscosity, and b) mixing length, for run E (bedload sheet bed configuration).

5-44

Figure 5.21: Normalised eddy viscosity plotted against dimensionless flow depth for specific bedform regions.

5-45

Figure 5.22: The distribution of eddy viscosity over fixed two-dimensional bedforms (Nelson *et al.*, 1993).

5-46

Figure 5.23: Spatially-averaged mixing length, normalised by flow depth, plotted against dimensionless flow depth.

5-48

Figure 5.24: Normalised mixing length plotted against dimensionless flow depth for specific bedform regions.

5-50

Figure 5.25: Spatial evolution of mixing length over a two-dimensional bedform (Nelson *et al.*, 1993).

5-50

Figure 5.26: Locations of selected LDA velocity time series.

5-51

Figure 5.27: Spectra of the time averaged a) downstream and b) vertical velocity at various locations over a low-relief bed wave. The 99.9 % significance level is shown.

5-53

Figure 5.28: Comparison of the predicted (MPM) and measured values of bedload transport rate.

5-61

Figure 5.29: Spatially-averaged mean flow (a, downstream velocity) and turbulence profiles (b, Reynolds stress; c, downstream turbulence intensity; d, vertical turbulence intensity; e, turbulence production). **5-68**

Figure I.1: Comparison of the filtered and original bed height record (Run F). **I-1**

Figure I.2: Comparison of the original and filtered record of water height (Run F). **I-1**

Figure I.3: Examples of the original LDA time series. **I-3**

Figure I.4: Application of the law-of-the-wall to filtered and unfiltered LDA time series. **I-9**

List of tables

Table 1.1: Factors controlling sediment transport, morphology and hydraulics within a fluvial channel.	1-2
Table 1.2: The bimodality parameter.	1-5
Table 1.3: Flow transverse bedforms developed in sand-gravel mixtures.	1-10
Table 1.4: Variations of the lift and drag forces. From Brayshaw <i>et al.</i> (1983).	1-12
Table 1.5: Effect of the percentage of gravel ($D_{50} = 6.4$ mm) and sand ($D_{50} = 0.45$ mm) in a sediment mixture on the bed configuration. From Ikeda and Iseya (1988).	1-19
Table 2.1: Grain size statistics for the bulk sediment mixture.	2-8
Table 2.2: Bedload samples.	2-13
Table 2.3: Characteristics of the unfocused ultrasonic probes.	2-14
Table 2.4: Ultrasonic probe measurements.	2-16
Table 2.5: Advantages and disadvantages of LDA.	2-17
Table 2.6: Key features of the LDA measurement system.	2-18
Table 2.7: Specifications of the LDA system employed.	2-19
Table 2.8: Sources of noise in the LDA signal.	2-21
Table 3.1: Mean equilibrium hydraulic conditions.	3-3
Table 3.2: Average values of bedform height and period for each experimental run.	3-8

Table 3.3: Morphological and dynamic characteristics of ripples, bedload sheets and low-relief bed waves.	3-10
Table 3.4: Morphological characteristics of bedforms generated in experimental runs with similar total water discharge, Q .	3-10
Table 3.5: Textural bedform characteristics.	3-12
Table 3.6: Textural variations over a low-relief bed wave.	3-18
Table 3.7: Summary of the sedimentological characteristics of the present experiments and previous work on bedforms in bimodal sediment mixtures.	3-19
Table 3.8: The entrainment, transport and deposition of sand and gravel size fractions.	3-31
Table 4.1: Hydraulic conditions for the fixed bed experiments and their equivalent mobile bed runs.	4-9
Table 4.2: The Reynolds number, pressure-gradient parameter and relative roughness for the experimental flows.	4-10
Table 4.3: Comparison of boundary shear stress and shear velocity determinations.	4-14
Table 4.4: Calculated values of y_0 , k_s , κ and Π for the present experimental data.	4-17
Table 4.5: Bed shear stress (Pa) over mobile and fixed bedforms derived from the projection of Reynolds stress to the bed.	4-20
Table 4.6: Comparison of the mean flow field over different bedforms.	4-21
Table 4.7: Predictions of the total friction factor and its form and drag components.	4-25
Table 4.8: Values of the grain related effective roughness height.	4-27
Table 4.9: Grain related friction factor for various multiples of characteristic grain sizes of the bulk sediment mixture.	4-27

Table 4.10: Values of von Kármán's constant and zero-velocity roughness height from previous studies.	4-29
Table 4.11: Values for Coles's (1956) wake coefficient from previous studies.	4-33
Table 4.12: The percentage difference between the depth-averaged velocity calculated from velocity measurements and the model of Wiberg and Smith (1991).	4-44
Table 4.13: Values of C derived in the present experiments from the linear flow layer.	4-48
Table 5.1: Coefficients of the exponential laws for turbulence intensity.	5-11
Table 5.2: Statistically significant peak frequencies (Hz) observed for both velocity components at a given measuring point.	5-52
Table 5.3: Predicted frequencies (Hz) for the recurrence of turbulence structures over a fixed low-relief bed wave.	5-53
Table 5.4: Variations in flow parameters between different regions over the bedforms.	5-63
Table 5.5: Contrasts and similarities between dunes, bedload sheets and low-relief bed wave.	5-65
Table 5.6: Summary of the changing morphology, sediment transport, flow and turbulent structure between characteristic bed states in the present experiments.	5-67
Table I.1: Differences between the original and filtered LDA time series shown as an absolute percentage of the original values.	I-7

List of plates

Plate 1.1: A well-developed particle cluster formed in poorly sorted fluvial gravels. From Best (1996).	1-11
Plate 2.1: Experimental facility.	2-3
Plate 2.2: Air diaphragm pump which recirculates bedload.	2-6
Plate 2.3: Bedload sediment trap.	2-9
Plate 2.4: Collection of a bedload sample from the accumulation tube.	2-11
Plate 2.5: Simultaneous measurement of flow velocity and bed height.	2-20
Plate 3.1: Ripple developed on a sand ribbon, run I.	3-14
Plate 3.2: Bedload sheet run K.	3-15
Plate 3.3: Low relief bed wave, run M.	3-16
Plate 4.1: The fixed a) bedload sheets and b) low-relief bed wave, with the transect along which velocity and turbulence measurements were taken.	4-3
Plate 5.1: Fixed bedload sheet.	5-6

List of symbols

ρ	Fluid density
σ	Sediment density
ρ_s	Porosity factor
τ_0	Bed shear stress (depth-slope product)
τ_{R0}	Bed shear stress (Reynolds stress projection)
τ_w	Bed shear stress (law-of-the-wall)
τ_R	Reynolds shear stress
τ_D	Form drag
U_*	Shear velocity
θ	Dimensionless bed shear stress
β	Shape factor (fraction of a rectangle, equivalent in height and length to the bedform, which is occupied by the bedform); pressure-gradient parameter
\bar{u}	Time-average downstream velocity
\bar{v}	Time-average vertical velocity
u_i	Instantaneous downstream velocity
v_i	Instantaneous vertical velocity
η	Transit time weighting
u_{skew}	Skewness of the downstream velocity component
v_{skew}	Skewness of the vertical velocity component
y_0	Zero-velocity roughness height
\bar{u}_{\max}	Maximum velocity at the upper limit of the boundary layer
γ_r	Ripple presence factor
ε	Kinematic eddy viscosity
ϕ_1	Modal grain size in phi units (primary mode)
ϕ_2	Modal grain size in phi units (secondary mode)
Φ	Angle between the incident and scattered light
u'	Instantaneous downstream velocity fluctuation
v'	Instantaneous vertical velocity fluctuation

u_R^2	Reference velocity at one bedform height above the crest
θ_i	Mobility parameter of size class i
θ_{cr}	Critical mobility parameter
ξ_i	Correction factor of class size i
B	Bimodality parameter
c	Bedform migration rate; speed of sound
C	Intercept of the velocity distribution
C_D	Drag coefficient
c_m	Concentration of each grain size fraction by volume
d	Flow depth
D_c	Modal grain size of coarse mode
D_f	Modal grain size of fine modal
D_x	Representative grain size, where X % of grains in the mixture are equal or finer in diameter e.g. D_{16} , D_{50} and D_{84} .
f	Darcy-Weisbach friction factor
f'	Grain roughness
f''	Form roughness
F_1	Sediment fraction in primary mode
F_2	Sediment fraction in secondary mode
F_c	Sediment fraction in coarse mode
f_D	Doppler shift
f_d	Frequency of turbulence structures produced by dunes
F_f	Sediment fraction in fine mode
f_i	Frequency of incident light
Fr	Froude number
f_s	Frequency of scattered light; Strouhal law frequency
f_v	Frequency of vortex shedding
f_w	Frequency of wake flapping
g	Acceleration due to gravity
h	Bedform height
H	Threshold value
k_s	Equivalent sand roughness
l	Mixing length; bedform length
n	Number of observations

p	Bedform period
pA_i	Percentages of the i 'th size fraction obtained by areal sampling
p_i	Percentage of size class i of the bed material
pV_i	Percentages of the i 'th size fraction obtained by volumetric sampling
Q	Flow discharge
q_b	Bedload transport rate
R	Correlation coefficient of Reynolds stress; hydraulic radius
r	Ratio of lee slope area and total bedform area
Re	Reynolds number
$rms\ u'$	Root-mean-square of the downstream velocity (turbulence intensity)
$rms\ v'$	Root-mean-square of the vertical velocity (turbulence intensity)
S	Water surface slope
T	Rate of turbulent generation
t	Time interval
U	Depth averaged velocity
u^+	Dimensionless velocity ($u^+ = \bar{u} / U_*$)
U_0	Mean velocity upstream of the point of separation
w	Flume width
x_r	Average length of the separation zone
y	Height above the bed
y^+	Dimensionless height above the bed ($y^+ = U_* y / \nu$)
δ	Height of the boundary layer
Δ	Roughness height
κ	von Kármán constant
λ	Low speed streak spacing
ν	Kinematic fluid viscosity
Π	Coles' (1956) wake coefficient

List of Acronyms

SR	Sand ribbon
R	Ripple
BLS	Bedload sheet
LRBW	Low-relief bed wave
LDA	Laser Doppler anemometry
ADV	Acoustic Doppler velocimetry
Q1	Quadrant one
Q1%	Percentage occurrence of quadrant one events
Q2	Quadrant two
Q2%	Percentage occurrence of quadrant two events
Q3	Quadrant three
Q3%	Percentage occurrence of quadrant three events
Q4	Quadrant four
Q4%	Percentage occurrence of quadrant four events
SA	Spatial average
1	Series 1 ($d = 0.18$ m)
2	Series 2 ($d = 0.14$ m)

Chapter 1 : Introduction and review of bedforms associated with a bimodal sand-gravel mixture

1.1 Interactions between bed morphology, turbulent flow structure and sediment transport

River channels are a vital and dynamic component of the natural environment, providing a conduit for the transfer of both water and sediment, and opportunities and threats to the human population. For example, alluvial channels can be exploited for irrigation, fisheries, gravel-mining, hydro-electric power generation, navigation and recreation proposes. Conversely, flooding, drought, bank erosion and excessive sedimentation can have adverse impacts on the local community. In order to maximise the potential of a river as a resource, and to mitigate any hazards, large-scale engineering and management is often undertaken (e.g. construction, dredging and straightening; Hey *et al.*, 1982; Gilvear, 1999; Pollard *et al.*, 2001). There is an increasing awareness of the need to ensure such projects are sustainable and consider all the competing demands (e.g. political, environmental, social and economic; Tunstall *et al.*, 2000; Nienhuis and Leuven, 2001). Furthermore, the greater focus on the multifunctional nature of river channels, and their complex response to manipulation, has led to a drive to 'restore' river morphology, flow dynamics and habitats (Sear, 1994; Petts and Calow, 1996; Muhar *et al.*, 1995; Boon, 1998; Klingeman, 1998; Harper *et al.*, 1999). There is therefore a great demand for increased understanding of the complex interactions and feedbacks between the key components of the fluvial system (i.e. bed morphology, turbulent flow and sediment transport; Figure 1.1 and Table 1.1).

Figure 1.1: The interrelationships and feedbacks between bedform development, sediment transport and the turbulent boundary layer structure. After Best (1993).

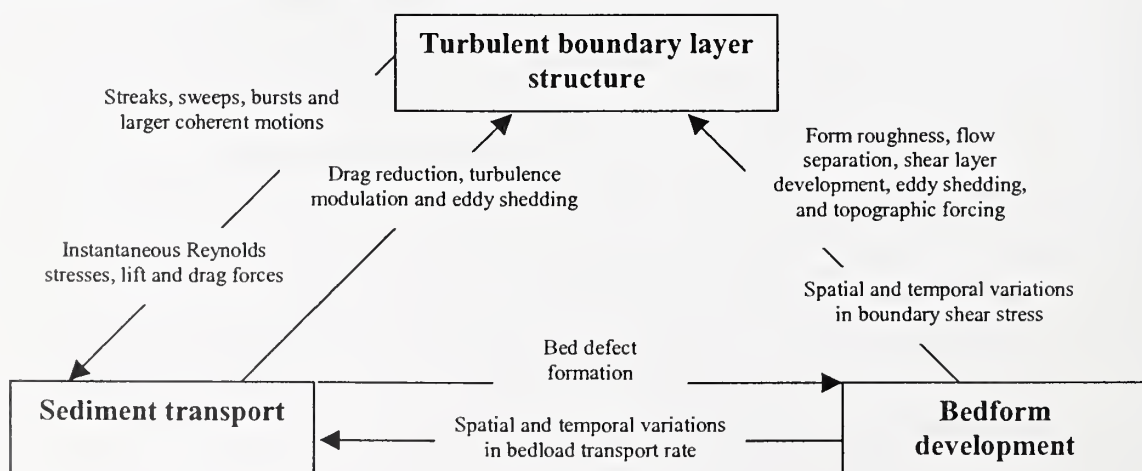


Table 1.1: Factors controlling sediment transport, morphology and hydraulics within a fluvial channel.

Components of the fluvial system	Controlling factors
1) Catchment (Influences other components of the fluvial system, but vary over temporal and spatial scales greater than those considered in the present study)	Climate Base level Geology Vegetation Land use Basin physiography Human intervention
2) Sediment transport	Grain size distribution Grain hiding and protrusion (Fractional) transport rates Transport mechanism: bedload and suspension Grain sorting: longitudinal and vertical
3) Hydraulic	Discharge Slope Depth Flow resistance Turbulence characteristics
4) Bed morphology	Development and migration of bedforms Superimposition and coexistence of different bedforms Development of barforms (length scales with channel width) Channel form

High instantaneous near-bed forces, due to the occurrence of turbulent flow structures, can cause the initiation of sediment transport over a deformable boundary (Drake *et al.*, 1988; Best, 1992, 1993). The movement of sediment over a mobile boundary enables grains to interact, and bed perturbations to be developed (Williams and Kemp, 1971; Southard and Dingler, 1971; Raudkivi and Witte, 1990; Best, 1992; Mazumder, 2000), which feed back to modify the spatial distribution of boundary shear stress (force exerted on the bed per unit bed area) and in turn sediment transport. Defects in the sediment bed a few grain diameters high may also give rise to flow separation and the shedding of turbulent eddies (Leeder, 1980; Bennett and Best, 1996), which drive sediment erosion and deposition, therefore influencing the morphology and spacing of features propagated downstream (McLean *et al.*, 1994; Werner and Kocurek, 1999). Bedforms scale either with flow depth or are smaller forms, whereas barforms scale with channel width. The development of bedforms enables the channel to adjust vertically (i.e. form roughness), which in conjunction with grain roughness and the quality and calibre of sediment in transport (bedload and suspended load) modifies the turbulent flow (Millar, 1999; Carboneau and Bergeron, 2000). Spatio-temporal variations in sediment transport rates result from the migration of bedforms, even when equilibrium flow conditions prevail (Iseya and Ikeda, 1987; Kuhnle and Southard, 1988).

Until fairly recently, research concerning bedforms has focused on sand sized sediment, although detailed studies have been conducted on gravel (Brayshaw, 1984; Dinehart, 1989, 1999; Buffin-Bélanger and Roy, 1998; Carling, 1999; Lawless and Robert, 2001) and mixed sand-gravel sediment (Chiew, 1991; Wilcock,

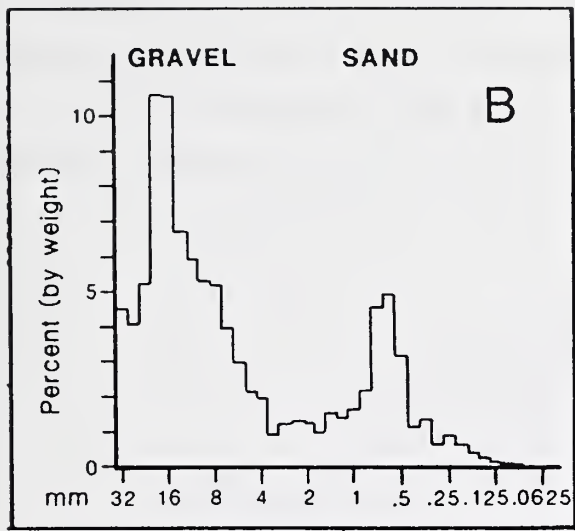
1992; Wilcock and McArdell, 1993), which exhibit different hydraulic and transport characteristics to unimodal sediment (Wilcock, 1993). Grain size segregation is present at a range of spatial scales in natural channels, including over bedforms (Whiting *et al.*, 1988; Bennett and Bridge, 1995), barforms (Church and Jones, 1982; Lanzoni, 2000), pools and riffles (Clifford, 1993), armour layers (Parker *et al.*, 1982a, b; Gomez, 1984), and the longitudinal profile of a river (i.e. the gravel-sand transition, Sambrook Smith and Ferguson, 1995). Furthermore, although investigations of the turbulent flow structure over smooth and rough (uniform sediment) boundaries (Grass, 1971; Kirkgoz, 1989; Grass *et al.*, 1991) and bedforms developed in sand-grade material (Nelson *et al.*, 1993; Bennett and Best, 1995, 1996) have been conducted, little information exists concerning the turbulent flow field over low-relief bedforms developed in bimodal mixtures (Bennett and Bridge, 1995; Livesey *et al.*, 1998), which can exhibit distinct textural discontinuities that significantly impact on the mean flow structure and turbulence characteristics (Robert *et al.*, 1992, 1996; Nezu *et al.*, 1993).

In the present study the morphology, sediment transport and turbulent flow structure associated with bedforms developed in a bimodal sand-gravel mixture are investigated by conducting a series of laboratory flume experiments. Laboratory flume experiments allow the key variables (e.g. shear stress, water depth, sediment size distribution) to be adjusted in a controlled manner, and enable detailed measurement of bedform morphology, sediment transport and turbulent flow structure under equilibrium conditions with excellent spatial resolution (Kuhnle and Southard, 1988; Nelson *et al.*, 1993; Bennett and Bridge, 1995; Bennett and Best, 1995, 1996). Conversely, in the field environment, the number of influencing factors, and the degree of variability increases. However, field data remains invaluable for increasing our understanding of fluvial processes (Whiting *et al.*, 1988; Ferguson *et al.*, 1989; Robert *et al.*, 1992; Buffin-Bélanger and Roy, 1998; Carling *et al.*, 2000a, b; Kostaschuk, 2000).

1.2 Characteristics of bimodal sediments

In the 1990's increasing focus was given to bimodal mixtures (Figure 1.2), which are characterised by two distinctly separate peaks in the grain size distribution (i.e. modes), and occur frequently in nature (e.g. Canada rivers, Shaw and Kellerhals, 1982; West Solent, UK, Williams, 1990; Goodwin Creek, USA, Kuhnle, 1993a; Gravel-sand transitions, Sambrook Smith, 1996). The origin of bimodality is uncertain (Sambrook Smith, 1996), but may result from 1) the differential weathering and breakdown of source rocks (Wolcott, 1988), 2) the preferential attrition and breakdown of fine gravel to sand (Shaw and Kellerhals, 1982), 3) the preferential entrainment of grain size fractions (Wolcott, 1988), and 4) point sources of bed material which result in local bimodality e.g. channel junctions.

Figure 1.2: A bimodal sediment distribution from the West Solent, UK, with characteristic peaks in the sand and gravel size ranges. From Williams (1990).



The infiltration of fines in bimodal sediments has been studied with reference to both the surface and subsurface (Carling and Reader, 1982; Diplas and Parker, 1992a), while research concerning sediment entrainment and sorting focuses on the bed surface (Iseya and Ikeda, 1987; Drake *et al.*, 1988; Kuhnle and Southard, 1988; Whiting *et al.*, 1988; Wilcock and Southard, 1988; Dietrich *et al.*, 1989; Ferguson *et al.*, 1989; Wathen *et al.*, 1995; Sambrook Smith and Ferguson, 1996; Livesey, 1998), although bedform migration can cause vertical grain size segregation (Bennett and Bridge, 1995; Khadkikar, 1999).

Due to the dual peaks in the grain size distribution of a bimodal mixture, the commonly used classification for an unimodal sediment, the mean grain size (D_{50} ; 50 % of clasts are an equal or finer in diameter), is essentially meaningless since that particular grain size may be present only in minimal quantities (i.e. it falls in between the two modes; Kuhnle, 1996). Furthermore, if the sediment is strongly bimodal, the D_{50} value may shift between modes for sediment samples with only small variations in grain size distribution. Fredlund *et al.* (2000) present equations which describe the grain size distribution of unimodal and bimodal soils, aiding their identification and categorisation. However, it is useful to be able to assign a characteristic value to a sediment mixture, and therefore attempts have been made to define the degree of bimodality (Table 1.2), which can significantly influence the mechanics of sediment transport (Kuhnle, 1993a). In order to define bimodality it is important to consider: 1) the separation of the two modes, 2) the fraction of sediment contained in the modal grain sizes, 3) the relative magnitude of the modes (considering just the sediment fraction contained in the modal grain sizes) and 4) the total amount of sediment in each mode. The equation presented by Wilcock (1993, Table 1.2) does not account for the latter two factors, while the formula of Sambrook Smith *et al.* (1997, Table 1.2) omits consideration of the total quantity of sediment in each mode in order to simplify calculation of the bimodality index. Consequently, there is a possibility of a sediment mixture being wrongly classified, and therefore it is also important to visually inspect any grain size

distributions. Furthermore, the grain size distribution, from which the bimodality index is calculated, can be determined using one of a range of areal and volumetric sampling methods, which do not necessarily concur (e.g. clay-piston samples, grid analysis of photographs, extraction of all particles down to the level of the height of the coarsest clast; Kellerhals and Bray, 1971; Church *et al.*, 1987; Diplas and Fripp, 1992). Finally, spatial grain size segregation (e.g. patches of fine sediment, Ferguson *et al.*, 1989; Paola and Seal, 1995; Laronne *et al.*, 2000) may make it difficult to collect sediment samples at representative locations.

Table 1.2: The bimodality parameter.

D_c , modal grain size of coarse mode (mm)	D_f , modal grain size of fine mode (mm)
F_c , fraction in coarse mode (width of 1 ϕ unit)	F_f , fraction in fine mode (width of 1 ϕ unit)
ϕ_1 , modal grain size in phi units (primary mode)	ϕ_2 , modal grain size in phi units (secondary mode).
F_1 , fraction in primary mode (width of 1 ϕ unit)	F_2 , fraction in secondary mode (width of 1 ϕ unit)

Reference	Bimodality parameter, B	Results	Value of B for the bulk sediment used in this study
Wilcock (1993)	$B = \left(\frac{D_c}{D_f} \right)^{1/2} (F_c + F_f)$	>1.7 entrained as bimodal sediment, <1.7 entrained as unimodal sediment.	2.3
Sambrook Smith <i>et al.</i> , (1997)	$B = \left \phi_2 - \phi_1 \right \left(\frac{F_2}{F_1} \right)$	Critical value 1.5-2. Bimodal if greater than the critical value.	3.6

1.3 Characteristics of bedforms

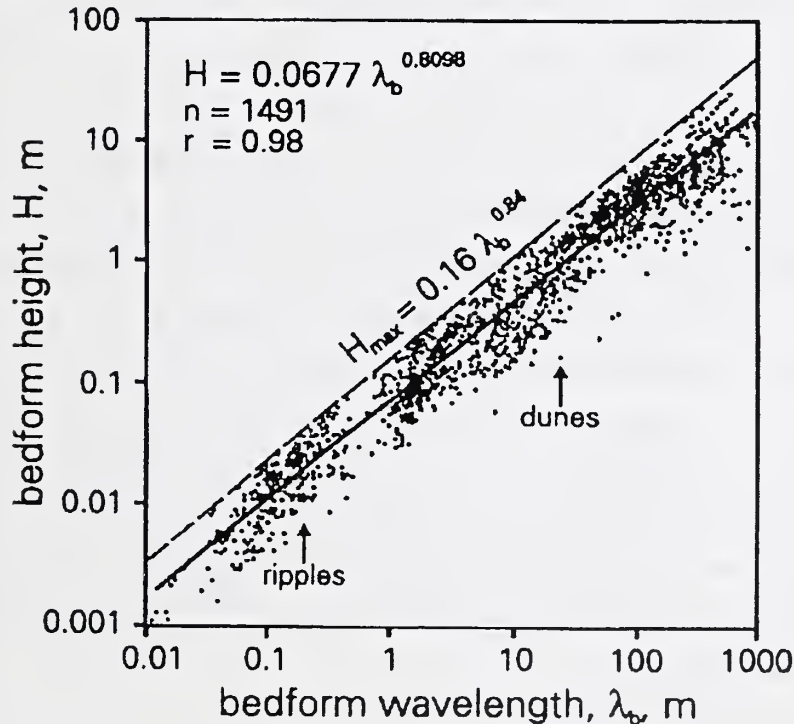
In the following section the key points concerning the morphology, sediment transport and associated turbulent flow structure of bedforms frequently referred to in this study are detailed.

1.3.1 Ripples and dunes

Ripples formed in a unidirectional flow exhibit a steep lee slope and gentle stoss side, and are therefore asymmetric in shape (Allen, 1968). Ripples have a height below 0.075 m, with a wavelength of less than 0.6 m (Ashley, 1990; Figure 1.3), resulting in a length/height ratio of 10-40 (Leeder, 1999). The dimensions of ripples are not determined by the flow depth (Raudkivi, 1997), but fluid stresses near the bed influence ripple wavelength weakly through variations in turbulence intensity at reattachment (affecting entrainment and the extent of scour), the downstream extent of flow separation (dictated by flow velocity and ripple height), and particle step length (Karahan and Peterson, 1980). The length of ripples has been observed to scale with sediment diameter, with ripple wavelength being equivalent to approximately 1000 grain diameters (Bass, 1999; Lopez *et al.*, 2000). The crest of a ripple can be straight, wavy or linguoid in planform, although given sufficient development time they become three-dimensional (Baas, 1993, 1999). Ripples only evolve in

sediment up to 0.7 mm in diameter (Costello and Southard, 1980; Leeder, 1980), since larger grains protrude above the viscous sub-layer and destroy the hydraulically smooth flow conditions required for ripple formation. The development of ripples from an initially flat bed occurs progressively (Southard and Dingler, 1971; Williams and Kemp, 1971), rather than spontaneously (Bagnold, 1956). The initiation of ripples may occur through the accumulation of mobile sediment by: 1) fast upstream particles sheltering downstream grains, leading to grouping (e.g. kinematic waves; Costello and Southard, 1980), 2) intermittent turbulent coherent flow structures eroding excess sediment for the flow capacity causing deposition (Williams and Kemp, 1971; Grass, 1983; Drake *et al.*, 1988; Best, 1992), and 3) the presence of non-uniform sediment. Best (1992) indicates that the movement of relatively high velocity fluid towards the bed occurs by multiple intermittent 'sweep' events, which are capable of eroding a larger area of the bed than a single sweep event. Furthermore, the sweep impacts result in the deposition of flow parallel ridges which focus subsequent sweep events, and associated sediment erosion, in-between the ridges. Once a defect attains a threshold height (2-3 grain diameters in sand; Best, 1992), flow separation and associated reattachment can drive the initiation of further defects and the growth and migration of the existing bedforms (Williams and Kemp, 1971, 1972; Gyr and Schmid, 1989). Liu (1957) suggested that ripples develop due to an instability at the sediment-fluid interface, and not by irregularities in the sediment bed or coherent turbulent structures. However, the observed amplification and downstream propagation of ripples cannot be accounted for by the instability mechanism (Gyr and Müller, 1996).

Figure 1.3: Plot of bedform height against wavelength for ripples and dunes, which are separated by a gap at a wavelength of approximately 0.8 m. From Ashley (1990).



Dunes have a similar shape and internal structure to ripples but are distinguished by their larger size (Figure 1.3) and associated turbulent flow structure (Figure 1.4), and can evolve from ripples as the fluid stress on the bed is increased (Figure 1.4). The height and wavelength of dunes scale with flow depth (a height of up to a third of the flow depth and a wavelength 4-8 times the flow depth; Jackson, 1976; Allen, 1984; Julien and Klaassen, 1995), and are greater than the dimensions of ripples (the wavelength of small dunes is greater than 0.6 m, while their height is in excess of 0.075 m; Ashley, 1990; Figure 1.3). The flow over ripples is weakly uniform (Wiberg and Nelson, 1992), whereas over dunes it is strongly non-uniform, with the water surface being out-of-phase with the dune bed (Figure 1.4; Engelund and Fredsoe, 1982; Nelson and Smith, 1989). Dunes are subject to a larger velocity differential in the lee side region compared with ripples, and therefore produce turbulent flow vortices of greater magnitude, which extend throughout the flow depth up to the water surface, whereas they are limited to the lowest 20 % of the flow depth when originating from ripples (Bennett and Best, 1995, 1996; Lopez *et al.*, 2000; Robert and Uhlman, 2001). The stresses on the bed are also greater at reattachment (the point where the separated flow in the lee region reattaches to the sediment boundary) over dunes compared with ripples (e.g. 2-3 and 6-9 times the average force on the bed over ripples and dunes respectively; Bennett and Best, 1995, 1996; Figure 1.4). Robert and Uhlman (2001) detail the non-linear increase in turbulence intensity, Reynolds stresses, momentum exchange and spatially variability over the ripple-dune transition. Over a dune bed, turbulence parameters are highly dependent on the position above and along the boundary (Robert and Uhlman, 2001), and spatially-averaged turbulence intensity declines away from the bed in contrast to ripples.

Large-scale flow separation often occurs in the leeside of dunes (Bennett and Best, 1995), however permanent reverse flow is not always observed (Best and Kostaschuk, in press). Macroturbulent structures dominate the flow over dunes (Jackson, 1976; Kostaschuk and Church, 1993; Nezu and Nakagawa, 1993), and are shed from a turbulent free shear layer resulting from the strong velocity gradient in the leeside caused the flow response to the topographic changes. The separation/deceleration zone generates a turbulent wake zone, and downstream of reattachment a boundary layer develops near the bed (Nelson and Smith, 1989; Nelson *et al.*, 1993; McLean *et al.*, 1994). Over a dune, spatially-averaged boundary shear stress increases towards the crest, peaking just upstream, enabling deposition at the crest due to the reduction in bed shear stress (Nelson and Smith, 1989). The intensity of turbulence, in both the downstream and vertical directions, is elevated in the free shear layer, peaking at reattachment. The development of the boundary layer over the stoss of the downstream dune causes the turbulence intensities to diminish and the area of relatively high turbulence intensity to be forced further from the bed. The interaction of wakes generated from upstream dune crests and vortices shed from the shear layer create a complex turbulent flow field (Smith and McLean, 1977; Nelson *et al.*, 1993; McLean *et al.*, 1994).

Figure 1.4: Schematic model of changing flow and turbulence structure across the ripple-dune transition.

a) Rippled bed, equilibrium flow

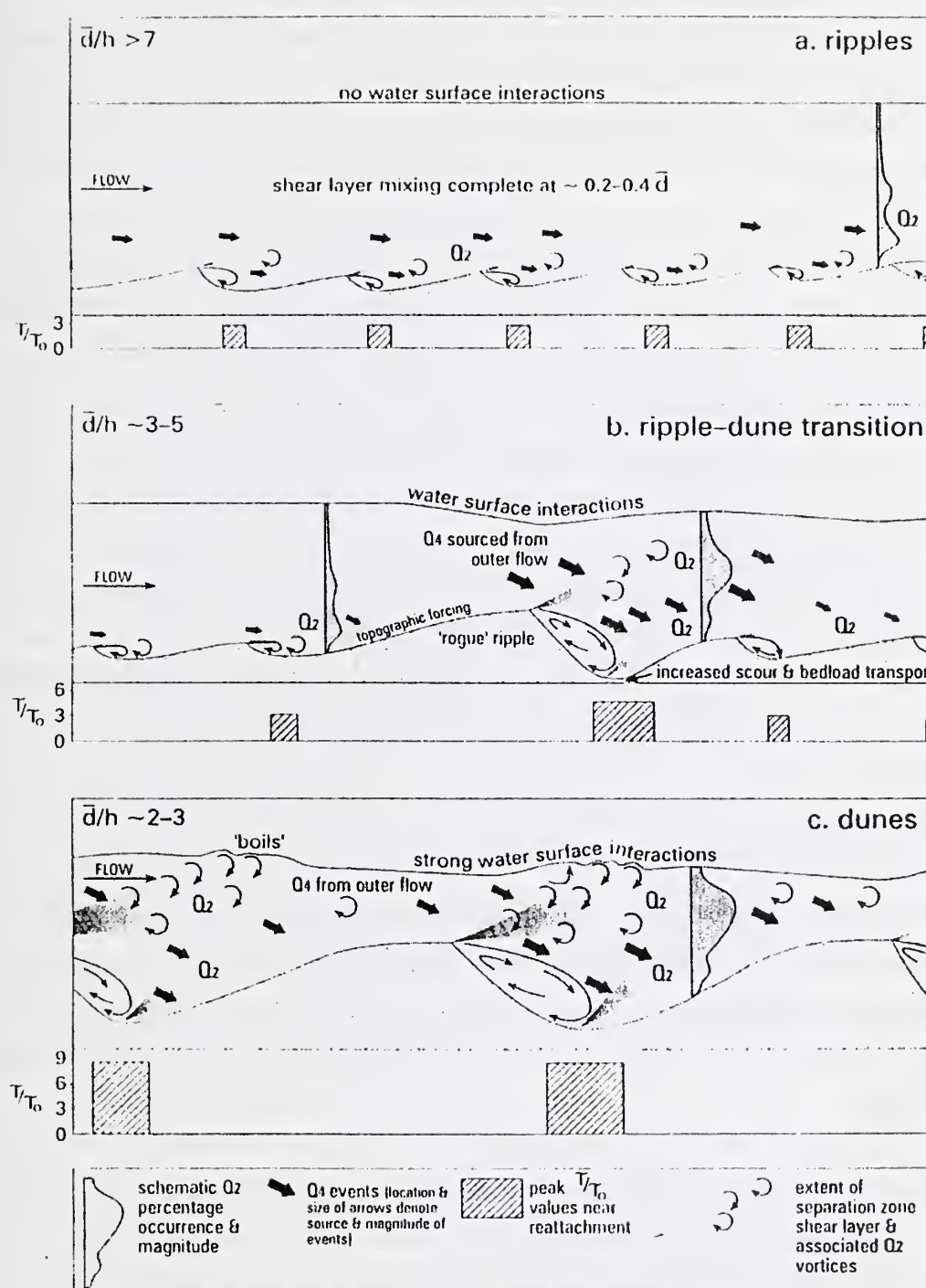
b) Rippled bed, non-equilibrium flow (increasing transport stage). Formation of a larger than average bedform ('rogue' ripple).

c) Dune bed, equilibrium flow

 τ / τ_0 : Approximate ratio of the time-averaged Reynolds stress (force exerted by the fluid) near reattachment to the spatially-averaged boundary Reynolds stress over the entire bedformQ₂: Quadrant 2 (ejection) events – slow, upwards moving fluid structuresQ₄: Quadrant 4 (sweep) events – fast, downwards moving fluid structures

d: Flow depth

h: Bedform height



Over bedforms that are traverse to flow, sediment is entrained from the stoss at reattachment and deposited on the lee, causing the ripple or dune to migrate downstream, and resulting in cyclical variations in sediment transport rate (Simons *et al.*, 1965; Kuhnle and Southard, 1988). Once the lee slope reaches the angle-of-repose, the accumulated sediment avalanches down the lee side, resulting in grain size segregation and characteristic cross bedding which may be preserved (McBride *et al.*, 1975; Carling, 1996; Khadkikar, 1999; Carling *et al.*, 2000a). Dunes are thought to evolve from the amalgamation of smaller forms (Costello and Southard, 1980; Whiting *et al.*, 1988; Gabel, 1993), large rogue bedforms (Leeder, 1980) and the distribution of bed shear stress over the bedform (Bennett and Best, 1996; Figure 1.4). Superimposed bedforms migrating upon the back of the larger, slower dunes control the periodic sediment input to the dune crest (Whiting *et al.*, 1988). However, dune formation and migration may also be influenced by sediment transported in suspension by turbulent flow structures where sand prevails (Jackson, 1976; Kostaschuk and Church, 1993; Lapointe, 1996; Roden, 1998; Kostaschuk, 2000), and grain interactions in mixed sized sediment (Brayshaw *et al.*, 1983; Best, 1996). Ripples and dunes have been studied at length in unimodal sand sized sediment mixtures, although the latter have also been observed in gravel (Hubbell *et al.*, 1987; Carling, 1999; Dinehart, 1999; Carling *et al.*, 2000a, b) and mixed sized sediment (Wilcock, 1992). Important questions remain concerning how ripples and dunes relate to other bedforms such as bedload sheets and upper-stage plane beds (Bennett and Best, 1995, 1996). For example, do the same formative processes operate across a wide range of grain roughnesses? Furthermore, the nature of the turbulent flow field and sediment transport regime over developing and equilibrium dunes in a range of grain sizes is still subject to uncertainty (Nelson and Smith, 1989; McLean *et al.*, 1994; Bennett and Best, 1995; Kostaschuk and Villard, 1996, 1998). For example, what conditions are necessary for flow separation to occur (Best and Kostaschuk, *in press*), and which turbulent events are dominant in moving coarse sediment (Drake *et al.*, 1988; Dinehart, 1992a)?

1.3.2 Bedforms in sediment mixtures

Bimodal sediment mixtures are found in a wide range of environments e.g. marine, lacustrine, riverine and terrestrial (Langhorne *et al.*, 1986). The interactions between fluid flow and different sediment size fractions in bimodal mixtures control sediment transport, grain size sorting, flow resistance and the depositional characteristics of these sediments. These effects are manifested through the development and migration of various low-relief bedforms.

Recognition of low-relief bedforms in gravel sized sediment has been fairly recent (Kuhnle, 1986; Whiting *et al.*, 1988; Kuhnle and Southard, 1988; Dietrich *et al.*, 1989; Wilcock, 1992; Bennett, 1992; Bennett and Bridge, 1995). Their identification is a result of more detailed observations, improved monitoring techniques and work conducted into the entrainment and bedload transport of different size fractions which compose heterogeneous sediments (Hammond *et al.*, 1984; Komar, 1987a, b; Ikeda and Iseya, 1988; Ashworth and

Ferguson, 1989; Kirchner *et al.*, 1990; Dinehart, 1992a, b; Kuhnle, 1993a, b; Wilcock, 1998). However, Bennett and Bridge (1995a) note that comparison with other studies is hindered by incomplete morphological and hydraulic data. Due to past technical difficulties of recirculating gravel sized sediment in a laboratory flume, there is currently a limited knowledge concerning the morphology and textural characteristics of bedforms generated in sand-gravel mixtures and their associated turbulent flow structure. Furthermore, direct observations and measurements of bedload motion in coarse-grained sediments are problematic, and therefore the dynamics of small-scale bedforms remains unclear. A range of flow-transverse bedforms have been previously identified in mixed sized sediment mixtures (Table 1.3). Longitudinal bedforms have also been observed in sand-gravel mixtures (i.e. sand ribbons; McLean, 1981; Nezu and Nakagawa, 1993; Livesey, 1995; Tsujimoto and Kitamura, 1996), which give rise to lateral variations in boundary roughness.

Table 1.3: Flow transverse bedforms developed in sand-gravel mixtures. θ represents the dimensionless bed shear stress.

Bedform	Height (mm)	Length (mm)	Migration rate (mm/s)	θ	Texture	References
Ripples	3-40	30-800	4-34	0.09	Sand fractions	1
Particle clusters	D_{95}	100-1200	Move by breaking up.	0.009	Coarse stoss, fine wake	2
Bedload sheets	4-13	70-1200	1-27	0.04-0.12	Coarse trough, fine stoss coarsens towards crest.	3
Low-relief bed waves	8-17	1700-4850	0.3-14	0.04-0.24	Coarse trough, fine stoss coarsens towards crest.	4
Dunes	100-100000	600-100000	30	0.1-0.3	Fine stoss coarsens towards crest. Coarse trough when sediment transport low.	5
Antidunes	10-1000	50-19000	Direction variable. Rate influenced by steepness.	0.2-2.5	Coarest clasts on or near the crest, few on the lee.	6
Transverse ribs	1-2 clast diameters	50-1250 (width) 200-2500 (wave-length)	Direction variable.	0.2-2.5	Coarse clasts, with fine infill and backfill.	7

1 Yalin (1992); Wilcock and McArdell (1993).

2 Dal Cin (1968); Brayshaw (1984); Naden and Brayshaw, 1987; Hassan and Reid, 1990; de Jong (1991); Reid and Hassan (1992).

3 Ikeda and Iseya (1988); Whiting *et al.* (1988); Dietrich *et al.* (1989); Bennett and Bridge (1995a, b).

4 Bennett and Bridge (1995a); Livesey *et al.* (1998).

5 Hubbell *et al.* (1987); Kuhnle and Southard (1988); Carling (1999); Dinehart (1999).

6 Kennedy (1963); Shaw and Kellerhals (1977); Whittaker and Jaeggi (1982); Mehrotra (1983); Yagishita and Taira (1994); Alexander and Fielding (1997).

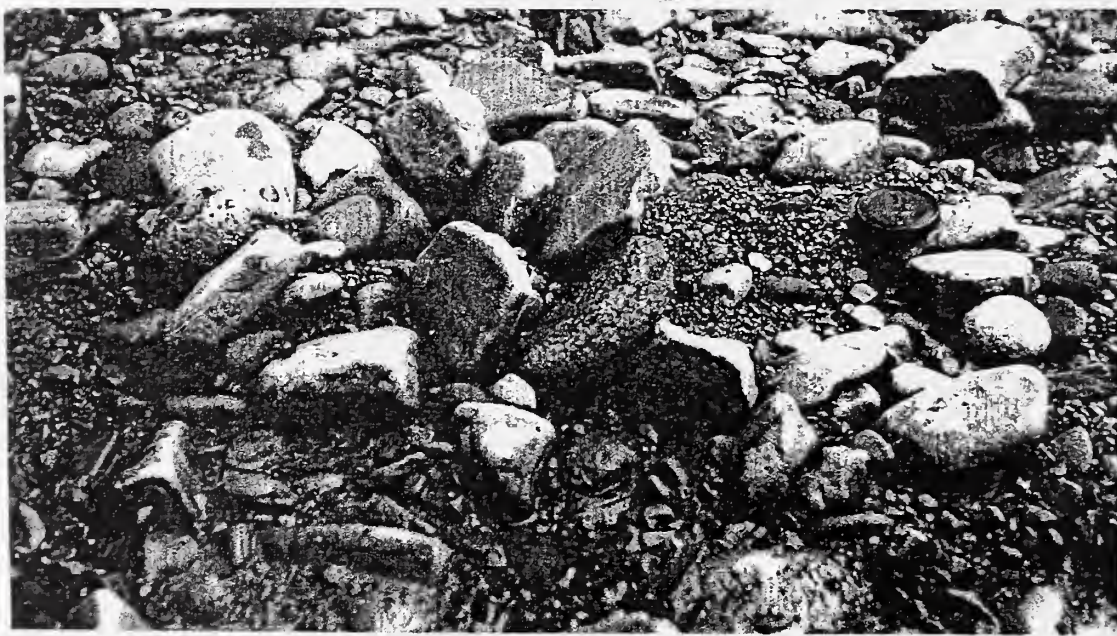
7 Koster (1978); McDonald and Day (1978); Rust and Gostin (1981); Allen (1983); Bluck (1987).

1.3.2.1 Pebble clusters

Increases in sediment calibre cause a corresponding expansion in the role of grain roughness and protrusion upon the flow. Cluster bedforms typically form around an exceptionally large obstacle clast (Plate 1.1; Dal Cin, 1968; Laronne and Carson, 1976; Brayshaw, 1984; Buffin-Bélanger and Roy, 1998). The other constituent particles are arranged so that the long axis of the pebble cluster is parallel to the flow, with relatively coarse grains in front of the main clast (stoss deposit), and finer sediment being deposited behind

the principal clast (wake deposit). Individual particles within a cluster can interact either directly via interlocking, or indirectly by affecting the amount of exposure of adjacent grains. Clusters range in streamwise length from 0.1 to 1.2m, with their length being approximately twice their width (Brayshaw, 1984). However, the geometrical dimensions of the cluster tend to increase with the size and degree of sorting of the bed material. Furthermore, the grain shape influences the relative lengths of the sediment accumulations in the wake and stoss (Brayshaw, 1984). For example, well-rounded particles encourage point contact, resulting in the two deposits, each forming roughly a third of the total cluster length. Conversely, tabular or disk shaped grains facilitate imbrication on the stoss side which then becomes dominant. In this latter case the obstacle clast may not necessarily be the largest in size. Clasts contained in clusters are better aligned with the flow, and more steeply imbricated, compared with particles resting on the plane bed, therefore aiding palaeocurrent interpretations.

Plate 1.1: A well-developed particle cluster formed in poorly sorted fluvial gravels. Flow is from left to right. Clasts are well imbricated on the stoss side and the relatively finer grained sediment accumulated in the leeside flow separation zone. From Best (1996).



Brayshaw (1984) has demonstrated the common occurrence of particle clusters, which occupy approximately 10% of the bed in streams of various lithologies, but are spatially non-periodic. No significant correlation between boundary shear stress at the peak flow of a flood and the area covered by clusters has been found (Brayshaw, 1984). Bennett and Bridge (1995a) observed that pebble clusters are predominant in the coarser areas of the bed, for example the troughs of bars and bedload sheets.

Projecting particles distort the flow, forming distinctive asymmetrical pressure and velocity fields (Figure 1.5; Brayshaw *et al.*, 1983), which can influence the entrainment, transport and deposition of other particles (i.e. mutual particle interference; Best, 1996). When a particle is in the disturbed flow field around an

obstacle grain, the size of the lift and drag forces it experiences will depend upon the obstacle and mobile particle's relative position and size (Table 1.4 and Figure 1.5). Measurement of the forces acting on bed particles has been hindered by technical problems and the complex 3-dimensional shape of the clusters.

Table 1.4: Variations of the lift and drag forces. From Brayshaw *et al.* (1983).

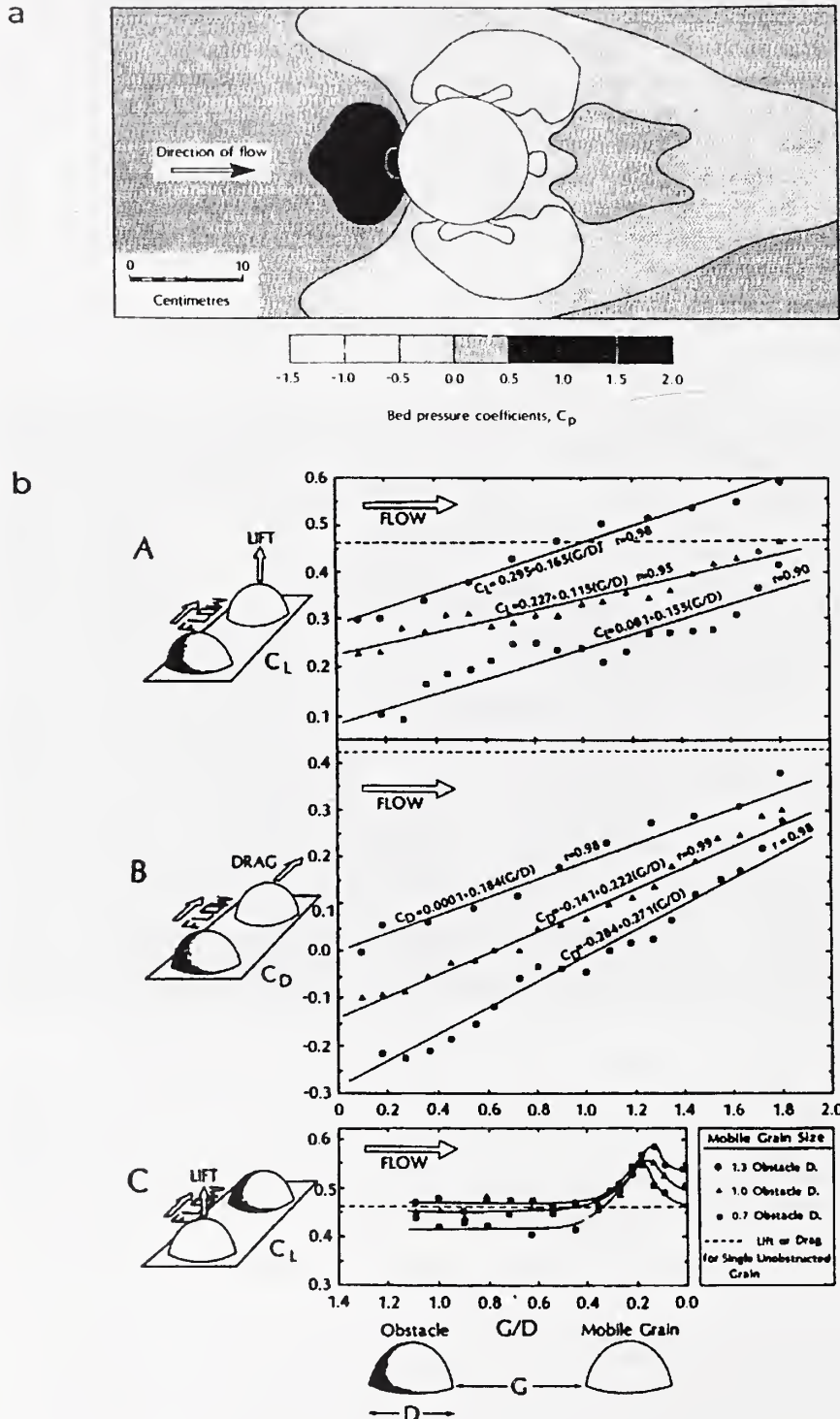
	Lift force	Drag force
In the wake of an obstructing particle (much reduced lift and drag forces than if exposed singly in the freestream)	Varies in direct proportion to particle separation. The distance over which an obstacle grain provides protection depends on size relations. At greater separations lift force still rises in response to an exaggerated imbalance in pressure due to exposure of upper surface to accelerated flow while base remains in low velocity of the obstacle's lee.	Varies in direct proportion to particle separation. The relative size of the obstacle and mobile grains determines the direction of drag in the immediate lee of the obstacle. Inverse relationship between the ratio of movable to obstacle grain size and the downstream extent of the obstacle's sphere of influence over bed particles in its train.
Stoss side of the cluster	Increases gradually when particle separation is small (below about 0.3 times the obstacle diameter) and reduced, arising from acceleration of flow around the flanks. Particles of like size, closely spaced, act as a single entity. Low pressure develops across the flow separation plane that encloses the diminishing gap between the particles, producing extra lift on the leeside of the leading particle, reducing its stability.	Uniform regardless of particle separation.

This mutual interference of adjacent particles has received little attention, and yet it is vital when considering incipient motion, which is delayed by the presence of clusters (Reid *et al.*, 1984; Hoey, 1992). In addition, clusters limit the availability of bed sediment for transportation. The complex and variable pattern of cluster bedforms partially accounts for the wide range in critical shear stresses for particles of similar size and shape (Brayshaw *et al.*, 1983). Pebble clusters are therefore a major component of sedimentary sorting, encouraging deposition of a wide range of particle sizes. Brayshaw (1984) observes that obstacle clasts reflect the largest grain size exhibited by the bed (D_{95}). Fine sediment, similar to that found in the sub-surface layer, is associated with the wake region (D_8 to D_{46}), while the stoss area is characterised by coarser grains (D_{74} to D_{94}). The surficial nature of clusters can be seen in cut sections, with the wake deposits observed to fine downwards. In natural clusters the stoss side deposit has a higher relief compared with the wake region.

Figure 1.5: Bed pressure and lift and drag forces acting on hemispheres.

a) Bed pressure coefficients around an isolated clast, i) high pressure upstream of clast due to the strong downflow of deflected fluid, ii) low pressure where flow accelerates around the flanks of the clast, but deposition hindered by high local boundary shear stress, iii) low pressure, and greatest chance of deposition for fine sediment, in the lee due to flow separation, vi) high pressure at reattachment.
 b) The influence of particle separation and size on the lift and drag forces exerted on a mobile grain near to an obstacle clast, A) coefficient of lift for particle in the lee of another clast, B) coefficient of drag for a particle in the lee of another clast, C) coefficient of lift for a particle upstream of another clast.

From Brayshaw et al. (1983).



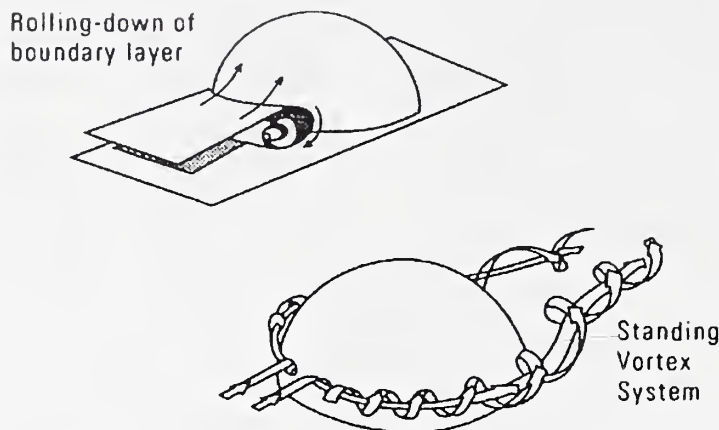
After the deposition of the obstacle clast at a relatively high flow level, downstream accumulation of fines begins (Dal Cin, 1968; Brayshaw, 1984). Only finer sediment is influenced by recirculating flow in the lee side, and therefore transported into the wake area, since the larger particles have too great a momentum. Minor scour may appear at the upstream edge of the obstacle clast, but deposition here only occurs at lower flow velocities since grains are carried around the main clast by local flow acceleration at higher flow speeds. Therefore a temporal difference between the accumulation of wake and stoss deposits exists, and the geometry of the cluster is influenced by the size of the obstacle clast. Higher velocities may actually increase the stability of the bedform, with stoss deposits being more firmly pushed against the main clast, and wake sediment accumulations being contained in the low pressure flow separation region. Mutual particle interference and interlocking cause the critical entrainment threshold of the clasts to be greater when they are part of a cluster than when they exist in isolation (Reid *et al.*, 1984). Teissyre (1977) contends that cluster development requires the same hydrodynamic conditions as imbrication i.e. turbulent, rapid flow conditions. Brayshaw (1984) suggests that clusters develop during the recession limb of a flood in which bedload movement occurred, and are therefore not equilibrium bedforms. Subsequent remobilisation of the constituent sediment occurs suddenly by flows which are competent to dislodge the obstacle clast (i.e. rising stage of a flood), leading to variations in the bedload transport rate. However, de Jong (1991) concluded from fieldwork observations that clusters are a relatively immobile component of the bed, and therefore are not as significant as previously thought in delaying sediment entrainment. Furthermore, the entrainment of sediment from a cluster does not require the main clast to be removed, facilitating the rebuilding of clusters. Typically stoss deposits are released in preference to grains which accumulate in the lee region (Brayshaw *et al.*, 1983; de Jong, 1991). de Jong (1991) observed clusters to be destroyed radially from the obstacle clast, with sediment being entrained laterally and occasional upstream. The arrangement of the grains in the cluster influences which particles are prone to entrainment (de Jong, 1991; James, 1993). In order to explain the selective entrainment of cluster particles, de Jong (1991) invokes the idea of local instantaneous flow conditions, not necessarily the flood flows envisaged by Brayshaw (1984).

Large individual particles can induce two main flow vortex systems (Figure 1.6; Acarlar and Smith, 1987a), whilst the occurrence of clusters is associated with the development of complex three-dimensional flow structures (Figure 1.7; Kirkbride, 1993; Robert *et al.*, 1996; Lawless and Robert, 2001). Six regions with characteristic vertical flow conditions have been observed over clusters: 1) flow acceleration on the stoss, 2) recirculation in the wake, 3) vortex shedding from the crest of the obstacle clast and shear layer, 4) flow reattachment, 5) upwelling downstream of reattachment and 6) flow recovery (Buffin-Bélanger and Roy, 1998; Lawless and Robert, 2001). Highly dynamic boundaries exist between these distinct flow regions,

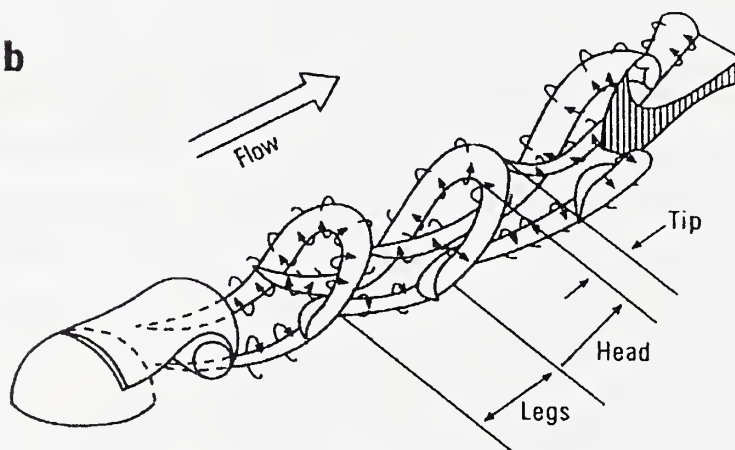
which are conducive to the generation of high magnitude, intermittent turbulent flow events (Buffin-Bélanger and Roy, 1998).

Figure 1.6: Vortex systems associated with an isolated particle, a) rolling down of the boundary layer in front of the clast and generation of a standing vortex system, b) horseshoe vortices generated from three-dimensional flow separation downstream of a particle, c) composite model for standing and hairpin vortices around an isolated clast. From Best (1996), after Acarlar and Smith (1987a).

a



b



c

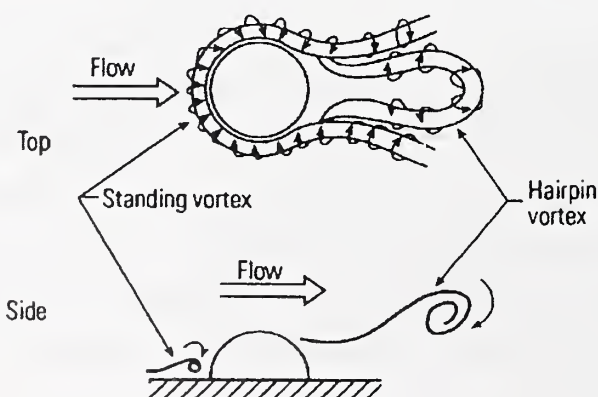
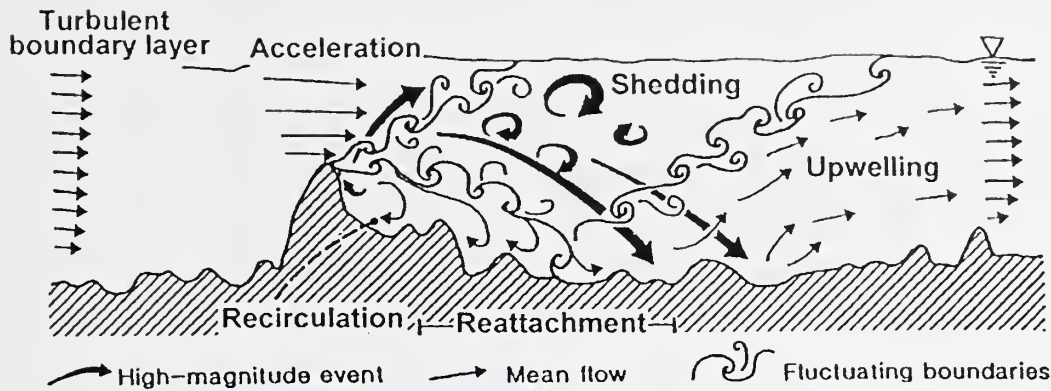


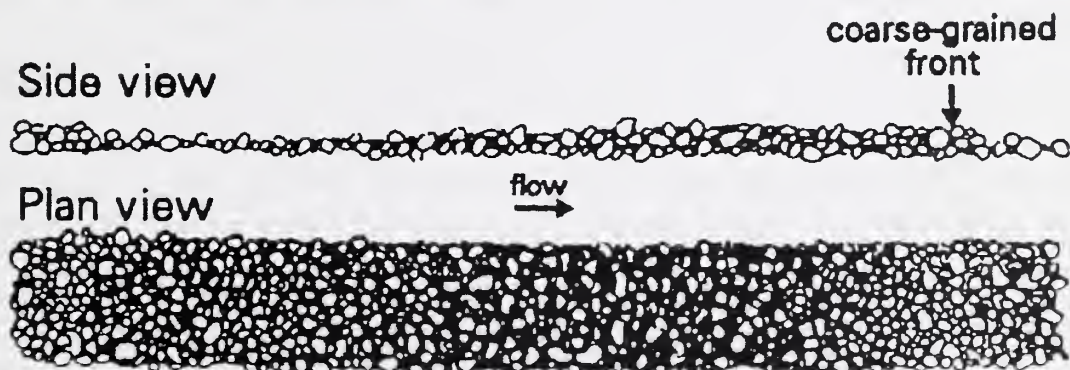
Figure 1.7: Flow regions associated with the presence of a pebble cluster on the turbulent flow field. From Buffin-Bélanger and Roy (1998).



1.3.2.2 Low-relief bedforms

Bedload sheets, first defined by Whiting *et al.* (1988; Figure 1.8), represent small amplitude (only a few coarse grain diameters in height) waves of sediment. The height of bedload sheets scales with grain size (Seminara *et al.*, 1996) rather than flow depth as is the case for dunes (Allen, 1984). The wavelength of bedload sheets is more variable than that of dunes, due to the relatively small zone of flow separation/deceleration (Bennett and Bridge, 1995). The length to height ratio of low-relief bedforms is greater than 60, and flow separation is not expected for values exceeding 14 (Dyer, 1986; Kostaschuk and Church, 1993). However, Whiting *et al.* (1988) did observe indications of local flow separation associated with bedload sheets. The mechanism responsible for sheet spacing is unclear, although Whiting *et al.* (1988) propose that size selective transport, elevated bed shear stress and sediment supply may play an important role.

Figure 1.8: Schematic diagram of a bedload sheet observed by Whiting *et al.* (1988) in Duck Creek, Wyoming. Lengths varied between 0.2-2 m, with heights of 2-20 mm. Flow direction is indicated by the arrow, which represents a distance of 50 mm.



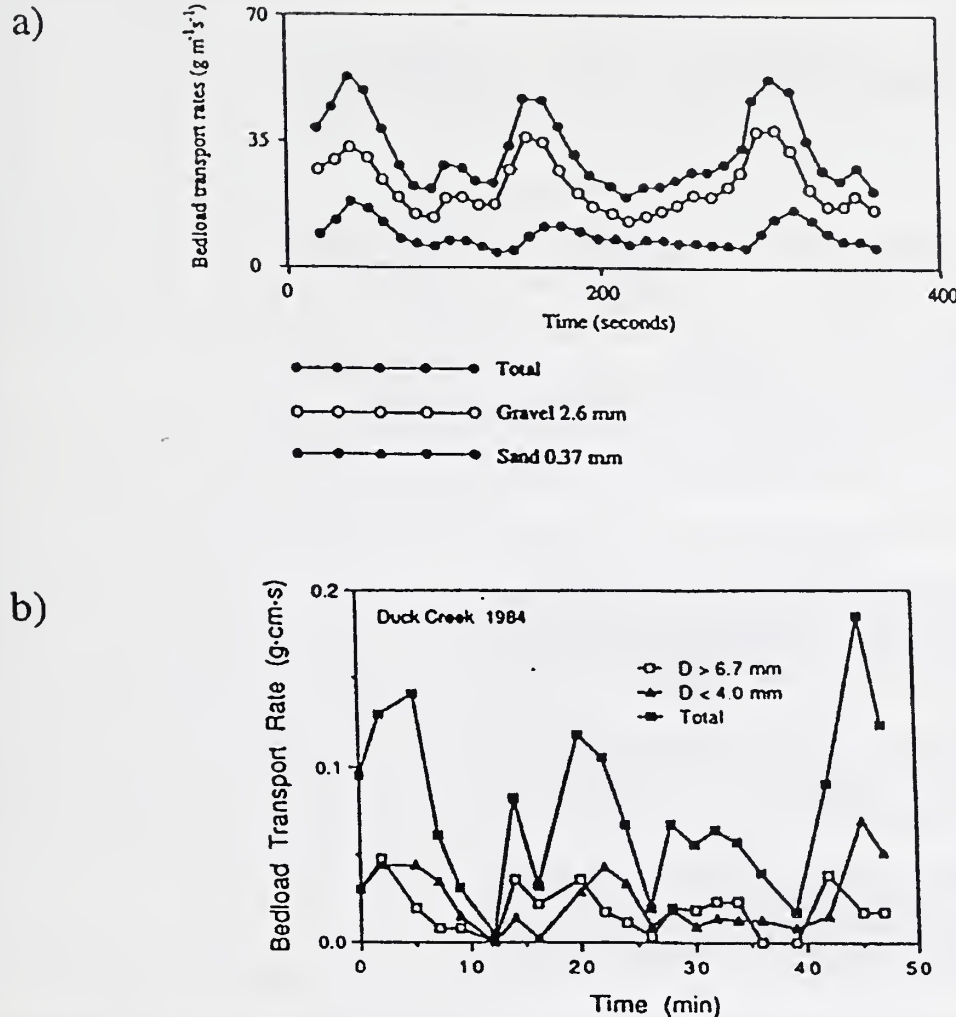
In addition to bedload sheets, asymmetric low-relief bed waves have been documented by Bennett and Bridge (1995a) and Livesey *et al.* (1998). The height of low-relief bed waves (10-17 mm) is dependent on flow depth, although it is similar to that of the bedload sheets (up to 12 mm; Bennett and Bridge, 1995).

However, low-relief bed waves have a much greater length (1.7-2.4 m) compared with bedload sheets (0.6-1.2 m). Bedload sheets can be superimposed on the stoss of the low-relief bed waves due to their greater migration rate.

Low-relief bedforms exhibit a sinuous crest, similar in texture to the bedload, a relatively fine grained stoss, and move over a coarse armour layer (Bennett and Bridge, 1995). Therefore, low-relief bedforms are characterised by distinct roughness transitions, although it is uncertain how this influences the local turbulent flow structure and sediment transport (Antonia and Luxton, 1971, 1972; Robert *et al.*, 1992, 1996; Best, 1996). Variations in transport rate along the length of a low-relief bedforms cause cyclical pulses in sediment transport rates of up to an order of magnitude to result from sheet migration (Iseya and Ikeda, 1987; Kuhnle and Southard, 1988; Whiting *et al.*, 1988). Most of the transported grains follow a dune like grain path (Wilcock and McArdell, 1993), being deposited in the lee, buried by the migrating bedform and exhumed and re-entrained with the passage of the bedform. However, gravel clasts move infrequently and at random due to local scour or collisions from large grains already in transport (Kuhnle and Southard, 1988). The coarsest fractions can overpass several bedforms, whilst finer sediment may be transported in suspension. The migration of low-relief bedforms causes systematic variations in both total and fractional bedload transport rates (Figure 1.9), with the discharge of coarse sediment peaking near the leading edge of the sheet and fine sediment peaking with the passage of the stoss. Furthermore, the distinct pattern of sorting over bedforms developed in mixed sized sediment controls the spatial availability of grain fractions for sediment transport. However, the interactions between bed morphology, turbulent flow structure and sediment transport are not fully understood.

Iseya and Ikeda (1987) quantified fluctuations in sediment transport under supercritical flow conditions over a sand ($D_{50} = 0.37$ mm) and gravel ($D_{50} = 2.6$ mm) mixture which was characterised by alternating smooth, congested and transitional regions in the streamwise direction (Figure 1.10a). The transport of sand sized fractions peaked with the passage of the smooth sections, while the gravel discharge was greatest at the leading edge of the coarse section. Variations in total and fractional bedload transport rates were attributed to the migration of bedload sheets in the experiments of Kuhnle and Southard (1988; $D_{50} = 3$ mm, standard deviation = 2.6 mm). The bed and water surface slopes increased over the congested areas. Water surface slope was observed by Bennett and Bridge (1995a) to increase over the crest of low-relief bars in bimodal sediment. Dietrich *et al.* (1989) determined that a low sediment supply caused the bed to coarsen due to preferential transport of finer grains, and sediment transport to become concentrated in a narrow ribbon at the centre of the channel (Figure 1.10b). Conversely, if the sediment supply exceeded the capacity of the flow to transport the mixture, bedload sheets developed and the surface of the bed did not coarsen. Consequently, Dietrich *et al.* (1989) suggested that temporal fluctuations in sediment supply led to the production of bedload sheets e.g. coarse regions result from local reductions in sediment supply.

Figure 1.9: Temporal variations in total and fractional transport rates due to grain size sorting over the surface of migration bedforms, a) Iseya and Ikeda (1987), and b) Whiting et al. (1988).



A heterogeneous sediment mixture is essential for development of bedload sheets and low-relief bed waves (Parker, 1991b; Seminara *et al.*, 1996; Tsujimoto, 1999), as exemplified by the flume experiments of Dietrich *et al.* (1989) where bedload sheets were only apparent with the addition of sand to fine gravel (Figure 1.10b). Furthermore the ratio of the different grain size fractions is important in the formation of these bedforms (Table 1.5; Iseya and Ikeda, 1987; Ikeda and Iseya, 1988). Dunes may form in preference to bedload sheets where sand dominates the sediment mixture (Kuhnle, 1996). Conversely, if there is a dearth of sand, finer size fractions will only be released once the gravel is in transport and bedload sheets will not form. It is critical to increase our understanding of the effect of bedforms on local surface sediment segregation, and the availability of different grain size fractions. Where bimodal sediments prevail it is uncertain whether or not the bedload is bimodal at all stresses, and if the mean grain size gradually increases, or abruptly switches from one mode to the other (Wathen *et al.*, 1995).

Figure 1.10: Schematic model of bedload transport, longitudinal sediment sorting and sediment supply. Flow and sediment transport is from left to right.

a) Iseya and Ikeda (1987).

BED STATE	CONGESTED	TRANSITIONAL	SMOOTH	CONGESTED
PLAN VIEW				
LONGITUDINAL VIEW				
PARTICLE MOVEMENT	INTERMITTENT	USUALLY CONTINUOUS	INTERMITTENT	
BEDLOAD TRANSPORT RATE	max		sand	gravel
min				
BEDLOAD BALANCE	in	out		
AGGRADING				AGGRADING
DEGRADING				
BED SLOPE	STEEP	INTERMEDIATE	GENTLE	STEEP
SEDIMENTARY STRUCTURE OF SUPERFICIAL LAYER	OPEN-WORK	HALF MATRIX-FILLED	MATRIX-FILLED	OPEN-WORK

b) Dietrich *et al.* (1989).

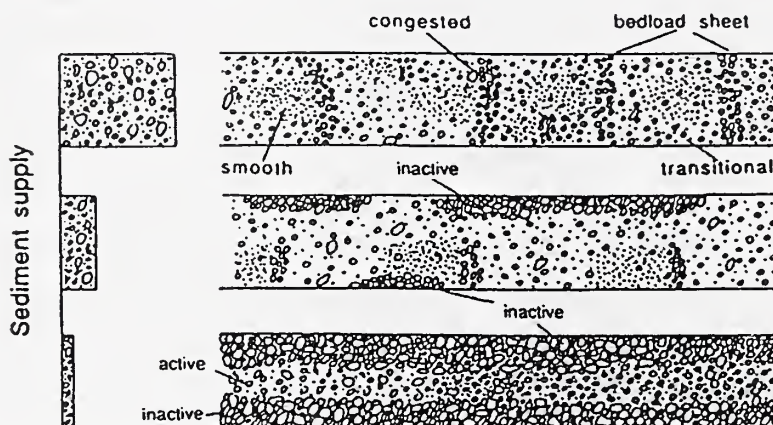


Table 1.5: Effect of the percentage of gravel ($D_{50} = 6.4 \text{ mm}$) and sand ($D_{50} = 0.45 \text{ mm}$) in a sediment mixture on the bed configuration. From Ikeda and Iseya (1988).

% of gravel	Description of the bed state
100	Plane bed
90-50	Low-relief linguoid bedforms. Crests composed of open-work gravel. Entire bed covered with gravel and interstices filled with sand.
< 50	Sharp, continuous crests. Patches of sand. Bedform height increases with sand content. Gravel (all matrix-filled) accumulates in troughs. Sand dominates bed, whilst most gravel particles are buried.

Wilcock (1992) found that the heights of dunes were diminished when developed in more poorly sorted log-normal sediments due to the coarse clasts protecting the bed from scour in the lee. Furthermore, the addition of finer sediment caused the dunes to develop at lower shear stresses. However, Klaassen (1992) observed dune height and length to both be greater in a log-normal mixture compared with a uniform sediment. Wilcock (1992) and Klassen (1992) employed similar standard deviations (1.1-2.3), but different median

grain sizes (1.83 and 0.6 mm respectively), which may be responsible for the contrasting observations. Klassen (1992) also noted that the dune crests were composed of finer, better sorted sediment compared with the trough, influencing fractional transport rates. Snishchenko *et al.* (1989) recorded reduced heights and lengths for dunes developed in non-uniform bedload compared with those developed in uniform sediment. Moreover, Kuhnle (1993a) observed the height of bedforms to fall as the proportion of gravel in the sediment mixture increased, and Lanzoni (2000) notes that the height of bars is dampened in bimodal sediments compared with bars generated in uniform sediment. If the separation between the modes is large, the two grain size populations behave independently i.e. isolated and starved bedforms form in the finer sediment and migrated over a coarse armour layer (Wilcock, 1992).

Bennett and Bridge (1995a) observed crude planar stratification and imbrication of the largest grains within bedload sheets. Thin planar laminae (less than 5 mm thick) are composed of alternating coarse and fine layers resulting from the migration of the bedload sheet trough and crest respectively (Livesey, 1995). Dune deposits are characterised by highly evolved cross-stratification, which is not associated with bedload sheets since well-developed lee slopes at the angle-of-repose are only associated with the largest bedload sheets, and any depositional patterns maybe disrupted by the large clasts. However, poorly developed, low-angle foresets ($< 20^\circ$) can occur due to the migration of bedload sheets which are superimposed on the back of low-relief bed waves and influence the supply of sediment to the crest of the bed wave (Costello and Southard, 1980; Whiting *et al.*, 1988; Raudkivi and Witte, 1990; Ditchfield and Best, 1992; Livesey, 1995).

Whiting *et al.* (1988) have proposed the 'catch and mobilise' theory regarding the formation and migration of bedload sheets. They believe that bedload sheets form due to the interactions of coarse and fine sediment during transport. Fine sediment infills the interstices of immobile coarse clasts causing the bed to be smoothed and the loss of momentum due to the collective wakes of the large particles to be decreased. Therefore any elevated, coarse grains will be subject to an increased drag force. Furthermore, infilling by fines diminishes the pivoting angles of the coarser sediment (Komar and Li, 1986). Consequently, the coarser clasts are remobilised as a result of the fine sediment infilling their interstices. However, the smoothing of the coarse grains will decrease the generation of vortices and eddy shedding, and cause the magnitude and frequency of turbulent events capable of entrainment to diminish. Furthermore, if the coarse grains are immobile, the pivoting angles will remain unchanged, but the deposition of finer material will cause the larger clasts to be smothered, further reducing their mobility. In order to explain the wave like nature of the bedload sheets, it is suggested by Whiting *et al.* (1988) that either the infilling with fine sediment is patchy, or that the coarser sediment is deposited as a cluster by particle interaction, forming a barrier to the movement of the finer material. However, the 'catch and mobilise' theory has not been backed up with quantitative data to date, and is not supported by the findings of Wilcock and McArdell (1993) and

Bennett and Bridge (1995a), who observed bedload sheets composed of relatively fine size fractions migrating over a coarse armour layer.

Ferguson *et al.* (1989) argue that boundary shear stress could not fully adjust over the length of a bedload sheet to the changing bed roughness, resulting in a similar boundary shear stress acting on both fine and coarse areas. However, the reduced grain pivoting angles (Komar and Li, 1986) of large clasts located on the fine grained crest compared with the coarse trough, results in lower critical shear stresses. Consequently, coarse grains will be moved from smooth areas associated with relatively low critical shear stress, and deposited in the next downstream coarse trough, characterised by large pivoting angles and critical shear stress. However, Livesey (1995) notes that boundary shear stress will not be similar over alternating regions of different roughnesses.

Bennett and Bridge (1995a) indicate that bedload sheets develop due to preferential transport of fine grains over a coarse armour layer, since the grain size distribution of the sheets is similar to that of the bedload. High bed shear stresses and turbulence intensities are associated with the coarse trough, and low values are located over the finer-grained crest, causing fine sediment to be entrained and winnowed from the trough and deposited on the bedform crest. Variations in shear stress over bedload sheets are thought by Bennett and Bridge (1995a) to result from changes in resistance provided to the flow by individual grains as they identified little or no form resistance (i.e. drag due to the presence of bedforms). Bed shear stress has been observed to initially overshoot when the boundary changes from smooth to rough (Antonia and Luxton, 1971), as occurs between the crest and trough.

Low-relief bedforms may be genetically related to two-dimensional dunes which develop in well sorted, coarse sand rather than sediment mixtures (Costello and Southard, 1980; Wilcock and Southard, 1989; Raudkivi and Witte, 1990; Ditchfield and Best, 1992; Coleman and Melville, 1994; Best, 1996). Two-dimensional dunes have a greater range of wavelengths compared with dunes, and a lower height (Costello and Southard, 1980), which is also true for low-relief bedforms. However, the length to height ratio of two-dimensional dunes is less than that of bedload sheets and low-relief bed waves (Bennett and Bridge, 1995; Livesey, 1998), and two-dimensional dunes do not exhibit distinct roughness transitions. The limited occurrence of flow separation, and therefore restricted shear layer development, helps account for irregular bedform spacing, variations in morphology and dynamics, and bedform amalgamation under equilibrium conditions. It is a matter of current debate whether bedload sheets and low-relief bed waves represent distinct bedforms, or are transitional dunes formed in a mixed-size sediment. The development of steeper, low-relief bedforms may raise the importance of flow separation and shear layer development, and increase their moderating affect on sediment transport and bedform spacing, facilitating the evolution of dunes. Formative processes for low-relief bedforms include bedform amalgamation, particle interaction, selective

entrainment and bed shear stress perturbations (Whiting *et al.*, 1988; Bennett and Bridge, 1995; Seminara *et al.*, 1996; Tsujimoto, 1999).

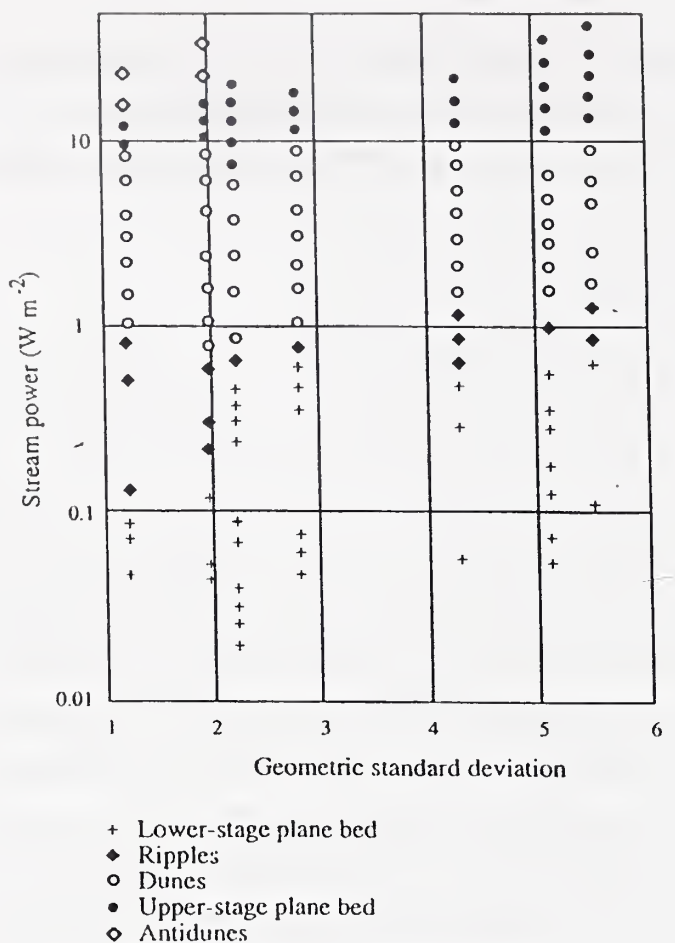
There still remains a dearth of data regarding the morphology, dynamics, bed surface sorting patterns, formation, stability, flow conditions and sediment transport of bedforms developed in bimodal sediment. Such information is vital when employing models to predict sediment transport, sorting, bedform development and stratigraphy.

1.4 Bedform stability fields

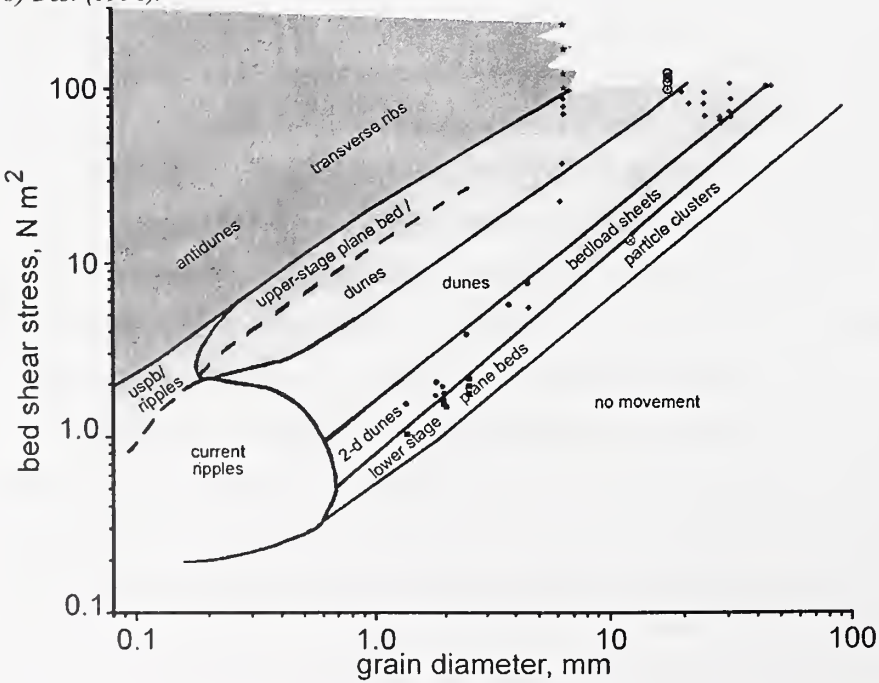
Bedforms are often classified by a mean sediment size and some function of the flow strength (e.g. stream power, shear stress and velocity), although other factors affect bedform development (e.g. flow depth, Southard and Boguchwal, 1990). Most work into the stability fields of bedforms has been undertaken in controlled laboratory flume experiments with equilibrium flow conditions, often using uniform, well-sorted sediment (Leeder, 1982; Allen, 1982; Southard and Boguchwal, 1990). Even in these simplified cases areas of overlap occur, due to different experimental arrangements and the presence of transitional bedforms. The great advantage of bedform stability diagrams (Figure 1.11) is that they can be used for both forward and reverse modelling. For example, if the flow and sediment characteristics are known the bed configuration can be predicted, and conversely the past flow conditions can be estimated from the dimensions of preserved bedforms. However, when applying bedform classifications it should be remembered that in natural streams both sediment and flow characteristics vary spatially and temporally, and there is often a lagged response and hysteresis effects. Therefore, the bedforms may not be in equilibrium with the prevailing flow conditions (Richards, 1982). Furthermore, since little data has been compiled from mixed sized sediment mixtures, sorting effects are also often not considered. In addition, the mean grain size may not be truly representative of a poorly sorted or multimodal sediment, potentially causing bedforms to be incorrectly plotted on stability diagrams. The need to construct a bedform phase diagram which accounts for more complex grain size distributions (e.g. Chiew, 1991; Figure 1.11a) is highlighted by the fact that some bedforms are not observed in uniform sediment mixtures e.g. bedload sheets (Dietrich *et al.*, 1989). Currently, the bedforms present for a given sand-gravel mixture and flow strength cannot be reliably predicted. The extrapolation of bedform phase diagrams to include greater grain sizes (Best, 1996; Figure 1.11b) is hindered by a lack of experimental data employing high flows over coarse sediment. Chiew (1991) observed that increasing the sorting of the sediment mixture caused ripple formation to occur at higher stream powers (Figure 1.11a). The increased number of less mobile coarse grains in more poorly sorted sediment mixtures inhibit flow separation over bed defects. The coarser clasts aid vertical mixing that counteracts variations in static pressure over bed defects, causing flow separation, defect amplification and ripple formation to be hindered (Leeder, 1980).

Figure 1.11: Bedform phase diagrams.

a) Chiew (1991): Employed seven unimodal sediment mixtures with different standard deviations (1.2 to 5.5, a measure of sediment sorting), but the same median diameter ($D_{50} = 0.6 \text{ mm}$).



b) Best (1996).



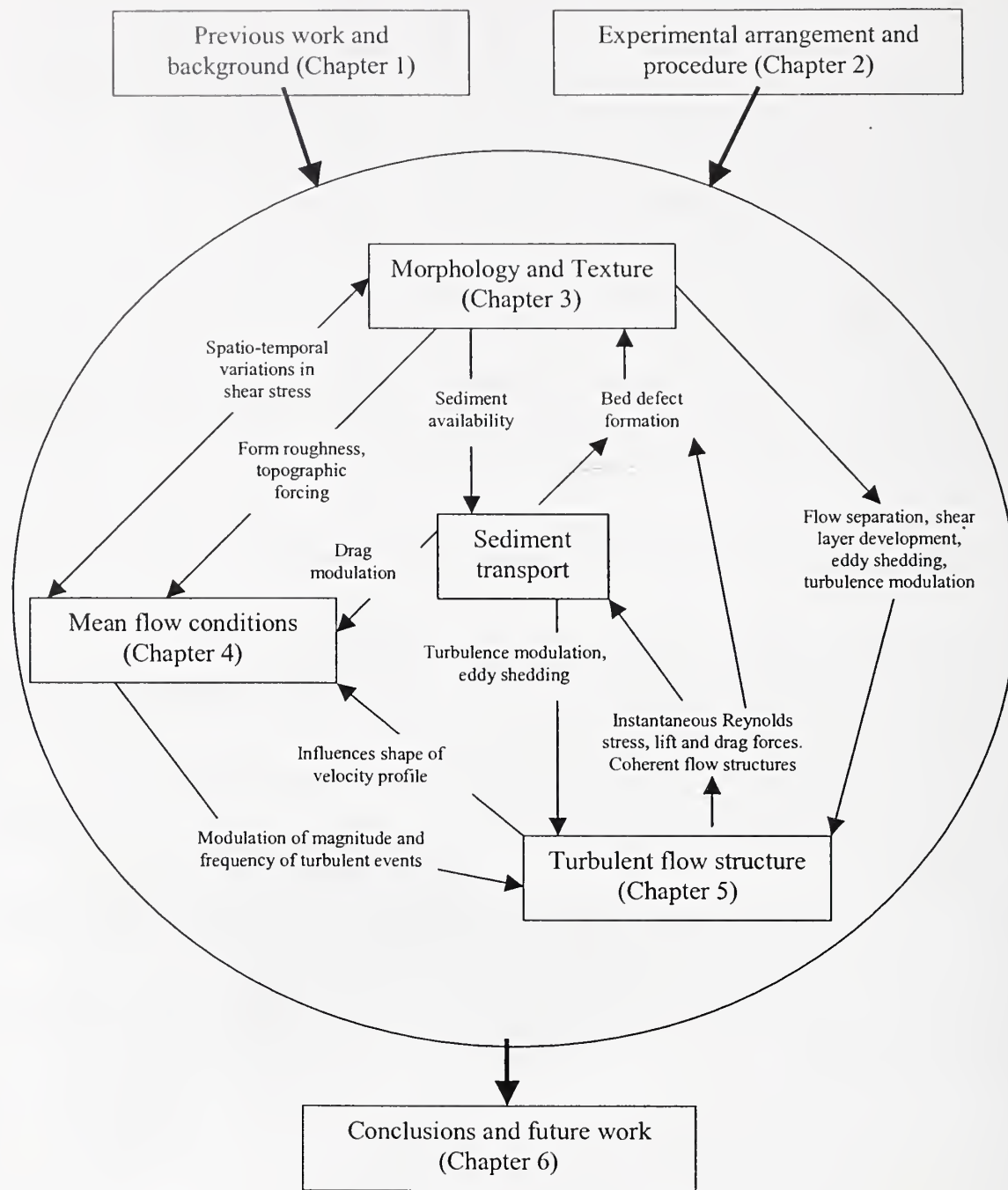
1.5 Aims and structure of thesis

Laboratory flume experiments have been conducted in order to investigate the morphology, sediment transport and associated turbulent flow structure of bedforms developed in a bimodal sand-gravel mix. Various measurements were taken under equilibrium flow conditions, over a range of shear stresses and flow depths, in order to accurately define the hydraulic and sedimentological characteristics, and highlight any correlations between variables and spatio-temporal trends. The data collected included velocity and turbulence time series (laser doppler Anemometer, LDA), water and bed surface profiles, samples of the surface texture, and total and fractional sediment transport rates. Further details of the experimental arrangement and procedure are considered in Chapter 2. The resulting data set is analysed and presented in three main sub-sets based on the type of measurement (e.g. (a) morphology and surface texture, (b) mean flow structure, and (c) turbulent flow structure), as illustrated in Figure 1.12. Measurements of sediment transport are considered at various points throughout the thesis. As highlighted by Figure 1.12, the sub-sets of data cannot be studied in isolation due to the dominant existence of feedbacks and interrelationships, which are vital in helping understanding how bedforms develop, evolve and migrate.

The analysis of the data collected enables the following hypotheses to be tested.

- Can different bedform populations be distinguished by their morphology?
- Do variations in flow discharge and depth influence bedform morphology, texture, total and fractional sediment transport rates, and mean and turbulent flow structure?
- Does large-scale flow separation occur over bedload sheets and low-relief bed waves?
- Does the turbulent flow structure, and total and fractional sediment transport rates, respond to changes in the bed roughness?
- Are bedload sheets and low-relief bed waves formed due to bedform amalgamations, spatial variations in shear stress, selective entrainment and interactions between particles?
- Do bedload sheets and low-relief bed waves exhibit a different morphology and associated turbulent flow structure to that of dunes?

Figure 1.12: The interrelationships and feedbacks between the main components characterised in the experimental flume experiments.



Chapter 2 : Experimental apparatus and procedure

2.1 Equilibrium flow and experimental program

2.1.1 Equilibrium conditions and the test section

All measurements were taken once the flume had attained uniform flow conditions. The equilibrium status was characterised by constant and parallel water and bed surface slope over time (only locally true where bedforms are present), no erosion or deposition of sediment, and consistent bedform configuration over time in the test section (Williams, 1967). The equilibrium stage was therefore identified from successive water and bed surface profiles and observations of bedform geometry. The test section was free from entrance and exit effects, extending 2.2 m from 10 m downstream of the headbox to 1.35 m upstream of the sediment trap. All experiments were run for at least eight hours before any measurements were recorded to ensure uniform flow conditions. The frequency and time period over which observations are made depends mainly on the bedform configuration (Guy *et al.*, 1966).

2.1.2 Experimental procedure

Figure 2.1 illustrates the basic procedure employed during an experimental run.

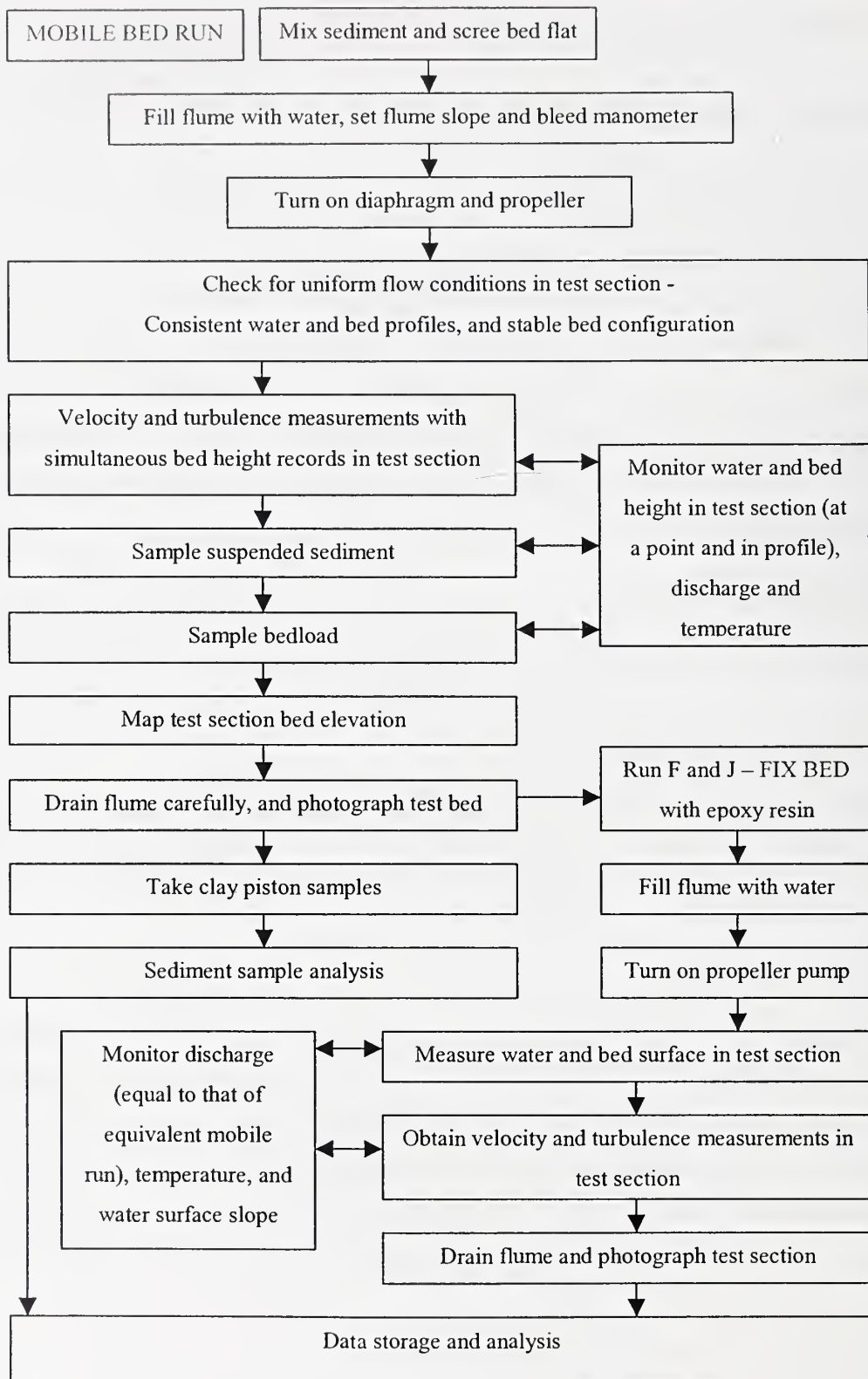
2.1.3 Mobile bed experiments

Fourteen experimental runs were conducted employing a mobile sediment bed. Eight of these experiments were characterised by a water depth of 0.17-0.18 m (*Series 1*), while the remaining six runs exhibited a flow depth of 0.14-0.15 m (*Series 2*).

2.1.4 Fixed bed experiments

A further two experimental runs were executed over an immobile sediment bed, formed during a previous mobile sediment bed experiment (i.e. Runs F and J). The bed configuration was preserved along the whole length of the flume by carefully applying epoxy resin (Araldite resin GY6010, hardener HY955). To prevent the resin sticking to the flume, aluminium foil was inserted between the sidewalls and the sediment using a thin metal strip, causing only minor distortion to the sediment bed. Once the resin had been applied and set, the foil could then be torn to the bed level, and the small gap left by its insertion filled with plasticine.

Figure 2.1: Experimental procedure.



2.2 Laboratory flume facility

The experimental runs were executed in an adjustable slope recirculating laboratory flume, with a channel 15.2 m long, 0.356 m wide and 0.457 m deep (Figure 2.2, Plate 2.1). A steel frame supported the flume, and the walls and base of the channel were constructed from perspex, enabling the water and sediment (which were recirculated separately) to be observed directly during the experiments. The experimental facility was located in the USDA-ARS National Sedimentation Laboratory in Oxford, Mississippi, USA.

Plate 2.1: Experimental facility.

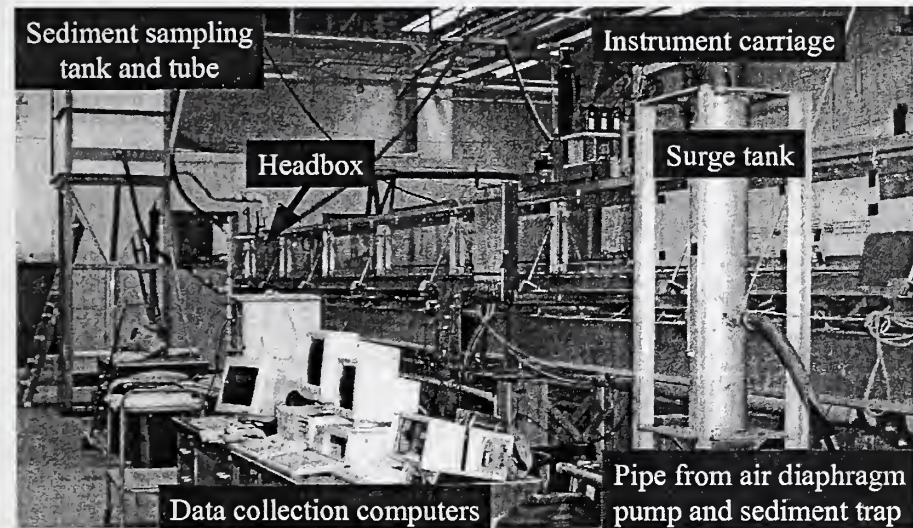
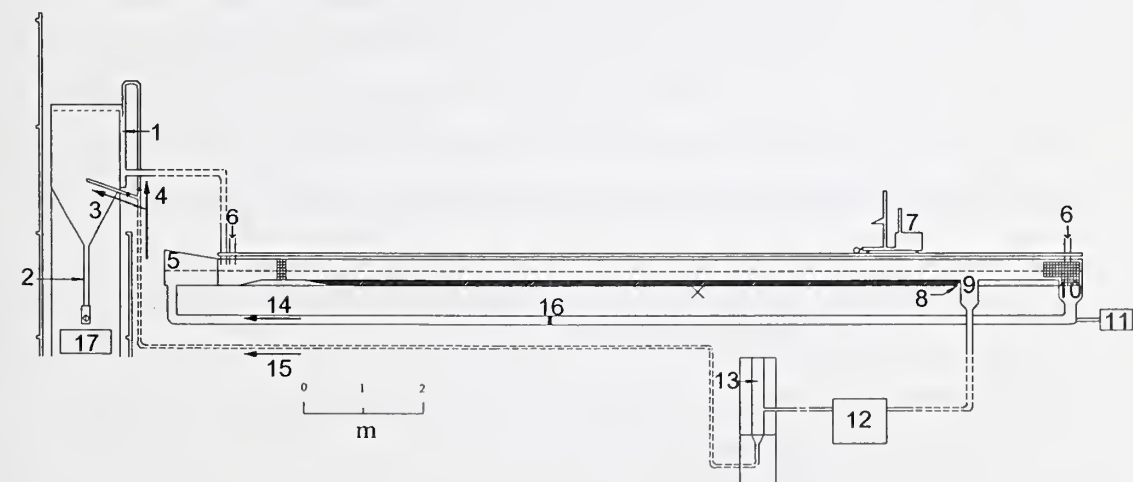


Figure 2.2: Schematic diagram of the laboratory flume employed. 1) overflow section, 2) accumulation tube, 3) sediment sampling, 4) sediment and water recirculation, 5) headbox, 6) water supply, 7) Instrument carriage, 8) sediment retaining wall, 9) sediment trap, 10) tail box, 11) propeller pump, 12) diaphragm pump, 13) surge tank, 14) water recirculation, 15) recirculation of water and sediment, 16) Venturi meter, 17) manometer and standpipes.



2.2.1 Flume channel

At the upstream end of the channel the water and sediment passed through a metal grid (0.05×0.05 m square openings) which covered the whole flume cross-sectional area and extended 0.15 m downstream. The grid helped to suppress large-scale turbulence. It was located at the upstream edge of a 1.7 m long roughened concrete false bottom, which was equal in thickness to the sediment bed (0.076 m). The false bed section aided the development of a turbulent boundary layer before the flow reached the mobile sediment bed. The ends of the false bed tapered off over a distance of 0.5 m to the level of the flume bottom. The mobile bed sediment was screed so that it formed an even surface with the fixed bed in this transitional zone.

Two coupled sets of screw jacks enabled the flume to be tilted about a pivot at its midpoint, allowing the flume channel slope to be fully adjustable. Adjustments of the flume slope (0-0.007) were made to facilitate the development of uniform flow conditions.

2.2.2 Water recirculation

After passing into the tailbox without overfall, the water was recirculated by a horizontal, adjustable speed propeller pump through a 0.152 m diameter pipeline which ran under the flume channel and up into the headbox. A piece of flat metal was installed in the headbox, the height of which could be adjusted to the water level in order to prevent stagnation and accumulation of any sediment. It also helped to dampen and break up any pump related turbulence flow structure in conjunction with the honeycomb baffle located just downstream.

2.2.3 Water discharge – Venturi meter and differential pressure transducer

The water discharge was adjusted using a computerised motor which controlled the rotation rate of the propeller pump. A Venturi meter (located 11 m downstream of the propeller pump in the return pipe) and associated differential pressure transducer were employed to determine the magnitude of the water discharge in the return pipe (Figure 2.3). The standpipes (2.1 and 5.8 m tall, differential head range of 5.5 m) allowed the differential pressure transducer to be calibrated and checked before each use. The transducer was connected to a computer which recorded the discharge over periods of five minutes. The value recorded remained very stable during and between readings taken regularly during the course of an experimental run.

The Venturi meter's calibration curve (provided by the manufacturer) and differential pressure transducer were verified by timing a cork over a distance of 6.4 m, and recording the flow depth and flume width, enabling an independent check of discharge. Five repeat measurements were taken at each propeller pump discharge setting. Simultaneously the discharge was recorded by the computer connected to the Venturi meter via the differential pressure transducer. During calibration the flume slope was set to zero, and the

flume contained no sediment allowing the diaphragm pump to be idle. The water discharge measurement equipment was checked over a range of flow strengths and demonstrated close agreement as illustrated in Figure 2.4.

Figure 2.3: Manometer.

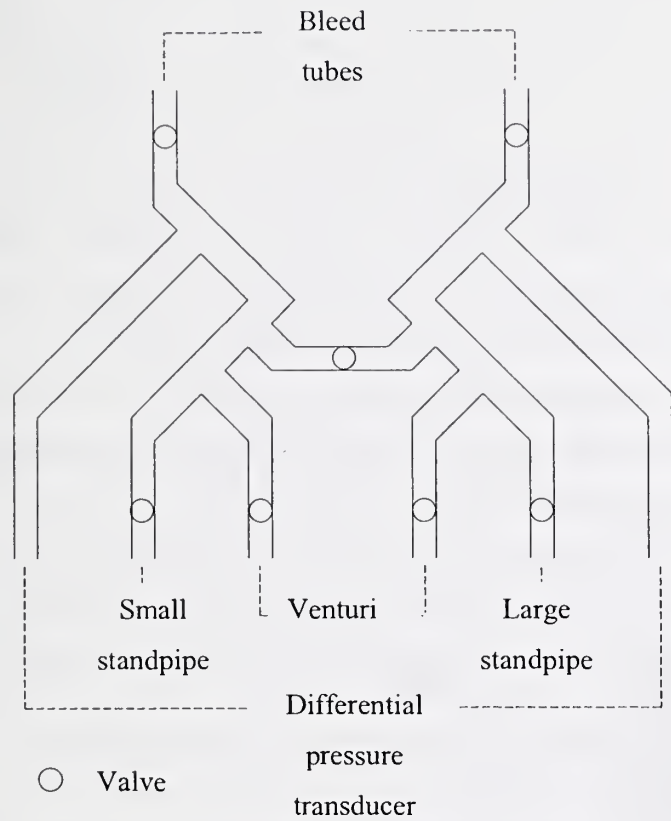
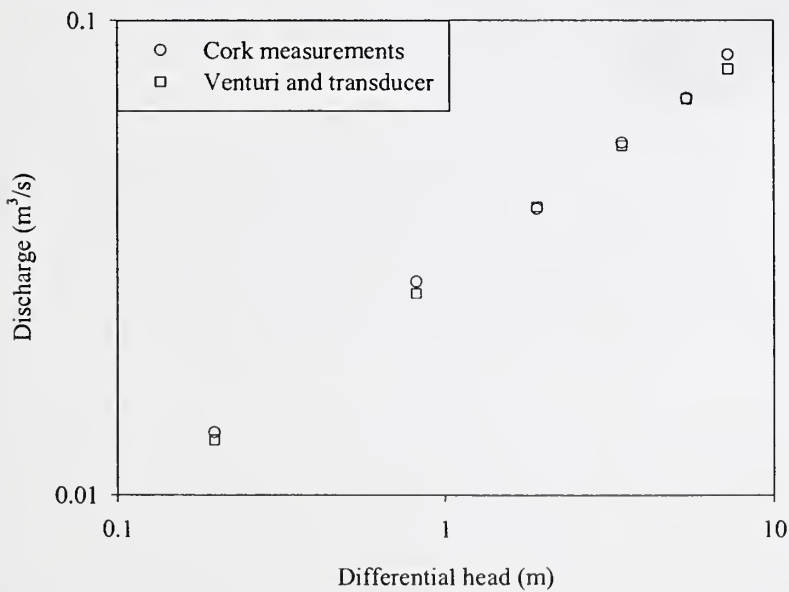


Figure 2.4: Calibration of the Venturi meter and differential pressure transducer.



Total water discharge also included a minor component resulting from the sediment recirculation system. In order to calibrate the air diaphragm pump (Plate 2.2), the pipe work leading from the overflow section of the accumulation tank was extended, enabling the system to be redirected into a V-notch weir. The container was filled to the bottom edge of the weir, and the water level measured with a point gauge. The air diaphragm pump was then run at intervals of 35 kPa. Water surface oscillations were minimised by a baffle that separated the discharge point of the inflow pipe from the measuring section and weir. At each pump setting the height of the water surface in the container was recorded. The point gauge was located in a narrow tube connected to the main chamber to further dampen any fluctuations in the water surface. However, fluctuations were observed, and so an average value was deduced from the point gauge readings of the maximum and minimum elevations of the water surface. In addition, for each pressure setting of the pump the time for 50 pump strokes was recorded (30-90 s). The procedure was repeated four times, and an average discharge for each pressure setting calculated (Figure 2.5). The diaphragm pump was set to a constant pressure in all experiments (345 kPa). Consequently, 0.0087 m³/s was added to the measured propeller pump discharge in order to calculate total water discharge (Figure 2.5). The discharge from the diaphragm pump accounted for 17-34 percent of the total discharge.

Plate 2.2: Air diaphragm pump which recirculates bedload.

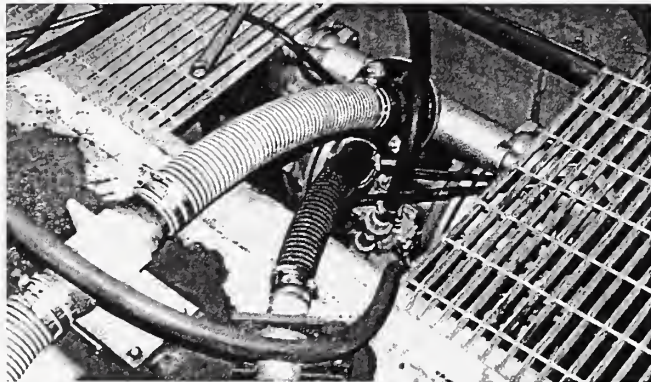
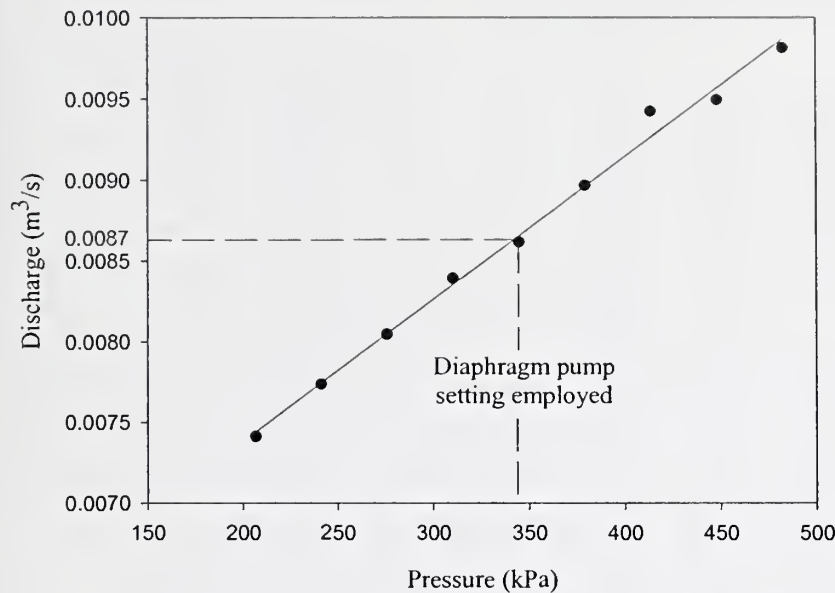


Figure 2.5: Calibration of the air diaphragm pump ($R^2 = 0.99$).



The water was not discharged from the weir back into the flume, and consequently water was continually added to the system. The water level in the flume varied, which may have slightly altered the performance of the air diaphragm pump. Changes in roughness in the recirculation system (e.g. sediment in transport, air bubbles, blockages and leaks) and variations in the discharge for each stroke of the pump, could cause the actual discharge of the air diaphragm pump to diverge slightly from the discharges predicted here.

2.3 Sediment mixture, recirculating and sampling

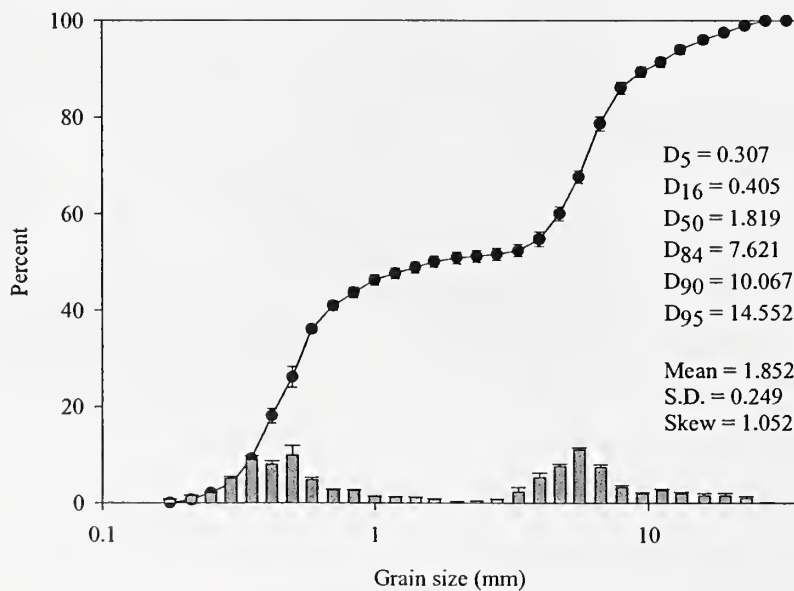
2.3.1 Bulk sediment mixture

In order to evaluate the grain size distribution of the bulk sediment mixture samples greater than 10 kg in weight were obtained (representative sample size equal or greater than 7.5 kg; Church *et al.*, 1987). Ten samples were taken before any runs had commenced. A further three samples were collected between runs C and K, in conjunction with clay-piston samples and photographs of the undisturbed sediment bed. Two final samples were obtained between runs F and J. As is illustrated in Table 2.1, good agreement was found between the samples. The experimental bimodal mixture has a peak in the sand (0.5 mm) and gravel (5.6 mm) sediment sizes, with grain sizes ranging from 0.177 mm to 32 mm (Figure 2.6).

Table 2.1: Grain size statistics for the bulk sediment mixture. The mean, standard deviation (SD) and skewness (skew) were calculated using moment analysis (Friedman, 1961).

Sample taken before	Percentile (mm)								
	5	16	50	84	90	95	Mean	SD	Skew
Run D	0.30	0.40	1.50	7.33	8.94	12.80	1.77	0.25	1.05
Run D	0.31	0.40	2.31	7.82	11.01	15.81	1.92	0.24	1.04
Run D	0.31	0.40	1.41	7.22	9.09	16.65	1.77	0.25	1.08
Run D	0.30	0.40	3.46	7.71	9.73	13.28	1.95	0.25	0.97
Run D	0.31	0.40	1.82	7.75	10.35	15.27	1.89	0.25	1.05
Run D	0.31	0.41	1.76	7.75	10.49	15.22	1.89	0.25	1.05
Run D	0.31	0.40	1.80	7.58	10.38	15.74	1.87	0.25	1.05
Run D	0.30	0.39	1.25	7.25	8.88	12.48	1.70	0.25	1.10
Run D	0.30	0.40	2.05	7.68	10.51	15.66	1.89	0.25	1.04
Run D	0.30	0.40	1.47	7.53	10.18	15.44	1.80	0.25	1.08
Run K	0.31	0.40	1.86	7.81	10.28	14.51	1.87	0.24	1.05
Run K	0.31	0.41	1.80	8.08	11.28	15.69	1.92	0.25	1.05
Run K	0.31	0.41	1.96	7.80	10.43	14.70	1.90	0.25	1.03
Run F	0.32	0.43	1.36	7.34	9.19	12.94	1.80	0.26	1.08
Run F	0.31	0.44	1.47	7.67	10.28	15.11	1.86	0.25	1.09
Average	0.31	0.41	1.82	7.62	10.07	14.55	1.85	0.25	1.05

Figure 2.6: Bulk sediment mixture used in the present experiments. Error bars represent the standard deviation of samples.



2.3.1.1 Mixing of the bed sediment

Before bulk sediment samples were taken, or an experimental run commenced, the sediment bed was mixed. The flume was divided lengthways into 36 mixing cells. In turn each cell was mixed, approximately half the sediment removed and replaced by an equivalent amount of sediment from another designated cell, and then

thoroughly mixed together. The procedure was repeated twice for every mixing cell. Before commencing an experimental run the bed was then screed flat before water was added to the system.

2.3.2 Bedload recirculation and sampling

A sediment trap, 0.26 m long and extending across the full flume width, was located 1.2 m upstream from the flume tailbox (Plate 2.3). Complete cross-sectional coverage is necessary for accurate determination of fractional sediment transport rates (Wilcock, 1992). All of the transported sediment, with the exception of some of the suspended fines at high discharges, fell down into the sediment trap. On the upstream side of the trap was located a small retaining wall which limited the extent of the sediment slip face. The top of the wall was approximately level with the deepest bedform troughs. The upper part of the sediment trap had vertical walls, which at the bottom became inclined in order to connect to the narrower piping. An air powered diaphragm pump transported the sediment, and some water, through a 0.51 m diameter pipe. A surge tank was installed on the pipeline to smooth out the rapid pulsing movement generated by the air diaphragm pump. The pipeline fed the sediment and water mixture vertically down into the flume channel, just downstream of the headbox, via the overflow section of the accumulation tank.

Plate 2.3: Bedload sediment trap. Flow is from bottom to top. The flume is 0.356 m wide.



Downstream of the sediment trap the flume base was raised to the level of the mobile sediment bed. Any sediment which overpassed the trap tended to settle and migrate along this section which extended to the tailbox. The trapping efficiency of the sediment trap is determined by how much of the total sediment transport is captured, and in mixed sized sediments it also relates to the proportion of each grain size of the transported sediment collected. The efficiency of a sediment trap varies with velocity, depth, particle size, bedload magnitude, trap dimensions and bed configuration (Hubbell, 1964).

Poreh *et al.* (1970) investigated the factors influencing sampling efficiency using eight unimodal sediments ranging from 0.7 to 4.5 mm in diameter. They found that the efficiency varied with the downstream extent of the sampling slot and the particle jump length. The latter was in turn influenced by the Froude number and the size of the sediment. Efficiency reached 100 percent for the bedload component when the slot length was equal to approximately 40 times their sediment diameter. The length of the trap (0.26 m) used in the present experiments is significantly greater than 40 times the D_{50} (1.819 mm) of the bulk sediment mixture (0.07 m). No gravel sized sediment was allowed to overpass the sediment trap in the present experiments as it would damage the propeller pump, limiting the maximum discharge which could be employed.

With everything else constant, efficiency decreased slightly with increasing particle size of the bedload in the experiments of Poreh *et al.* (1970), which may have implications for the measurement of the natural cyclical variations in bedload transport. Furthermore, some of the suspended sediment evaded capture (Murphy and Amin, 1979; Poreh, 1970). Additional experiments were conducted by Poreh *et al.* (1970) using a graded sediment mixture produced by combining equal parts by weight of all the unimodal sediments previously employed. It was found that each fraction in the mixture was trapped with the same efficiency as when tested in isolation as an unimodal sediment.

Sediment samples were acquired and sieved in order to determine the total transport rate and the grain size distribution of the sediment in transport (Plate 2.4). The sediment entering the trap was collected by diverting the flow through a settling tank (accumulation tank cross-sectional area equals 1.3 m^2) before the water returned to the upstream end of the main channel. The water and sediment mixture entered the accumulation tank horizontally, 1 m below the overflow level which allowed the water to be returned to the recirculating system. The minimal vertical velocities in the tank facilitated the deposition of all size fractions into an upright accumulation tube attached to the bottom of the tank (0.115 m diameter). Four scales were attached to the side of the transparent accumulation tube and enabled the height of the sediment deposit to be read off at known times.

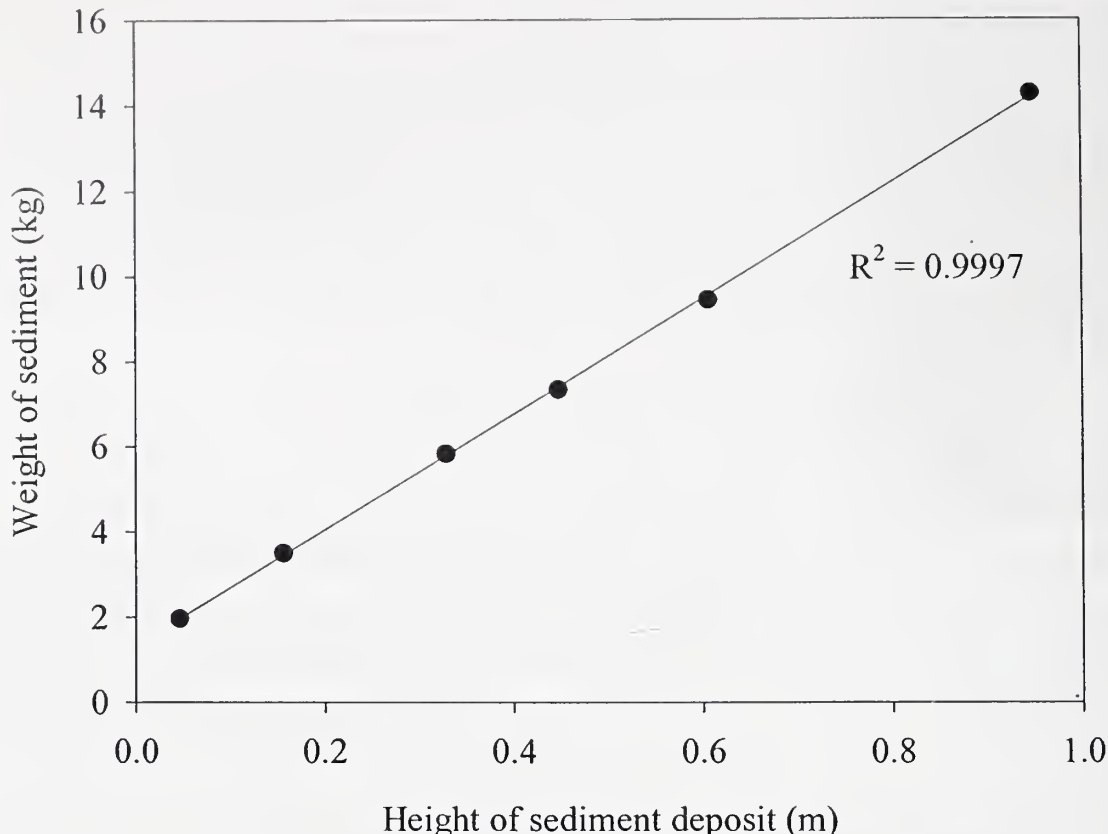
Plate 2.4: Collection of a bedload sample from the accumulation tube.



The accumulation tube was calibrated (Equation 2.1, Figure 2.7) in order that the retained sediment could be substituted by an equivalent mass of bulk sediment mix. Calibration was achieved by collecting sediment when running both pumps, and thereby causing the bed sediment to be transported, and also by tipping the bulk sediment mixture down the sediment trap with only the air diaphragm pump in operation. Both methods provided very similar results. Once a calibration sediment sample had been collected, part of the deposit was removed, dried and weighed, and the vertical adjustment of the sample in the tube recorded. Calibration was performed on six separate sediment samples. The length of time the sample is left in the tube, the specific region of a bedform being sampled and whether or not the tube is tapped, can cause the results to differ from that predicted by Equation 2.1.

$$\text{Weight of sediment (kg)} = 13.56 \times \text{height of deposit (m)} + 1.327 \quad (2.1)$$

Figure 2.7: Calibration of the accumulation tube.



Calibration of the tube enabled the mass of the sample to be repeatedly calculated from the height of the accumulating deposit, allowing an equivalent amount of bulk sediment to be manually added to the upstream end of the flume during the sampling process. Where the bedload was predominately sand, just the sand fraction of the bulk mixture was added into the flume channel. During low and moderate flows, the coarse size fractions are underrepresented in the grain size distribution of the transported sediment. However, since these coarse grain sizes occur in the tail end of the size distribution of the original sediment mix, the bulk mixture should resemble the transported sediment reasonably well. Furthermore, at low transport rates, the samples were relatively small compared with the total amount of material contained in the sediment bed. In order to minimise any effect of the replacement sediment, samples of the mobile sediment were acquired at the end of an experimental run. In addition to replacing the sampled sediment, its equivalent volume of water was removed from the headbox in order to keep the amount of water in the flume channel constant.

Bedload samples are subject to uncertainty resulting from bed morphology adjustments during sampling, natural variability and the difficulty of defining the contributing area of the bed due to the different mechanisms of entrainment, transport and deposition for each size fraction (Wilcock and McArdell, 1993).

Bedload samples were removed from the accumulation tube, dried, sieved and weighed. Grain size analysis was performed at $1/4 \phi$ intervals, where $\phi = -\log_2 D$ (mm), using sieves and associated shakers. Errors in the measurement of the size distribution can arise from grains passing diagonally through the square sieve openings, and by analysing samples which are too small to be representative. A larger sample is required as grain size increases. Where the largest clast represents 0.5 percent by weight of the total sample, this corresponds to a representative sample size of 7.5 kg for the bulk mixture used in the present experiments (Church *et al.*, 1987). All the bedload samples were typically significantly greater in weight than 7.5 kg with the exception of runs A, B and I (0.638, 2.583 and 7.030 kg respectively). However, these runs were characterised by the lowest water and sediment discharges, and the associated bedload was deficient in the coarser particles, which require a larger sample size to be adequately represented.

The bedload sample collection period varied from 60 to 1500 s depending on the sediment transport rate. Ideally a whole number of bedforms were collected. During experimental runs characterised by high rates of sediment transport, more than one bedload sample was taken (Table 2.2).

Table 2.2: Bedload samples

Run	Collection period (s)
A	1200
B	1200
C	840
D	580
E1	347
E2	373
F	295
G1	213
G2	190
H1	177
H2	145
H3	405
I	1500
J	561
K	522
L1	260
L2	416
M1	81
M2	133
M3	196
N1	80
N2	70
N3	60

2.3.3 Suspended sediment sampling

The suspended sediment load was sampled by a tube (0.01 m diameter) which protruded to the middle of the return pipe, and was situated just upstream of the propeller pump. At this point any particles which overpassed the sediment trap were assumed to be uniformly suspended throughout the return pipe due to the turbulence generated by the pump. The sample tube was first purged before six 20 s samples of water and sediment (about 3 litres each) were siphoned off into tarred buckets during an experimental run. Water was added to the flume in order to replace that removed. The sample buckets and contents were then weighed,

and the sediment allowed to settle. The majority of the water was then drawn off with a vacuum tube and the damp sediment transferred to dishes for oven drying (105 °C). Once cooled for two hours in a dessicator, the sediment was reweighed in the tarred dishes.

2.3.4 Sediment bed surface samples – clay piston sampler

The sediment bed surface was sampled at various points over any bedforms present (e.g. crest, stoss and trough) by employing a clay piston sampler with a diameter of 0.155 m (Parker *et al.*, 1982b; Wilcock and Southard, 1989; Bennett and Bridge, 1995a; Diplas and Fripp, 1992). The sampler was pressed firmly onto the surface of the sediment, which adhered to the clay within the sampler. The sediment was separated from the clay by washing the surface of the sample in a 180 µm sieve. The sediment was then oven dried, cooled in a dessicator, sieved at 0.25 phi intervals and weighted.

The sediment sampled was slightly damp and therefore was subject to capillary tension (Diplas and Fripp, 1992). When large clasts adhered to the clay, sand tended to mound around them. Therefore a layer greater than 1 grain diameter thick was sampled in these cases.

2.4 Measurement devices

2.4.1 Sediment bed and water surface elevations, and water surface slopes – ultrasonic probes

The acoustic profilers (Table 2.3) determine the distance between the probe head and the bed, or water, surface by employing the principle of an ultrasonic pulse-echo. The time difference between the emission of a sound wave and the interception of the reflected ultrasonic echo, as well as the velocity of sound in the intervening fluid must be known.

Table 2.3: Characteristics of the unfocused ultrasonic probes used to measure the elevation of the water (WS) and sediment bed surface (SB) (Derrow, 1993). NCPA stands for the National Centre for Physical Acoustics at the University of Mississippi.

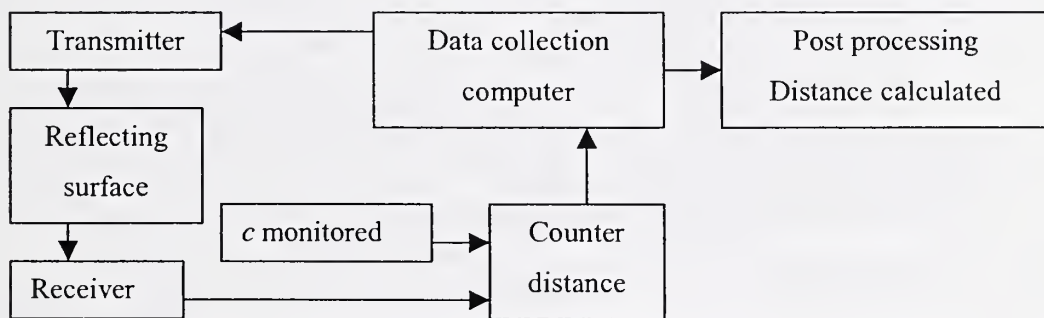
Make	Use	Frequency (Hz)	Beam Width (°)	Resolution (mm)	Dimensions (mm)	Near Field (mm)
Contaq	WS	13	12	0.17	44 116 177	51
NCPA	SB	10	4	0.5	59 30 30	43

Figure 2.8 illustrates how the distance between the ultrasonic probe head and the surface to be measured is recorded. The distance, d , is calculated by multiplying the speed of sound in water, c , by half the time it takes for the ultrasonic pulse to be transmitted, reflected and returned, t (Equation 2.2).

$$d = \frac{tc}{2} \quad (2.2)$$

In order to correctly correlate pulses and echoes, the transmission of each pulse must be separated by a time interval greater than t . The system is controlled and timed by the data collection computer. It is vital for c to be constantly monitored as it is influenced by the temperature of the transmitting fluid. Consequently, the NCPA probes include a circuit for measuring water temperature and adjusting the distance calculation accordingly. The Contaq probe system accounts for variations in c by simultaneously using two probes, one of which measures a known, fixed distance. The latter probe is therefore used to calibrate the data collected by the main measurement probe. Data was transferred to another computer for storage and processing.

Figure 2.8: Distance measurement with ultrasonic probes.



The accuracy of the NCPA ultrasonic probes appeared to be unaffected by the presence of suspended sediment (0.00009-0.018 kg/s), and when the water was turbid (Best and Ashworth, 1994). Erratic signals were filtered (Appendix I), and resulted from abrupt changes in the bed morphology. For example a moving coarse particle may result in multiple reflections due to the height variations within the measuring area. Alternatively a static large clast in the measuring zone may obscure the actual changes in the sediment bed height. The probe head surface was regularly checked for dirt and air bubbles which can cause measurement errors. It was also ensured that the temperature probe was immersed in the flume, and that all connections were correct.

Data from the Contaq probe also required filtering (Appendix I) as it produced occasional erroneous values due to the choppy nature of the water surface, resulting from the recirculation of the water and sediment by the two pumps. The erratic signals may therefore result from the reflection of the ultrasonic pulse from

nearby steep, transient changes in the water surface. At greater flow velocities the water surface became more variable due to additional turbulence and the presence of bedforms.

The recorded distance between the bed or water surface and the bottom of the sensor was converted to a bed or water elevation relative to the flume base. Table 2.4 details the types of measurements collected using the ultrasonic probes.

Table 2.4: Ultrasonic probe measurements.

Ultrasonic probe	Measurement	Data
NCPA	At a point, 1 probe, 5 or 10 minute samples..	Bed surface elevation. Height and period of bedforms.
	At a point, 2 probes separated by a known distance, 20 minute samples.	Bedform migration rate and geometry changes.
	Profile, with measurements taken at 8 mm (\pm 1 mm) intervals down the channel centreline.	Bed surface elevation. Bedform length.
	Grid, with measurements taken at 8 mm (\pm 1 mm) intervals along 25 longitudinal profiles 13 mm apart (\pm 0.1 mm) in the test section.	Map of bed elevation.
Contaq	At a point, 5 minute samples.	Water surface height.
	Profile, with measurements taken at 6 mm (\pm 1 mm) intervals down the channel centreline with both static and dynamic water surfaces.	Water surface slope.

2.4.2 Motion control system

The ultrasonic sensors were supported on a motorised carriage which traversed angle rails mounted above the channels sidewalls. The position of a probe could be adjusted in the longitudinal, lateral and vertical directions using the computerised motion control system. In the lateral and vertical directions a single pulse of the motor represents 0.0007 mm. However in the longitudinal direction the chain links along which carriage moved, and variations in the position of the sprocket on the chain, caused the distance to be accurate to \pm 2 mm. Individual or sequences of changes in the position of an instrument could be programmed into the control computer.

2.4.3 Water elevation and surface slope - Point gauges

Point gauge readings of the dynamic and static water elevation were regularly taken down the centreline of the test section (0.3 m \pm 0.005 m intervals), in order that the water surface slope could be deduced. The vernier scale on the point gauges could be read to \pm 0.1 mm. Furthermore, the use of point gauges was time consuming, and limited by the accuracy of the experimenter in aligning the gauge with the fluctuating water surface (\pm 0.5 mm).

In the fixed bed experiments a point gauge was also used to determine the bed height in the test section at 5 mm (± 0.5 mm) intervals. Since the sediment formed a solid surface, the bed height measurement error resulted only from reading the vernier scale (± 0.1 mm).

2.4.4 Velocity and turbulence measurements –laser Doppler anemometry (LDA)

Laser Doppler anemometry (LDA) is one of a number of methods for determining fluid flow velocity (Buchhave and George, 1979), and offers numerous advantages as listed in Table 2.5.

Table 2.5: Advantages and disadvantages of LDA. From Nezu and Nakagawa (1993), Biron et al. (1995) and Adrian (1996).

Advantages	Disadvantages
<ul style="list-style-type: none"> • Non-intrusive. • Absolute measurement – no calibration required. • Does not depend on the thermophysical properties of the fluid. • Measures up to 3 velocity components. • Reversed flow can be detected. • Very accurate. • Can measure high frequency velocity fluctuations. • Can measure velocities from less than $10 \mu\text{m s}^{-1}$ to 1 km s^{-1}. • Can be used successfully in various types of flow e.g. supersonic, turbulent, capillary blood flow etc. • Excellent spatial resolution due to small measuring volume. 	<ul style="list-style-type: none"> • Cannot be used in opaque flows. Data collection rates reduced in the presence of high levels of suspended sediment. • Difficult to measure close to bed, especially with more than one velocity component. • Unevenly spaced data. • Actually measure the speed of the seeding particles rather than the fluid. • Expensive.

Laser light has the following characteristics – monochromatic, coherent, linearly polarised, low divergence, and a Gaussian intensity distribution. The key features of the LDA measurement system are illustrated in Figure 2.9 and Table 2.6.

Figure 2.9: Main components of the LDA measuring system. From Dantec (2000).

Velocity = distance/time

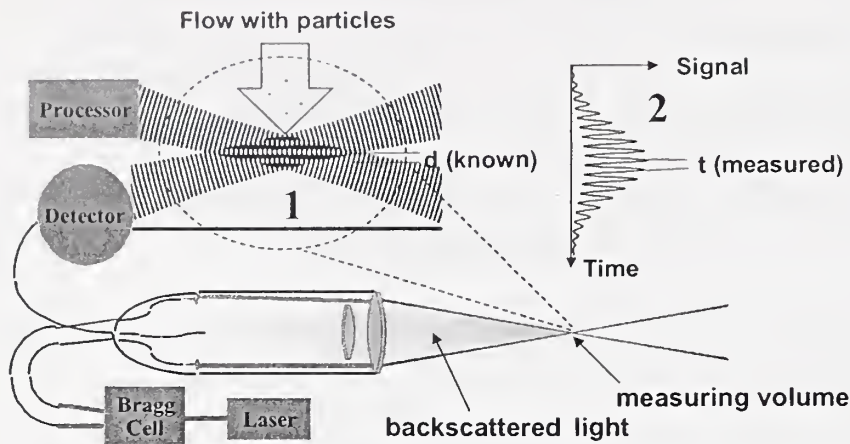


Table 2.6: Key features of the LDA measurement system. From Durst et al. (1987), Livesey (1995), Adrian (1996) and Dantec (1996, 1998, 2000).

Feature	Operation	Result
Doppler shift	A particle moving relative to a fixed source of laser light scatters the light at a different frequency to that of the incident beams. The Doppler frequency shift represents the difference between the two frequencies, and can be directly related to particle velocity by. $f_D = f_s - f_i = \frac{2u_i}{\lambda} \sin\left(\frac{\Phi}{2}\right)$ where f_D , f_s and f_i are the Doppler shift, scattered and incident light frequencies respectively, u_i is the instantaneous particle (flow) velocity, and Φ the angle between the incident and scattered light.	Particle velocity can be determined, and therefore fluid velocity inferred.
Fringe model	Focused laser beams intersect to produce interference fringes of high and low intensity which form the measurement volume (see 1 in Figure 2.9). When a particle crosses through the fringe pattern the scattered light intensity fluctuates with a frequency equal to particle velocity divided by fringe spacing.	Measurement volume.
Frequency shift (Bragg cell)	Identical signals and frequencies are produced by particles moving forwards or backwards if the light beams have the same frequency. If one beam's frequency is shifted relative to the other, the interference fringes appear to move at the shift frequency.	Allows low and negative velocities to be detected.
Doppler Burst	The Doppler signal comprises a low frequency pedestal and high frequency fringe crossing components (see 2 in Figure 2.9).	Velocity measurement.
Backscatter mode	The majority of light is scattered away from the laser. However, enough is scattered back towards the transmitter to allow accurate measurements. Employing the backscatter mode enables the transmission and receiving optics to be housed together.	Easy to align and use.
Seeding particles	Particles must be small enough to accurately track the flow (also influenced by shape), but large enough to scatter sufficient detectable light. Particles should be neutrally buoyant ideally. In the current experiments no particles were added to the flow, which already contained sufficient impurities.	The velocity of the particle can be directly measured and from that the speed of the fluid it is suspended in inferred.

The specifications of the 300 mW Ar-Ion laser system employed in the present experiments are detailed in Table 2.7. Velocity measurement resolution (i.e. half the minimum difference between any two values in a given record) was calculated to be 0.0001 m s^{-1} for both the downstream and vertical components. The laser measurement probe was supported on precision axes, with attached scales. The horizontal axis was aligned

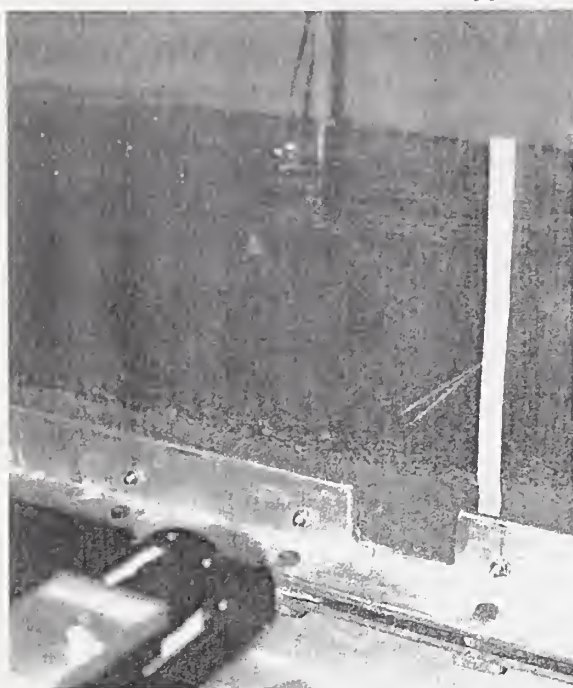
parallel to the flume base, accounting for the slope of the flume, and the vertical axis was perpendicular to this. The probe could be aligned to an accuracy of ± 0.5 mm in both horizontal and vertical directions.

Table 2.7: Specifications of the LDA system employed.

Feature	Specification	
	Green	Blue
Wavelength (nm)	514.5	488
Focal length (mm)	400	400
Beam diameter (mm)	1	1
Fringe spacing (um)	5.422	5.143
Number of fringes	48	48
Measurement volume (mm ³)	0.379	0.325
Dx (mm)	0.262	0.249
Dy (mm)	0.262	0.249
Dz (mm)	5.523	5.238
Signal gain (dB)	35	
Coincidence time (ms)	0.17	

In the mobile bed experiments, one vertical profile was taken in the test section, at the channel centre. Depending on the magnitude of the bedforms, each profile point was sampled for either 5 or 10 minutes. Records of the bed height were taken concurrently with an ultrasonic probe, a known distance downstream of the measuring volume, in order to eliminate any flow disturbance due to the immersed ultrasonic probe (Plate 2.5). The vertical elevation of the profile points were measured relative to the bottom of the ultrasonic probe. Measurements near the sediment bed and the water surface recorded only the downstream velocity component since the beams which assess the vertical velocity component are either intercepted by the sediment bed, or are not fully immersed in the water since they converge at an angle in the vertical plane. Starting as close as possible to the bed, the first ten profile points were collected at 1 mm intervals, the next five at 2 mm intervals, the subsequent two at 5 mm intervals and the remaining points at 10 mm intervals until the water surface is reached. During the series 1 experiments, approximately thirty points were taken to complete the velocity profile, whereas about twenty-seven were obtained for the runs in series 2.

Plate 2.5: Simultaneous measurement of flow velocity and bed height. Flow is from right to left.



When the bed was immobile, velocity measurements were taken for 1 minute. In the first fixed run, sixty vertical velocity profiles were recorded 0.01 m apart down the centreline of the test section. During the second fixed bed case, forty two vertical profiles were measured. The central profiles were also spaced at 0.01 m, but this increased to 0.02 m for the up and downstream profiles (± 0.2 mm). For both fixed bed runs, the lowest four points in each profile were separated by 2 mm, the next point by 4 mm, the subsequent three points by 5 mm, and the remaining points by 10 mm. A grid of nearly 1000 points was established for both fixed bed cases.

Potential sources of noise in the LDA signal are detailed in Table 2.8. It is vital to select appropriate laser power and optical parameters, and maintain reasonable water quality in order to maximise the signal to noise ratio (SNR). Visual inspection of the laser records demonstrates that the level of noise was minimal in the current experiments, with an extremely low occurrence of spikes i.e. excessively high or low measurements (Appendix I). The removal of spikes by eye is subjective, and consequently a filter can be used. However, the choice of filter is also subjective, and in the present case, the use of a filter is illustrated in Appendix I to also eliminate elements of the real signal and be influenced by the rate of data collection. Furthermore, the implementation of a filter is demonstrated to have negligible influence on the velocity and turbulence parameters calculated from the laser records when compared with the unfiltered data presented here (for more details refer to Appendix I).

Table 2.8: Sources of noise in the LDA signal. From Livesey (1995), Adrian (1996) and Dantec (1996, 1998, 2000).

- Photodetection shot noise (generated by the detector itself, limiting the SNR). Incoherent signals can result when a range of particle sizes are present.
- Secondary electronic noise, thermal noise from preamplifier circuit.
- Higher order laser modes (optical noise).
- Light scattered from outside the measurement volume, dirt, scratched windows, ambient light, multiple particles etc.
- Unwanted reflections e.g. windows, lenses and mirrors.
- Misaligned beams.

2.4.5 Camera and video

A 50 mm camera was mounted on the instrument carriage, and employed to take photographs of the test section from above at the end of each experimental run, requiring the water to be drained slowly from the flume first. Care was needed in order to minimise any disturbance to the sediment bed. A scale and a reference for the location in the flume were included in every photograph. During the experimental runs photographs and video recordings of the bedforms present were taken.

2.4.6 Temperature

The temperature of the water in the flume was measured regularly with a thermometer to ± 0.1 °C. The average temperature of the experimental runs varied from 22-28 °C.

2.5 Comparison of recirculating and sediment feed flumes and field observations

In the present experiments, both water and sediment are constantly recirculated within the flume system. Alternatively, sediment can be fed in at the upstream end of the flume, and the downstream sediment discharge removed from the system. Uniform sediments behave in the same manner for both recirculating and sediment feed flumes, but this is not the case for mixed sized or density mixtures as explained below (Parker and Wilcock, 1993). In order to achieve equilibrium, the quantity and grain size distribution of the sediment entering and leaving the system must be identical.

In a recirculating system only those grains which are entrained in the flume are present in the upstream sediment input. Differences in grain mobility therefore result in partial transport (transport rates for coarser fractions are less than those of the finer fractions), which can exist in a steady state in a recirculating system since the input of less mobile size fractions is reduced compared with their occurrence in the bulk sediment mixture (Wilcock and McArdell, 1993). The texture of the bed under steady state conditions is determined by the imposed hydraulic conditions (discharge, slope and depth), fractional grain mobility and the distribution of the bulk sediment mixture.

Where sediment is fed into the flume (transport rate and size distribution set by experimenter), any less mobile clasts concentrate on the bed surface, thereby increasing their potential for entrainment. The concentration of less mobile grains occurs until the transport and feed rate are equal for all size fractions under steady state conditions i.e. equal mobility constraint (Parker and Klingeman, 1982; Wilcock and Southard, 1989). If large quantities of less mobile sediment are deposited, the bed and water surface slope may increase, again enhancing entrainment of the less mobile fractions. Furthermore, fine, mobile sediment may be deposited into sheltered voids between the coarse particles. Consequently, the steady state bed surface grain size distribution is not related to the initial bed sediment mixture, but rather the water flow and sediment input. The proportion of a given grain size fraction in transport determines the proportion of that sediment size on the bed surface. Under steady state sediment feed conditions, partial transport cannot be maintained (Wilcock and McArdell, 1993). If the bulk bed sediment mixture is fed into the flume at a constant rate, equilibrium can only be achieved if both the grain size distribution of the bed and transported material are identical i.e. equal mobility (Parker *et al.*, 1982a, b).

At high discharges, where all fractions are fully mobile, equal mobility is achieved in both recirculating and sediment feed systems. However, despite similar initial conditions, equilibrium transport conditions can differ between recirculating and sediment feed systems. Variations in equilibrium conditions arise due to mobility differences between size fractions and the movement of fines into the bed (vertical sorting). Therefore if different flume systems are employed, direct comparisons between studies of hydraulic, sediment transport and bedform data may not be valid even if the same or similar sediment mixture was used. For example the characteristics of bedforms are influenced by the mobility of different grain size fractions, and the grain size distribution of the transported sediment should ideally be compared with the texture of the bed surface rather than the bulk mixture.

Natural rivers combine elements of both recirculating (as used in the present experiments) and sediment feed systems to varying degrees depending on the temporal and spatial scale of interest (Wilcock and Southard, 1989). For example, the sediment feed case is analogous to long term (years) sediment transport on a catchment scale, whereas the recirculating system is more applicable to short temporal (minutes to hours) and spatial (reach) scales e.g. development of low relief bedforms. Equilibrium conditions are not ubiquitous in natural channels, and consequently information derived from laboratory flumes with uniform flow must be applied with care.

Chapter 3 : Morphological and textural characteristics of bedforms generated in a bimodal sand-gravel mixture

3.1 Introduction

Only relatively recently have low-relief bedforms in sand-gravel bimodal sediments been recognised (Kuhnle, 1986; Kuhnle and Southard, 1988; Whiting *et al.*, 1988; Dietrich *et al.*, 1989; Wilcock, 1992; Bennett and Bridge, 1995a; Livesey, 1995). Several factors have led to the identification of low-relief bedforms: more detailed observations, improved monitoring techniques and work conducted into the entrainment and bedload transport of different size fractions which compose heterogeneous sediments (Hammond *et al.*, 1984; Komar and Li, 1986; Drake *et al.*, 1988; Ikeda and Iseya, 1988; Ashworth and Ferguson, 1989; Dinehart, 1989; Ferguson *et al.*, 1989; Kirchner *et al.*, 1990; Kuhnle, 1993a; Wilcock, 1998). However, our quantitative knowledge of the morphological and textural characteristics of low-relief bedforms remains limited due to past technical difficulties of recirculating gravel sized sediment in a laboratory flume, incomplete data sets, the vast range of potential sediment mixtures, and the difficulty of classifying both bedforms and mixed-size sediment mixtures.

This chapter details the distinctive morphological, textural and dynamic characteristics of bedform populations identified by cluster analysis over a range of discharges in a bimodal sand-gravel mixture. In addition the method of bedform development and migration, and the resulting impact on sediment transport is examined.

3.2 Data analysis

3.2.1 Hydraulic conditions

The mean flow depth in the test section, d , was determined by subtracting the mean values of the filtered ultrasonic records of bed and water surface elevation at a point. The depth integrated velocity, U , was calculated from the velocity profile. Water surface slope, S , was obtained by subtracting the dynamic water surface elevations from the static heights and applying a least-squares linear regression. An average value calculated was calculated for each experiment by repeating the procedure several times. The slope was used to determine the spatially averaged boundary bed shear stress, τ_0 , from

$$\tau_0 = \rho g d S \quad (3.1)$$

where, ρ is fluid density, and g is gravitational acceleration. This value was corrected using the method detailed by Williams (1970) and shown in Equation 3.2, where d is water depth and w is flume width.

$$\text{Sidewall correction factor} = \frac{I}{I + 0.18 \left(\frac{d}{w^2} \right)} \quad (3.2)$$

Mean dimensionless bed shear stress, θ , was calculated using the D_{50} (grain diameter equal to or greater than that of 50 % of clasts in a sediment mixture) of the bedload:

$$\theta = \frac{\tau_{ro}}{(\sigma - \rho)gD_{50}} \quad (3.3)$$

where, σ is sediment density and τ_{ro} is the value of bed shear stress derived from the projection of Reynolds stress measurements to the boundary, which is considered in more detail in Chapter 4.

3.2.2 Sediment bed elevation records

The height and period of bedforms with discernible relief (more than 2 mm high, and a period greater than 5 s) were determined. First the ultrasonic records of bed elevation at a point over time were filtered to remove spikes. Then a moving average of 15 was superimposed before measurements of bedform height and period were taken (± 0.25 mm, ± 0.5 s). Typically 200 bedforms were considered for each experimental run. Bedform migration rate was determined by correlating bedforms (approximately 20 for each experimental run) across two simultaneous bed height records, which were taken a known distance apart. The separation distance was divided by the average temporal difference between the two records for the front and back of each bedform. Bedform length was calculated by multiplying the migration rate by the period.

3.2.3 Transport rates and grain size distributions for bedload, suspended load and the bed surface

Bedload transport rates were obtained from the average of volumetric and weight measurements taken over known time periods. Moments were calculated for the grain size distributions of the bedload and surface sediment samples.

The suspended sediment transport rate was determined by multiplying the sediment concentration (sediment weight divided by the combined water and sediment weight) by the weight of water being discharged per second, divided by the flume width.

The areal clay-piston surface sediment samples were converted to volumetric values using the following conversion (Kellerhals and Bray, 1971):

$$pV_i = CpA_i D_i^x \quad (3.4)$$

where, pV_i and pA_i are the percentages of the i 'th size fraction obtained by volumetric and areal sampling respectively, D_i is the mean grain diameter of the i 'th size fraction, x is the conversion factor (-0.16),

dependent on the sampling technique, and C is a proportionality constant unique for each sample. The conversion factor was determined by comparing volumetric and clay piston samples of the bulk sediment mixture (Diplas and Fripp, 1992).

3.3 Results

3.3.1 Hydraulic conditions

The mean equilibrium hydraulic conditions are detailed in Table 3.1.

Table 3.1: Mean equilibrium hydraulic conditions. d is flow depth ($\pm 3\%$), U is the depth averaged velocity, Q is mean flow discharge ($\pm 4\%$), S is water surface slope ($\pm 12\%$), Fr is the Froude number ($Fr = U / \sqrt{gd}$), τ_{ro} is the bed shear stress obtained from projections of Reynolds stress measurements, θ is the mean dimensionless bed shear stress and f is the Darcy-Weisbach friction coefficient ($f = 8gds/U^2$). SR, R, BLS and LRBW represent sand ribbon, ripple, bedload sheet and low-relief bed wave respectively.

Run	d (m)	U (m/s)	Q (m^3/s)	S ($\times 10^{-3}$)	Fr	τ_{ro} (Pa)	θ	f
<i>Series 1 ($d = 0.18 \text{ m}$)</i>								
A (SR)	0.172	0.51	0.026	1.87	0.39	1.73	0.195	0.053
B (R)	0.172	0.58	0.032	1.96	0.45	2.63	0.285	0.063
C (BLS)	0.181	0.68	0.038	2.20	0.51	3.36	0.378	0.058
D (BLS)	0.173	0.74	0.039	2.27	0.57	3.62	0.393	0.053
E (BLS)	0.176	0.82	0.045	2.65	0.62	4.01	0.344	0.048
F (LRBW)	0.178	0.87	0.047	3.09	0.66	3.43	0.291	0.036
G (LRBW)	0.176	0.88	0.049	3.51	0.67	5.99	0.441	0.062
H (LRBW)	0.177	0.95	0.052	4.33	0.72	6.51	0.457	0.058
<i>Series 2 ($d = 0.14 \text{ m}$)</i>								
I (R)	0.138	0.59	0.025	2.32	0.51	4.05	0.464	0.093
J (BLS)	0.141	0.70	0.029	2.51	0.60	3.37	0.366	0.055
K (BLS)	0.150	0.71	0.031	2.88	0.59	3.46	0.345	0.055
L (LRBW)	0.142	0.79	0.034	3.59	0.67	4.12	0.327	0.053
M (LRBW)	0.139	0.90	0.040	4.89	0.77	6.11	0.194	0.060
N (LRBW)	0.141	1.04	0.047	6.08	0.88	7.92	0.176	0.059

3.3.2 Bedform classification, morphology and dynamics

Figures 3.1 and 3.2 highlight the height and period of the bedforms recognised in the bed records. The shape of the bedforms in the ultrasonic profiles depends on the size of the form relative to the sediment transport rate and local bed roughness, its orientation, the occurrence of any superimposed features and how long it has existed.

Cluster analysis is a multivariate technique which identifies groupings within data sets when the number of groups and group membership are not known. However, there is no underlying theoretical model. In order

to classify the observed bedforms into discrete populations k -means and hierarchical cluster analysis were performed for each experimental run using the SPSS software package (Anderburg, 1973; Hartigan, 1975; Everitt, 1993; SPSS, 1998). The procedure first required the logarithm of the bedform height and period to be taken, and these values then scaled between 0 and 1.

Figure 3.1: Example bed records over a range of flow depths and discharges. Flow is from right to left. R, BLS and LRBW represent ripple, bedload sheet and low-relief bed wave respectively. The height and period of each bedform type is highlighted.

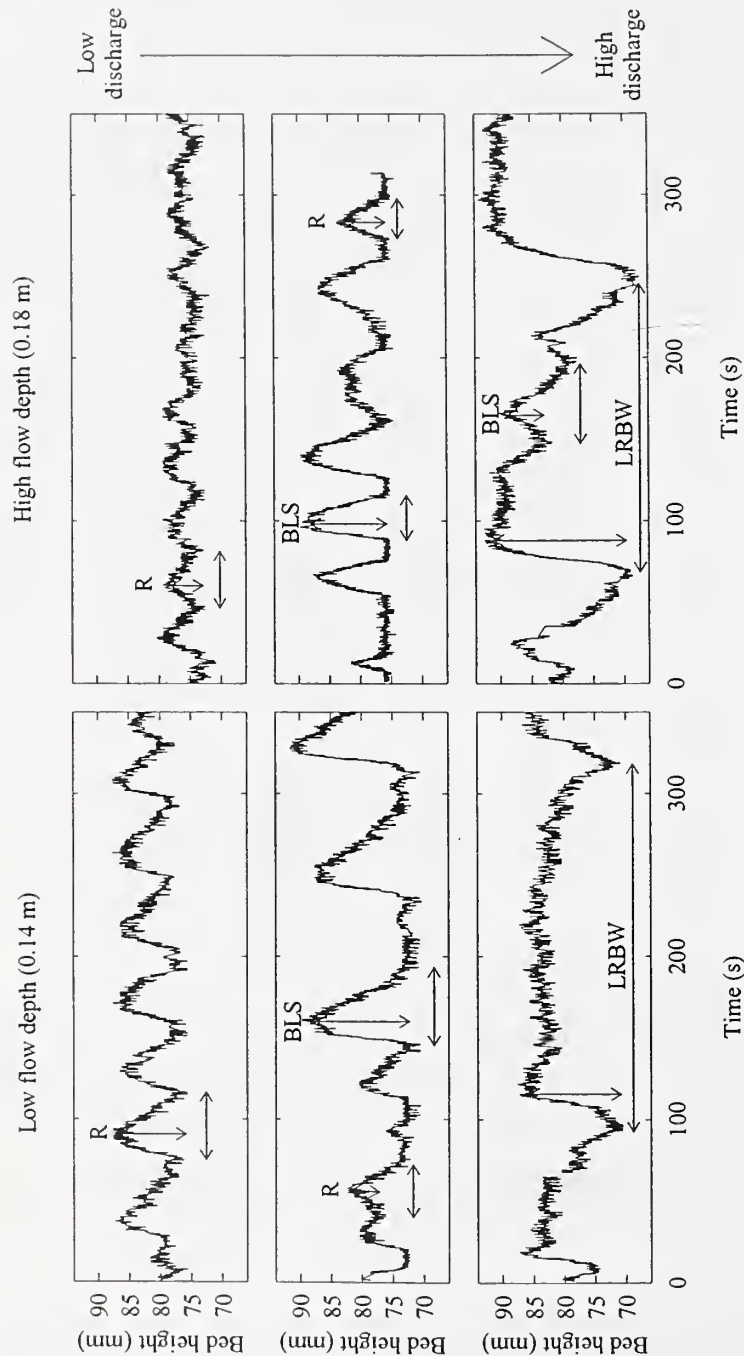
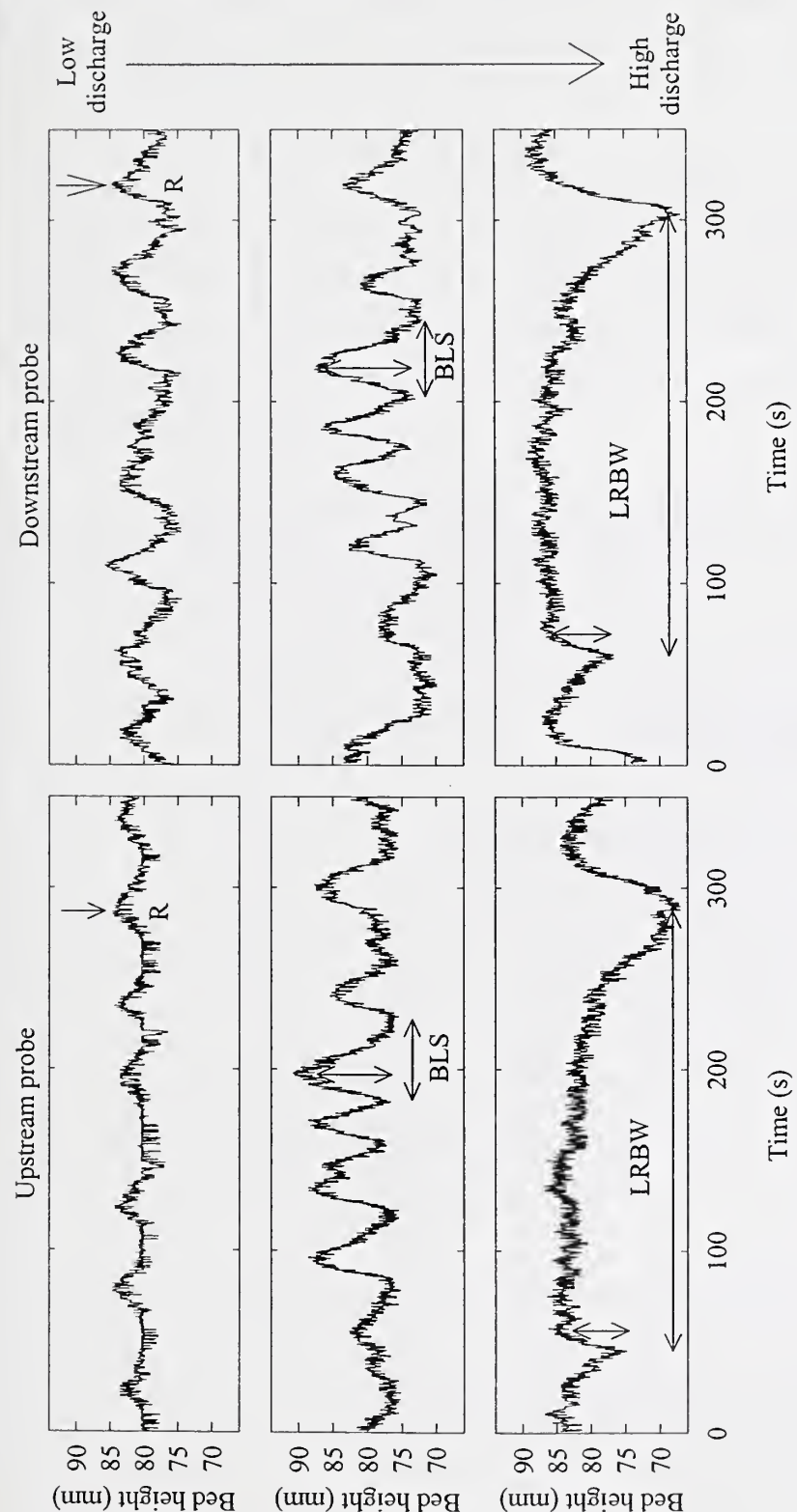
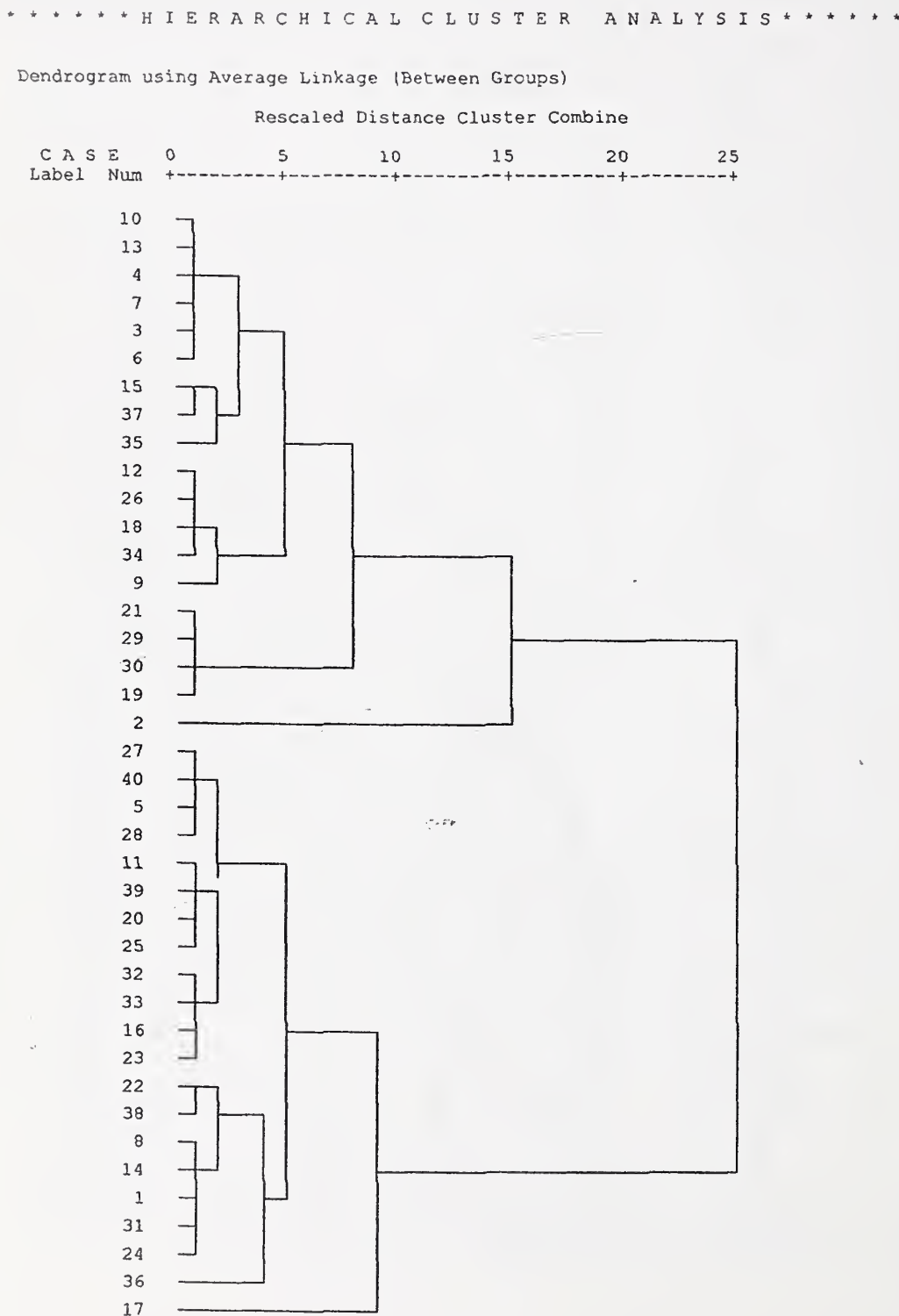


Figure 3.2: Simultaneous bed records taken a known distance apart. Examples of each bedform type are taken over a range of discharges. Flow is from right to left. R, BLS and LRBW represent ripples (Run B), bedload sheets (Run K) and low-relief bed waves (Run H). Where only ripples were present, migration rates could be calculated from the position of the crest when the bed record was 'stunted' by the presence of a coarse clast in the measuring volume.



Hierarchical clustering joins together the closest groups, as determined from the squared Euclidean distance. Once in a cluster, a data point can not be removed from that grouping. The steps involved in combining groups until only one cluster remains are illustrated by a dendrogram (Figure 3.3)

Figure 3.3: Dendrogram for run M.



K-means clustering uses the first k (the number of clusters specified by the user) data points as initial estimates for the cluster centres. Every bedform is then assigned to the closest cluster centre, which are then recalculated. An iterative procedure allows the final cluster centres to be determined. The distance of a point from the cluster centre can help indicate outliers. Cluster centres can also be specified based on earlier analysis. Therefore the measurements of bedform migration rate and length can be assigned to the predetermined populations if the associated bedform height and period are also known.

K-means analysis was repeated for different numbers of cluster centres. The hierarchical method was used on a subset of the data (40 individual bedforms each time). Graphical and statistical output enabled the number of bedform populations for each run to be determined and compared (Figure 3.4). The cluster analysis technique identified three distinct bedform populations based on bedform height and period measurements (Table 3.2). Due to inherent variability, bedform populations rather than individuals are discussed here (Roden, 1998).

Figure 3.4: Example plot of bedform period against height for run M illustrating cluster membership. The logarithm of bedform period and height is taken and scaled from 0 to 1. BLS and LRBW represent bedload sheets and low-relief bed waves respectively.

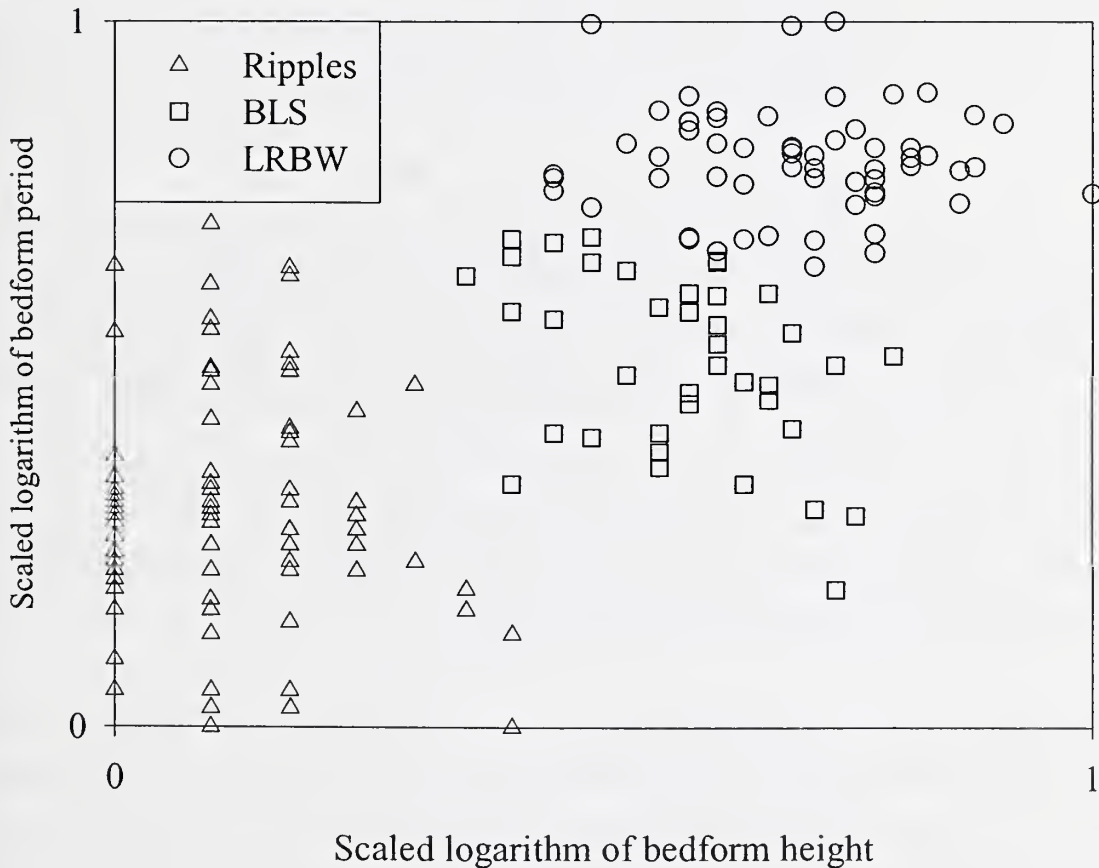


Table 3.2: Average values of bedform height and period for each experimental run.

Bedform	Run	Height (mm)	Period (s)
<i>Series 1 (d = 0.18 m)</i>			
Ripples	B	3	16
	C	4	30
	D	4	27
	E	4	28
	F	3	44
	G	3	46
	H	3	36
	C	7	42
Bedload sheets	D	9	41
	E	11	45
	F	10	52
	G	8	55
	H	8	62
	F	14	232
Low-relief bed waves	G	13	237
	H	15	199
	<i>Series 2 (d = 0.14 m)</i>		
Ripples	I	5	31
	J	5	30
	K	4	27
	L	3	38
	M	3	36
	N	3	25
Bedload sheets	J	12	44
	K	11	45
	L	10	36
	M	8	69
	N	7	30
Low-relief bed waves	L	10	256
	M	10	180
	N	8	116

At low flow discharges, the sand fraction tends to accumulate in flow parallel strips, migrating across the coarser, immobile particles (e.g. run A; Iseya and Ikeda, 1987; Ferguson *et al.*, 1989; Tsujimoto and Kitamura, 1996). The stationary ultrasonic probe does not detect the sand ribbons due to the transitions in roughness occurring in the lateral rather than longitudinal direction.

As discharge increases, the sandy regions tend to widen and deform into asymmetrical features. These bedforms are relatively small in height (3-5 mm), length (30-802 mm), and period (16-46 s), with a relatively high migration rate (4-34 mm/s). They are characterised by a steep lee side, and more gentle stoss, with a rounded crest. Furthermore the features appear to be regularly spaced, are similar in character to ripples (Yalin, 1992; Baas, 1999, Figures 3.1 and 3.2 and Table 3.3), and were observed in every experiment except run A.

The second bedform population identified by cluster analysis develops with further increases in bed shear stress. These bed features are characterised by heights of 7-12 mm, lengths of 71-1061 mm, periods of 30-69 s and migration rates of 8-27 mm/s. Between the individual forms it is common to find an area of gravel lag since the flow is not capable of moving all the grain size fractions available in the bed. These bedforms share many similarities with previous observations of bedload sheets (Table 3.3 and Figures 3.1 and 3.2), and are less regularly spaced and taller than ripples, which can be superimposed on the stoss of the bedload sheets. Bedload sheets are present in all experimental runs with the exception of A, B, and I.

At the highest flow discharges employed, the largest bedforms developed, the height and migration rate of which was dependent on flow depth. Where flow depth was 180 mm, these bedforms exhibited heights of 13-15 mm and migration rates of 9-14 mm/s. This changed to 8-10 mm and 11-25 mm/s respectively when flow depth was reduced to 140 mm. However, the length (2.3-4.8 m) and period (116-256 s) were not affected by the change in the depth of flow. These bedforms (termed here low-relief bed waves) were differentiated by their much greater length, crestal platform and gentle stoss side, on which both bedload sheets and ripples were superimposed (Figures 3.1 and 3.2 and Table 3.3). The trough appeared fairly flat, and is dominated by a gravel armour which can be mobile (i.e. at the highest bed shear stress employed the flow was capable of moving all grain size fractions). Low-relief bed waves were observed in runs F, G, H, L, M and N.

The total water discharge during runs C/D, F/G and J/K are similar, and the morphological characteristics of the bedforms generated are comparable (Table 3.4) illustrating the repeatability of the results presented here. However, Werner and Kocurek (1999) caution that bedform spacing in laboratory flumes may vary depending on the size of the test section, and may also differ from that found in the field.

Table 3.3: Morphological and dynamic characteristics of ripples, bedload sheets and low-relief bed waves. The average ripple and bedload sheet lengths for run 12 are excluded since they are unrepresentative. D , h , l , p , d and w represent grain diameter, bedform height, bedform length, bedform period, flow depth and flume width respectively.

Source	Bedform	h (mm)	l (m)	p (s)	l/h	l/d	l/w	h/l	l/p (mm/s)
Present study									
	Ripples	3-5	0.03-0.80	16-46	104	2-3	0.1-2.3	0.010	4-34
	BLS	7-12	0.07-1.06	30-69	60	3-4	0.2-3.0	0.017	8-27
	LRBW (1)	13-15	2.68-3.89	119-237	234	18-24	7.5-10.9	0.004	9-14
	LRBW (2)	8-10	2.30-4.85	116-256	397	20-26	6.5-13.6	0.003	11-25
Baas (1993)									
	Ripples	17	0.14		8	0.4	0.3	0.125	
Bennett and Bridge (1995a)									
	BLS	4-13	0.60-1.20	572-1008	56-338	4-12	0.9-2.0	0.018-0.003	1-1.5
	LR bars	10-17	1.70-2.40	2800-6770	131-200	17-24	2.8-3.9	0.008-0.005	0.3-0.9
Kuhnle (1986)									
	BLS	2-4	0.5-3	-	583	24-49	2-12	0.002	5-10
	Dunes	10	0.6	-	60	9	4	0.017	30
Whiting <i>et al.</i> (1988)									
	BLS (Duck Creek)	10-20	0.5-2	-	83	3.6	0.2	0.012	2-4
	BLS (Muddy Creek)	2-4	0.2-0.6	-	133	1.3	0.07	0.008	-
Dietrich <i>et al.</i> (1989)									
	BLS	1-2 D	-	-	-	-	-	-	-
Wilcock (1992)									
	BLS (MC50)	1-2 D	1000-2000	-	-	-	-	-	-
	2D dunes (MC50)	-	800-1200	-	-	-	-	-	-
Livesey (1995)									
	BLS	1-17	0.01-0.47	43-60	2-60	2.2	0.8	0.5-0.017	2-3
	LR bedforms	5-25	0.4-1.7	342-1040	70	9.5	3.5	0.014	0.5-1

Table 3.4: Morphological characteristics of bedforms generated in experimental runs with similar total water discharge, Q .

Run	Q (m ³ /s)	Bedform	Height		Period (s)	Length	Migration rate (mm/s)	
			(mm)	(mm)				
C	0.0379	R	4	7				
		BLS	30	42				
D	0.0385	R	4	9				
		BLS	27	41				
F	0.0473	R	3	44				
		BLS	10	52				
G	0.0485	LRBW	14	232				
		R	3	46				
J	0.0287	BLS	8	55				
		LRBW	13	237				
K	0.0310	R	5	30				
		BLS	12	44				
		R	4	27				
		BLS	11	45				

3.3.3 Bedform texture and bedload transport

Due to their low-relief, bedforms were most noticeable from their characteristic concentrations of fine and coarse bed material. As discharge increased, the mean grain size of the bedload and crestal surface tended to become greater, whilst the standard deviation and skewness fell (Table 3.5). At the lowest transport rates, the finer and coarser fractions are under-represented in the bedload when compared with their occurrence in the bulk sediment mix (either immobile or partially mobile, Wilcock and Southard, 1989). The finer sediment sizes may be underrepresented in the bedload due to suspension and hiding effects (Wilcock and McArdell, 1993), whereas coarser particles typically require a greater shear stress for entrainment. When all the exposed clasts of a given size interval are entrained and transported at least some of the time, that grain size can be considered fully mobile. Near incipient motion the central grain size fractions are most mobile. However, as shear stress increases the difference in mobility between grain size fractions is reduced, and in the case of run N equal mobility is nearly attained. Runs C/D and F/G experienced similar total water discharge, and the grain size distribution of the bedload is also comparable (Table 3.5) indicating the reproducibility of the results.

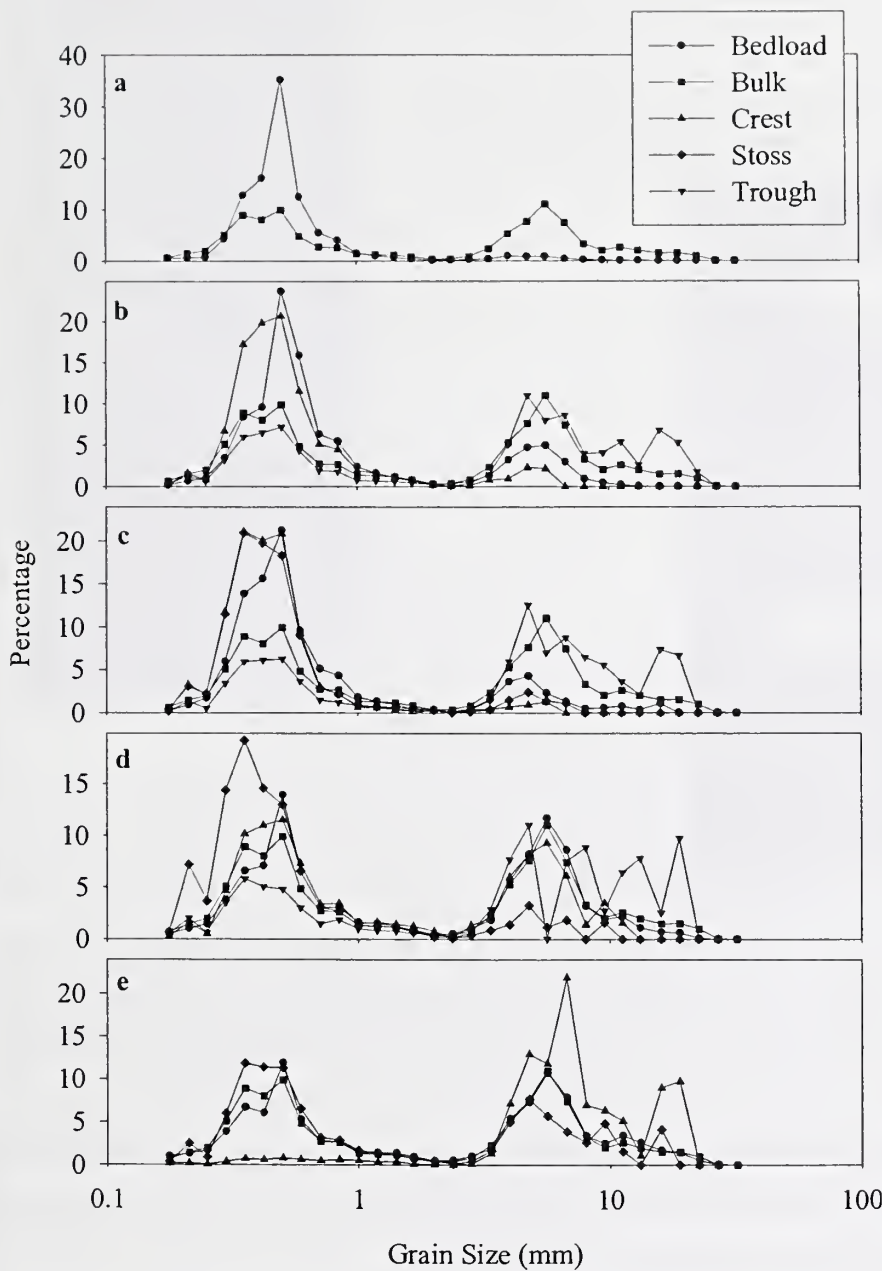
The mean, standard deviation and skewness of the grain size distributions for the trough and stoss regions are fairly stable for the ranges of discharges investigated here (Table 3.5). Divergent values may result from the presence of superimposed bedforms on the stoss, and coarse, immobile particles protruding through the thin bedform.

Table 3.5: Textural bedform characteristics. SD and skew are the standard deviation and skewness.

Sample	Percentile (mm)						Mean (mm)	SD (mm)	Skew	
	5	16	50	84	90	95				
BULK	0.31	0.41	1.82	7.62	10.07	14.55	1.85	0.25	1.05	
<i>Series 1 (d = 0.18 m)</i>										
A	Bedload	0.35	0.41	0.55	0.80	0.91	1.11	0.58	0.65	4.12
B	Bedload	0.36	0.43	0.57	0.83	0.95	1.24	0.62	0.63	4.83
C	Bedload	0.32	0.39	0.55	3.40	4.94	6.42	0.79	0.37	2.88
	Trough	0.35	0.48	5.41	13.29	17.58	19.87	3.40	0.24	0.68
	Crest	0.28	0.35	0.46	0.64	0.74	1.19	0.50	0.58	6.21
	Stoss	0.28	0.35	0.47	0.69	0.98	4.66	0.55	0.49	4.90
D	Bedload	0.32	0.39	0.57	5.02	6.02	7.07	0.92	0.34	2.05
E	Bedload	0.31	0.39	0.72	6.16	6.97	8.14	1.29	0.29	1.33
	Crest	0.30	0.36	0.50	1.25	6.25	10.56	0.72	0.35	3.45
	Stoss	0.32	0.41	4.77	11.61	13.90	15.96	2.41	0.23	0.87
F	Bedload	0.33	0.44	0.73	6.08	6.87	7.94	1.32	0.30	1.37
G	Bedload	0.32	0.41	0.84	6.21	6.97	7.96	1.40	0.29	1.24
	Trough	0.33	0.45	4.81	11.14	13.77	15.60	2.60	0.24	0.82
	Crest	0.37	0.50	4.08	7.15	8.14	9.46	2.17	0.30	0.81
	Stoss	0.30	0.36	0.50	5.55	9.21	14.00	0.85	0.29	2.58
H	Bedload	0.30	0.39	0.88	6.38	7.39	8.97	1.37	0.28	1.30
	Trough	0.34	0.53	5.52	17.68	23.43	25.11	4.16	0.23	0.67
	Crest	0.49	1.15	5.90	11.18	12.65	14.17	4.50	0.35	0.43
	Stoss	0.27	0.35	0.52	1.24	4.00	5.21	0.66	0.42	2.81
<i>Series 2 (d = 0.14 m)</i>										
I	Bedload	0.34	0.40	0.54	0.73	0.91	1.51	0.59	0.57	6.59
J	Bedload	0.34	0.42	0.57	1.13	4.15	5.65	0.75	0.45	3.34
K	Bedload	0.35	0.44	0.62	4.31	5.50	6.61	0.90	0.38	2.34
	Trough	0.35	0.48	5.32	13.67	17.66	20.35	3.19	0.24	0.75
	Crest	0.32	0.38	0.52	0.85	1.18	4.28	0.60	0.52	4.34
L	Bedload	0.31	0.41	0.78	6.30	7.15	8.46	1.36	0.29	1.33
	Trough	0.34	0.52	5.84	17.67	19.76	21.14	4.00	0.24	0.64
	Stoss	0.25	0.33	0.44	0.71	1.25	5.33	5.33	0.45	4.89
M	Bedload	0.33	0.45	1.95	7.04	8.11	10.73	1.79	0.28	1.05
	Trough	0.33	0.48	5.25	14.60	18.72	20.71	3.56	0.24	0.67
	Crest	0.33	0.41	0.82	6.29	7.24	9.55	1.42	0.29	1.22
	Stoss	0.23	0.31	0.45	0.94	3.39	5.47	0.58	0.41	3.58
N	Bedload	0.31	0.44	2.78	8.20	10.82	14.37	2.03	0.26	0.99
	Crest	1.12	4.83	7.30	16.89	18.95	20.71	7.21	0.45	0.31
	Stoss	0.31	0.39	0.69	7.04	9.68	12.06	1.38	0.26	1.38

Figure 3.5a shows representative grain size distribution curves for the bedload and bulk sediment mixture of a ripple bed state. The predominant component of bedload is sand (i.e. less than 2 mm diameter), with the mode at 0.5 mm. Ripples can only form in sediment up to 0.7 mm in diameter since they require a hydraulically smooth flow (Leeder, 1980; Costello and Southard, 1980). It is therefore informative that although the majority of the bedload is less than this critical threshold, sediment up to 16 mm was also actually transported during a ripple bed configuration. However, gravel sized sediment is dramatically under-represented in the bedload. Furthermore sediment larger than 16 mm (up to 32 mm) is completely immobile, and therefore forms a static armour layer which is exposed in the erosive trough regions (Plate 3.1).

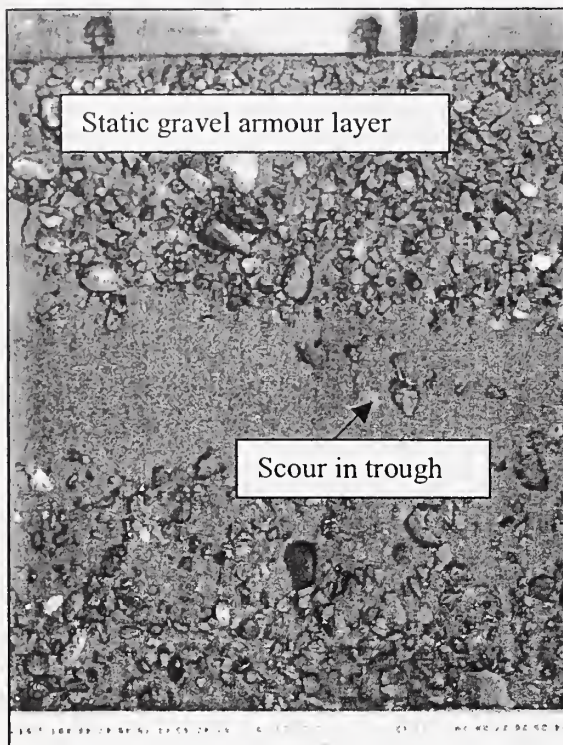
Figure 3.5: Representative grain size distributions for a ripple (a, run I), bedload sheet (b and c, run K and C) and low-relief bed wave (d and e, run M and N) bed configurations. Note the difference percentage scales used.



An armoured surface is characteristically coarser and better sorted than the underlying bed sediment/bulk mixture, with a thickness of one grain diameter (Gomez, 1983). A variety of interchangeable terms have been used to describe this surface feature (Proffitt and Sutherland, 1983; Komar, 1987b; Parker, 1991a; Richards, 1991; Kuhnle, 1992; Reid *et al.*, 1992). Gomez (1984) suggests that a stable/static armour represents a segregated surface which is inactive under the prevailing flow conditions, whereas an unstable/mobile armour experiences periodic movement. Gravel can be segregated on the bed surface by three mechanisms: concentration of particles at the base of the active layer, winnowing of fines and deposition of coarse particles (Gomez, 1984). An armour layer limits the availability of sediment for

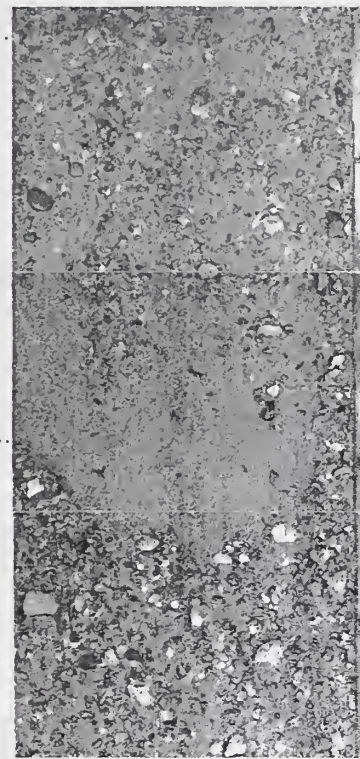
transportation, and therefore can cause bedload transport rates to be less than predicted (Gomez, 1983). The presence of a static armour inhibits erosion in the trough region, limiting bedform height (Richards, 1991; Roden, 1998).

Plate 3.1: Ripple developed on a sand ribbon, run I. Flow is from left to right. In the ripple trough the flow scours down to the underlying gravel armour. Flume width is 0.356 m.



When ripples and bedload sheets are present (Figure 3.5b and c), the sand size fractions are still over-represented in the bedload, although to a lesser extent compared with a rippled bed. Consequently, the gravel component is under-represented in the bedload. In Figure 3.5b and c, no sediment greater than 16 mm is found in the bedload. Therefore, a static armour layer exists in the trough regions (Plate 3.2; Bennett and Bridge, 1995a). The texture of the crest and stoss follow a similar trend to that of the bedload (Whiting *et al.*, 1988; Bennett and Bridge, 1995a), but with a smaller gravel component. The grain size distributions of the trough are characterised by a large proportion of very coarse particles.

Plate 3.2: Bedload sheet run K. Flow is from top to bottom. Channel width is 0.356 m.



In the case of low-relief bed waves, the grain size distributions of the crest, bedload and bulk mixture are comparable (Figure 3.5d). However, the very coarsest size fractions of the bulk mix are under-represented or absent in the bedload and crest. In this case, the bedload, crest and bulk mix contain no particles greater than 26.9, 13.2 and 32 mm respectively. These coarsest particles characterise the trough and represent a static armour (Plate 3.3). Sediment samples from the bedform stoss confirmed visual observations that it was predominantly composed of sand, with small quantities of overpassing pea gravel (Plate 3.3).

In run N (low-relief bed waves), all size fractions were represented in the bedload, which exhibits a grain size distribution akin to the bulk sediment mix (Figure 3.5e). Evidently this flow was capable of moving all the sediment available in the bed (up to 32 mm). Therefore the crest, which is characterised by an overpredominance of the coarsest grains, represents a mobile armour layer. Bennett and Bridge (1995a) speculated that when the bed material is fully mobile (Wilcock and McArdell, 1993), the grain size contrast between bedform crests and troughs is eliminated, or even reversed. The grain size distribution of the stoss was similar to that of the bedload and bulk mixture, although marginally finer.

The observations from Figure 3.5 confirm that as discharge increases, and different characteristic bed configurations dominate, the bedload and crestal region coarsen. Furthermore the dynamics of the coarse armour layer change as flow strength increases and the large clasts become mobile.

In the case of low-relief bed waves (Figure 3.6), the surface tends to coarsen along the stoss as the crest is approached. This is especially evident from the sand mode of the grain size distributions (Figure 3.6, Table 3.6), which accounts for a smaller percentage of total weight as samples further downstream are considered. However, the stoss remains significantly finer than the trough and crestral regions. As the mean grain size increases, the skewness and standard deviation of the distribution are reduced along the stoss. It was not possible to investigate the coarsening of the stoss for bedload sheets and ripples due to their smaller length.

Plate 3.3: Low relief bed wave, run M. Flow is from top to bottom. Flume width is 0.356 m.

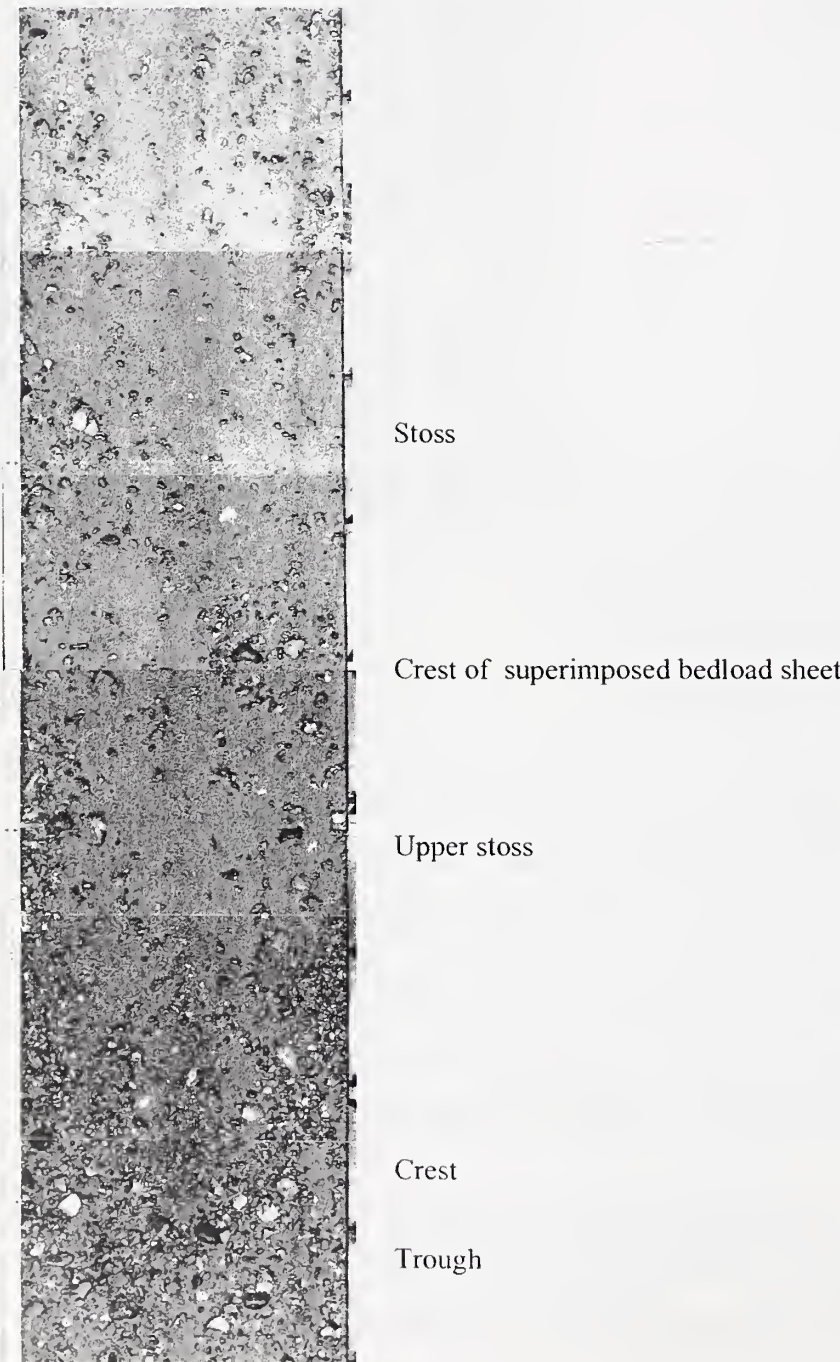


Figure 3.6: Textural variations over a low-relief bed wave, run G, series 1. Flow is from right to left. C, T and S represent samples of the crest, trough and stoss respectively. Average values for the trough and crest are used in the grain size distribution curve.

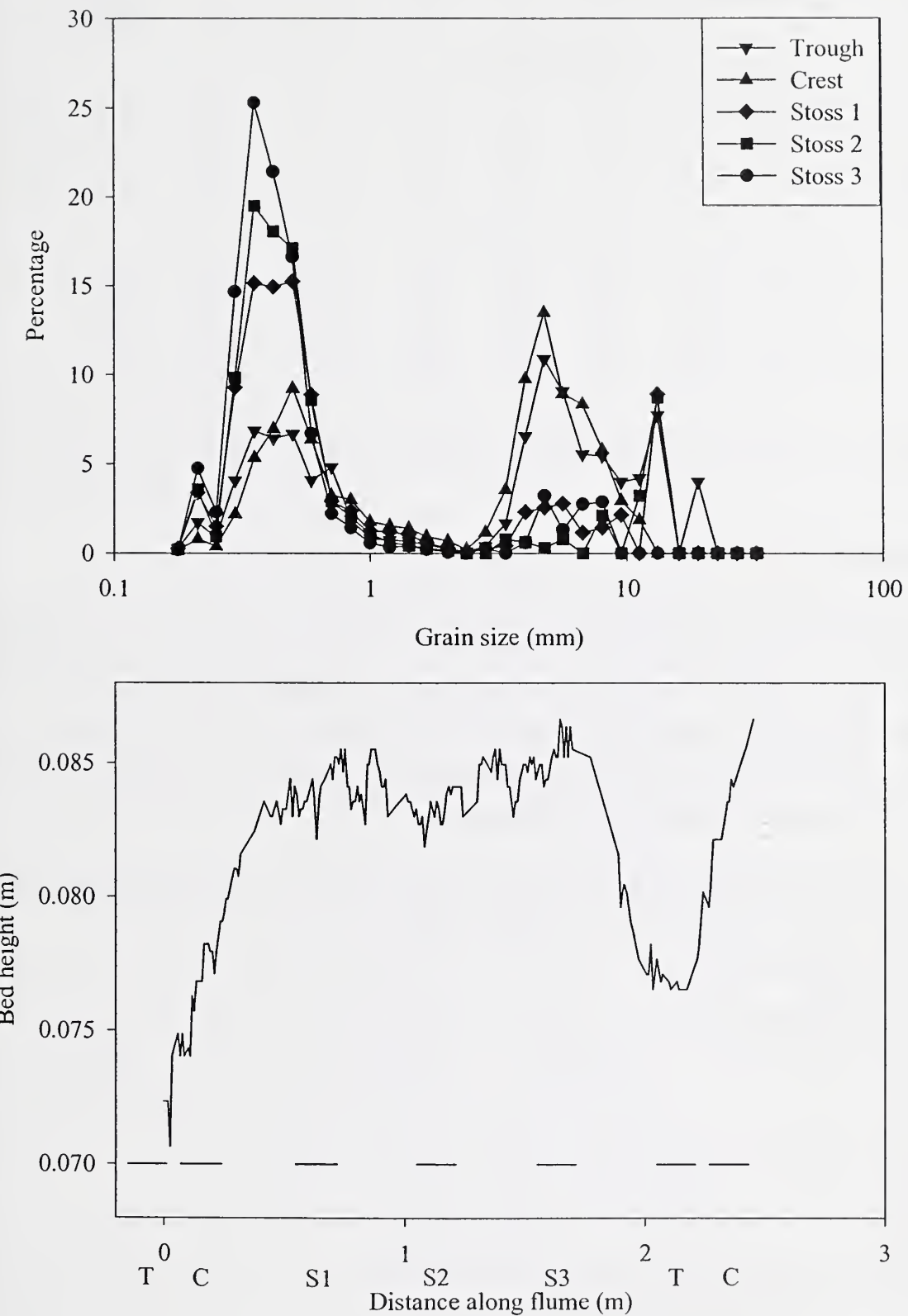


Table 3.6: Textural variations over a low-relief bed wave. SD and skew represent standard deviation and skewness

Sample	Percentile								
	5	16	50	84	90	95	Mean	SD	Skew
	Run G, series 1								
Trough	0.33	0.45	4.81	11.14	13.77	15.60	2.60	0.24	0.82
Crest	0.37	0.50	4.08	7.15	8.14	9.46	2.17	0.30	0.81
Stoss 1	0.29	0.36	0.53	5.74	10.29	14.36	0.92	0.28	2.35
Stoss 2	0.23	0.36	0.49	1.27	11.28	13.77	0.78	0.29	3.16
Stoss 3	0.25	0.33	0.43	0.59	0.67	0.94	0.55	0.40	4.68
	Run M, series 2								
Trough	0.33	0.48	5.25	14.60	18.72	20.71	3.56	0.24	0.67
Crest	0.33	0.41	0.82	6.29	7.24	9.55	1.42	0.29	1.22
Stoss 1	0.27	0.35	0.52	1.49	4.53	5.81	0.69	0.40	2.71
Stoss 2	0.24	0.32	0.46	1.57	5.09	7.77	0.66	0.36	3.00
Stoss 3	0.22	0.27	0.39	0.58	0.71	1.42	0.44	0.53	2.77

A summary of the textural characteristics of the bedforms observed here and in other studies is found in Table 3.7.

3.3.4 Suspended sediment

Any sediment that passed the sediment trap is assumed to be in suspension (Murphy and Amin, 1979; Poreh *et al.*, 1970). At a discharge of approximately $0.025 \text{ m}^3 \text{ s}^{-1}$ the level of suspended sediment was minimal at both flow depths. However, with rising discharge the transport of suspended sediment increases exponentially (Figure 3.7), contributing up to 8 % of the total sediment transport (typically 1-3 %). This exponential increase was greatest under the shallower flow conditions. The standard deviation of the suspended sediment transport also increases with discharge.

Figure 3.7: Suspended sediment transport. The bottom point of series 1 was not included in the regression.

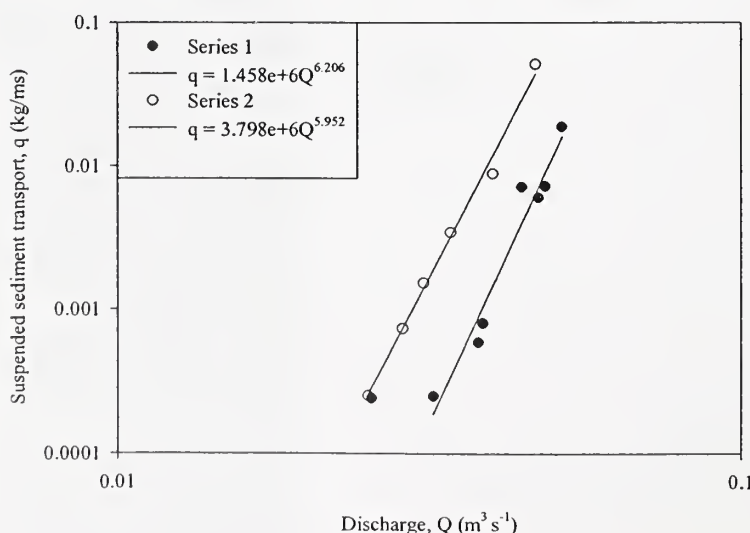


Table 3.7: Summary of the sedimentological characteristics of the present experiments and previous work on bedforms in bimodal sediment mixtures. θ is the dimensionless bed shear stress and q_b is the total bedload transport rate.

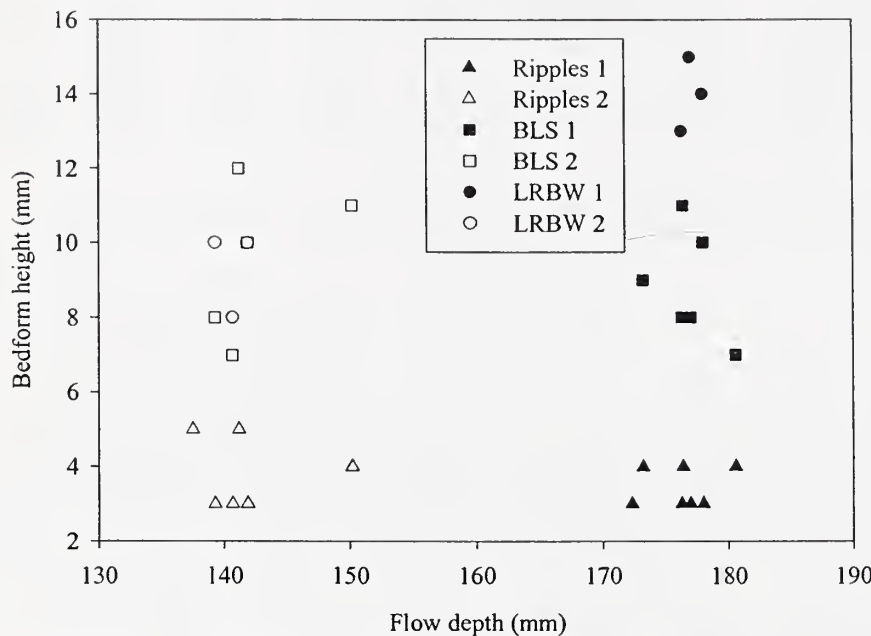
Source	Bedform	Bulk sediment		θ	q_b (kg/ms)	Texture D_{50} (mm)			
		D_{50} (mm)	$\sqrt{D_{ss} / D_{ls}}$			Bed Load	Crest	Stoss	Trough
Present study									
	Ripples	1.819	4.3	0.09	0.006- 0.014	0.603	-	-	-
	BLS	1.819	4.3	0.10- 0.12	0.036- 0.101	0.929	0.609	1.481	3.292
	LRBW (1)	1.819	4.3	0.14- 0.21	0.241- 0.253	1.365	3.332	0.755	3.377
	LRBW (2)	1.819	4.3	0.14- 0.24	0.157- 0.591	1.725	4.315	2.429	3.777
Baas (1993)									
	Ripples	0.238		0.14- 0.52					
Bennett and Bridge (1995a)									
	BLS	1.9-2.0	1.7-1.9	0.04- 0.10	0.010- 0.043	2.33	1.5-3.1	Mixed	2.3-5.4
	LR bars	1.9-2.0	1.7-1.9	0.04- 0.10	0.010- 0.043	2.33	-	-	-
Kuhnle (1986)									
	BLS	2.8	2.6	0.12- 0.16	0.034- 0.098	-	1-4	-	4-16
	Dunes	2.8	2.6	0.16	0.9	-	-	Fine	Coarse
Whiting <i>et al.</i> (1988)									
	BLS (DC)	4.6	2.6	0.07- 0.11	0.038	-	6.1	-	4.1
	BLS (MC)	4.6	2.6	-	-	-	-	-	-
Dietrich <i>et al.</i> (1989)									
	BLS	3.7	2.2	0.08- 0.09	0.010- 0.029	-	4.7	2.7	3.7
Wilcock (1992)									
	BLS	2.6	1.7	0.07- 0.10	0.018- 0.063	-	Coarse	Well mixed or fine	
	(MC50)								
	2D dunes	2.6	1.7	0.12- 0.14	0.131- 0.223	-	-	-	-
	(MC50)								
Livesey (1995)									
	BLS	1.07	1.57	0.086- 0.145	0.068- 0.129	1.2	Fine	Mixed	Coarse
	LR bedforms	1.07	1.57	0.086- 0.145	0.068- 0.129	1.2	1.0	1.1	1.4

3.4 Discussion

3.4.1 Bedform length and time scales

The morphology and stability of bedforms is affected by bed shear stress, the proportion of each grain size in the bed sediment, flow depth (Figure 3.8) and width, Froude number, suspended sediment, generation time, temperature and sediment availability.

Figure 3.8: Variations in the height of low-relief bed waves (LRBW) with flow depth. BLS represents bedload sheets. Series 1 has a flow depth of 0.18 m and series 2 has a flow depth of 0.14 m.



In a laboratory flume, changes in discharge can only be accommodated by adjustments in velocity, flow depth and bedform height. In the field, the river channel and bedforms can also alter their width in order to adapt to discharge variations. Therefore the width of the flume channel influences the morphology and dynamics of bedforms, due to the physical restrictions on lateral bedform development (Crickmore, 1970). However, this effect has not been quantified for heterogeneous mixtures. Williams (1970) found that in a narrower channel, dune height tends to be reduced and migration rate enhanced. Where the width/depth ratio of the flume channel is less than 5, secondary circulation cells develop and the velocity maxima dips below the free surface (Nezu *et al.*, 1985; Nezu and Nakagawa, 1993), restricting bedform height. In the present experiments the width/depth ratios were 2 and 2.5 for series 1 and 2 respectively. The secondary circulation in the laboratory flume when empty of sediment was determined using an Acoustic Doppler Velocimeter (ADV; Figure 3.9). With a flow depth of 0.18 m and depth averaged velocity of 0.29 m s^{-1} , the lateral velocity did not exceed 5.2 percent of the downstream value. For a flow depth of 0.14 m and a depth averaged velocity of 0.18 m s^{-1} the equivalent figure was 5.7 percent. However the across stream velocity

was typically a much smaller percentage of the downstream velocity component, although the depth averaged velocities generated in the experimental runs were considerably larger. Secondary circulation generated due to a low width/depth ratio can also cause variations in the spanwise distribution of bed shear stress. In order to allow comparison between data sets any sidewall effect must be accounted for (Equation 3.2; Williams, 1970).

Figure 3.9: Secondary flow circulation ($m s^{-1}$) with a flow depth of a) 0.18 m and b) 0.14 m. No sediment was present in the flume. Flow is into the diagram, with the area from the left sidewall looking downstream to the centre of flume shown.

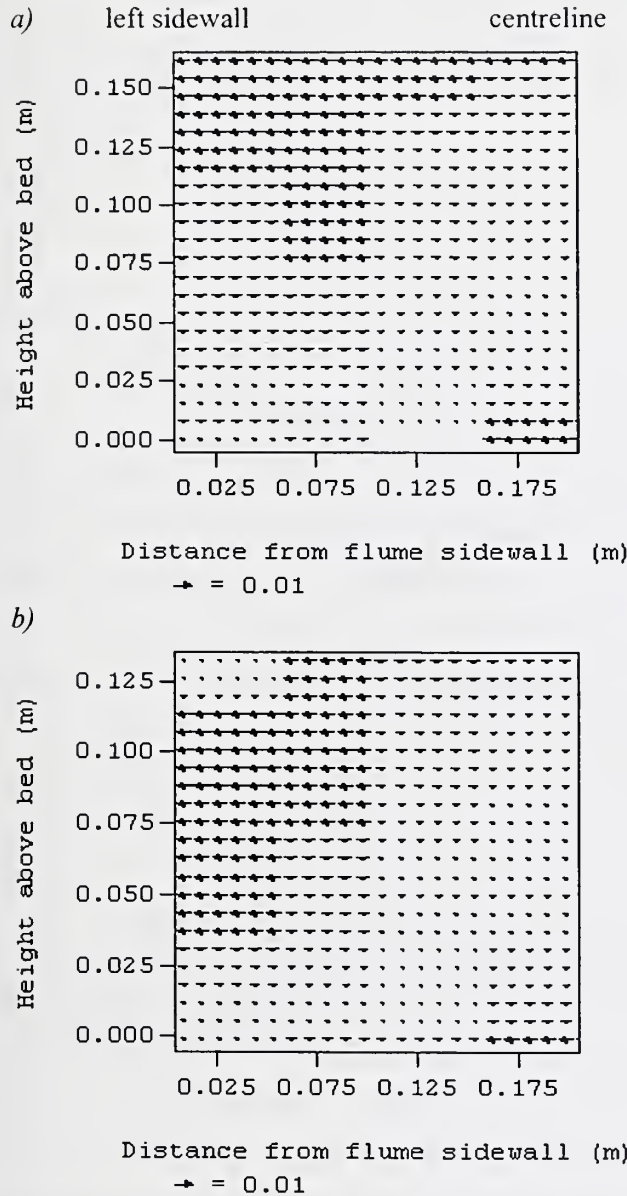
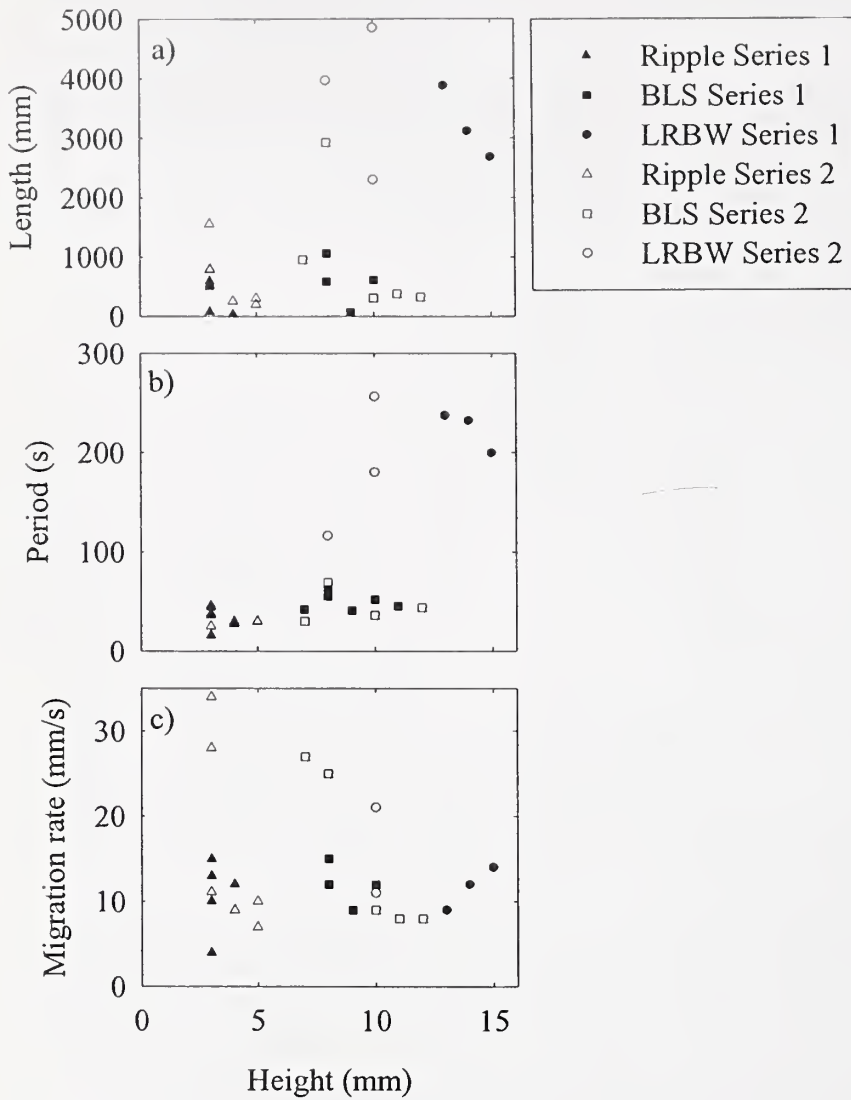


Figure 3.10 highlights the fact that both the length and period of ripples and bedload sheets are similar. These two features are therefore morphologically distinguished by their height, which is greater for the bedload sheets. Low-relief bed waves are longer than the other two bedform populations identified, and their height is dependent on the flow depth, which under the present flow conditions is either similar or greater

than that of the bedload sheets. The steepness of the low-relief bed waves (height/length) is reduced under the lower flow conditions (Carling, 1999).

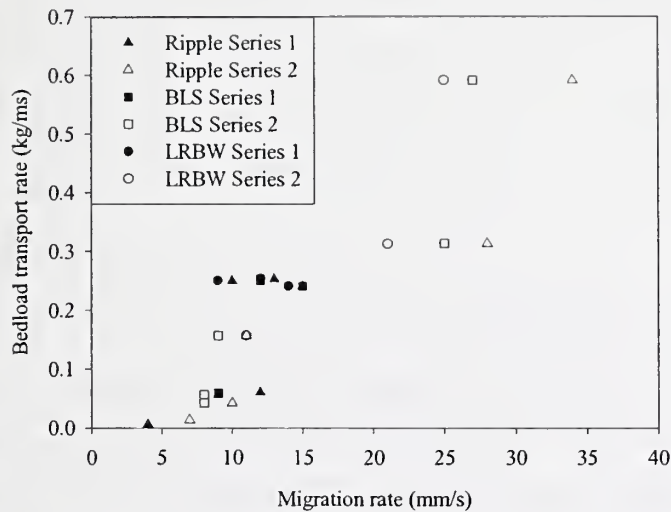
Figure 3.10: Bedform height versus a) bedform length, b) period and c) migration rate. BLS and LRBW represent bedload sheets and low-relief bed waves respectively.



Ripples exhibit the greatest migration rate, followed by bedload sheets and then low-relief bed waves, implying that an increase in height corresponds with a fall in bedform celerity. However, viewing all the points as a whole on Figure 3.10c, there is no obvious relationship between bedform height and celerity. However, higher velocities tend to be associated with smaller bedload sheets. Furthermore, the velocity of the low-relief bed waves is greater when shallower flow prevails and their height is reduced. The maximum migration rate of the low-relief bed waves under the highest flow depth investigated is approximately half that of the bedload sheets, as was observed in the experiments of Bennett and Bridge (1995a), although the actual magnitude of the migration rates differ. Variations in migration rate between bedform types agrees with the observation of superimposed bedload sheets traversing the stoss of the slower moving low-relief bed

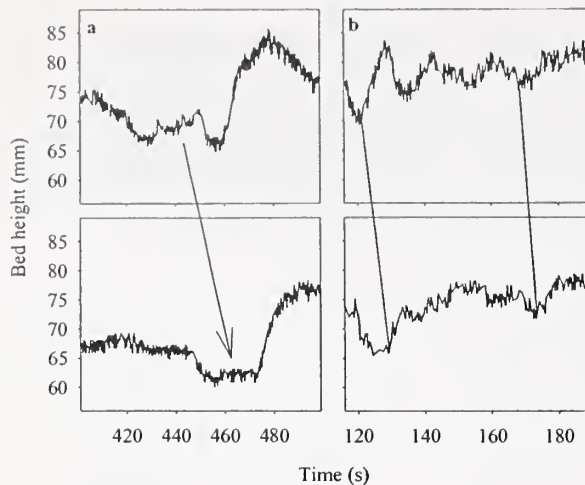
waves. The migration rate of all bedform populations is directly related to the spatially averaged bedload transport rate (Figure 3.11), which is expected as suspended sediment transport is minimal. All bedforms seem to have a greater migration rate under shallower flow conditions at the highest discharges (i.e. run M and N).

Figure 3.11: Bedload transport as a function of bedform migration rate. Each point represents an average value for a particular bedform and run. BLS and LRBW represent bedload sheets and low-relief bed waves respectively.



Gabel (1993) noted four ways in which bedforms transform morphologically. Examples of amalgamation and destruction from the present experiments are shown in Figure 3.12. For each case there are two simultaneous bed height records, taken a known distance apart (typically 0.2 m), enabling specific bed features to be correlated. Firstly, bedforms can be destroyed by simply dying out i.e. diminution (Figure 3.12a). Bedforms can also combine together (Figure 3.12b). This often occurs when a bedform travels up the stoss of a slower moving downstream feature and the two amalgamate so that only one lee side is present. Conversely, a bedform can split into two separate features. Finally, a bedform can simply develop from a previously flat area of the bed. However, evidence for these last two morphological transformations was not observed in the present experiments. Carling *et al.* (2000a) proposes a fifth classification to describe bedforms which are regenerated on the stoss side of larger features. However, this is associated with changes in flow stage and is therefore not applicable to the bedforms generated in the present experiments under uniform flow conditions.

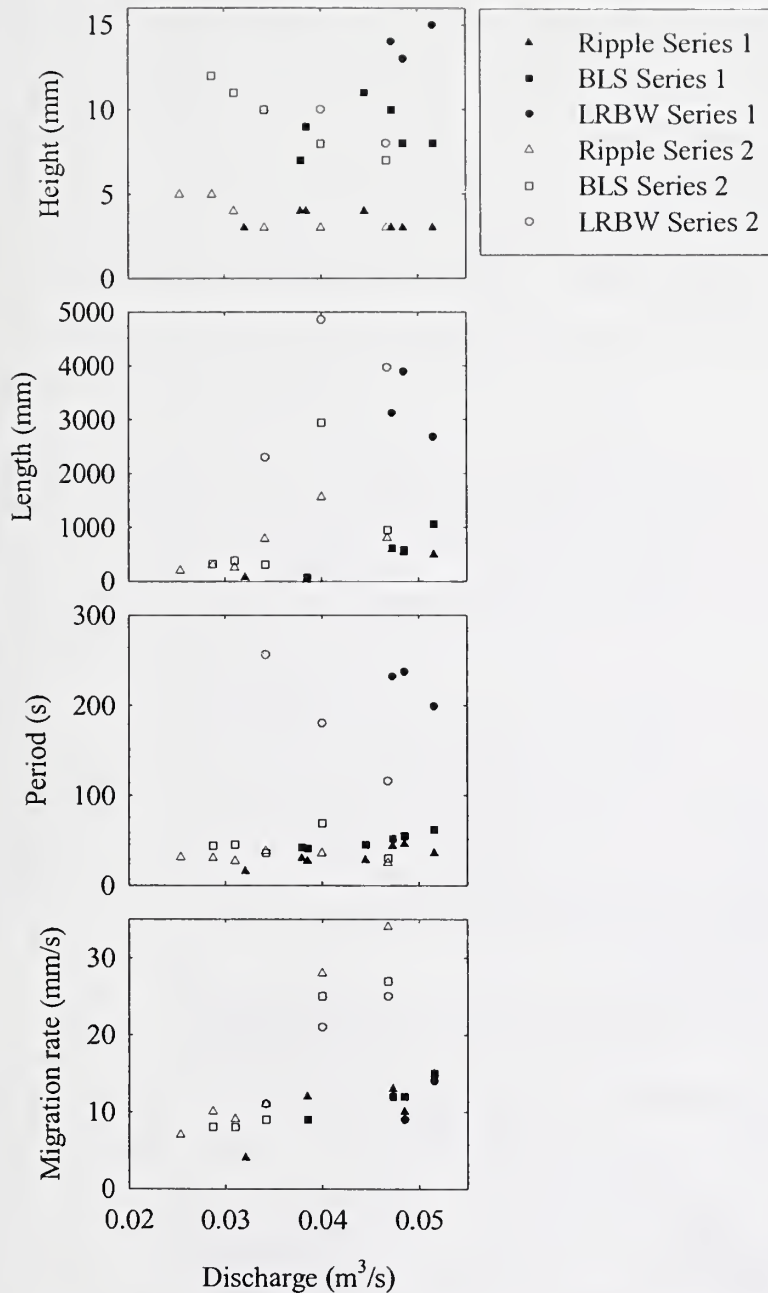
Figure 3.12: Morphological perturbations of bedforms. Bedforms were observed in the present experiments to die out (diminution, a), and combine together (b).



3.4.2 Effect of flow on bedform geometry and texture

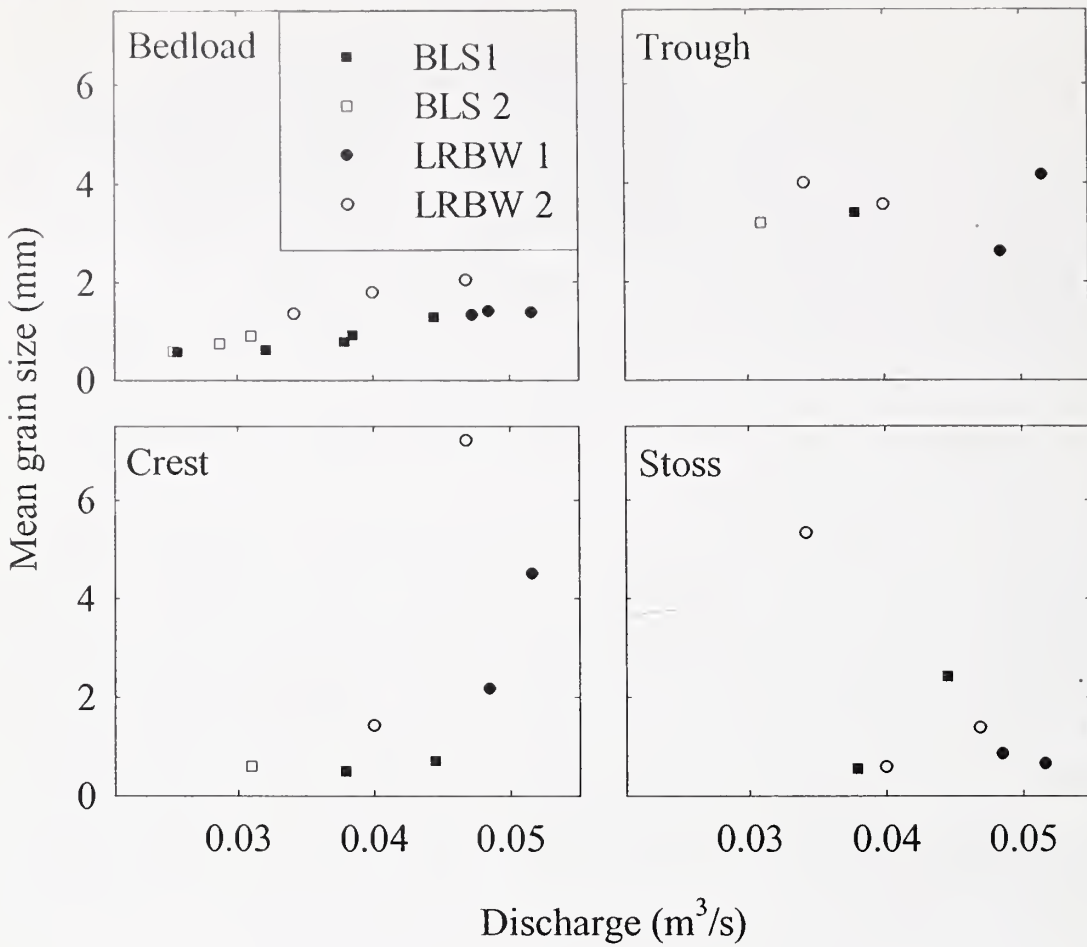
With increasing discharge, the length and migration rate of ripples and bedload sheets tends to increase slightly (Figure 3.13). Low-relief bed waves also travel at a greater velocity with increasing discharge, but their period diminishes (Bennett and Bridge, 1995a). The rate of increase in bedform celerity is greater when the flow is shallower (series 2). There is no obvious trend in bedform height with rising discharge, with the exception of bedload sheets, which diminish in height under the shallower flow conditions (series 2). Some of the variations in bedform geometry with discharge may be an artefact of the cluster analysis classification process.

Figure 3.13: Variations in bedform height, length, period and migration rate with discharge. BLS and LRBW represent bedload sheets and low-relief bed waves respectively.



As discharge increases the mean grain size of the bedload and crestal region increases (Figure 3.14). This effect is enhanced under shallower flow conditions (Series 2), where bed shear stresses are greater for a given discharge (Table 3.1). Rapid coarsening of the crest is linked to the development of low-relief bed waves, which first occur at a lower discharge under the shallower flow conditions. The texture of the trough seems to remain fairly similar under a wide range of conditions, whereas the stoss region exhibits no obvious trend.

Figure 3.14: Variations in mean grain size of bedload and specific bedform areas with discharge. BLS and LRBW represent bedload sheets and low-relief bed waves respectively.

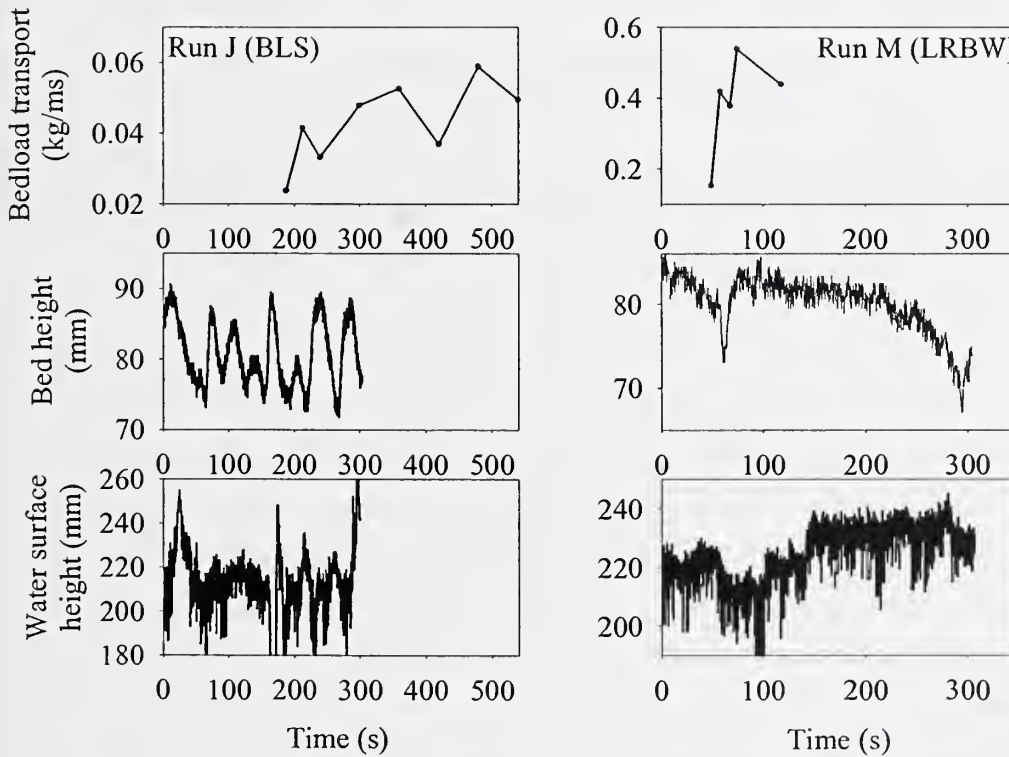


3.4.3 Relation of bedform geometry to bedload and suspended load

At all discharges, regions of distinct roughness transitions were apparent (Iseya and Ikeda, 1987), which are thought to result in alterations of the turbulent flow structure (Robert *et al.*, 1992; Livesey, 1995), and may in turn affect sediment transport at the local scale (Best, 1996). This is illustrated by bedload sheets and low-relief bed waves which are discernible by variations in transport rate along their length (Kuhnle, 1986; Iseya and Ikeda, 1987; Kuhnle and Southard, 1988; Whiting *et al.*, 1988). With the approach of the crest, the transport rate of the coarse fraction peaks first. Observations from video footage indicate that once entrained from the trough/stoss boundary, the coarser particles tend to travel farther and faster compared with the sand fractions, and are deposited or decelerated just downstream of the crest. The peak in the transport rate of the coarse fractions occurs shortly before the maximum transport rate for the total bedload and the sand component (Kuhnle and Southard, 1988). The bedload transport peak results from the passage of the crest, which has a similar composition to the bedload. Maximum transport rates for the finer sand fractions are associated with the movement of the fine grained stoss. The sand transport peak maybe delayed due to these size fractions infilling the voids in the coarse trough (Iseya and Ikeda, 1987). Furthermore, the fine sediment

buried beneath the coarser clasts can only be exposed to the flow once the larger grains have been entrained (Kuhnle and Southard, 1988). The stoss side of the low-relief bed waves were observed to fine in the present experiments in the upstream direction, which explains why Kuhnle and Southard (1988) measured the maximum transport rate being further delayed for decreasing sand size fractions. In the case of bedload sheets and low-relief bed waves, the approach of the bedform crest also caused the water surface to dip (Bennett and Bridge, 1995a; low-relief bars). Consequently, bedload sheet and low-relief bed wave migration cause periodic variation in bed shear stress and bedload transport rate (Figure 3.15) of up to ten orders of magnitude (Whiting *et al.*, 1988). Where bedload sheets are superimposed on low-relief bed waves, secondary fluctuations in bedload flux can be observed (Gomez *et al.*, 1989; Bennett and Bridge, 1995a; Livesey *et al.*, 1998).

Figure 3.15: Variations in bedload transport rate. Records of the bed and water surface height are shown alongside in order to give an impression of the bed morphology and water surface slope during bedload transport sampling. Although the measurements of bedload transport overlap temporally with the other records, they are not simultaneous. The water and bed surface measurements were taken concurrently. However the water surface measurement probe was located 0.145 m upstream of the bed height measurement probe.



In the case of bedload sheets and low-relief bed waves, the crest and bedload exhibited a similar grain size distribution, indicating that any mobile sediment is transported within the migrating bedform. Grain size samples from the surface of ripples could not be collected due to their small size relative to the area sampled using the clay piston technique. However, visual observations and the grain size distribution of the bedload indicate that ripples were composed mainly of sand. The average bedload sediment transport rate, q_b , for

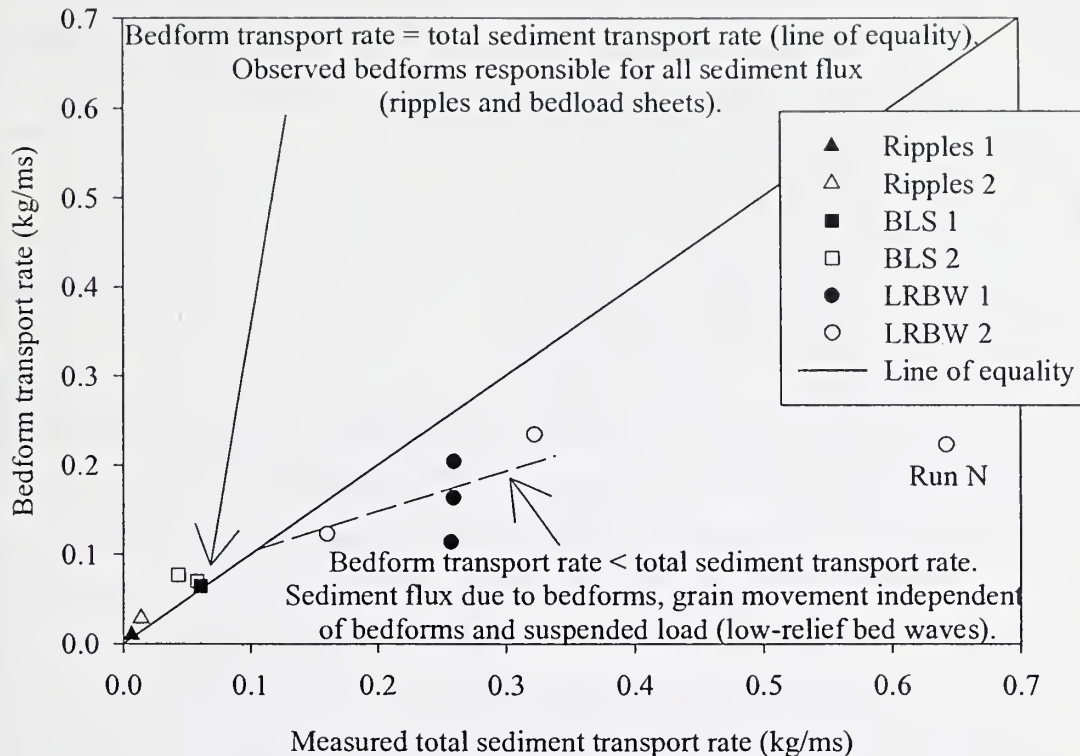
the highest order bedform observed in each experimental run was calculated (Simons *et al.*, 1965; Crickmore, 1970; van Rijn, 1993) using the following equation:

$$q_{bf} = \beta(1 - \rho_s)\sigma ch \quad (3.5)$$

where β is the shape factor (i.e. the fraction of a rectangle, equivalent in height and length to the bedform, which is occupied by the bedform), ρ_s is the porosity factor (0.4 for poorly sorted coarse sand; van Rijn, 1993), σ is the sediment density (2650 kg/m^3), c is the average bedform migration rate and h is mean bedform height. In order to calculate a value for the shape factor, 20 examples of each bedform type were traced and superimposed. An average value for the shape factor was calculated from the largest and smallest resulting features. The shape factor was found to vary between 0.41 and 0.80, with average values of 0.51, 0.50, 0.61 and 0.70 for ripples, bedload sheets, low-relief bed waves in series 1 and low-relief bed waves in series 2 respectively.

Estimates of bedload transport rates from Equation 3.5 are compared with measured values for total sediment transport rates in Figure 3.16. At discharges below approximately $0.045 \text{ m}^3/\text{s}$ (sediment transport rate of 0.1 kg/ms) total sediment transport is accommodated by the migration of ripples and bedload sheets. At higher discharges low-relief bed waves develop, and bedform migration no longer completely accounts for total sediment transport. Additional contributions to total sediment transport may include grains moving independently of the bedforms, even longer low relief bedforms not recognised here and sediment in suspension. All the bedload samples taken for Run N included just the front section of a low-relief bed wave, which experiences maximum sediment flux, causing total sediment transport to be overestimated.

Figure 3.16: Comparison of bedload and bedform transport rate. BLS and LRBW represent bedload sheets and low-relief bed waves respectively.



3.4.4 Conceptual model for sediment transport in bimodal mixtures

In bimodal mixtures, the relatively fine grain sizes are entrained first, forming isolated longitudinal stripes of finer material (Iseya and Ikeda, 1987; Ferguson *et al.*, 1989; Parker, 1991b; Nezu and Nakagawa, 1993; Tsujimoto and Kitamura, 1996; Tsujimoto, 1999). As these sandy patches grow in volume and migrate over a static armour consisting of the coarse size fractions, they eventually develop into ripples (Allen, 1968; Southard and Dingler, 1971; Williams and Kemp, 1971; Leeder, 1980; Ikeda and Iseya, 1988; Baas, 1999). With further increases in mean bed shear stress, larger clasts are entrained from the surrounding coarse armour layer. Although ripples have been shown to be absent in uniform sediment mixtures containing a grain size greater than 0.7 mm (Leeder, 1980), the present experiments in a bimodal sediment mixture generated ripples with clasts greater than 0.7 mm in diameter (Figure 3.5). The occurrence of larger grains within the ripple forms is explained by the overpassing of coarser particles. Isolated gravel clasts were observed to be entrained at roughness transitions (e.g. the boundary of the fine grained stoss and the coarse armour layer) and proceed quickly along the sandy stoss of the bedforms, this being promoted by a low friction angle and high relative protrusion.

With increasing flow strength, ripples develop into bedload sheets as the bedload incorporates more coarser clasts, although a static armour remains in the bedform trough. The increased mean size of sediment in

transport is responsible for changing the grain roughness within the bedform, and therefore altering the flow structure, aiding erosion in the trough and thus increasing the height of bedload sheets compared with ripples. Further increases in the quantity and calibre of mobile sediment are accommodated by the development of low-relief bed waves that are associated with a slight increase in bedform height and substantial increase in wavelength (Wilcock and McArdell, 1993; Coleman and Melville, 1994). Since coarser particles are increasingly prone to transport as flow strength increases, the armoured trough eventually becomes mobile. Low-relief bed waves studied in series 2 (shallow flow conditions) and bedload sheets are approximately equivalent in height to the D_{90} (10.07 mm) of the bulk bimodal sediment mixture, whereas low-relief bed waves observed in series 1 are equal in height to the D_{95} (14.55 mm). The maximum grain size class for the bedload was 13.2, 19 and 26.9 mm for ripples, bedload sheets and low-relief bed waves respectively. Bedform height therefore increases with the coarsest fractions found in the mobile sediment, and is approximately half the size of the largest clast in transport. The similar nature of the grain size distribution of the crest, stoss and bedload in the case of bedload sheets, and the correspondence of the bedload, crest and bulk mixture when low-relief bed waves are present also supports this contention. When coarser clasts are transported, they experience greater exposure to the flow, increase bed roughness and changing the turbulent flow structure. As flow strength increases, the additional volume of sediment entrained and transported is also accommodated by increases in bedform length. However, it appears that the wavelength is not regulated by any large-scale flow structures such as flow separation in the bedform lee, which will be considered in more detail in Chapters 4 and 5, and suggests that grain roughness effects are still critical. The growth of bedforms is influenced by many factors including bedform amalgamation, the lateral entrainment of sediment, particle interaction and bed shear stress perturbations, which are also considered further in Chapters 4 and 5.

The majority of the clasts transported over a bedload sheet or low-relief bed wave were deposited in the trough region, becoming buried by the advancing bedform and subsequently re-exposed and entrained following the passage of the bedform i.e. a dunelike grain path (Wilcock and McArdell, 1993; Table 3.8). However, as shear stress increased and bedload sheets and low-relief bed waves developed, the finest fractions were transported in suspension, whilst the coarsest grains were carried as bedload over several bedforms. Sediment suspension and overpassing thus make it difficult to define the area of the bed contributing to bedload transport (e.g. a bedform unit), since sediment in transport over a specific bedform is not necessarily entrained from that feature, especially in the case of low-relief bed waves (Wilcock and McArdell, 1993). Furthermore, the occurrence of different sediment transport mechanisms also leads to variability in bedform wavelength.

Table 3.8: The entrainment, transport and deposition of sand and gravel size fractions.

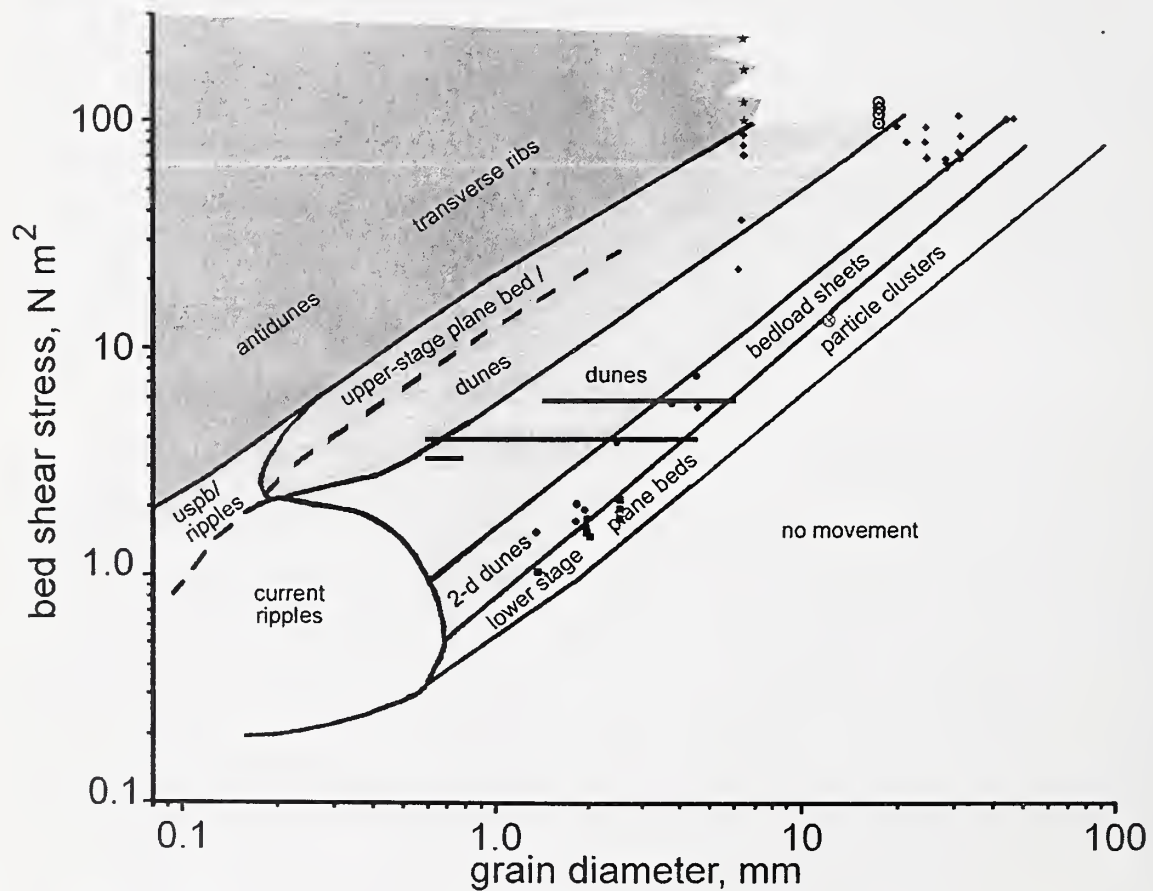
Action	Sand	Gravel
1 Entrainment (Transitional)	Sand is entrained along the bedform stoss.	Where the interstices of the gravel are filled with sand from the upstream region of the stoss, the loss of momentum due to the collective wakes is decreased. Therefore any elevated, coarse grains will be subjected to an increased drag force (exposure effect of Iseya and Ikeda; 1987). The fine infilling may also diminish the frictional resistance experienced by the coarser sediment (i.e. smoothing). As larger grains are entrained more bed sediment is exposed to the flow (Wilcock and McArdell, 1993). In the trough, gravel clasts were entrained from their stable position by scour and collision (Kuhnle, 1986; Kuhnle and Southard, 1988).
2 Transport (Smooth)	Sand tends to move in long, low waves in order to traverse the gravel armour (Kuhnle, 1986), but can also be suspended. Coarse sand grains move across the bedform in spatially and temporally fluctuating streaks (Wilcock and McArdell, 1993).	Transported gravel is elevated above the sandy stoss whilst in motion. Step lengths are very long, and the clasts move rapidly in isolation (Wilcock and McArdell, 1993). Streaks and patches of coarser sediment can be observed which may represent the trough/crest of superimposed bed features.
3 Deposition (Congested)	Sand avalanches down the lee side of the bedform and is buried by subsequent sand grains. The sand also covers any immobile coarse particles contained in the trough region.	As the gravel grains reach the coarse trough/crest they interact and are either deposited or decelerated. The coarse trough is characterised by greater roughness and lower near-bed flow velocities and higher shear stresses (Kuhnle, 1996). At high discharges large grains can move over the stoss of the next downstream bedform without being deposited in the trough region (Wilcock and McArdell, 1993). It becomes less likely to find a stable rest position with increasing discharge and grain size. This size selective trapping may influence fractional transport rates.

3.4.5 Comparison with dunes

Bedload sheets may be genetically related to two-dimensional dunes which develop in well sorted, coarse sand (Costello and Southard, 1980; Wilcock and Southard, 1989; Raudkivi and Witte, 1990; Ditchfield and Best, 1992; Best, 1996). The average, equilibrium hydraulic conditions associated with each of the three bedform populations identified in the present study were all found to plot as dunes on the bedform phase diagrams presented by Southard and Boguchwal (1990, p. 663, Figure 2N, O and P for ripples, bedload sheets and low-relief bed waves respectively). However, Southard and Boguchwal's (1990) bedform phase plot does not specifically classify bedload sheets and low-relief bed waves. Figure 3.17 illustrates that the present data plots in either the dune, two-dimensional dune or bedload sheet region of Best's (1996) bedform phase diagram depending on the selection of a representative grain size. The height of low-relief bedforms scale with the largest grains in transport, and are reduced compared with those of dunes (Ashley, 1990). Furthermore, dunes are steeper (0.08; Carling, 1999) than the low-relief bedforms observed in this study

(<0.02). However, the height of both dunes and low-relief bed waves scales with flow depth, and coarse grained lags may exist in their trough region when sediment transport is low. Furthermore, bedform height may be suppressed in coarse sediment (Snishchenko *et al.*, 1989), possibly accounting for the low-relief of the bedforms observed in the present study. In addition, Carling (1996) notes that dunes require deep flow to form, and therefore the bed features observed may be depth limited in the present experiments. Dunes can form in uniform sediment, whereas bedload sheets require a poorly sorted sediment mixture to develop (Iseyama and Ikeda, 1987; Dietrich *et al.*, 1989). In addition to the morphological and textural contrasts, flow separation, often associated with dune bedforms and considered in more detail in Chapters 4 and 5, has not been measured in the lee of two-dimensional dunes, bedload sheets and low-relief bed waves (Bennett and Bridge; 1995a). Furthermore, dunes have previously been observed to develop from bedload sheets in the field (Whiting *et al.*, 1988) and flume environment (Wilcock, 1992). It is therefore questioned whether bedload sheets and low-relief bed waves represent a transitional feature or a stable bed configuration.

Figure 3.17: Bedform phase diagram from Best (1996). Ripples (red), bedload sheets (blue) and low-relief bed waves (green) observed in the present study are plotted using lines extending from the D_{50} to the D_{85} of the bedload.



3.5 Conclusions

- 1) With increasing bed shear stress the following traverse to flow bedform populations were observed: ripples (up to 5 mm high and 802 mm long), bedload sheets (up to 12 mm high and 1061 mm long) and low-relief bed waves (up to 10-15 mm high (dependent on flow depth) and 4849 mm long). The latter two bedform types have received little detailed attention in the literature, due to their relatively recent recognition. The bedforms were identified from their morphological dimensions (i.e. height and period) using the multivariate technique of cluster analysis.
- 2) The extensive data set presented enables variations in bedform morphology and texture to be documented over a wide range of discharges, from near incipient motion to just below supercritical flow conditions. With increasing shear stress the similar grain size distributions of the crest and bedload both coarsen, and the dynamics of the armour layer change. The height of the low-relief bed waves scales with the largest grains in transport. However, the height of the low-relief bed waves is also dependent on flow depth.
- 3) Fluctuations in both total and fractional bedload transport are related to bedform migration, which is established by the similar nature of the bedload and bedform crest grain size distributions, and the correspondence of bedload and bedform transport rates. However, while the migration of ripples and bedload sheets accommodates all the sediment in transport, this is not the case when low-relief bed waves are present, and additional contributions are made to total sediment transport. Ripples have periods up to 46 s and migrate at up to 34 mm/s. The period of bedload sheets extends to 69 s, and their maximum velocity is 27 mm/s. Low-relief bed waves are characterised by a period of up to 256 s and a maximum celerity of 25 mm/s. The variations in migration rate facilitates bedform superimposition and amalgamation.
- 4) A conceptual model of sediment transport in a bimodal mixture is presented. Sediment composing the bedforms moves along a dune-like grain path. Exceptions to this are the finer particles which are transported in suspension and the coarsest particles which once entrained can rapidly traverse several bedforms before being deposited. With increases in bed shear stress, these alternative transport mechanisms become more predominant.

Chapter 4 : Mean flow over bedforms developed in a bimodal sand–gravel mixture: evaluation of the law-of-the-wall, velocity defect-wake law and velocity distribution models

4.1 Introduction

Detailed LDA measurements of flow velocity have not previously been collected over a bimodal sand-gravel bed with grain sizes up to 32 mm and bedforms. However, limited mean flow data is available in the literature concerning mixed sized sediments and associated bedforms (Bennett and Bridge, 1995; Livesey, 1995; Livesey *et al.*, 1998; Whiting *et al.*, 1988; Wilcock and McArdell, 1993). Furthermore, a vast literature exists detailing the velocity field over smooth boundaries (Nezu and Rodi, 1986; Cardoso *et al.*, 1989), uniform sediments (Kirkgoz, 1989) and dunes and ripples from both field and laboratory studies (Nelson *et al.*, 1993; Bennett and Best, 1995, 1996; Kostaschuk and Villard, 1996; Carling *et al.*, 2000b; Robert and Uhlman, 2001), which share some salient similarities with the present experimental data. In this chapter, velocity profiles collected during the present experiments are compared with previous empirical and theoretical work (e.g. the law-of-the-wall, the velocity defect-wake law, the velocity profile models of Wiberg and Smith (1991) and Nikora *et al.* (2001)), and between different regions over the bedforms, each with characteristic morphology and texture, in order to identify the most influential factors determining the velocity distribution. Furthermore, the form and grain components of the bed roughness are evaluated.

4.2 Data analysis

4.2.1 Hydraulic conditions – fixed bed

The turbulent flow, sediment and bed morphology interact in a complex manner, making it difficult to focus on each aspect individually (McLean *et al.*, 1994). However, as the bed morphology adjusts relatively slowly, it is possible to ‘fix’ the bedforms (i.e. the bedforms are set with resin and stationary), thereby eliminating sediment transport, and improving the quality and quantity of hydraulic data e.g. longer and more accurately positioned velocity records. In the present experiments the mean flow depth, d , was determined by subtracting point gauge measurements of the bed height from the water surface elevation throughout the test section. Water surface slope, S , was obtained by subtracting the dynamic water surface elevations from the static heights and applying a least-squares linear regression (Figure 4.1). This procedure was repeated several times for each experiment and an average value calculated.

Figure 4.1: Representative examples of the determination of water surface slope over a fixed bed. A linear least-squares regression (significant at 95%) is applied to the measured static water elevations once the equivalent dynamic values have been subtracted for all points greater than 7 m downstream of the headbox.

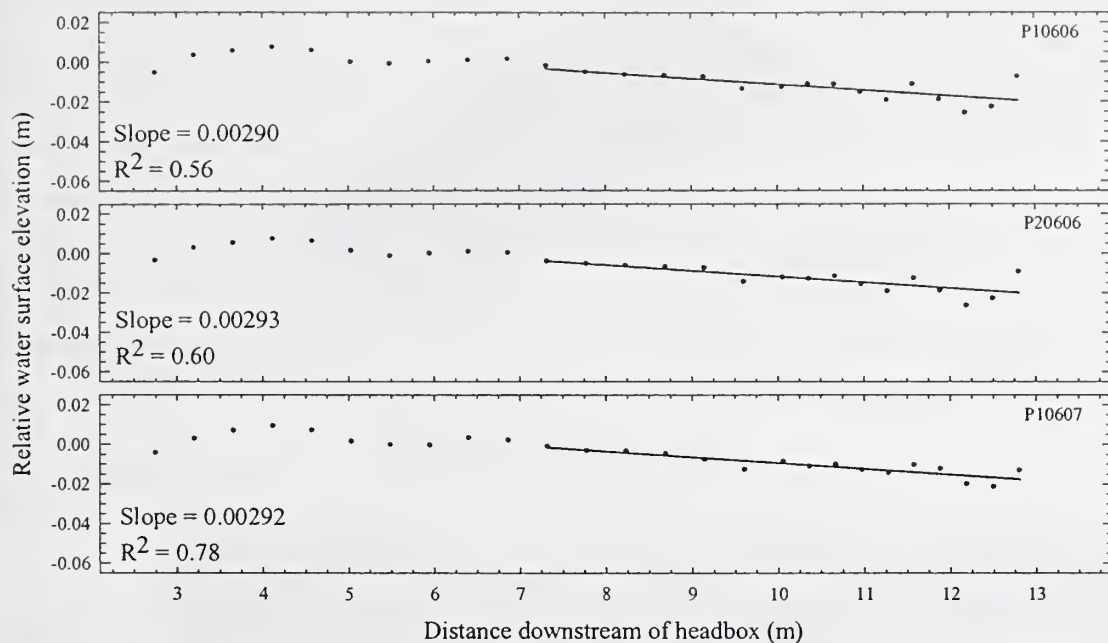
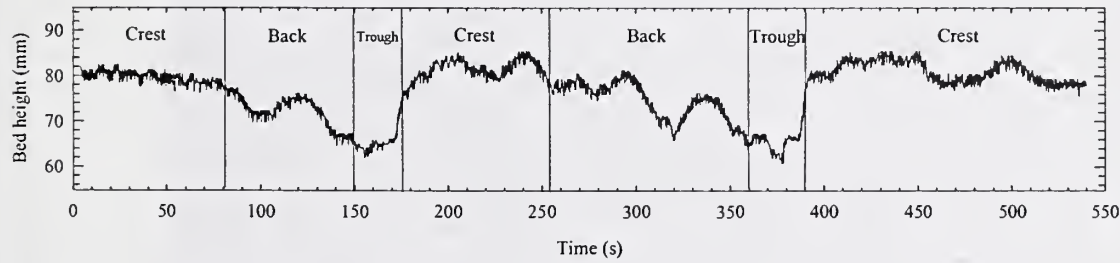


Figure 4.2: Division of the bed height time series into specific bedform regions. The example is taken from run F where low-relief bed waves are the highest order bedform group present.



4.2.2

Sediment bed-elevation records

In the mobile bed experiments, the ultrasonic time series of bed elevations at-a-point were filtered to remove spikes, before the time averaged bed height was calculated. A mean bed height was also determined for specific sections of the bed record. In accord with Livesey (1995), the bed height time series was subdivided based on bedform morphology i.e. crest, stoss and trough of the highest order bedform group present, with ripples being the lowest order and low-relief bed waves the highest (Figure 4.2). In the fixed bed cases, the bed height was measured with a point gauge at the location of each velocity profile.

4.2.3 Laser Doppler anemometry (LDA) records – flow velocity profiles

For each at-a-point measurement of flow velocity, various time-averaged parameters were determined, which also represent spatial averages over a number of bedforms in the mobile bed cases. However, in the fixed

bed experiments, time-averaged parameters correspond to a specific location along and above the bedform within the test section, which contained one representative bedload sheet (F1) and the crestal area of a low-relief bed wave (F2). For the mobile bed experiments, the time-averaged parameters were also calculated for specific sections of the LDA velocity record, which was subdivided based on bedform morphology i.e. crest, stoss and trough (i.e. a spatial and temporal average for each region). Spatio-temporal averages of flow parameters over a fixed bed ideally require at least one complete, representative bedform in the test section, which was only possible in the case of the smaller bedload sheets (F1). Time-averaged velocity parameters are averaged over one bedform length at each height band above the mean test section bed level in order to determine the spatio-temporal average profile (McLean *et al.*, 1999; Nelson *et al.*, 1993). Plate 4.1 and Figures 4.3-4.6 illustrate the transect along which velocity and turbulence measurements were taken, and the location of each time-averaged point measurement and characteristic profiles.

Plate 4.1: The fixed a) bedload sheets and b) low-relief bed wave, with the transect along which velocity and turbulence measurements were taken highlighted in red (0.6 m). Flow is from right to left.

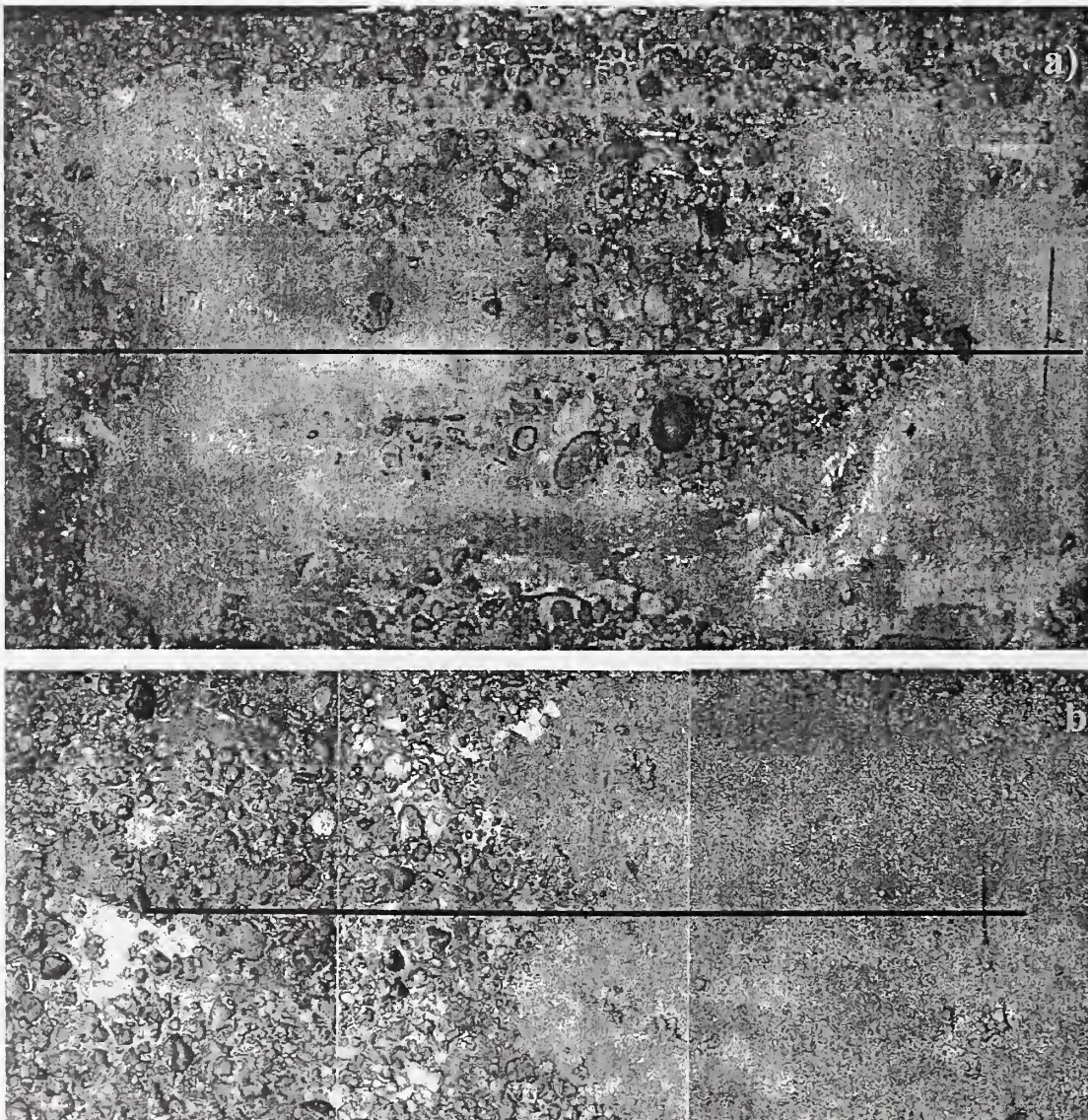


Figure 4.3: Bed elevation map of the test section dominated by bedload sheets. The position of the transect (0.6 m) along which velocity and turbulence measurements were taken is shown by the black line. Flow is from right to left.

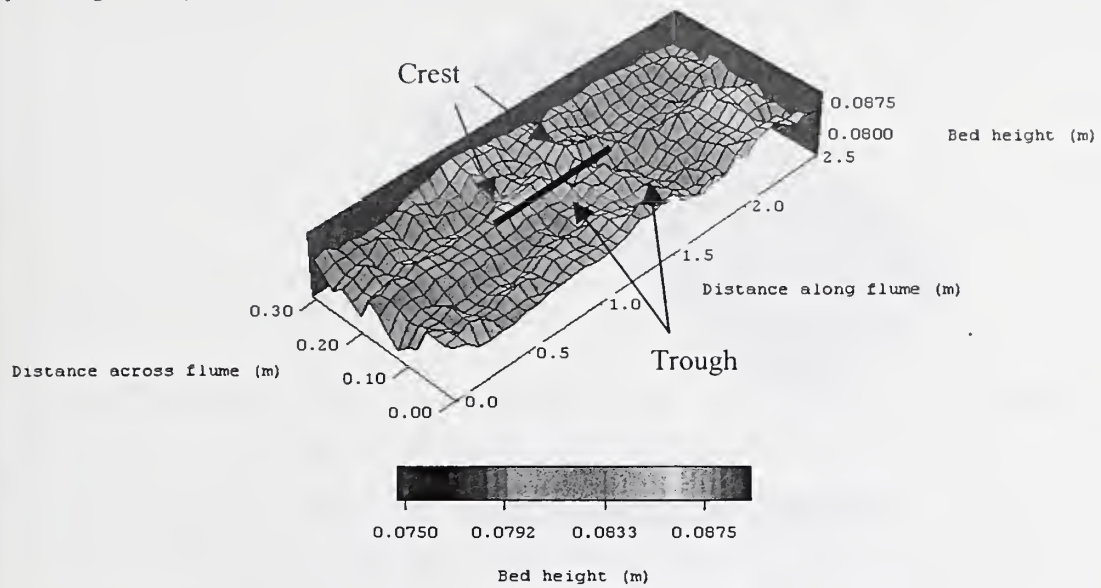


Figure 4.4: Position of velocity and turbulence measurement points over a bedload sheet. Flow is from right to left. Solid and white symbols represent one and two component measurements respectively.

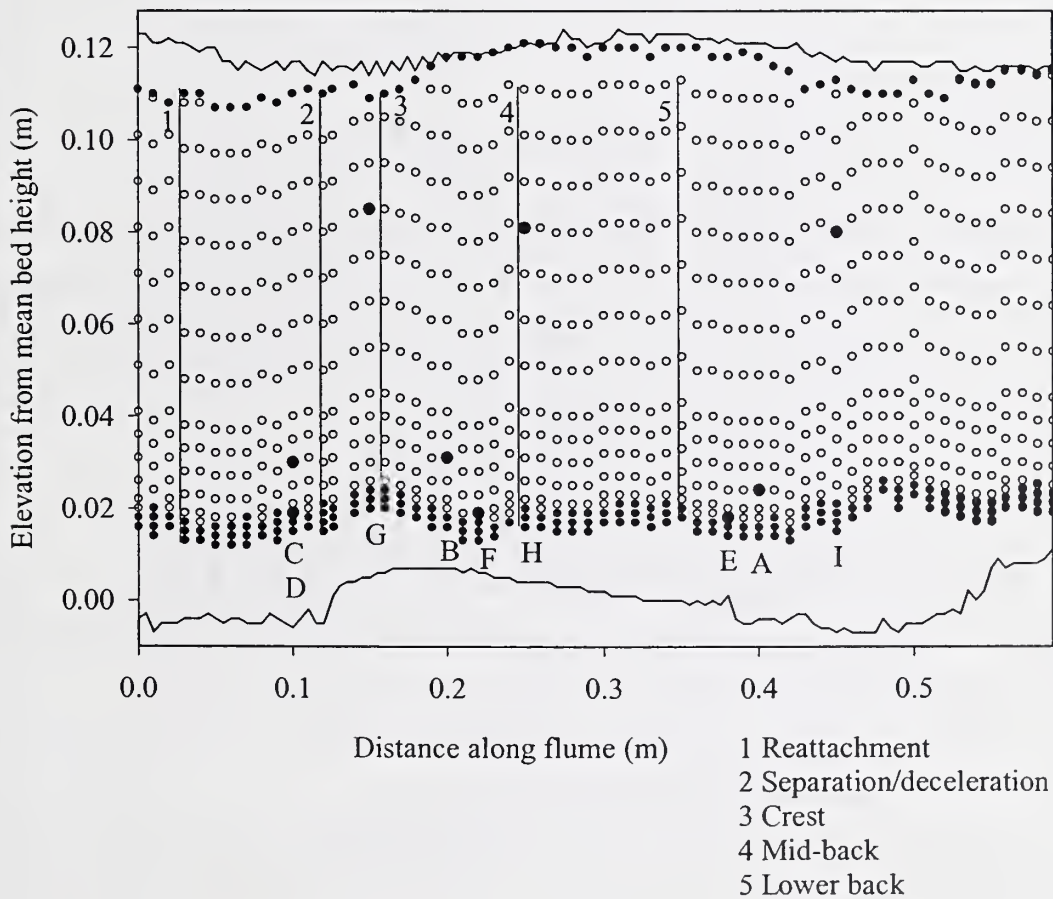


Figure 4.5: Bed elevation map of the test section containing the region around the crest of a low-relief bed wave. The position of the transect along which velocity and turbulence measurements were taken is shown by the black line.

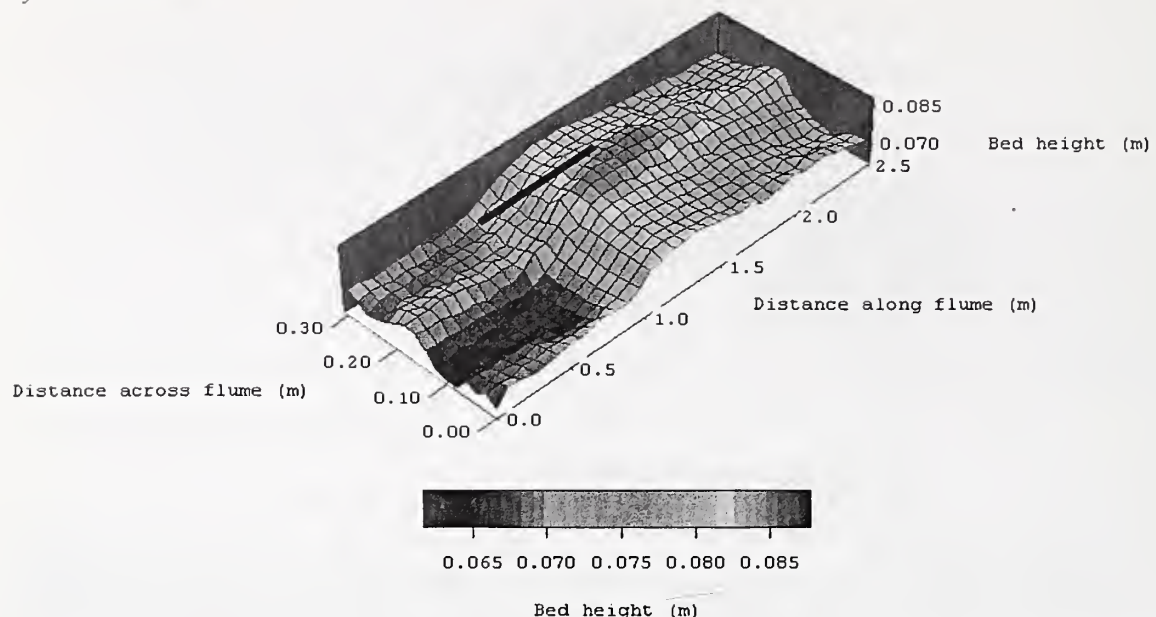
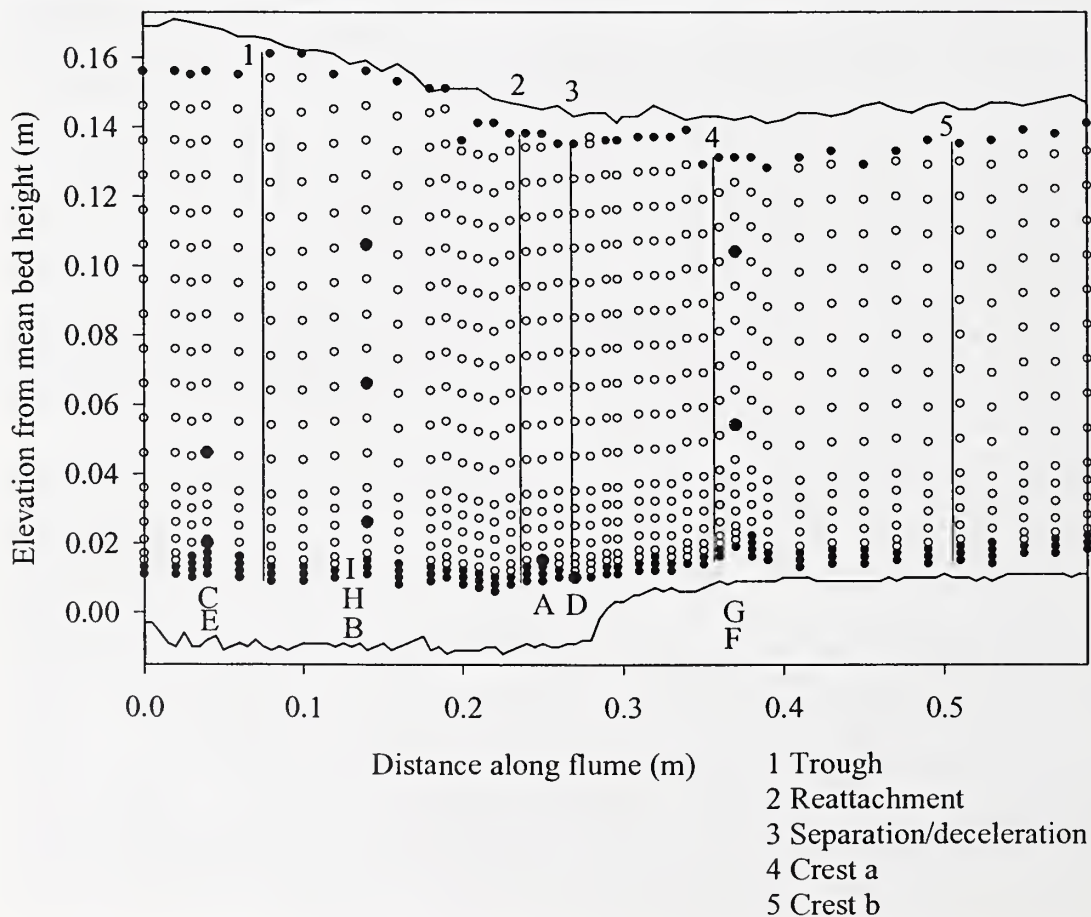


Figure 4.6: Position of velocity and turbulence measurement points in the vicinity of the crest of a low-relief bed wave. Flow is from right to left. Solid and white symbols represent one and two component measurements respectively.



The time-averaged downstream and vertical velocities were determined using Equations 4.1 and 4.2 respectively. The velocity biasing effect was corrected for using the transit-time weighting technique (Equation 4.3; Hosel and Rodi, 1977; McLaughlin and Tiederman, 1973).

$$\bar{u} = \sum_{i=1}^n \eta_i u_i \quad (4.1)$$

$$\bar{v} = \sum_{i=1}^n \eta_i v_i \quad (4.2)$$

$$\eta = \frac{t_i}{\sum_{i=1}^n t_i} \quad (4.3)$$

where \bar{u} and \bar{v} are the time averaged downstream and vertical velocities respectively, n is the number of observations, u_i and v_i are the instantaneous downstream and vertical velocities, η is the transit time weighting and t_i is the transit time of the i 'th particle passing the LDA measuring volume. The depth averaged downstream velocity (U), the root-mean-square of the downstream ($rmsu'$) and vertical ($rmsv'$) velocity components are calculated from Equations 4.4, 4.5 and 4.6 respectively.

$$U = \frac{I}{d} \int_0^d \bar{u} dy \quad (4.4)$$

$$rmsu' = \left[\sum_{i=1}^n \eta_i (u_i - \bar{u})^2 \right]^{0.5} \quad (4.5)$$

$$rmsv' = \left[\sum_{i=1}^n \eta_i (v_i - \bar{v})^2 \right]^{0.5} \quad (4.6)$$

where d is mean flow depth and the instantaneous downstream and vertical velocity fluctuations from the mean are represented by $u' = u_i - \bar{u}$ and $v' = v_i - \bar{v}$. The skewness of the downstream and vertical velocity distributions (u_{skew} , v_{skew}) were evaluated using:

$$u_{skew} = \sum_{i=1}^n \eta_i \left[\frac{(u_i - \bar{u})}{rmsu'} \right]^3 \quad (4.7)$$

$$v_{skew} = \sum_{i=1}^n \eta_i \left[\frac{(v_i - \bar{v})}{rmsv'} \right]^3 \quad (4.8)$$

Reynolds shear stress (τ_R) was calculated by

$$\overline{u'v'} = \sum_{i=1}^n \eta_i (u_i - \bar{u})(v_i - \bar{v}) \quad (4.9)$$

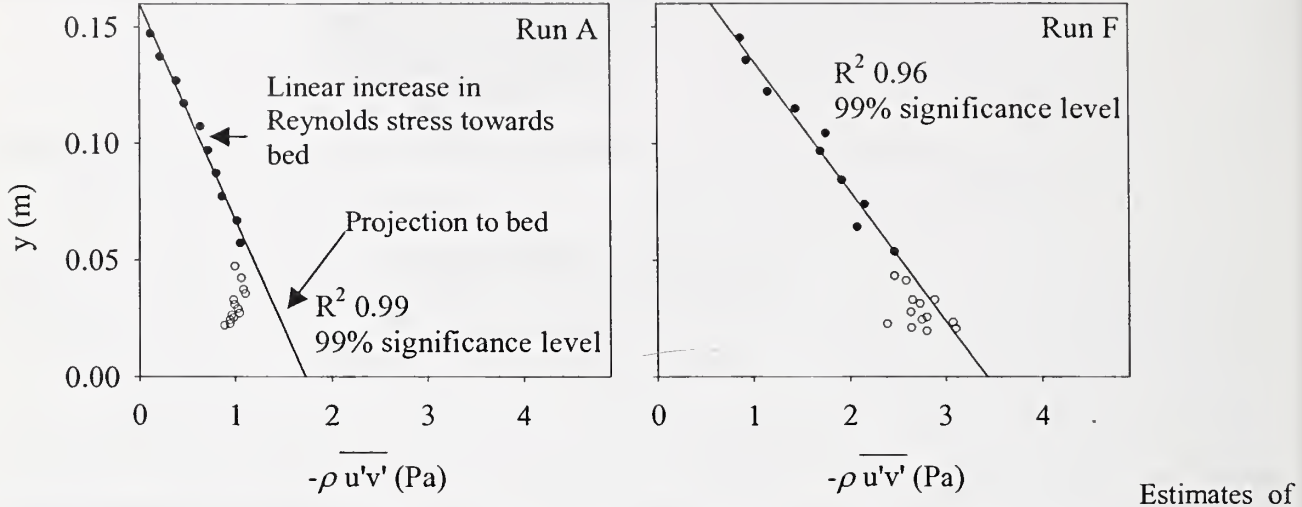
$$\tau_R = -\rho \overline{u'v'} \quad (4.10)$$

where ρ is fluid density. In order to estimate the boundary Reynolds shear stress (τ_{R0}), at-a-point Reynolds stresses were plotted against y/d . A least squares regression of the upper linear section of the Reynolds stress

profile was then projected to the bed (i.e. $y/d = 0$, Figure 4.7; Lyn, 1993; Nezu and Rodi, 1986) assuming that the Reynolds stress varies vertically as described by Equation 4.11.

$$\tau_R = \tau_{R0} \left(1 - \frac{y}{d} \right) \quad (4.11)$$

Figure 4.7: Examples of the projection of Reynolds stress measurements to the bed. Solid points are included in the least squares regression. Near the bed (approximately $y < 0.05$ m) the Reynolds stress measurements diverge indicating the presence of a roughness layer.



Estimates of boundary shear stress can also be obtained from the depth-slope product (Equation 4.12, in conjunction with Williams' (1970) correction for smooth side walls) and the Kármán-Prandtl law-of-the-wall (Equation 4.13), which is applicable only in the bottom 20 percent of the flow excluding the viscous sublayer in turbulent boundary layers, based on the assumptions listed in Equations 4.14-4.17.

$$\tau_0 = \rho g d S \quad (4.12)$$

$$\frac{\overline{u}}{U_*} = \frac{1}{\kappa} \ln \left(\frac{y}{y_0} \right) \quad \frac{\partial \overline{u}}{\partial y} = \frac{U_*}{\kappa y} \quad (4.13)$$

$$\tau_w = \rho U_*^2 \quad (4.14)$$

$$\tau_R = -\rho \overline{u'v'} = \rho l^2 \left(\frac{\partial \overline{u}}{\partial y} \right)^2 \quad (4.15)$$

$$l = \kappa y \quad (4.16)$$

$$\tau_{R0} \approx \tau_w \quad (4.17)$$

where g is gravitational acceleration, S is mean water surface slope, U_* is shear velocity, κ is the von Kármán constant (0.41 in clear water; Nezu and Nakagawa, 1993, p. 51), y is measurement height above the bed, y_0 is the zero-velocity roughness height and l is mixing length. Equations 4.11 and 4.18 illustrate the vertical variation in time-averaged shear stress and mixing length respectively, the latter being made dimensionless with flow depth. When the mixing length term in Equation 4.15 is represented by Equation

4.18 rather than 4.16, the law-of-the-wall is able to maintain the same form but potentially be applicable throughout the whole flow profile since the flow depth is incorporated (Nezu and Rodi, 1986).

$$\frac{l}{d} = \frac{\kappa y}{d} \left(1 - \frac{y}{d}\right)^{0.5} \quad (4.18)$$

In order to obtain the velocity-defect law (Equation 4.20), which describes the outer flow field, the maximum velocity (\bar{u}_{max}) at the upper limit of the boundary layer (δ , not necessarily where $y = d$) is introduced into the law-of-the-wall (Equation 4.19). The original law-of-the-wall (Equation 4.13) is then subtracted from the modified version (Equation 4.19) resulting in the velocity-defect law (Equation 4.20).

$$\frac{\bar{u}_{max}}{U_*} = \frac{1}{\kappa} \ln \left(\frac{\delta}{y_0} \right) \quad (4.19)$$

$$\frac{\bar{u}_{max} - \bar{u}}{U_*} = \frac{1}{\kappa} \ln \left(\frac{\delta}{y} \right) = -\frac{1}{\kappa} \ln \left(\frac{y}{\delta} \right) \quad (4.20)$$

Coles (1956) proposed a wake coefficient (Π) to correct for the under-prediction of velocity by the law-of-the-wall and velocity-defect law in the outer region of turbulent boundary layers (i.e. $y/d > 0.2$). The wake coefficient is an empirical correction function, which represents the various influences (e.g. secondary circulation and turbulent wakes) on the velocity distribution throughout the flow depth. Equation 4.20 is therefore surpassed by the velocity defect-wake law (Equation 4.21), which was empirically derived for smooth turbulent flows, not for flows which are hydraulically rough or have bedload, suspended sediment or bedforms. The velocity defect-wake law can be used to obtain the velocity at the free surface where measurements are difficult.

$$\frac{\bar{u}_{max} - \bar{u}}{U_*} = -\frac{1}{\kappa} \ln \left(\frac{y}{\delta} \right) + \frac{2\Pi}{\kappa} \cos^2 \left(\frac{\pi}{2} \frac{y}{\delta} \right) \quad (4.21)$$

In the near-surface region, secondary currents can negate the wake effect, and consequently the law-of-the-wall and the velocity-defect law may apply to the whole flow depth (Ferro and Baiamonte, 1994). The ability to assess the validity of the law-of-the-wall and the velocity defect-wake law is dependent on the quality of the data collected. Ideally, a non-intrusive method, with a high temporal and spatial resolution should be employed e.g. LDA used in the present experiments. For example, precise measurement of \bar{u} and y in the wall region ($y/d \leq 0.2$) and accurate determination of U_* are necessary for evaluating κ . Furthermore, the flow should be as close to a uniform condition as possible (i.e. in the test section), and the channel aspect ratio should be as large as is feasible to avoid the influence of secondary flows. Non-uniform flow and secondary currents negatively impact on the shape of vertical profiles of time averaged velocity parameters. Consequently, comparisons between the laws and experimental data are confined to the region below the downstream velocity maximum at $y = \delta$.

4.3 Results

4.3.1 Hydraulic conditions – fixed bed

The fundamental hydraulic parameters for both fixed bed examples and their associated mobile bed experiments are shown in Table 4.1.

Table 4.1: Hydraulic conditions for the fixed bed experiments and their equivalent mobile bed runs. d is flow depth ($\pm 4\%$ for fixed beds), U is depth-averaged velocity, Q is mean flow discharge ($\pm 4\%$ for fixed beds), S is water surface slope ($F1 \pm 1\%$, $F2 \pm 6\%$), Fr is Froude number ($Fr = U / \sqrt{gd}$), τ_{R0} is Reynolds stress projected to the bed, θ is dimensionless bed shear stress ($\theta = \tau_{R0} / (\sigma - \rho)gD_{50}$, where σ is sediment density taken to be 2650 kg m^{-3}) and f is the Darcy-Weisbach friction coefficient. BLS and LRBW represent bedload sheets and low-relief bed waves respectively.

Run	d (m)	U (m/s)	Q (m^3/s)	S ($\times 10^{-3}$)	Fr	τ_{R0} (Pa)	θ	f
F1 (Bedload sheets)	0.119	0.77	0.029	2.91	0.71	1.53	0.166	0.021
J (Bedload sheets)	0.141	0.70	0.029	2.51	0.60	3.37	0.366	0.055
F2 (Low-relief bed waves)	0.151		0.047	3.55				
F (Low-relief bed waves)	0.178	0.87	0.047	3.09	0.66	3.43	0.291	0.036

Reasons for the difference in flow depth over the mobile and fixed bed cases may include:

- *Different measuring apparatus used.* Ultrasonic probes were used in the mobile bed runs, while point gauges were employed in the fixed bed cases. Marks were placed on the flume as a rough guide to check that the flume was not losing water and that the flow depth was maintained. The water level markings, although a simple technique, resulted in the flow depths for each series of the mobile bed experiments falling into a relatively narrow range, and were also employed during the fixed bed experiments.
- *Different technique used.* At-a-point measurements were made over a period of five minutes in the mobile bed runs. Flow depth was therefore collected over several bedforms, in order to account for variations between individual bedforms. In the fixed bed cases, data collection was confined to a) the length of one complete bedload sheet and b) the area surrounding the crest of the low-relief bed wave.
- *Slope effects.* The flume slope is the same for equivalent fixed and mobile bed runs and yet the water surface slope differs. This implies that exact uniform, equilibrium flow was not achieved over the fixed bedforms.
- *Sediment effects.* In the fixed bed runs the layer of sediment previously in transport during the mobile experiments is deposited and immobile, increasing the height of the solid bedform. Conversely, before the sediment bed is coated in resin, the flume is drained and left too partially dry, facilitating the removal of water and air from within the bed and therefore possibly reducing bedform height.

Song and Graf (1994) employ a pressure-gradient parameter, β , defined as

$$\beta = \frac{d}{\tau_0} g \rho \left(-S + \frac{\partial d}{\partial x} \right) \quad (4.22)$$

where, S is the bed slope (assumed to be equal to the water surface slope for the present experiments), and $\frac{\partial d}{\partial x}$ is the longitudinal variation in water depth (assumed here to be equal to 0). The pressure-gradient parameter indicates the degree of uniformity of the flow. When $\beta = -1$, the flow is uniform, and decelerating and accelerating flows are distinguished by higher and lower values respectively (Table 4.2). In accelerating flows, the velocity maximum is below the water surface, while it coincides with the water surface during decelerating flow conditions. In uniform flow at-a-point vertical velocities are close to zero, with the depth average value equalling zero. The Reynolds number ($Re = Udp/v$) of each experimental flow are also listed in Table 4.2, along with estimates of the relative roughness of the runs. Relative roughness was calculated using the average height of the highest bedform population present, and also the equivalent sand roughness, k_s , derived from the law of the wall.

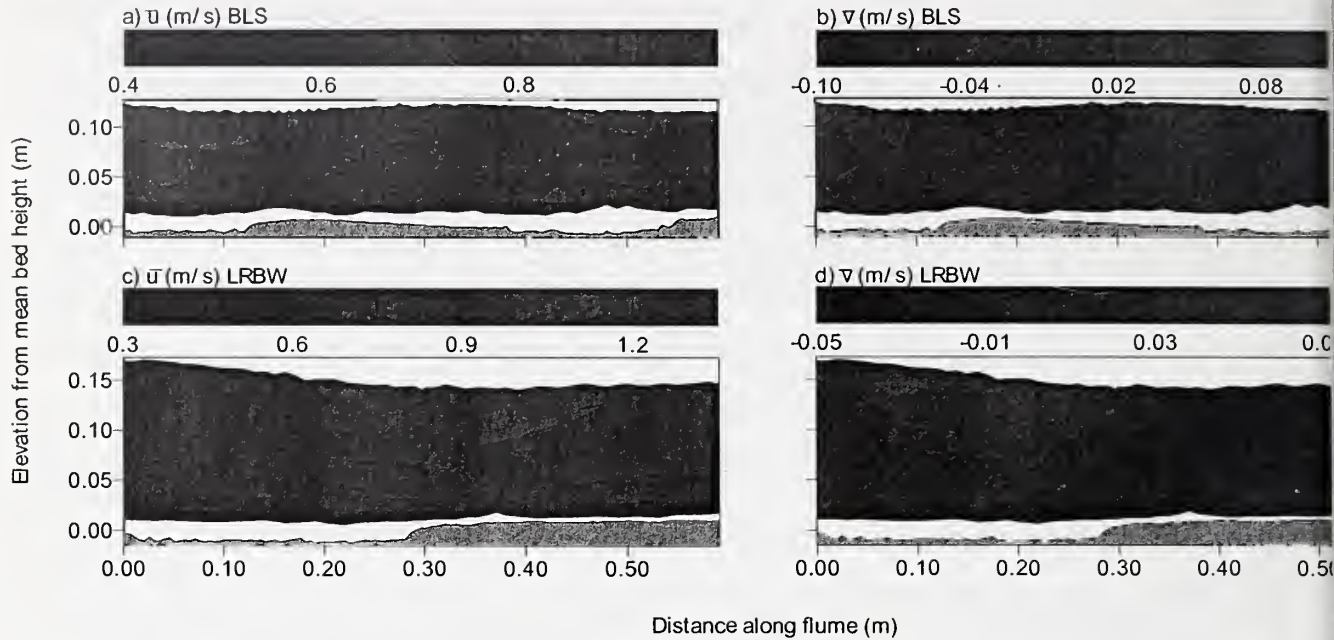
Table 4.2: The Reynolds number, pressure-gradient parameter and relative roughness for the experimental flows.

Run	Reynolds number, Re	Presure-gradient, β	Relative roughness	
			(using bedform height)	(using k_s)
<i>Series 1, d = 0.18 m</i>				
A	76947	-1.8	0.011	0.169
B	87509	-1.3	0.017	0.320
C	107965	-1.2	0.039	0.287
D	112298	-1.1	0.052	0.613
E	126596	-1.1	0.063	0.597
F	135842	-1.6	0.079	0.669
G	135860	-1.0	0.074	0.591
H	147500	-1.2	0.085	0.379
<i>Series 2, d = 0.14 m</i>				
I	71421	-0.8	0.036	1.152
J	86579	-1.0	0.085	1.057
K	93421	-1.2	0.073	0.447
L	98404	-1.2	0.070	0.303
M	109737	-1.1	0.072	1.424
N	128632	-1.1	0.057	1.000
<i>Fixed</i>				
F1 (J)	80377	-2.2	0.13	0.588

4.3.2 Mean flow field over a fixed bed

The flow maps presented here (Figure 4.8) are produced by extrapolation between laser measurement points, which formed an extensive grid over the fixed bedforms (Figure 4.4 and 4.6). No measurements were possible very close to the bed (< 10 mm), due to the presence of large clasts which obstructed the laser beams.

Figure 4.8: Contour maps of mean flow over bedload sheets (BLS) and the crestal region of a low-relief bed wave (LRBW). Flow is from right to left. a) time-averaged downstream velocity (BLS), b) time-averaged vertical velocity (BLS), c) time-averaged downstream velocity (LRBW), d) time-averaged vertical velocity (LRBW). The bedform morphology is shaded grey, with a white zone above indicating where laser velocity measurements were impossible. The top area shaded white highlights the water surface.



The greatest downstream velocities over a bedload sheet ($> 0.9 \text{ m s}^{-1}$) occur at and downstream of the crest, near the water surface ($> 0.08 \text{ m}$ above the mean bed height, Figure 4.8a). The largest near-bed velocities ($> 0.7 \text{ m s}^{-1}$) are located at and just upstream of the crest. Downstream of the crest, flow expansion is present and large negative near-bed vertical velocities (-0.04 to -0.07 m s^{-1}) occur at, and just downstream of, the crest (Figure 4.8b). Topographic forcing results in flow acceleration over the upper stoss and crest, and average flow conditions are essentially identical at both bedload sheet crests.

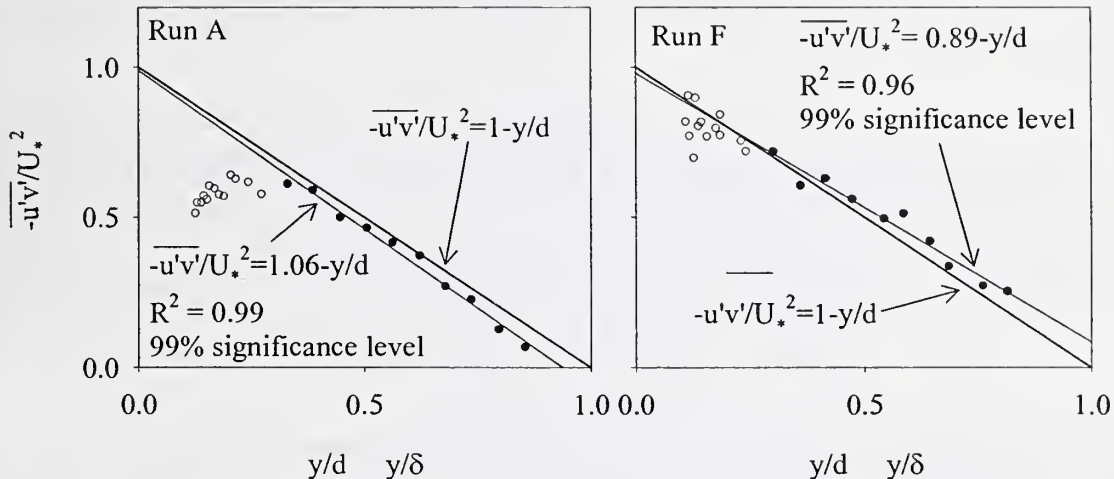
Downstream velocity reaches a maximum ($> 1.2 \text{ m s}^{-1}$) just upstream of the low-relief bed wave crest in the vicinity of the water surface (Figure 4.8c). High near-bed negative vertical velocities (-0.03 to -0.05 m s^{-1}) are apparent over the crest, and extend into the trough region. Flow expansion over the trough causes the lower part of the flow to be directed towards the bed, whereas the upper flow exhibits a tendency to move towards the water surface (Figure 4.8d).

4.3.3 Boundary shear stress and shear velocity

The maximum downstream flow velocity in both the mobile and fixed bed cases is at or close to the water surface. Furthermore, in the upper part of the flow, Reynolds shear stress increases linearly from the bed (Figure 4.7). Consequently, secondary circulation is thought to be negligible despite the low width/depth

ratios of 2 and 2.5 for series 1 and 2 respectively (Nezu *et al.*, 1985). The linear sections of Reynolds shear stress profiles can be projected to the bed in order to determine boundary shear stress and shear velocity (Figure 4.7, Table 4.3), which can then be used to non-dimensionalise flow velocity and turbulence measurements (Lyn, 1993; Nezu and Rodi, 1986). Figure 4.9 illustrates Reynolds shear stress profiles made dimensionless with shear velocity, which demonstrate the close correspondence of the experimental data to the linear decrease in stress away from the bed indicated in Equation 4.11, and verify the use of linear extrapolation of shear stress to the bed.

Figure 4.9: Examples of Reynolds shear stress profiles normalised by shear velocity against dimensionless flow depth.



Boundary shear stress and shear velocity is also determined from Equations 4.12 (depth-slope product) and 4.13 (law-of-the-wall). With the exceptions of the fixed bedload sheet, and mobile bed runs A and I (i.e. the lowest discharge mobile run at each flow depth), the boundary shear stress determined by the depth-slope product (Equation 4.12) and Reynolds stress projection (Equation 4.11) were within $\pm 30\%$ of each other (Table 4.3). However, the law-of-the-wall (Equation 4.13) gave erroneous results due to the large roughness elements in the region of the flow closest to the bed. The wakes associated with these coarse particles and the bed relief destroy the logarithmic velocity profile inherent in the assumptions of the law-of-the-wall and characteristic of flow over a smooth boundary. The percentage errors for the estimates of boundary shear stress from the law-of-the-wall ranged from ± 17 to $\pm 171\%$, with an average of $\pm 67\%$, while the minimum, maximum and mean percentage errors for shear velocity were ± 8 , ± 85 , $\pm 33\%$ respectively at a 95 % confidence level using the error determination method of Wilkinson (1984). Robert *et al.* (1992) note that the mean percentage errors for their shear velocity estimates are $\pm 13\%$, with the largest errors being $\pm 61\%$. The percentage error for bed shear stress is twice that for shear velocity when derived from the law-of-the-wall, and the accuracy of both depends on the number of measurements employed in the regression (Biron *et al.*, 1998; Wilkinson, 1984). The bed shear stresses derived from Reynolds stress measurements were compared for mobile runs with similar discharges (i.e. C and D, F and G, and J and K), and found to agree

within 7, 43 and 3 percent respectively, with the value of run F being lower than expected, and run G higher than anticipated. Reynolds stress projections (least squares linear regressions were significant at the 95% confidence level or higher, with the exception of the stoss region of bedforms in run J) are thought to be the most accurate method for determining bed shear stress since they are based on actual turbulence measurements, whereas it is difficult to accurately measure water surface slope ($\pm 12\%$) which is used in Equation 4.12, and to account for sidewall effects. Application of the depth-slope product in the present experiments was associated with errors of ± 12 and 6% for bed shear stress and shear velocity determinations respectively. Furthermore, Reynolds stress projections can be calculated for both spatially averaged values and specific regions/points of the bed, whereas the depth-slope product gives only spatially averaged values which may mask any variations over a bedform and associated changes in bed morphology and texture.

Table 4.3: Comparison of boundary shear stress and shear velocity determinations using the depth-slope product (τ_0 , Equation 4.12; corrected for sidewall effects using Equation 3.2 (Williams, 1970)), Reynolds stress projections (τ_{R0} , Equation 4.11) and the law-of-the-wall (τ_w , determined from the bottom 20 % of the flow, Equation 4.13).

Run	τ_0 (Pa)	U_* using τ_0 (m/s)	τ_{R0} (Pa)	U_* using τ_{R0}	τ_w (Pa)	U_* using τ_w (m/s)
MOBILE, SPATIALLY-AVERAGED						
A (Sand ribbon)	2.53	0.0539	1.73	0.0416	2.20	0.0469
B (Ripple)	2.66	0.0503	2.63	0.0513	4.60	0.0678
C (BLS)	3.10	0.0515	3.36	0.0580	5.53	0.0744
D (BLS)	3.09	0.0557	3.62	0.0602	12.34	0.1111
E (BLS)	3.66	0.0556	4.01	0.0633	14.04	0.1185
F (LRBW)	4.30	0.0605	3.43	0.0586	20.33	0.1426
G (LRBW)	4.84	0.0656	5.99	0.0774	17.76	0.1333
H (LRBW)	6.00	0.0696	6.51	0.0807	13.73	0.1172
I (Ripple)	2.62	0.0775	4.05	0.0636	12.09	0.1100
J (BLS)	2.89	0.0512	3.37	0.0581	16.21	0.1273
K (BLS)	3.49	0.0538	3.46	0.0588	8.09	0.0900
L (LRBW)	4.16	0.0591	4.12	0.0642	7.05	0.0839
M (LRBW)	5.56	0.0645	6.11	0.0782	49.59	0.2227
N (LRBW)	7.00	0.0746	7.92	0.0890	29.90	0.1729
MOBILE, AVERAGED OVER SPECIFIC BEDFORM REGIONS						
J Back		3.52	0.0593	23.49	0.1533	
J Crest		3.42	0.0585	7.29	0.0854	
J Trough		3.71	0.0609	13.74	0.1172	
F Back		3.65	0.0604	19.65	0.1402	
F Crest		3.18	0.0564	20.00	0.1414	
F Trough		3.78	0.0615	69.17	0.2630	
FIXED, SPECIFIC VERTICAL PROFILES						
F1 (J) Reattachment		1.48	0.0385	6.73	0.0821	
F1 (J) Separation		1.57	0.0396	8.06	0.0898	
F1 (J) Crest		1.30	0.0361	1.97	0.0443	
F1 (J) Mid back		1.12	0.0334	5.02	0.0709	
F1 (J) Lower back		1.69	0.0411	4.16	0.0645	
F2 (F) Trough		7.13	0.0844	6.59	0.0812	
F2 (F) Reattachment		5.22	0.0722	74.01	0.2720	
F2 (F) Separation		5.19	0.0720	105.09	0.3242	
F2 (F) Crest a		3.83	0.0619	5.76	0.0759	
F2 (F) Crest b		4.79	0.0692	5.38	0.0734	
FIXED, SPATIALLY-AVERAGED						
F1 (J)	2.90	0.0539	1.53	0.0391	15.24	0.1234

4.3.4 Comparison of vertical profiles of time-averaged downstream velocity with the law-of-the-wall and the velocity defect-wake law

Comparisons of the vertical profiles of time-averaged downstream velocity with the law-of-the-wall were conducted by applying a least squares linear regression between \bar{u} and $\ln y$, where y is the independent variable (Bergeron and Abrahams, 1992; Figure 4.10a). κ and y_0 can then be derived (Equations 4.23 and 4.24) using the slope ($\partial u / \partial \ln(y)$) and intercept (C) of the regression, and U_* deduced from the projection of Reynolds stress to the bed (Table 4.3).

$$\kappa = \frac{U_*}{\partial u / \partial \ln(y)} \quad (4.23)$$

$$y_0 = \exp\left(\frac{-C}{\partial u / \partial \ln(y)}\right) \quad (4.24)$$

However, the estimates of y_0 using the law-of-the-wall in the present experiments have a minimum, maximum and mean percentage error of ± 74 , ± 817 and ± 252 % at a 95% confidence level. Bennett and Bridge (1995) state a percentage error of ± 100 % for their derivations of y_0 , Wilkinson (1984) records an error of ± 77 % while Robert *et al.* (1992) note an average error of ± 35 %.

κ can also be evaluated from the velocity defect-wake law (Equation 4.21), and is equal to the value derived using the law-of-the-wall when the shear velocity estimated from the Reynolds stress projections is employed. Both κ and the Π coefficient are deduced from the velocity defect-wake law (Equations 4.25

and 4.26, and Figure 4.10c) using the slope $\left(\partial \left(\frac{\bar{u}_{\max} - \bar{u}}{U_*} \right) / \partial \ln \left(\frac{y}{d} \right) \right)$ and intercept (C) of the least squares linear regression of $\frac{\bar{u}_{\max} - \bar{u}}{U_*}$ against $\ln \left(\frac{y}{d} \right)$, with $\frac{y}{d}$ as the independent variable.

$$\kappa = -\frac{1}{\partial \left(\frac{\bar{u}_{\max} - \bar{u}}{U_*} \right) / \partial \ln \left(\frac{y}{d} \right)} \quad (4.25)$$

$$\Pi = \frac{\kappa C}{2} \quad (4.26)$$

Calculated values of κ , y_0 and Π are listed in Table 4.4.

4.3.4.1 The present experimental values of κ , y_0 and κ , y_0 and k_s over a mobile bed

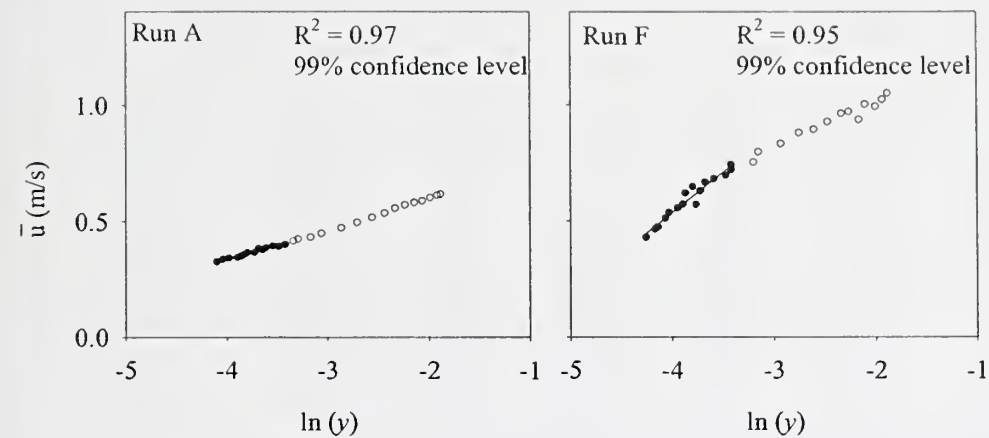
In the spatially-averaged case, κ values ranged from 0.144 to 0.363 in the wall region ($y / \delta \leq 0.2$), and are much reduced from the clear water value of 0.41. When derived over the whole of the boundary layer the κ

values were more consistent, ranging from 0.207 to 0.332. Lower κ values were also found for the wall region (0.096 – 0.281) compared with the whole boundary layer (0.217 – 0.284) when specific bedform regions noted in Table 4.4 were considered. Calculated spatially averaged values of y_0 ranged from 0.961 to 6.569 mm in the wall region, whereas over specific bedform regions, y_0 extended from 1.979 to 12.045 mm.

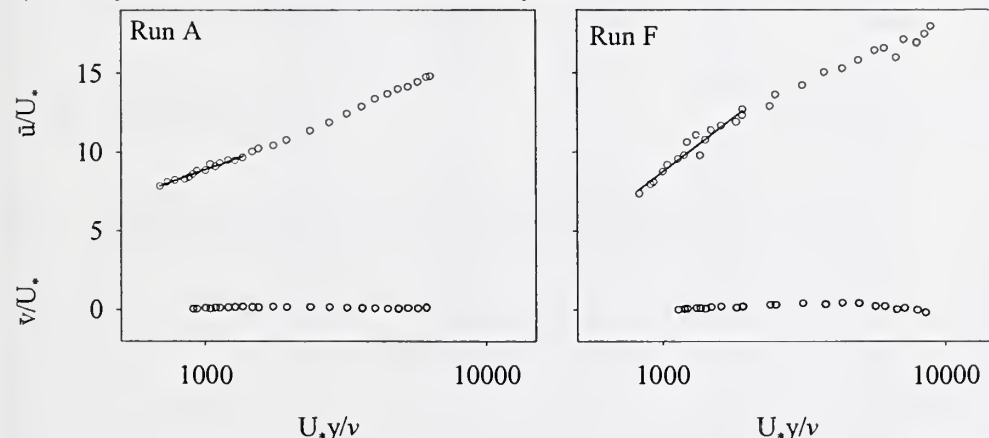
The equivalent sand roughness height ($k_s = 30.2y_0$, for hydraulically rough flows where $\frac{U_*k_s}{\nu} > 70$ and ν is the kinematic fluid viscosity, Table 4.4) extended from 0.029 to 0.198 m for the spatially averaged values, and 0.060 to 0.364 m over specific bedform areas.

Figure 4.10: Examples of the application of the law-of-the-wall and velocity defect-wake law using linear least squares regression.

a) Law-of-the-wall.



b) Law-of-the-wall shown in dimensionless form.



c) Velocity defect-wake law.

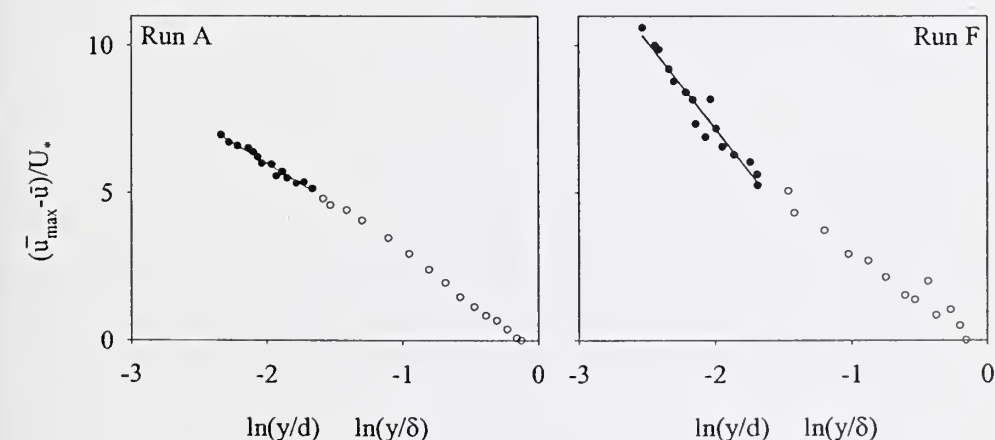


Table 4.4: Calculated values of y_0 , k_s , κ and Π for the present experimental data.

Run	y_0 ^a (mm)	k_s ^a (m)	κ ^b	Π ^b	κ ^c	Π ^c	U_*k_s/v
MOBILE, SPATIALLY-AVERAGED							
A (Sand ribbon)	0.961	0.029	0.363	0.091	0.317	-0.042	1206
B (Ripple)	1.830	0.055	0.310	-0.107	0.332	-0.033	2821
C (BLS)	1.727	0.052	0.320	-0.047	0.309	-0.082	3014
D (BLS)	3.525	0.106	0.222	-0.296	0.293	-0.088	6378
E (BLS)	3.482	0.105	0.219	-0.178	0.254	-0.064	6649
F (LRBW)	3.957	0.119	0.168	-0.395	0.245	-0.095	6969
G (LRBW)	3.430	0.104	0.238	-0.308	0.314	-0.057	8049
H (LRBW)	2.213	0.067	0.282	-0.137	0.304	-0.070	5406
I (Ripple)	5.255	0.159	0.237	-0.220	0.296	-0.057	10119
J (BLS)	4.941	0.149	0.187	-0.237	0.260	0.016	8650
K (BLS)	2.215	0.067	0.268	-0.083	0.283	-0.026	3941
L (LRBW)	1.422	0.043	0.314	0.096	0.274	-0.055	2760
M (LRBW)	6.569	0.198	0.144	-0.423	0.264	-0.050	15477
N (LRBW)	4.678	0.141	0.211	0.072	0.207	0.006	12548
MOBILE, AVERAGED OVER SPECIFIC BEDFORM REGIONS							
J Back	6.073	0.183	0.159	-0.338	0.263	0.037	
J Crest	1.979	0.060	0.281	0.011	0.284	0.012	
J Trough	4.842	0.146	0.213	-0.166	0.263	-0.028	
F Back	4.218	0.127	0.177	-0.344	0.245	-0.087	
F Crest	3.233	0.098	0.163	-0.462	0.241	-0.142	
F Trough	12.045	0.364	0.096	-0.539	0.217	-0.092	
FIXED, SPECIFIC VERTICAL PROFILES							
F1 (J) Reattachment	0.716	0.022	0.192	-0.094	0.223	0.036	
F1 (J) Separation	0.925	0.028	0.181	-0.284	0.254	-0.063	
F1 (J) Crest	0.019	0.001	0.333	-0.012	0.344	-0.017	
F1 (J) Mid back	0.401	0.012	0.193	-0.399	0.282	-0.084	
F1 (J) Lower back	0.252	0.008	0.261	-0.413	0.446	-0.088	
F2 (F) Trough	1.563	0.047	0.426	0.240	0.310	-0.087	
F2 (F) Reattachment	8.930	0.270	0.109	-0.524	0.237	-0.077	
F2 (F) Separation	10.192	0.308	0.091	-0.616	0.237	-0.139	
F2 (F) Crest a	0.098	0.003	0.334	-0.308	0.392	-0.156	
F2 (F) Crest b	0.113	0.003	0.387	-0.237	0.423	-0.141	
FIXED, SPATIALLY-AVERAGED							
F1 (J)	2.325	0.070	0.130	-0.500	0.271	-0.093	

$$k_s = 30.2 y_0$$

v is the kinematic fluid viscosity.

^a Values determined for $y \leq 0.2\delta$, where δ is the boundary layer thickness.

^b Values determined for $y \leq 0.2\delta$ using τ_{ro} .

^c Values determined for $y \leq \delta$ using τ_{ro} .

4.3.4.2 The present experimental values of κ , y_0 and k_s over a fixed bed

In the wall region κ values fell between 0.091 and 0.426, whereas for the whole boundary layer values were greater, ranging from 0.223 to 0.446. When compared with the mobile bed results, the values for κ obtained over the fixed beds are closer to the clear water value of 0.41 (Nezu and Nakagawa, 1993). Values for y_0 and k_s calculated from the bottom 20 % of the flow depth, extended from 0.02 to 10.20 mm and 1 to 308 mm respectively at specific points over the fixed bedforms.

4.3.4.3 The present experimental values of Π over a mobile and fixed bed

The wake coefficient ranged from -0.423 to 0.096 when derived for $y/\delta \leq 0.2$ with spatially-averaged velocities over a mobile bed. Over the whole of the boundary layer, the derived values extend over a smaller range from -0.095 to 0.016 . For specific bedform regions noted in Table 4.4 over a mobile bed, Π values derived from the wall region ($y/\delta \leq 0.2$) and entire boundary layer ($y/\delta > 0.2$) extend from -0.539 to 0.011 and -0.142 to 0.037 respectively. In the fixed bed runs, Π values derived from the wall region and complete boundary layer range from -0.616 to 0.240 and -0.156 to 0.036 respectively.

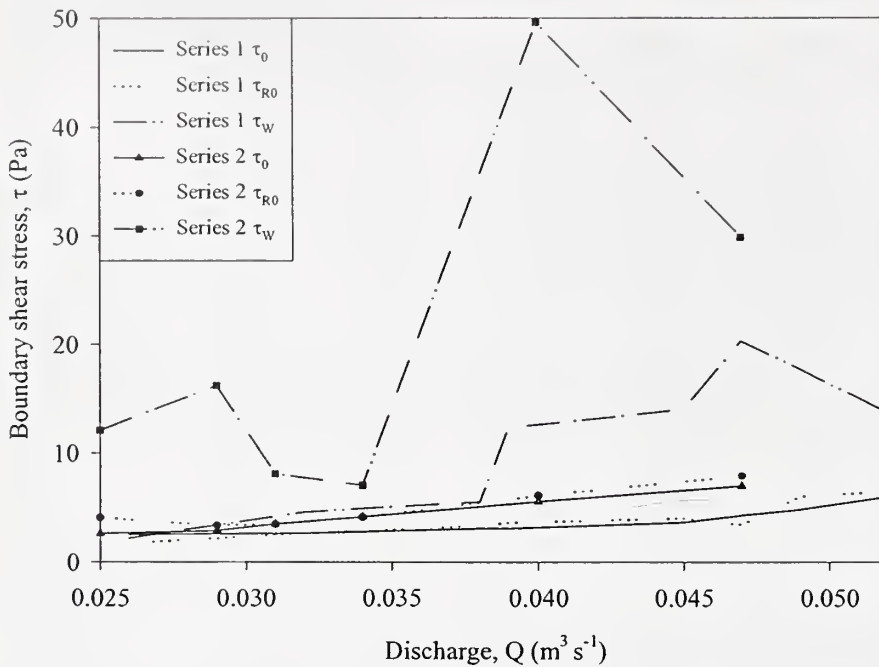
The velocity defect-wake law fits the experimental data well over the whole flow profile when adjusted values for κ and Π are used, with R^2 values above 0.93 at the 99% significance level (Figure 4.10c). When the law-of-the-wall is applied in the lower 20 % of the flow, R^2 values range from 0.530 to 0.995 (Figure 4.10a). The greater range of R^2 values may be due to the lower number of measurements included in the regression compared with the velocity defect-wake law over the whole flow depth. Furthermore, there is a tendency for greater data scatter near the bed, despite more intensive velocity measurements in this region.

4.4 Discussion

4.4.1 Boundary shear stress determination

Bed shear stress values calculated from Reynolds stress projections and the depth-slope product agreed within 30 %. However, the law-of-the-wall was not successful in predicting accurate boundary shear stresses, except when the discharge was below $0.037 \text{ m}^3 \text{ s}^{-1}$ under the higher flow conditions (Figure 4.11). The shear stresses predicted by the law-of-the-wall show greater deviation from the true values under lower flow conditions, causing the relative roughness to be increased, which is in great contrast to the assumption of a smooth boundary explicit in the derivation of the law-of-the-wall. When the flow was shallower, the boundary shear stress estimated from both Reynolds stress projections and the depth-slope product increased more rapidly with discharge. A similar range of boundary shear stresses (0.42-7.27 Pa) were used in the experiments of Wilcock and McArdell (1993), while Bennett and Bridge (1995) report values below 4 Pa. The depth-slope product predicted similar bed shear stresses for the fixed and mobile bedload sheets, of 2.90 and 2.89 Pa respectively. However, the values obtained from Reynolds stress projections differed substantially, e.g. 1.53 and 3.37 Pa for the fixed and mobile example respectively. Although the estimates of boundary shear stress from the law-of-the-wall concur for the fixed and mobile bedload sheet (15.24 and 16.21 Pa respectively), these predictions are much greater than those derived from the depth-slope product and the projection of Reynolds stresses. The boundary shear stress determined from projections of Reynolds stress to the bed is reduced for the fixed bedload sheet due to lower flow resistance resulting from the absence of bedload (Wiberg and Rubin, 1989) and lower porosity of the fixed bedforms (Mendoza and Zhou, 1992).

Figure 4.11: Estimates of boundary shear stress with varying flow depth and discharge using the depth-slope product (τ_0 , Equation 4.12, corrected for sidewall effects using Equation 3.2), Reynolds stress projections (τ_{R0} , Equation 4.11) and the law-of-the-wall (τ_w , in the bottom 20 % of the flow, Equation 4.13). The calculated values are also listed in Table 4.3.



4.4.2 Spatial variations in time-averaged flow velocities and Reynolds stresses

The greatest velocities (exceeding the spatial average) are obtained over the crest (red symbols in Figure 4.12) of both mobile and fixed bedload sheets and low-relief bed waves, with reduced velocities over the back, reaching a minimum in the trough region (blue symbols in Figure 4.12). Data collected over the fixed bedload sheet (Figure 4.12c) indicates that velocity is above the spatial average at the point of flow deceleration/separation and reattachment. The variations in velocity over different bedform regions are less ambiguous in the case of the low-relief bed wave due to their greater morphological dimensions, shear stresses and sediment sorting.

Reynolds shear stress also varies spatially, but in the opposite manner to downstream velocity i.e. Reynolds stress is greatest over the trough, declining over the back and at a minimum over the crest (Table 4.5). The fixed bedload sheet has a very low and narrow range of shear stresses values (< 2 Pa, Table 4.5), while the fixed low-relief bed wave experiences higher shear stresses over a greater range of values (3.8-7.1 Pa, Table 4.5). Elevated values of bed shear stress are associated with the generation of turbulent wakes from the crests of bedforms and coarse clasts, which occur most frequently in the trough region. Over the low-relief bed waves textural and morphological transitions are more distinct and occur on a greater spatial scale compared with the bedload sheets, causing greater adjustment of the bed shear stress.

Figure 4.12: Spatial variations in time-averaged flow velocities, a) Run J, bedload sheet, b) Run F, low-relief bed wave, c) Fixed 1, bedload sheet and d) Fixed 2, low-relief bed wave. SA represents the spatial average of the time-averaged downstream velocity.

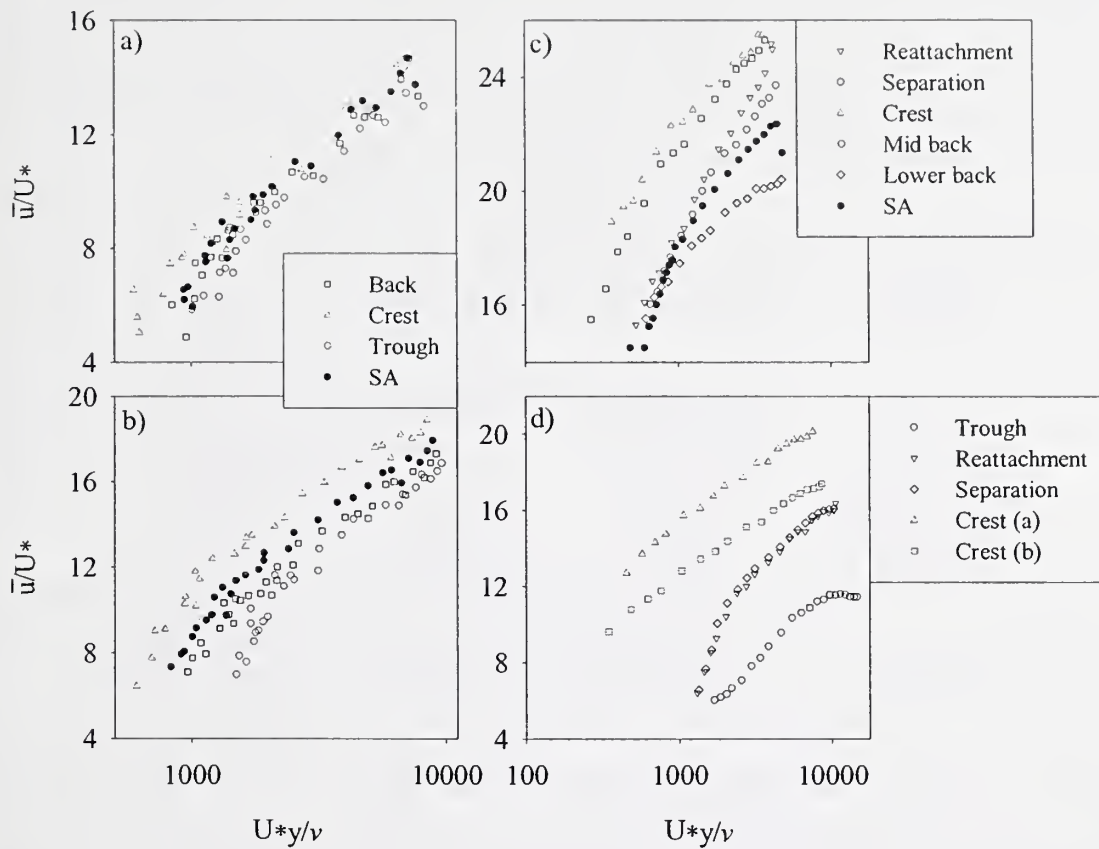


Table 4.5: Bed shear stress (Pa) over mobile and fixed bedforms derived from the projection of Reynolds stress to the bed.

Bedform region/point	Bedload sheets	Low-relief bed waves
<i>Mobile bed cases</i>		
Back	3.52	3.65
Crest	3.42	3.18
Trough	3.71	3.78
<i>Fixed bed case</i>		
Reattachment	1.48	5.22
Separation	1.57	5.19
Crest	1.30	3.83-4.79
Mid-back	1.12	
Lower back	1.69	
Trough		7.13

4.4.3 Comparison of the mean flow field over bedforms

The mean flow field over dunes and ripples have previously been mapped (Bennett and Best, 1995, Figure 5 p. 502; Bennett and Best, 1996, Figure 15.2 p. 291), and are compared in Table 4.6 with the present

distributions of time-averaged downstream and vertical velocity over bedload sheets and low-relief bed waves (Figure 4.8). The surface of the fixed dunes and ripples investigated by Bennett and Best (1995, 1996) were coated with uniform 0.22 mm diameter glass spheres. The coarser bimodal mixture used in the present experiments makes it impossible to take LDA measurements very close to the bed (e.g. in the zone of possible flow separation) due to obstruction of the laser beams by large clasts. Furthermore, the flow structure over the bedload sheets and low-relief bed waves reflects the influence of both texture and bedform morphology, whilst in the work of Bennett and Best only the latter is considered.

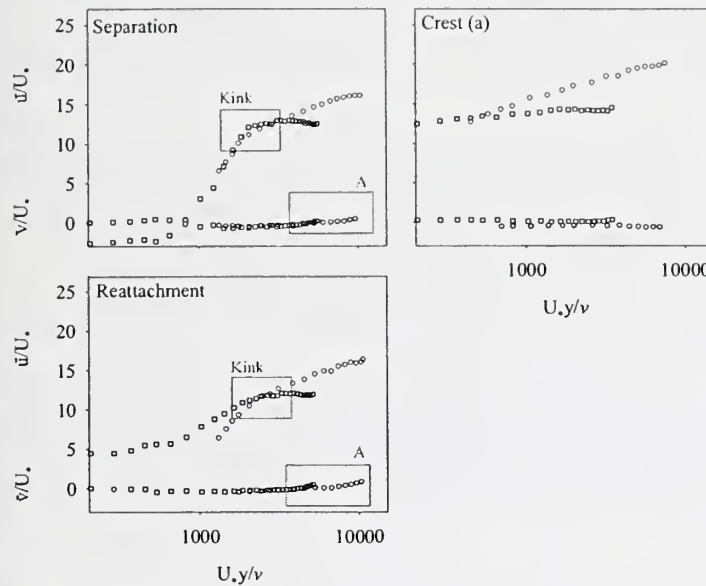
Table 4.6: Comparison of the mean flow field over different bedforms.

Mean flow parameter	Ripples	Bedload sheets	Low-relief bed waves	Dunes
Vertical influence of bedforms	0.2d	Whole flow depth	Whole flow depth	Whole flow depth
\bar{u} , trough, near-bed ($y/d < 0.3$)	Flow decelerated/reversed	Flow decelerated	Flow decelerated	Flow decelerated and reversed
\bar{u} , crest, outer flow ($y/d > 0.3$)	Similar values (0.5 m s^{-1}) recorded over all bedform locations in the outer flow.	Maximum ($> 0.9 \text{ m s}^{-1}$)	Maximum ($> 1.2 \text{ m s}^{-1}$)	Maximum ($> 0.5 \text{ m s}^{-1}$)
\bar{v} , trough, near-bed ($y/d < 0.3$)	Towards bed	Towards bed	Towards bed	Towards bed, although flow can move upwards in the separation zone
\bar{v} , stoss, near-bed ($y/d < 0.3$)	Away from bed	Away from bed	Away from bed	Away from bed

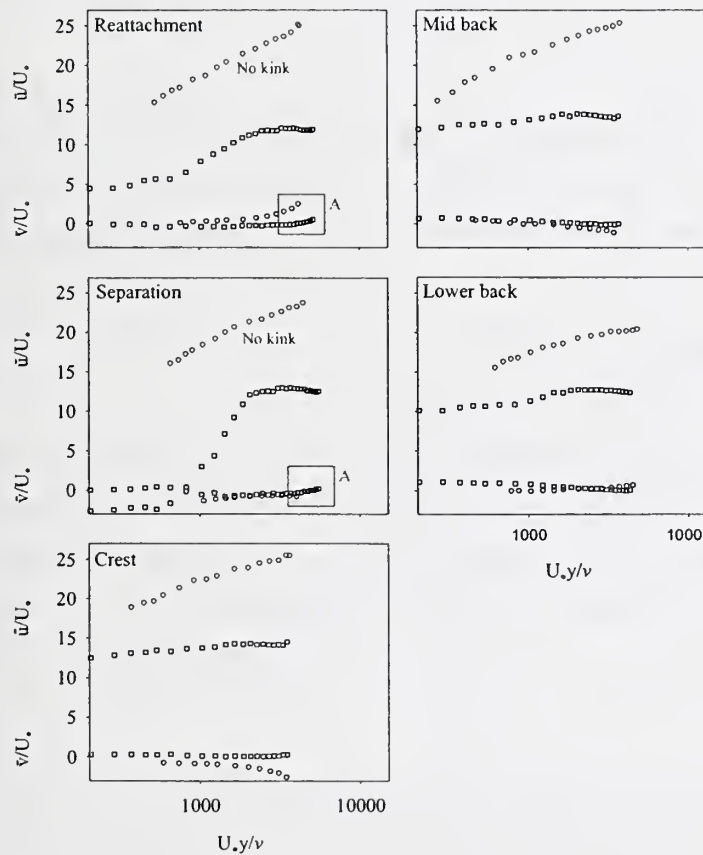
Selected profiles of downstream and vertical velocity over fixed bedload sheets, low-relief bed waves and dunes (Bennett and Best (1995)) are compared in Figure 4.13. The downstream velocity profiles in the separation and reattachment region of the low-relief bed wave show a slight kink (Figure 4.13a), similar to that observed over dunes, indicating the presence of flow separation downstream of the bedform crest. However, no obvious change of slope is apparent in the separation or reattachment region of the bedload sheet (Figure 4.13b), suggesting the absence of flow separation. At reattachment and separation, the vertical velocity increases near the water surface ($y/d > 0.9$, highlighted by the letter A in Figure 4.13) for all three bedform types due to flow expansion. The normalised velocity profiles over the crestal regions of the fixed bedforms are straight, and McLean *et al.* (1999a) note that at the crest, flow is most similar to a uniform boundary layer. However, significant flow deceleration/separation distorts the linear velocity profile (kinks identified in Figure 4.13). The profiles of downstream velocity over the dune stoss (Figure 4.13) illustrate the recovery of the mean flow downstream of separation back to crestal conditions, assisted by topographic acceleration. The normalised downstream velocities are greater over the bedload sheet compared with the other fixed bedforms, indicating that the bedload sheets provide less resistance to the flow due to their smaller morphological dimensions.

Figure 4.13: Comparison of selected profiles of normalised downstream and vertical velocity over bedload sheets, low-relief bed waves and dunes (Bennett and Best (1995)). Box A highlights increases in vertical velocity near the water surface.

a) Low-relief bed wave (F2, circles) compared with a fixed dune (squares).



b) Fixed bedload sheet (F1, circles) compared with a fixed dune (squares).



4.4.4 Flow resistance

Predictions of bed roughness are hindered by the interdependence of the bed morphology, bed roughness, flow and turbulence parameters and sediment transport (Nikora *et al.*, 1998; Millar, 1999). Furthermore, in the field, discharge varies almost continuously with changes in flow stage (van Rijn, 1993). Bed roughness can be estimated using two basic approaches:

- 1) Employing bedform and grain-based parameters, for example bedform height, length and steepness, and grain diameter (Vanoni and Hwang, 1967; Engelund, 1977; van Rijn, 1984, 1993; Karim, 1995; McLean *et al.*, 1999a, b). This method is more universal and is also applicable in non-steady conditions.
- 2) Using integral parameters, for example mean depth, mean velocity and grain diameter (Engelund and Hansen, 1967; Smith and McLean, 1977).

The total friction presented to the flow by the bed (f), can be divided into the resistance provided by the skin friction of the individual sediment grains (f'), and the form drag generated by the pressure forces operating over the bedforms (f'' ; Einstein and Barbarossa, 1952):

$$f = f' + f'' \quad (4.27)$$

Bed shear stress (τ_0) is also divided into grain and form components, and is related to the friction factor by the Darcy-Weisbach equation:

$$f = \frac{8\tau_0}{v^2 \rho} \quad (4.28)$$

Nikuradse (1933) presented the concept of an equivalent/effective sand roughness height (k_s), which was developed during experiments in pipes roughened with uniform sand. The total effective roughness is the sum of the grain and form roughness components, and can be linked to the friction factor by the Keulegan equation:

$$f = 0.24 \left(\log \left(\frac{12d}{k_s} \right) \right)^{-2} \quad (4.29)$$

Over a bedform skin friction is reduced in the separation/deceleration zone and elevated over the crest, while form drag is related to the distribution of fluid pressure (van Rijn, 1993). Fluid pressure falls as the flow contracts and accelerates over the bedform crest, and then increases as the flow expands and decelerates in the lee. When considering the entire length of the bedform, a net horizontal pressure force is exerted on the bedform.

4.4.4.1 Form roughness

Form roughness cannot typically be directly measured (Millar, 1999). Total flow resistance is minimised when form drag is zero, and only grain roughness plays a role (e.g. Nikora *et al.*, 1998). The minimum value of total flow resistance is exceeded with the development of bedforms. Form roughness can be a significant component of total flow resistance, for example Millar (1999) calculated that up to 90 % of total resistance

can be attributed to form drag at bankfull conditions. Form drag is a function of bedform height (h), steepness (h/l ; where l is bedform length) and bedform shape (β ; the fraction of a rectangle, equivalent in height and length to the bedform, which is occupied by the bedform). In the present experiments, the shape factor (β) was determined by tracing and superimposing 20 bedforms of each type, and calculating β for the smallest and largest resulting feature. The shape factor ranged from 0.41-0.80, and average values of 0.51, 0.50, 0.61 and 0.70 were obtained for ripples, bedload sheets, low-relief bed waves for series 1 and low-relief bed waves for series 2 respectively. Roden (1998) demonstrates that the shape factor varies with flow depth and does not adequately describe whether flow separation will occur. The present experimental data has been employed in the following equations (4.30-34), all of which include bedform related parameters, in order to determine the form friction factor (f'') in conjunction with equations 4.27-29. The average dimensions of the highest order bedform group (transverse to flow) of each experimental run are used, with ripples being the lowest order, bedload sheets intermediate, and low-relief bed waves the highest. The equation of van Rijn (1984, 1993) requires the average dimensions of the two highest bedform groups present in a given experimental run.

Vanoni and Hwang (1967)

Ripples and dunes

$$(f'')^{-0.5} = 3.5 \log\left(\frac{d}{rh}\right) - 2.3 \quad (4.30)$$

Engelund (1977)

Dunes

$$f'' = 10 \frac{h^2}{dl} \left(r^{-2.5h/d}\right) \quad (4.31)$$

van Rijn (1984, 1993)

Ripples and dunes

$$\text{Ripples: } k_s'' = 20\gamma_r h \left(\frac{h}{l}\right) \quad (4.32)$$

$$\text{Dunes: } k_s'' = 1.1\beta h(1 - \exp(-25h/l))$$

Karim (1995)

969 flows, sand and gravel rivers

and flume data.

$$\frac{f}{f'} = 1.20 + 8.92 \left(\frac{h}{d}\right) \quad (4.33)$$

McLean *et al.* (1999a, b)

Dunes and 2-D bedforms

$$\tau_D = 0.5 \rho C_D u_R^2 \frac{h}{l} \quad (4.34)$$

where, d is flow depth, h is bedform height, l is bedform length, r is the ratio of the lee slope area and the total bedform area (~0.11 for the present experiments), γ_r is the ripple presence factor (1 for ripples alone, 0.7 for superimposed ripples), β is the shape factor, τ_D is form drag, C_D is a drag coefficient (= 0.19) and

u_R^2 is the reference velocity at one bedform height above the crest (in the present experiments a reference velocity of 1.5 times the bedform height above the mean bed level was used).

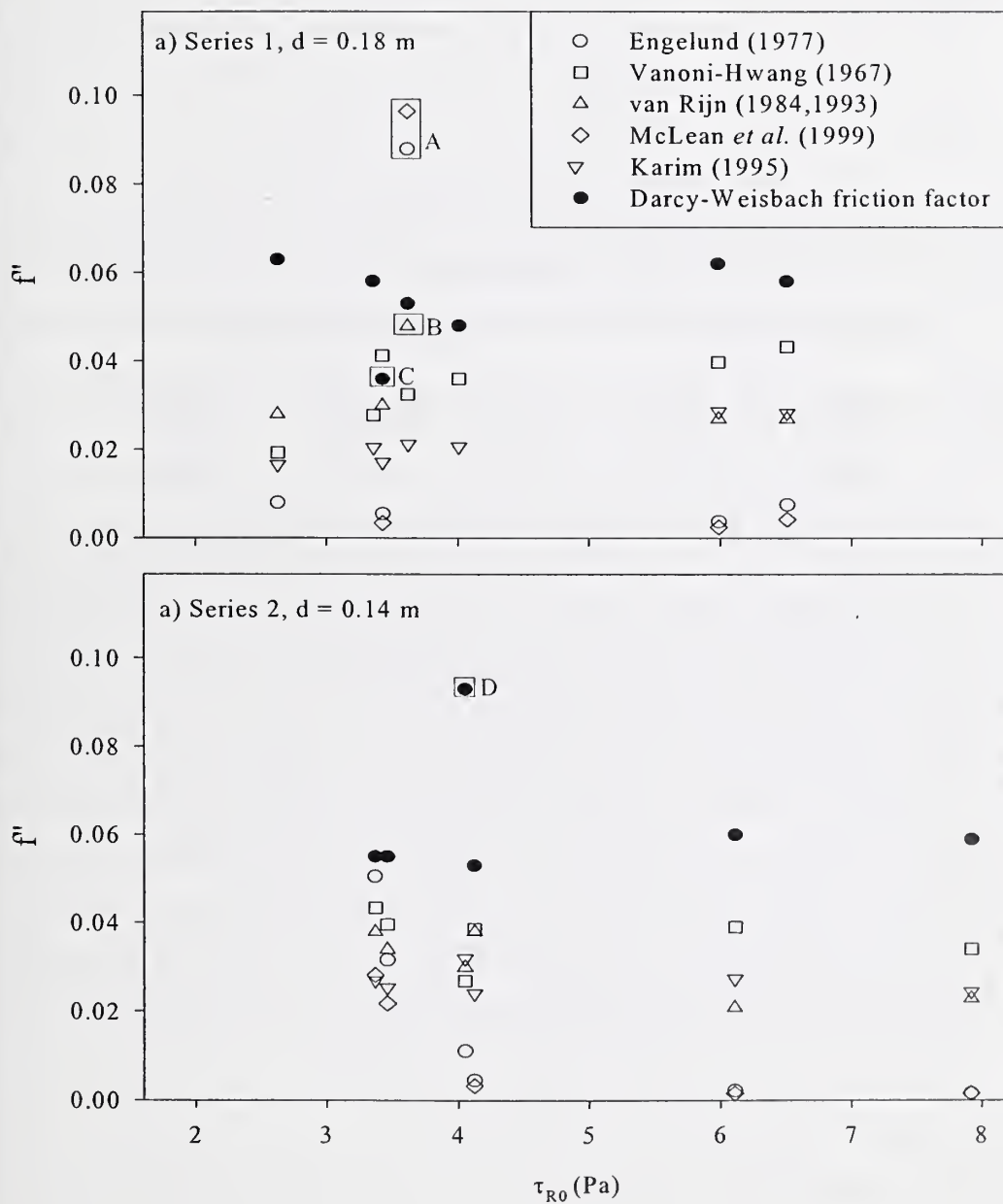
Table 4.7: Predictions of the total friction factor and its form and drag components.

Run	Form related friction factor (f'')						Darcy- Weisbach total friction factor (f)	Grain related friction factor (f')
	Vanoni and Hwang (1967)	Engelund (1977)	van Rijn (1984, 1993)	Karim (1995)	McLean <i>et al.</i> (1999a, b)	Average		
<i>Series 1, d = 0.18 m</i>								
A				0.009		0.009	0.053	0.044
B	0.019	0.008	0.028	0.017		0.018	0.063	0.045
C	0.028			0.020		0.024	0.058	0.034
D	0.032	0.088	0.048	0.021	0.096	0.027	0.053	0.026
E	0.036			0.021		0.028	0.048	0.020
F	0.041	0.005	0.030	0.017	0.003	0.020	0.036	0.016
G	0.040	0.004	0.027	0.029	0.003	0.020	0.062	0.042
H	0.043	0.008	0.027	0.028	0.004	0.022	0.058	0.036
Average						0.021		0.033
<i>Series 2, d = 0.14 m</i>								
I	0.027	0.011	0.030	0.032		0.025	0.093	0.068
J	0.043	0.051	0.038	0.027	0.028	0.037	0.055	0.018
K	0.040	0.032	0.034	0.025	0.022	0.030	0.055	0.025
L	0.039	0.005	0.038	0.024	0.003	0.022	0.053	0.031
M	0.039	0.002	0.021	0.027	0.002	0.018	0.060	0.042
N	0.034	0.002	0.023	0.024	0.002	0.017	0.059	0.042
Average						0.025		0.038
Overall average						0.023		0.035

The estimates of the form friction factor are tabulated (4.7) along with the calculated Darcy-Weisbach total friction factor and the grain related friction factor, which is derived by subtracting the average form related friction factor from the total friction factor. The form related and total friction factors are illustrated in Figure 4.14, with erroneous values highlighted. Boxes A and B in Figure 4.14 identify overestimations of the form related friction factor for Run D, obtained using the equations of Engelund (1977), van Rijn (1984, 1993) and McLean *et al.* (1999a, b), which are excluded from the grain related friction factor calculations. For each experimental run, it was possible to measure bedform height and length from about 200 and 20 examples respectively. Measurement of bedform length was limited since two simultaneous readings of the sediment bed height were required. Therefore, measurements of bedform length contain a greater margin of error compared with bedform height measurements in the present case. The average length of the bedload sheets derived for Run D is relatively short compared with other experimental runs. Furthermore, all the equations which overestimate the form related friction factor for Run D use bedform length, which is absent from the remaining formulas. Moreover, the small height of the bedforms and the importance of grain related roughness will reduce the dominance of any flow separation, resulting in greater variability in

bedform length. Lanzoni (2000) notes that the effect of mixture sorting on bedform wavelength is not clear, whereas bedform height is observed to be damped with increasingly strong bimodal mixtures (i.e. indices of bimodality, Section 1.2). The vast majority of the data used to construct the semi-empirical equations listed above is derived from sand sized sediments. The equations of Engclund (1977) and McLean *et al.* (1999a, b) typically produce the lowest estimates of form related friction factor, whilst Vanoni and Hwang (1967) generate the highest. Boxes C and D in Figure 4.14 highlight anomalous values of the Darcy-Weisbach total friction factor due to low and high values of bed shear stress for runs F (series 1) and I (series 2) respectively, which are derived from projections of Reynolds stresses to the bed.

Figure 4.14: The Darcy-Weisbach friction factor (solid symbols) and estimations of the form related friction factor (white symbols). The anomalous boxed values are discussed in the text.



4.4.4.2 Grain roughness

The equivalent grain roughness height (k_s') is approximately to D_{50} in uniform sediment (Millar, 1999). However, in non-uniform sediment the value of k_s' is typically a multiple of a characteristic grain size D_x , as illustrated in Table 4.8. In the present experiments the average grain related friction factor is 0.033 and 0.038 for series 1 and 2 respectively, ranging from 0.016 to 0.069. The overall average form related friction factor (0.023) is less than the overall average grain related friction factor (0.035). The average value of f' corresponds to a k_s' value equivalent to 2-3 D_{50} (Table 4.9). However, Smart (1999) proposes that flow resistance over mobile boundaries is not dependent on grain size.

Table 4.8: Values of the grain related effective roughness height.

Reference	k_s'
Millar (1999)	D_{50}
Parker and Peterson (1980)	$2 D_{90}$
Hey (1989)	$3.5 D_{84}$
Whiting and Dietrich (1990)	$3 D_{84}$
Prestegaard (1983)	D_{84}
Griffiths (1989)	D_{50}

Table 4.9: Grain related friction factor for various multiples of characteristic grain sizes of the bulk sediment mixture.

Multiple	f' series 1, $d = 0.18$ m			f' series 2, $d = 0.14$ m		
	D_{50}	D_{84}	D_{90}	D_{50}	D_{84}	D_{90}
1	0.025	0.040	0.044	0.027	0.044	0.049
2	0.031	0.052	0.058	0.034	0.058	0.065
3	0.036	0.062	0.070	0.039	0.069	0.079

When the boundary shear stress is equal to the critical shear stress, the bed resistance should be at a minimum (Nikora and Goring, 2000). However, Nowell and Church (1979) believe that the boundary characteristics of gravel-bed rivers cause flow resistance to be maximised, inducing stability. Hassan and Church (2000) determined that 17-4 % of bed shear stress was carried by surface structures on a gravel bed, less than 4 % by the bedload, and the excess was carried by individual grains. Mobile sediment can cause the roughness of the bed to increase by 1-3 orders of magnitude compared with the roughness of a stationary bed (Section 5.4.2; Wiberg and Rubin, 1989). However, Whiting and Dietrich (1990) identified no changes in bed roughness with increasing sediment transport from field measurements (Muddy and Duck Creek, Wyoming, $D_{50} = 0.9$ and 4.6 mm respectively), and therefore concluded that the coarse, largely immobile grains determine the resistance to flow, and little momentum is extracted by sediment saltation. Pitlick (1992) confirms from measurements in the North Fork Toutle River, Washington, that a flat gravel bed (grain size up to approximately 100 mm) remains planar up to stresses approximately three times the critical value before bedforms develop, which distort velocity profiles and increase flow resistance. Plane bed conditions are resumed at the highest sediment transport conditions observed (approximately 7 times the critical bed

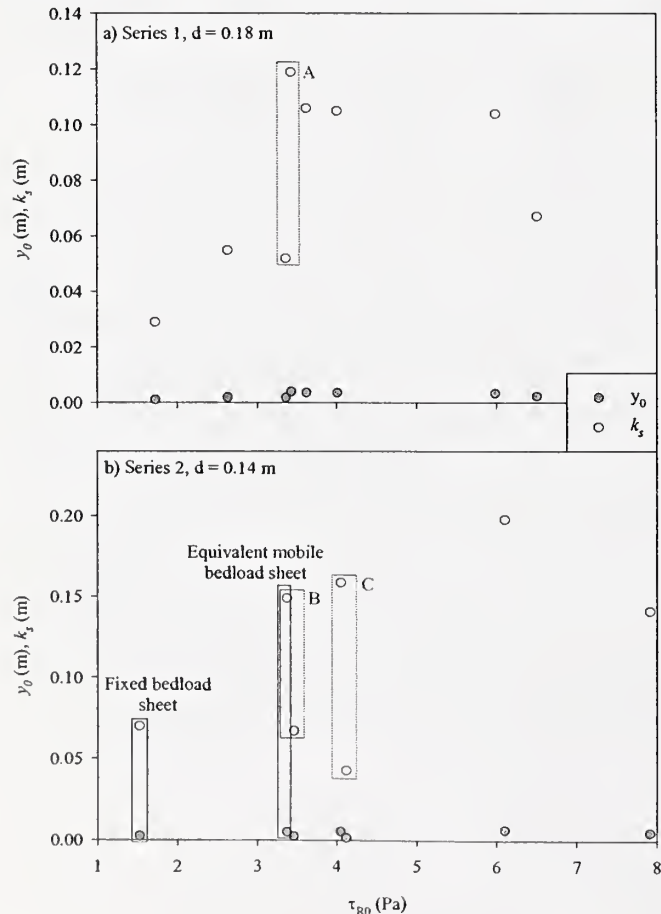
shear stress), although the transition to upper stage plane beds occurs at lower transport rates compared with a sand bed stream. If all the clasts are in motion at some time, the distinction between the material in the bed and the bedload is not critical for calculating roughness (Pitlick, 1992; Whiting and Dietrich, 1990). The model of Wiberg and Smith (1991) indicates that bed roughness is influenced by the degree of sediment sorting, however, this is not confirmed by the analysis of Millar (1999). In his analysis, Millar (1999) considers grain protrusion effects to be a component of form roughness. Conversely, Whiting and Dietrich (1990) and Nikora *et al.* (1998) attribute the effect of prominent clasts to grain roughness. Nikora *et al.* (1998) explain that the effective bed roughness height of a gravel-bed river is characterised by three independent scales e.g. bed elevations are analysed as a three-dimensional random field (i.e. a topographic map of the sediment bed), which varies in the downstream, traverse and vertical directions. No form roughness due to bedforms was observed in the examples studied by Nikora *et al.* (1998). Furthermore, using one characteristic grain size to estimate the effective grain related roughness height provides only a rough alternate to the random field approach, although is much less labour and time intensive. Van Rijn (1993) cautions that roughness predictors do not adequately account for the effects of water temperature, channel pattern and sediment discharge on the resistance to flow provided by the bed. Furthermore, the influence of the grain size distribution on the bed roughness is poorly understood, partly due to the unclear effects of sediment gradation on bedform length (Lanzoni, 2000) and particle protrusion (Millar, 1999), sorting (Wiberg and Smith, 1991) and characteristic size (Sambrook Smith *et al.*, 1997).

4.4.5 Comparison of calculated y_0 , k_s , κ , and Π values with previous results

Estimates of zero-velocity roughness height fall within the range deduced in previous work (Table 4.10) despite the large associated errors. The occurrence of errors in the calculations of y_0 and k_s ($k_s = 30.2y_0$) is highlighted by the contrasting values of spatially-averaged k_s shown in Figure 4.15 (Boxes A-C) for similar boundary shear stresses. Values of y_0 and k_s tend to increase at a flow depth of 0.18 m with rising bed shear stress and the growth of bedforms, although this levels off at boundary shear stresses greater than ~ 3.5 Pa (Figure 4.15a). However, no obvious trend of y_0 and k_s with bed shear stress is apparent at a flow depth of 0.14 m. The value of k_s for the fixed bedload sheet (0.070 m) is more similar to the value obtained in run K (0.067 m, exhibits bedload sheets) than run J (0.149 m), which is the equivalent mobile run (Figure 4.15b). However, the bed shear stress of runs J and K are similar (3.37 and 3.46 Pa respectively), but greater than that of the fixed bedload sheet (1.53 Pa) which offers less resistance to the flow due to the absence of bedload. It is therefore not possible to assess the impact of fixing the bed on the spatially-averaged values of y_0 and k_s , especially in light of the substantial percentage errors associated with their determination.

Table 4.10: Values of von Kármán's constant and zero-velocity roughness height from previous studies.

Reference	κ	y_0 (mm)	Notes
Smith and McLean (1977)	0.38	0.1-3.2	Sand dunes, Columbia River.
Gust and Southard (1983)	0.32 (mobile)		0.16 mm quartz grains, mobile and fixed. No bedforms.
Robert <i>et al.</i> (1992)		Up to 12	Roughness transitions in flume and field. y_0 varied in a similar manner to U_* . Increases with greater bed roughness.
Nelson <i>et al.</i> (1993)		0.01	2-D fixed bedforms (dunes).
McLean <i>et al.</i> (1994)		0.3-5.3	Fixed ripples.
Bennett and Bridge (1995a)	0.32	0.02-0.08 (using $\kappa = 0.4$)	Low-relief bedforms in a mixed size and mixed density sediment (flume).
Nelson <i>et al.</i> (1995)		0.003	Backward facing step in flume, 40 mm high.
Bennett and Best (1995)		0.008	Fixed 2-D dunes, 40 mm high.
Bennett and Best (1996)		0.57	Fixed ripples, 5-25 mm high.
Bennett <i>et al.</i> (1998)	$(y \leq 0.2d)$ 0.286 mobile 0.415 fixed $(y \leq d)$ 0.331 mobile 0.397 fixed	0.006-0.28	Low-relief bed waves on an upper stage plane bed, 2.5 mm mean height.
Smart (1999)		2-346	Gravel-bed rivers in New Zealand with an uneven and mobile sediment bed.
Carling <i>et al.</i> (2000b)		2-60	Sand dunes, River Rhine

Figure 4.15: Spatially-averaged values of y_0 and k_s over a range of bed shear stresses. The red boxes highlight the wide range of y_0 and k_s values for a similar bed shear stress.

The greatest k_s values calculated in the present study are ten times larger than the coarsest grains found in the bulk sediment mixture. Nezu and Nakagawa (1993) highlight that it is difficult to determine k_s over irregular surfaces, since when applying a logarithmic velocity profile to a rough bed, it is problematic to identify the position of zero velocity, which influences the values of y_0 , k_s and U_* (Nezu and Nakagawa, 1993; Smart, 1999).

Values of y_0 and k_s are greatest in the separation region of both the fixed bedload sheet (Figure 4.16) and low-relief bed wave (Figure 4.17), and at a minimum over the crest. Minimum values of y_0 and k_s in the crestal region were confirmed by the results over the mobile bedload sheets and low-relief bed waves (Table 4.4). High values of y_0 were noted by Carling *et al.* (2000b) at the crest and in the lee of sand dunes. They found that the confidence limits for y_0 were especially broad over the crest and stoss due to topographic accelerations and a poorer fit of the law-of-the wall to the velocity profiles. Furthermore, non-logarithmic velocity profiles were associated with the lee of the sand dunes and superimposed features. The latter increases the roughness length along the stoss and crest of the host bedform. Robert *et al.* (1992) observed an increase in roughness height with the transition to greater bed roughness. Indeed, in the present experiments, y_0 and k_s appear to increase immediately downstream of the bedform crest due to flow expansion and a rapid transition to greater surface roughness.

Figure 4.16: The distribution of time-averaged y_0 and k_s over a fixed bedload sheet.

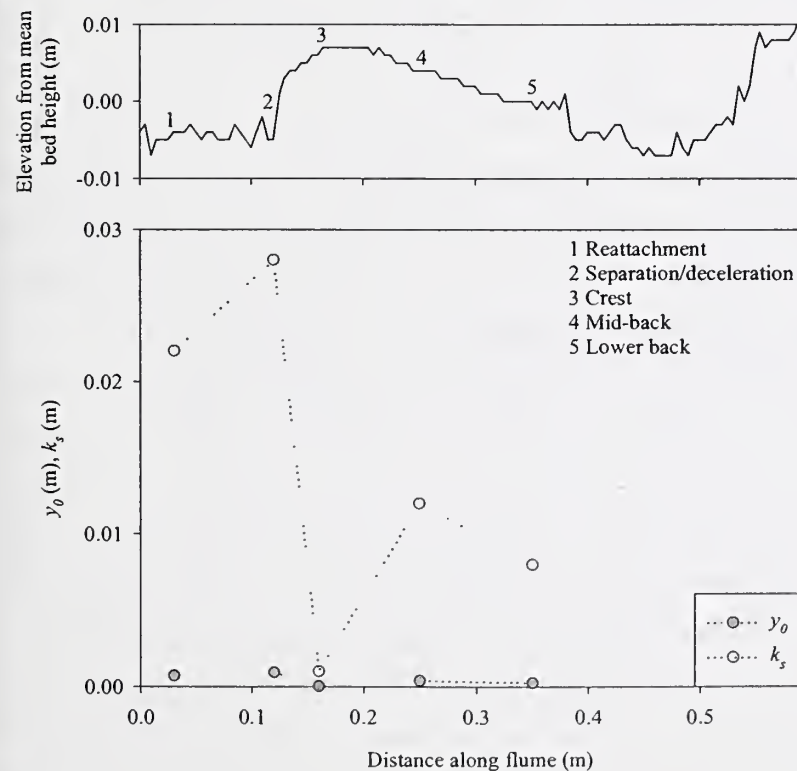
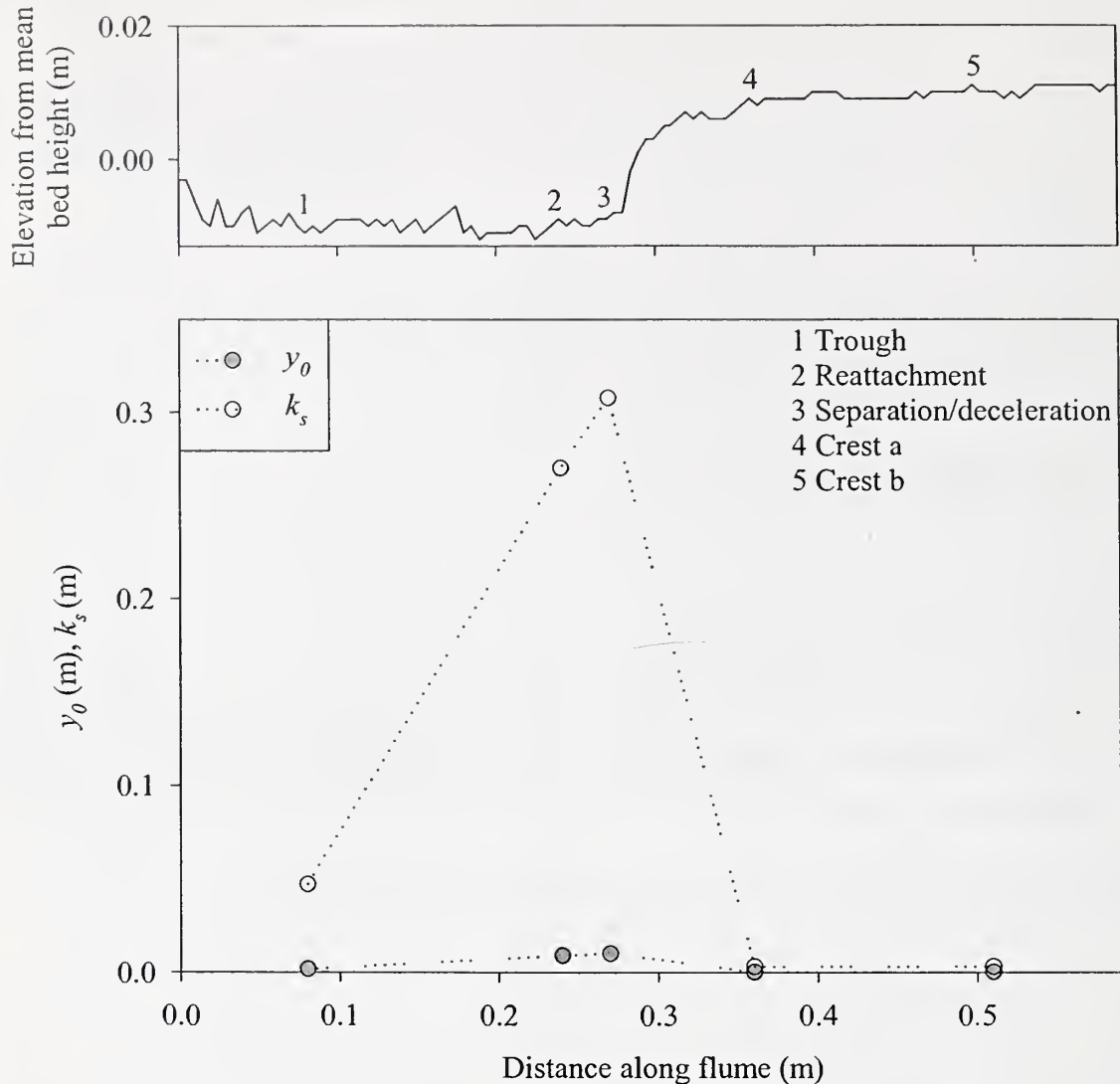


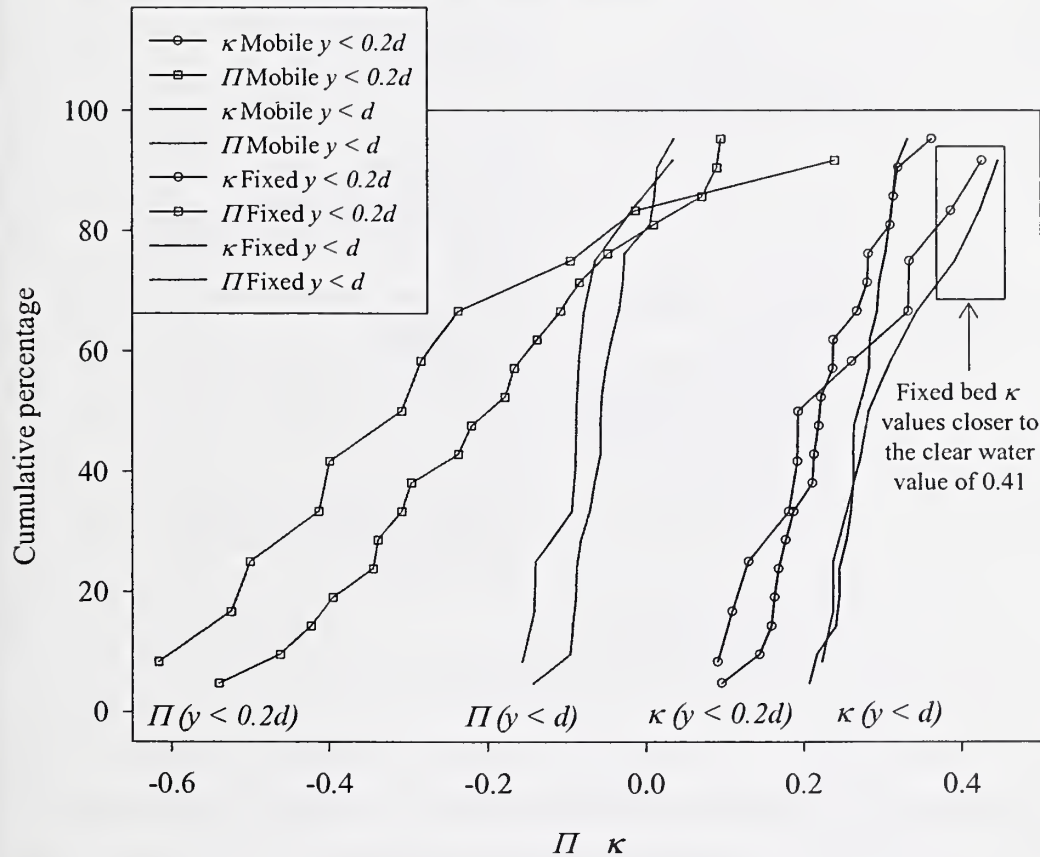
Figure 4.17: The distribution of time-averaged y_0 and k_s over a fixed low-relief bed wave.



Reduced κ values (i.e. $\kappa < 0.41$) derived in the present experiments have also been noted elsewhere (Table 4.10), and Nezu and Nakagawa (1993) state that in order to obtain a proper fit for the law-of-the-wall, κ often requires adjustment. Wiberg and Smith (1991) state that once the flow is significantly modified by large clasts, the profile being integrated is no longer quasi-logarithmic, and consequently the value of κ could vary, approaching 0.41 for low values of relative roughness. The fixed bed values extend closer to the clear water value for κ of 0.41 compared with the mobile bed results (Figure 4.18), and yet have a greater relative roughness (Table 4.2). Bennett *et al.* (1998) also found greater values of κ over a fixed bed (Table 4.10). Higher κ values may be expected in the fixed bed cases due to the lack of sediment in transport, both bedload and suspended sediment, which influences the properties of the fluid in a manner not yet fully understood (Best *et al.*, 1997). Mendoza and Zhou (1992) present κ values of between 0.26 and 0.29 over a porous bed, and note that the origin of the velocity profile is located within the porous material. They conclude that as porosity increases, so the value of κ decreases. The porosity of a sediment depends on the sediment packing arrangement and grain size distribution (Pye, 1994). Due to the bimodal nature of the

present experimental sediment, the mixture would be expected to be relatively porous compared with a uniform mixture, and therefore reduced κ values would be anticipated. However the porosity will vary over the length of a bedform due to grain sorting and alignment. Furthermore, grain sorting will cause transitions in bed roughness, which Antonia and Luxton (1972) believe causes the law of the wall to be invalid, a reduction in the associated constant of integration, and deviations from a value of 0.41 for κ . Values for κ also tend to be lower when predicted using only the bottom 20% of the flow rather than the whole flow depth in the present experiments, since the sediment boundary has greatest influence in this region of the flow. The range of κ values calculated over the fixed beds is greater than over the mobile beds due to the inclusion of a greater proportion of bed specific values in Figure 4.18, which exhibit greater variation than spatially-averaged results that are more common for the mobile bed condition.

Figure 4.18: Cumulative frequency of the wake coefficient and von Kármán's constant derived for mobile and fixed bed experimental runs from spatio-temporally-averaged downstream velocity in both the bottom 20 % of the flow depth ($y \leq 0.2d$) and the whole flow depth ($y \leq d$).



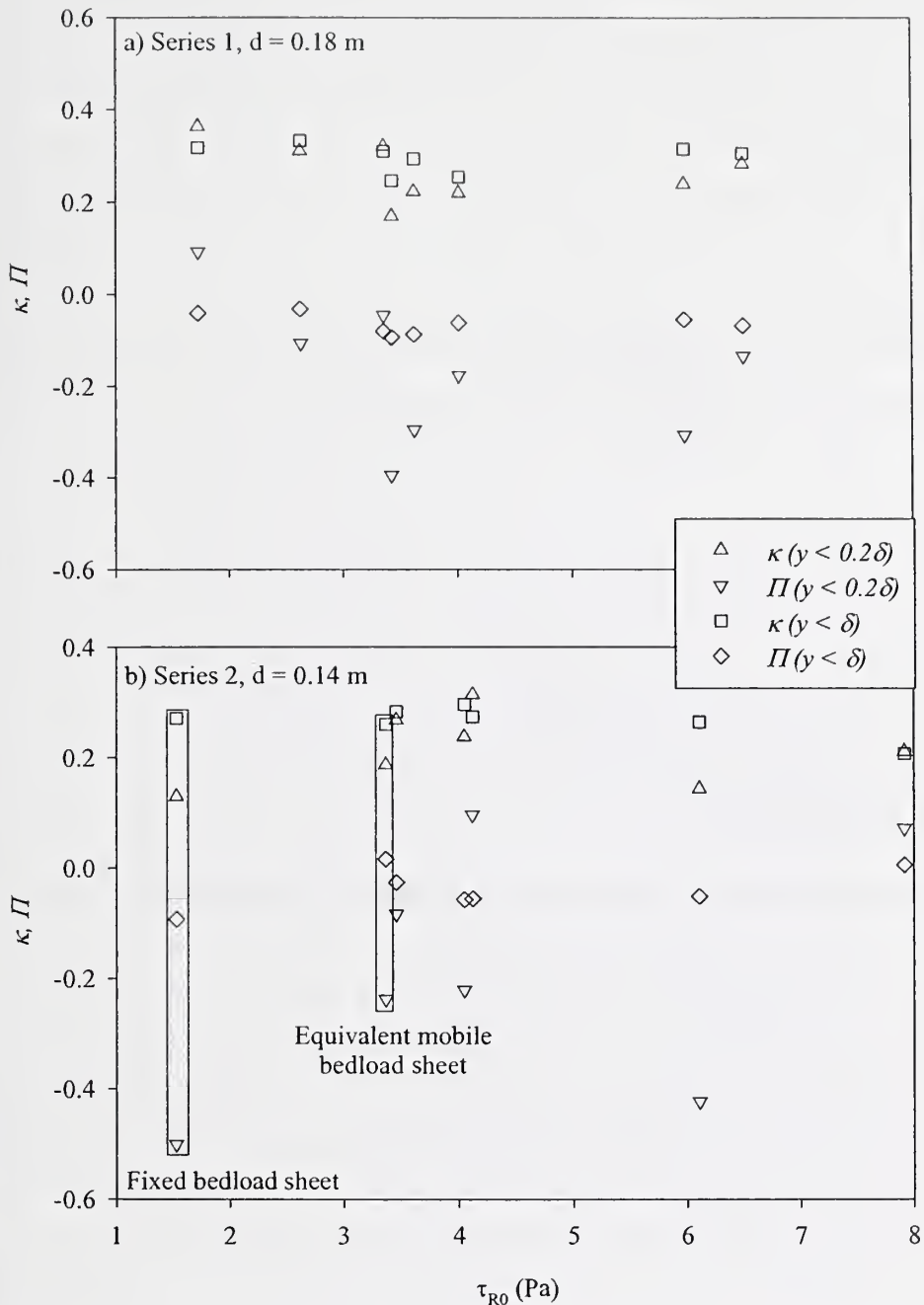
Previous work over a variety of bed conditions (Table 4.11), typically report positive Π values, which are found to increase with greater suspended sediment concentrations over flat beds. However, the present experimental data and that of Bennett *et al.* (1998) predominantly find negative Π values (Figure 4.18). Since Π is an empirical correction function, representing various influences on velocity throughout the flow depth, the negative values reported here may occur for several reasons e.g. sediment transport and a velocity

defect. Furthermore, when Π is derived from velocity measurements taken in the lower 20 % of the flow, where sediment concentrations would be expected to be greatest, the results show greater negative values (down to approximately -0.6) compared with the more consistent values calculated using the whole flow profile (greater than -0.2; Figure 4.18), which is in agreement with the mobile bed results of Bennett *et al.* (1998; Table 4.11). The characteristics of the sediment bed (e.g. bedload, porosity, bedforms), and their impact on the flow, vary between experimental runs, and are accentuated when only the bottom 20% of the flow is considered in the determination of Π . When Π is calculated for the bottom 20% of the flow depth, there is a greater range of values for the fixed bed measurements compared with the mobile bed results due to the greater proportion of bed specific values of Π considered, which tend to vary more than a spatially-averaged value.

Table 4.11: Values for Coles's (1956) wake coefficient from previous studies.

Reference	Π	Notes
Steffler <i>et al.</i> (1985)	0.08-0.15	Smooth flume bed.
Nezu and Rodi (1986)	0-0.253	Smooth flume bed.
	~ 0.2 (Reynolds number $>10^5$)	
Cardoso <i>et al.</i> (1989)	0.08	Smooth flume bed.
Kirkgoz (1989)	0.1	Smooth and fixed rough boundaries. $D_{90} = 2.36, 5, 10$ and 20 mm.
Ferro and Baiamonte (1994)	0.2 (Reynolds number $>10^5$)	Flume with gravel bed, D_{50} up to 25 mm.
Song <i>et al.</i> (1994)	0.08, ranging from 0.01 to 0.15. 0.108 with bedload, slightly greater without bedload.	Movable gravel bed, $D_{50} = 12.3$ mm, $D_{16} = 9$ mm, $D_{84} = 16.5$ mm.
Bennett <i>et al.</i> (1998)	-0.20 mobile, -0.03 fixed ($y \leq 0.2d$)	Mobile and fixed upper stage plane beds, glass beads 0.1-0.3 mm in diameter.
	-0.05 mobile, -0.08 fixed ($y \leq d$)	

When κ and Π are calculated from the bottom 20% of the flow depth, there is greater range of values with varying bed shear stress compared with values determined using the whole flow depth (Figure 4.19). However, no consistent relationship is observed between boundary shear stress and κ or Π . Values of κ or Π calculated from the lower 20% of the flow may exhibit more scatter due to fewer data points used in the least squares linear regression and the greater influence of the sediment boundary characteristics on measurements taken near the bed ($y/d < 0.2$). The fixed bedload sheet is associated with more negative Π values compared with all the results from the mobile bed runs (Figure 4.19b) due to the absence of sediment and the occurrence of a velocity defect.

Figure 4.19: Values of κ and Π determined over a range of bed shear stresses.

The values of κ and Π tend to rise over the crest of the fixed bedload sheet (Figure 4.20) and low-relief bed wave (Figure 4.21), and diminish immediately downstream with the onset of flow deceleration and expansion. The only exception is the trend of Π calculated over the whole flow depth for the fixed low-relief bed wave, which exhibits slightly raised values downstream of the bedform crest. The slope of the

regression used to determine κ and Π $\left(\partial \left(\frac{\bar{u}_{\max} - \bar{u}}{U_*} \right) \right) / \partial \ln \left(\frac{y}{d} \right)$ is reduced over the bedform crest compared

with the region of flow deceleration/separation immediately downstream, and accounts for the greater values of κ and Π over the crest.

Figure 4.20: Variations in κ and Π over a fixed bedload sheet. Flow is from right to left.

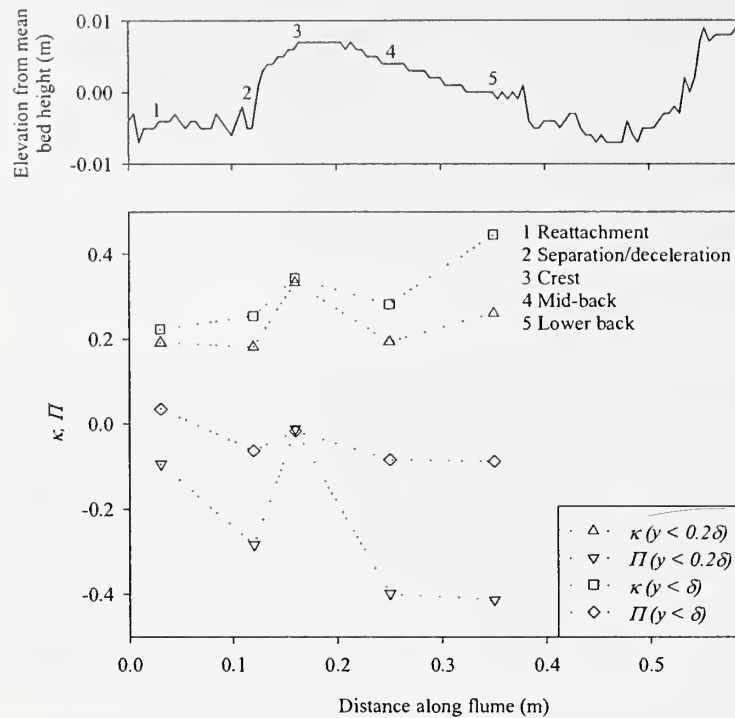
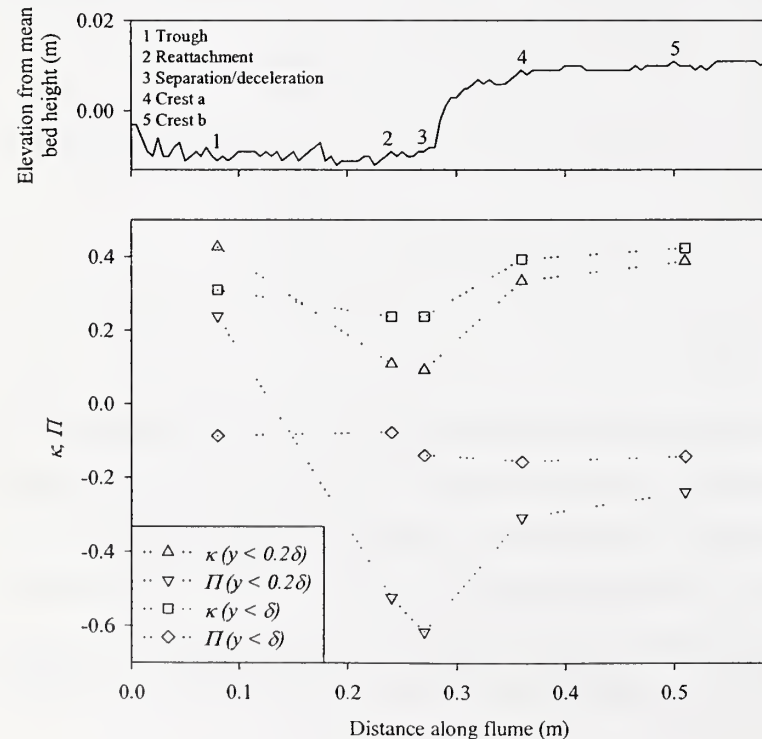


Figure 4.21: Variations in κ and Π over a fixed low-relief bed wave. Flow is from right to left.



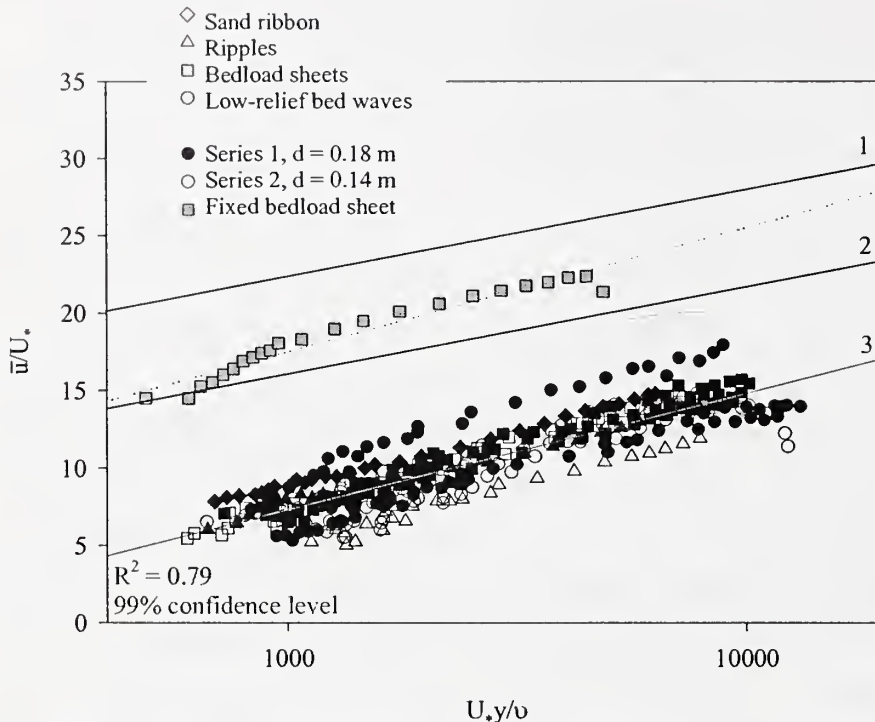
Kironoto and Graf (1994) attribute negative wake coefficients to retardation effects, caused by the velocity maxima falling below the water surface, and variations in pressure gradients (i.e. non-uniform flow). When Cardoso *et al.* (1989; aspect ratio ranged from 4.7-7.4) determined wake coefficients over smooth beds using just the velocity profile below the maximum downstream velocity, negative values were obtained. Kironoto and Graf (1994) deduced that $\Pi = 0.88\beta$ when the aspect ratio is 2 (close to the present experimental values). Since all the current experimental values of β are negative, Π values would therefore also be anticipated to be negative.

4.4.6 Comparison of spatially-averaged velocity data with the law-of-the-wall

In order to compare the present spatially-averaged velocity measurements with the law-of-the-wall, the data is plotted in non-dimensional form with \bar{u} / U_* against $\frac{U_* y}{\nu}$ (Figure 4.22, where U_* is derived from the projection of Reynolds stress to the bed), in accord with previous studies e.g. Kirkgoz (1989) and Nezu and Rodi (1986). The same linear trend is exhibited by all the spatially-averaged flow data collected over a mobile bed in the present experiments, with an intercept value of -15.22 (Figure 4.22, regression line 3). However, the linear least squares regression lines of LDA measurements taken by Kirkgoz (1989) over smooth (1) and rough (2) surfaces exhibit greater intercept values (5.5 and -0.8 respectively), and therefore plot above the present mobile bed data, as illustrated in Figure 4.22. The current experimental data plot below Kirkgoz's (1989) empirical equations due to the fact that additional roughness is introduced by the presence of both mobile sediment and bedforms. Kirkgoz's (1989) LDA data was collected in a laboratory flume with similar dimensions to that employed in the present experiments (i.e. 12 m long and 0.3 m wide), in which the 'rough' surfaces consisted of a single layer of fixed aggregate (i.e. the D_{90} of the rough surfaces were 2.36, 5, 10 and 20 mm), and consequently these are most similar to the fixed bed cases considered in the present experiments where bedload is absent. The spatially-averaged flow over the fixed bedload sheet plots between the two curves proposed by Kirkgoz (1989) for smooth and rough beds (Figure 4.22). The fixed bedload sheet data does not concur with Kirkgoz's (1989) experimentally derived curve for rough beds since he did not consider the influence of bedforms, grain sorting and mixture bimodality on the velocity distribution.

Figure 4.22: The law-of-the-wall fitted to the present data and compared with the empirical equations of Kirkgoz (1989).

- 1) $\frac{\bar{u}}{U_*} = 2.44 \ln\left(\frac{U_* y}{v}\right) + 5.5$ (Kirkgoz, 1989, smooth)
- 2) $\frac{\bar{u}}{U_*} = 2.44 \ln\left(\frac{U_* y}{v}\right) - 0.8$ (Kirkgoz, 1989, rough)
- 3) $\frac{\bar{u}}{U_*} = 3.26 \ln\left(\frac{U_* y}{v}\right) - 15.22$ (Present data, mobile bed)



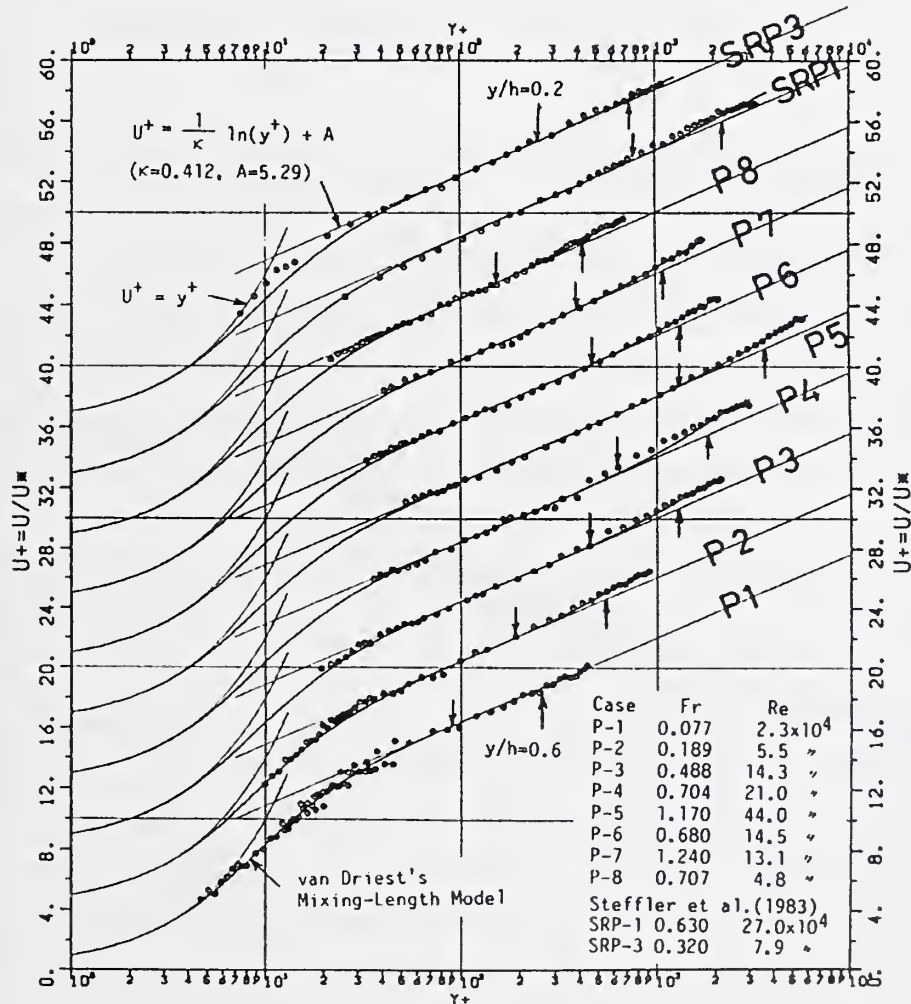
The data collected at the lower flow depth (0.14m) plot slightly below that collected at the higher flow depth (0.18 m), perhaps due to the greater relative roughness. Furthermore, Ligiani and Moffat (1986) note that the intercept value (i.e. the constant of integration of the log law) is different in smooth compared with fully rough turbulent flow. However, it is not just the value of the intercept value that differs between the present experiments and the work of Kirkgoz (1989); the regression for the present mobile experiments also exhibits a greater slope compared with the fixed smooth and rough beds of Kirkgoz (1989). The variation in slope between the present study and Kirkgoz's (1989) does not result from the mobility of the sediment in the current work, since the fixed bedload sheet is also associated with a greater gradient (the dotted line in Figure 4.22). The contrast in the slope of the linear least squares regression for the present data and previous work (Kirkgoz, 1989; Nezu and Rodi, 1986) is due to the range of $\frac{U_* y}{v}$ over which the regression is calculated.

The values of $\frac{U_* y}{v}$ are comparatively large in the present experiments compared with Kirkgoz (1989) and

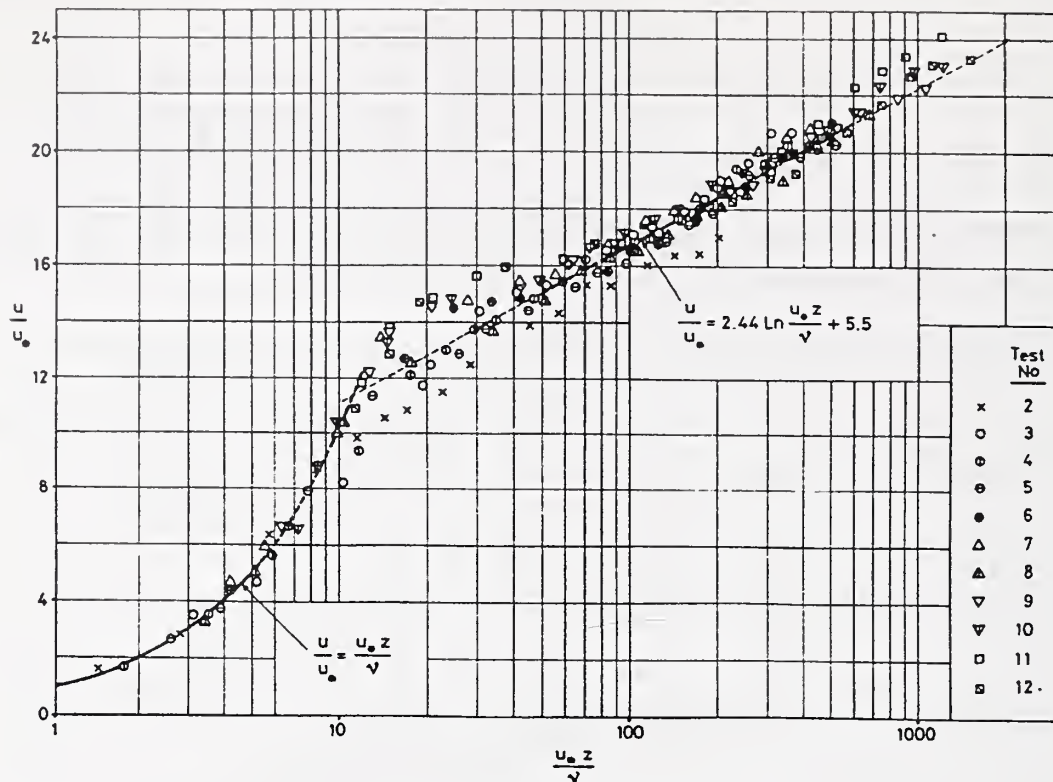
Nezu and Rodi (1986) due to the relatively high shear velocities experienced (up to 0.0890 m s^{-1} in the present experiments, 0.0466 m s^{-1} in the study of Nezu and Rodi (1986) and 0.0382 m s^{-1} for Kirkgoz (1989)), despite intensive velocity measurements near the bed. Greater values of shear velocity are also associated with sediment sorting and the development of bedforms, which can distort velocity profiles from a logarithmic shape. The present experimental data does not include values of $\frac{U_* y}{\nu}$ below approximately 500 (Figure 4.22), whereas the linear region conforming to the law-of-the-wall in the work of Nezu and Rodi (1986) and Kirkgoz (1989) falls below this value (Figures 4.23a-c). Divergence from the law-of-the-wall, resulting in a steeper slope, occurs at around $\frac{U_* y}{\nu} \geq 500$ i.e. the range of the present experiments. Since κ is inversely related to the slope, the values of κ derived from the law-of-the-wall in the present experiments are reduced compared with the standard value of 0.41 (Nezu and Nakagawa, 1993).

Figure 4.23: The application of the law-of-the-wall to velocity profiles.

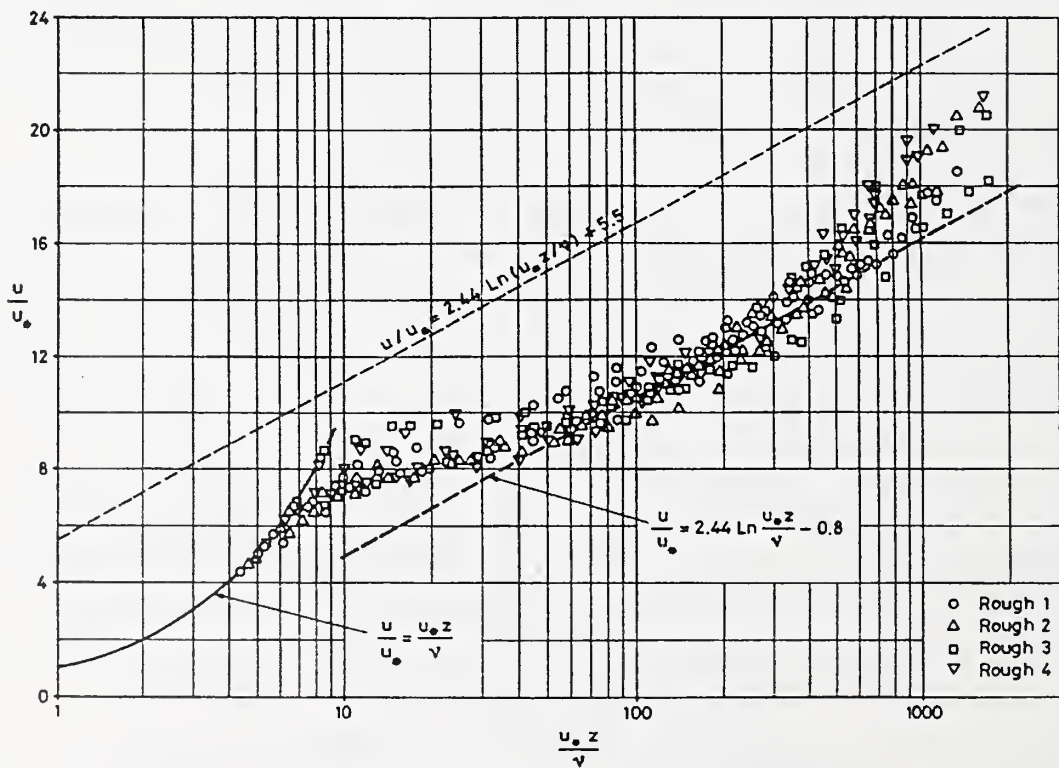
a) Experimental data of Nezu and Rodi (1986) and Steffler et al. (1985), $y^+ = U_* y / \nu$.



b) Experimental data of Kirkgoz (1989) over a smooth bed. z is height above the bed.



c) Experimental data of Kirkgoz (1989) over a fixed rough bed. z is height above the bed.



Kirkgöz's (1989) experimental curve for flow over a smooth bed $\left(\frac{\bar{u}}{U_*} = 2.44 \ln\left(\frac{U_* y}{\nu}\right) + 5.5\right)$ is in close agreement to that derived empirically by Nezu and Rodi (1986) for flow over a smooth boundary i.e. $\frac{\bar{u}}{U_*} = 2.43 \ln\left(\frac{U_* y}{\nu}\right) + 5.29$. Furthermore, visual inspection of the linear least squares regressions in Figure 4.23a and b supports the value of the gradient reported by Kirkgöz (1989) and Nezu and Rodi (1986), which corresponds to the clear water value for κ of 0.41. However, Kirkgöz (1989) assumes that the slope of the linear least squares regression is equivalent for his smooth and rough fixed bed cases, in order for κ to assume a constant value of 0.41. The distribution of measurement points over the rough beds of Kirkgöz (1989) do not appear to follow a linear trend, but instead plot as a curve (Figure 4.23c), shedding doubt on the value for κ employed and the validity of the law-of-the-wall over rough surfaces. Since experimental data diverges from the law-of-the-wall for the values of $\frac{U_* y}{\nu}$ obtained in the present experiments, resulting in erroneous results, the current experimental data will now be compared with the velocity defect-wake law.

4.4.7 Comparison of spatially-averaged velocity data with the velocity defect-wake law

Spatially-averaged profiles of downstream velocity are plotted in Figure 4.24 and 4.25 $((\bar{u}_{\max} - \bar{u})/U_*$ against $\ln(y/d)$), and follow a linear trend over a smooth boundary but demonstrate considerable scatter over rough beds, preventing the derivation of an empirical description of the velocity distribution above a rough surface (Kirkgöz, 1989). In the experiments of Kirkgöz (1989), the data scatter over the rough beds may be due to the generation of wakes from the coarse roughness elements. Nowell and Church (1979) found that the velocity defect law was not valid in the presence of wake interference flow, and concluded that in gravel-bed rivers the velocity distribution did not correspond to the law-of-the-wall.

Spatially-averaged profiles of downstream velocity for the present experiments (Figure 4.25) show little scatter in the top 60 % of the flow depth i.e. $\ln\left(\frac{y}{d}\right) > -1$. Furthermore, the data conforms with Kirkgöz's (1989) empirical curve (Figure 4.25, curve 1) for smooth beds in this region of the flow column, although the linear least squares regression through the present data set (curve 2) is slightly steeper than curve 1. Due to the inverse relationship of κ with slope, the greater gradient agrees with the reduced κ values calculated for the present experimental data (Table 4.4). The value of the intercept of curve 2 (-0.25) indicates the predominately small and negative nature of the estimates of κ in the present experiments (Table 4.4). There is increased data scatter as the bed is approached in accord with experiments of Kirkgöz (1989; Figure 4.24), due to the influence of the boundary conditions, which vary between the present experimental runs e.g. grain

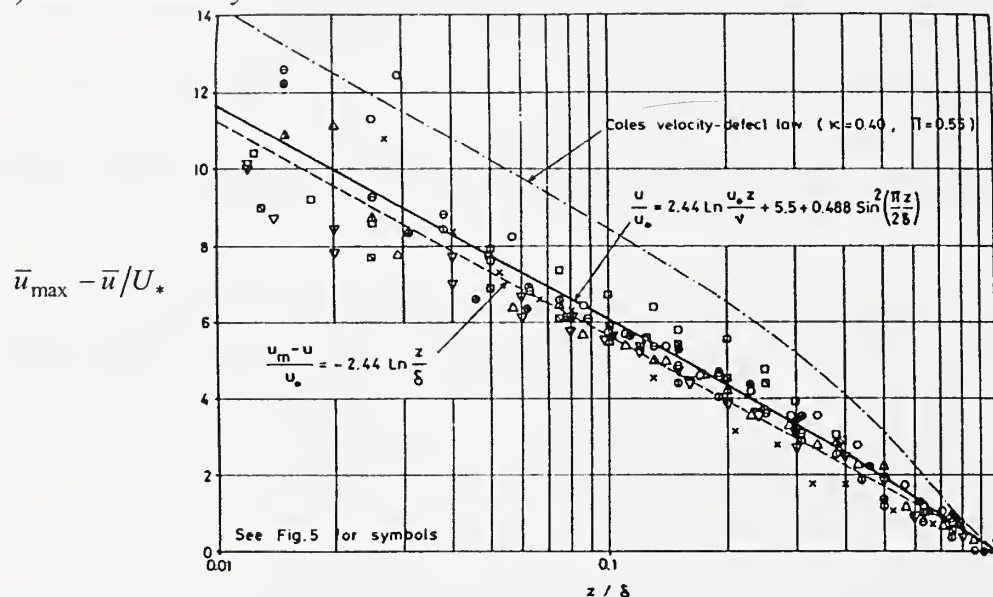
size sorting and bedform development. The velocity data collected over the fixed bedload sheet collapses within the limits of the measurements made over mobile beds, indicating that sediment transport does not

affect the application of the velocity defect-wake law in the outer flow i.e. $\ln\left(\frac{y}{d}\right) > -1$, where experimental

scatter is minimised. The data collected at the lower flow depth in the current experiments plots towards the higher end and above the measurements obtained at the higher flow depth, perhaps as a result of the difference in relative roughness. In the present experiments, the velocity defect-wake law can only describe the complete data set when $y/d > 0.6$, due to the divergence of individual experimental runs when $y/d < 0.4$, as a result of the diversity in boundary conditions.

Figure 4.24: The application of the velocity defect-wake law to velocity profiles over fixed boundaries (Kirkgoz, 1989). z is height above the bed.

a) Smooth boundary



b) Rough boundary

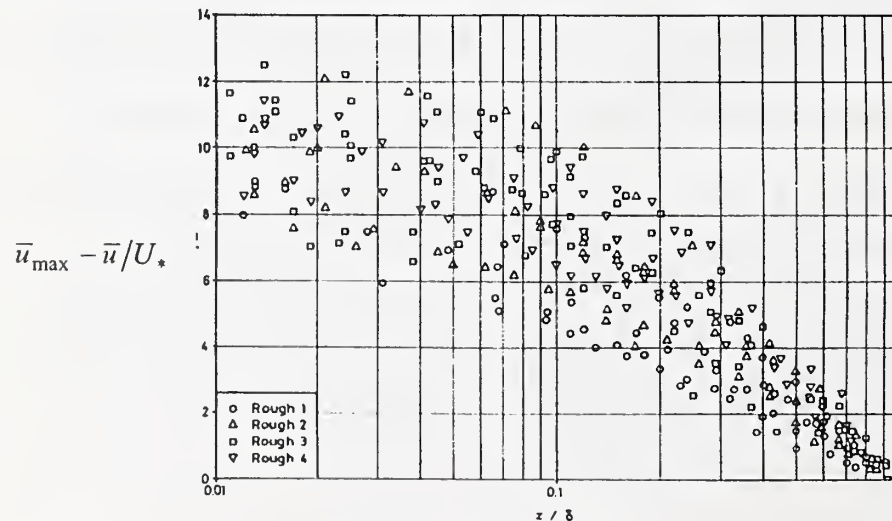
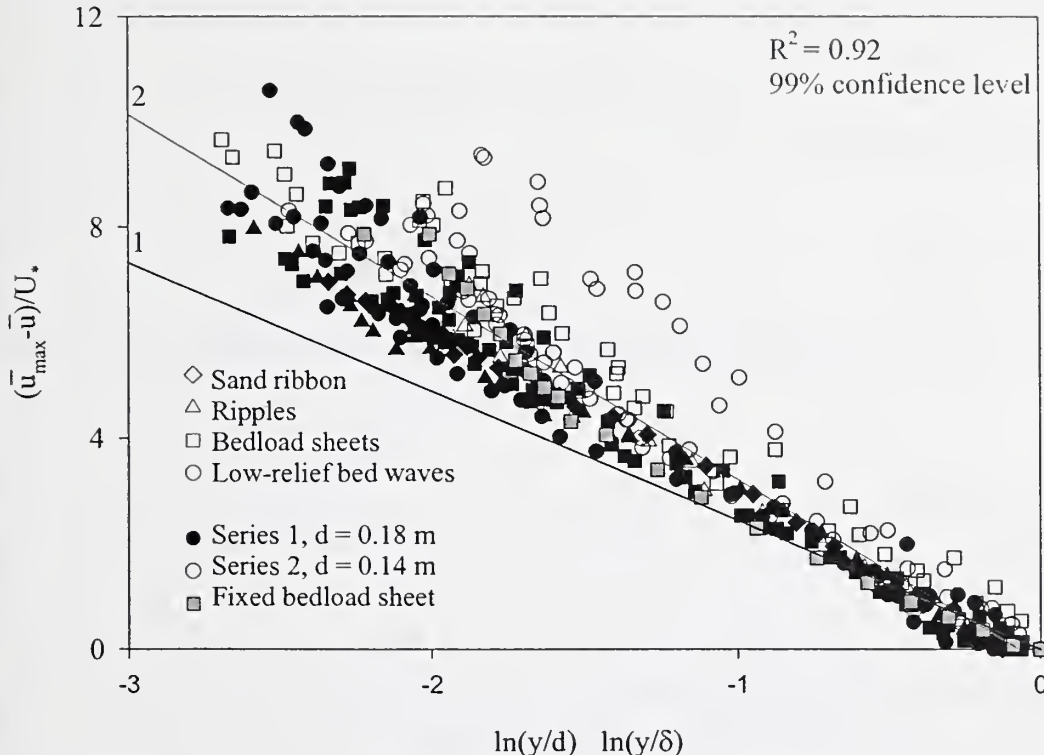


Figure 4.25: The velocity defect-wake law for the present data compared with the empirical equation of Kirkgoz for flow over smooth beds.

$$1) \frac{\bar{u}_{\max} - \bar{u}}{U_*} = -2.44 \ln\left(\frac{y}{\delta}\right) \text{ (Kirkgoz, 1989, smooth)}$$

$$2) \frac{\bar{u}_{\max} - \bar{u}}{U_*} = -3.46 \ln\left(\frac{y}{\delta}\right) - 0.25 \text{ (Present data)}$$



4.4.8 Comparison of time-averaged velocity with theoretical models

Wiberg and Smith (1991) derived a model for the spatially-averaged velocity field over a poorly sorted bed, which accounts for the shear stress attributable to coarse bed particles. Velocity profiles predicted by the model are valid for bed sediment distributions where $D_{84} > 2D_{50}$, although mean velocity values can also be calculated for uniform sediment. The present experimental data was used in the model of Wiberg and Smith (1991; Equations 4.35 and 4.36), accounting for the bimodal nature of the sediment mixture. A first approximation of the spatially-averaged velocity profile is expressed by:

$$\tau_D(y) \approx \frac{3}{4} \rho \int_{y_0}^{y_i} u^2 dy (C_D) \sum_{m=i}^M \frac{c_m}{D_m} \quad (4.35)$$

$$\frac{\partial u}{\partial y} = \frac{U_*}{L} \left\{ \left(1 - \frac{y}{d} \right) - \frac{\tau_D}{\tau_0} \right\}^{0.5} \quad (4.36)$$

where:

τ_D = Shear stress due to large particles

ρ = Fluid density

y = Height above the bed

u = Spatially-average downstream velocity

C_D = Drag coefficient

D_m = Grain size (M is the maximum value)

c_m = Concentration of each grain size fraction by volume

$\frac{\partial u}{\partial y}$ = Gradient of the velocity profile

τ_0 = Bed shear stress ($= \rho g d S$)

U_* = Shear velocity ($= \sqrt{g d S}$)

L = Length scale for turbulent mixing (combination of eddy viscosity and wake effects, and influenced by vertical position)

d = Flow depth

g = Acceleration due to gravity

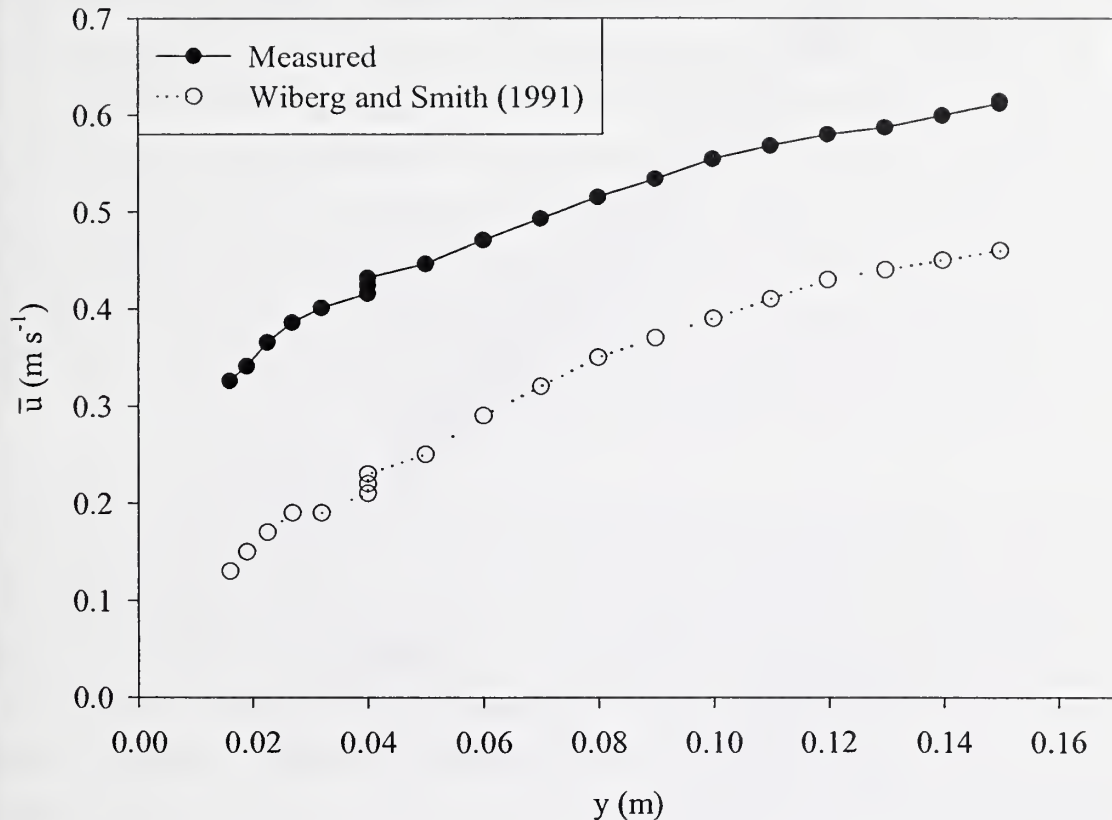
S = Water surface slope.

The spatially-averaged velocity profiles derived from the model of Wiberg and Smith (1991) for run A is compared in Figure 4.26 with the measured spatially averaged velocity profile. The two velocity profiles have a similar shape, but the predicted values from the model of Wiberg and Smith are much less than the measured values e.g. the maximum velocity estimated by the model is 75 % of the measured value. Furthermore, the depth-averaged velocities calculated from velocity measurements and the model of Wiberg and Smith (1991) differ by a significant percentage ($> 35 \%$), as detailed in Table 4.12. The under-prediction of velocity may result from the limited number of velocity measurements possible between the bed and the top of the largest clast. In the present study, the presence of bedload and coarse clasts hindered near-bed measurements ($y/d < 0.2$). The model of Wiberg and Smith is specifically derived for flow in high gradient streams with a coarse bed, where the largest clasts can be comparable to flow depth, enabling many measurements to be taken below the top of the coarse sediment clasts. Since both velocity measurements and sediment concentration information are required by the model for each location above the bed, only 4 points were considered below $y/d < 0.2$.

Table 4.12: The percentage difference between the depth-averaged velocity calculated from velocity measurements and the model of Wiberg and Smith (1991).

Run	Depth-averaged velocity (Percentage difference)
A (Sand ribbon, lowest discharge, $d = 0.18$ m)	35 %
H (Low-relief bed wave, highest discharge, $d = 0.18$ m)	47 %
I (Ripples, lowest discharge, $d = 0.14$ m)	48 %
N (Low-relief bed wave, highest discharge, $d = 0.14$ m)	53 %

Figure 4.26: Comparison of the measured and predicted spatially-averaged velocity profile for Run A.



The overall trend of the measured and predicted spatially-averaged velocity profiles can be compared by plotting them non-dimensionally (Figure 4.27). The spatially-averaged velocity profiles predicted by the model of Wiberg and Smith (1991) display a lesser gradient than the experimental data, although the model predictions fall within the range of experimental measurements at a flow depth of 0.14 m when $y/d < 0.4$. The reduced slope of the model predictions indicate that the drag effect of the coarse particles on the flow is overestimated by the model, causing underestimation of the near-bed velocities ($y/d < 0.4$). Consequently, in the outer flow ($y/d > 0.4$) velocity estimates are too high since the model compensates for the erroneous low velocity estimates in the near-bed flow region ($y/d < 0.4$). The experimental values demonstrate greater variability in normalised velocity at a given height above the bed compared with the model predictions due to the range of boundary conditions experienced, whereas the model assumes that each grain size is randomly distributed on the bed (the concentration of the grains in the bulk mixture is used in the model), and does not account for sediment sorting and bedform development. At the lower flow depth the experimental data

exhibits a greater range of normalised velocity values for a given height above the bed than the higher flow depth, perhaps due to the greater relative roughness.

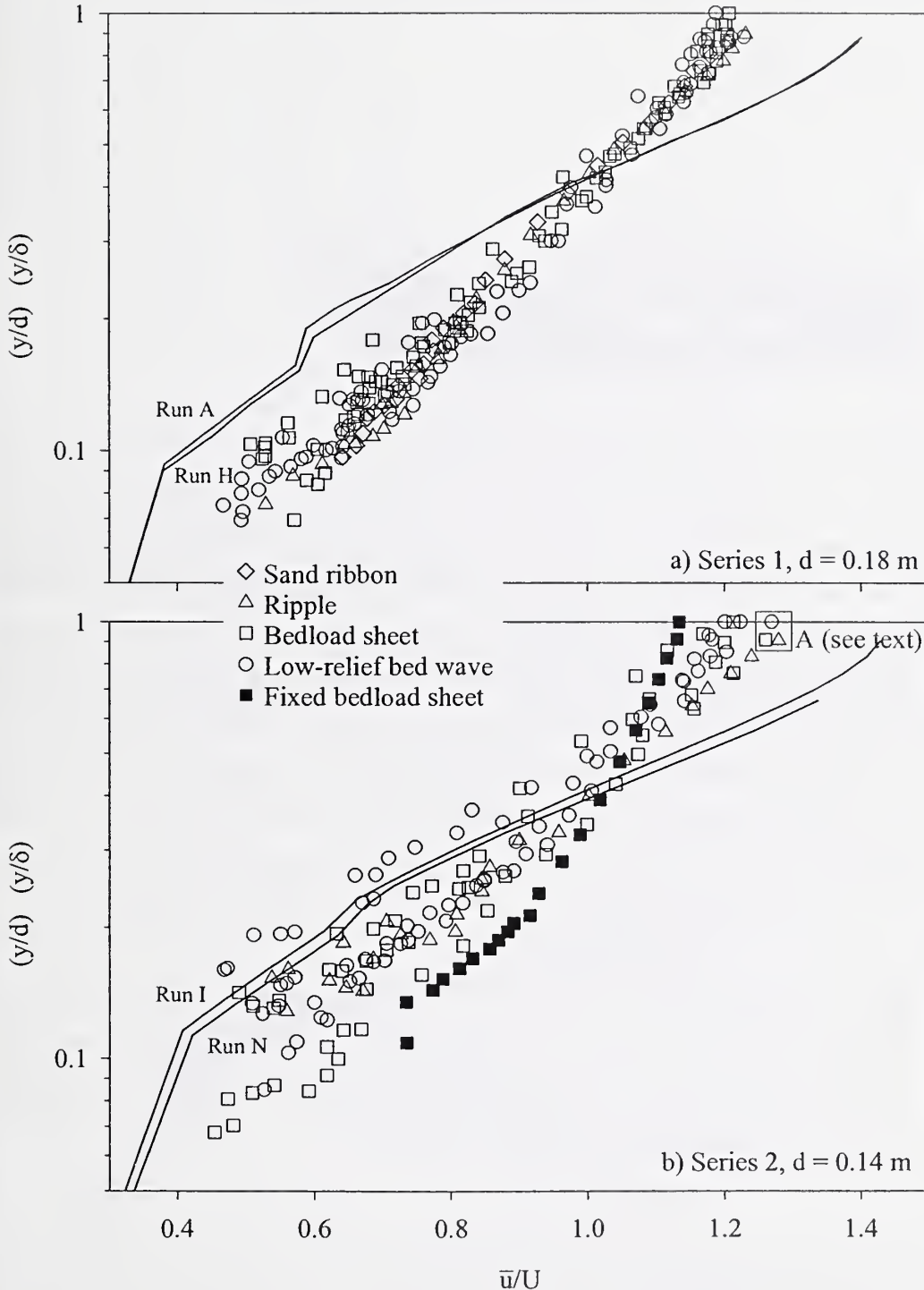
Model simulations performed by Wiberg and Smith (1991) demonstrate that in the lower 30% of the flow \bar{u}/U is higher for deeper flows, and this situation is reversed for the upper 60 % of the flow depth. Wiberg and Smith (1991) explain that roughness elements of a given size, and their associated low momentum flow, extend relatively further into shallower flows (i.e. greater relative roughness), causing the peak downstream velocity to be closer to the water surface compared with deeper flows. The present experiments conducted at the lower flow depth (Series 2) exhibit a wider range, and the lowest values of, normalised velocities at all points above the bed. However, when $y/d > 0.8$, the largest values of normalised velocity are also attained under the lower flow depth (box A in Figure 4.27), as would be anticipated by Wiberg and Smith (1991). The effect of flow depth on the velocity profile is not apparent in the field measurements of Marchand *et al.* (1984; gravel streams in Colorado), which were used by Wiberg and Smith (1991) to verify their model. The influence of relative roughness may be difficult to discern in the present experiments and those of Marchand *et al.* (1984) due to the relatively small variations in flow depth considered.

The spatially-averaged normalised velocity profile over the fixed bedload sheet (Figure 4.27b) displays a greater gradient compared with the mobile bed cases. Bedload, which is absent from the fixed bedload sheet, increases the boundary roughness (Wiberg and Rubin, 1989) causing retardation of the near bed flow ($y/d < 0.5$) in the mobile cases compared with the fixed bedload sheet. Consequently, the velocity is raised near the water surface ($y/d > 0.5$) over the mobile beds, relative to the fixed bed example, in order to compensate for the greater near-bed flow resistance. Furthermore, the roughness of the fixed bedload sheet maybe reduced compared with the equivalent mobile bed run due to the coarser particles sinking in the finer sediment, potential smoothing effects of the resin and the elimination of bed porosity (Mendoza and Zhou, 1992).

The model of Wiberg and Smith (1991) raises some important issues, for example the influence of low near-bed velocities associated with large clasts on the entrainment and transport of sediment. Furthermore, relative roughness and the degree of sediment sorting impacts on the distribution of velocity, which needs to be detailed in order to derive mean velocities and construct stage-discharge curves for rivers. Where intensive measurements are not feasible e.g. remote mountain streams with coarse, poorly sorted sediment beds, it is very useful to be able to employ a model to predict the spatially-averaged velocity distribution. However, the model of Wiberg and Smith (1991) has been shown to be quantitatively inappropriate for the present experimental data as it fails to account for the sorting of sediment over the bed surface and the development of traverse to flow bedforms, and overpredicts the retardance of the sediment on the flow. The model of Wiberg and Smith (1991) maybe more applicable and beneficial in the case of natural gravel-bed rivers (Marchand *et al.*, 1984; Byrd *et al.*, 2000), since bedforms transverse to flow are typically poorly

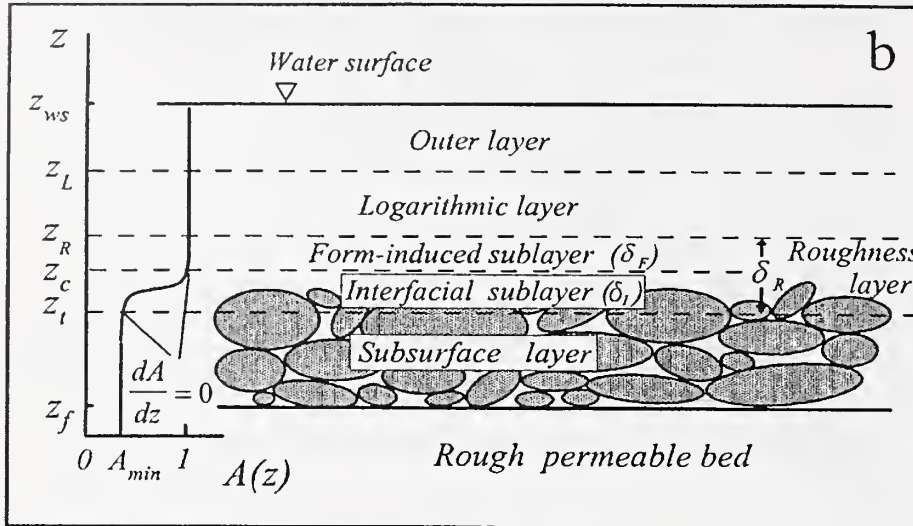
developed, larger diameter clasts are present and sediment sorting does not occur in such a regular manner e.g. pebble clusters (Reid and Hassan, 1992) and patches (Laronne *et al.*, 2000).

Figure 4.27: Comparison of the present data with the model of Wiberg and Smith (1991). Time-averaged velocity, normalised by depth averaged velocity, is plotted against normalised depth. The spatially-averaged velocity profiles of the experimental runs with the highest and lowest discharge at each flow depth are predicted by the model.



Nikora *et al.* (2001) present a model to describe the vertical distribution of downstream velocity in a spatially averaged, 2-D, steady, uniform, flow with a flat free surface over a fixed rough bed. However, Nikora *et al.* (2001) note that the model can also be applied to mobile bed cases. The flow regions considered by Nikora *et al.* (2001) are illustrated in Figure 4.28.

Figure 4.28: Subdivision of the flow into specific layers from Nikora *et al.* (2001). Z is height above the bed.



In order to employ the model of Nikora *et al.* (2001) the roughness height, Δ , has to be evaluated. An average value of 10 mm was selected since the height of the bedforms is approximately 10 mm, and the D_{90} of the bulk sediment mixture is 10 mm. The roughness layer describes the region between the sediment bed and approximately 2-5 times the roughness height. Assuming the roughness layer thickness, δ , is equivalent to 3 times the roughness height, a value of 30 mm is obtained for δ . However, Nikora *et al.* (2001) note that δ varies with the grain size distribution, shape and arrangement, and therefore may vary between experimental runs. The velocity distribution in the roughness layer is described by Equation 4.37 (Figure 4.29).

$$\frac{\bar{u}}{U_*} = C \frac{y}{\delta} \quad (4.37)$$

where, δ is the height of the roughness layer, assumed to be 30 mm for the present experiments, \bar{u} is the spatio-temporally-averaged downstream velocity, U_* is the shear velocity and y is the height above the bed. C is a parameter of the velocity distribution dependent on the roughness geometry (i.e. particle size distribution, particle shape and spatial arrangement) and is expressed as:

$$C = \frac{\bar{u}\delta}{U_*} \quad (4.38)$$

Values for C range from 8.5 for homogeneous sand roughness to 5.3-5.6 for natural and artificial gravel beds (Nikora *et al.*, 2001). Although measurements were limited below the roughness crests in the present

experiments, a linear least squares regression of measurements from the roughness layer ($y < 30$ mm) gives an average value of $C = 5.3$ for the mobile bed experiments, ranging from 4.0 to 9.5 (Table 4.13; red line in Figure 4.30).

Table 4.13: Values of C derived in the present experiments from the linear flow layer. Modified from Nikora et al. (2001).

Present experimental run or Reference	C
A	4.0
B	4.9
C	4.2
D	5.0
E	6.7
F	9.5
G	6.9
H	5.1
I	5.3
J	6.6
K	6.2
L	6.1
M	8.6
N	5.6
Present experimental average	5.3
Nikitin (1980); glued down gravel particles which had a similar size distribution to natural streams.	5.6
Dittrich and Koll (1997); flume experiments, gravel with narrow size distribution.	5.3
Shimizu et al. (1990); glass beads.	5.7-6.0
Nikora et al. (2001); fixed spherical segments (Figure 4.29).	7.1
Nikora et al. (2001); homogeneous sand roughness	8.5

Nikora et al. (2001) state that the outer flow region is described by the velocity defect-wake law (Equation 4.21), while the region $(2 - 5)\Delta < y < 0.2d$ is characterised by a logarithmic trend (Figure 4.29):

$$\frac{\bar{u}}{U_*} = \frac{1}{\kappa} \ln\left(\frac{y}{\delta}\right) + C \quad (4.39)$$

Figure 4.29: Comparison of the measured and predicted downstream velocity distribution from Nikora et al. (2001). C is 7.1, κ is 0.4 and δ is 21 mm. Z equals the height above the bed.

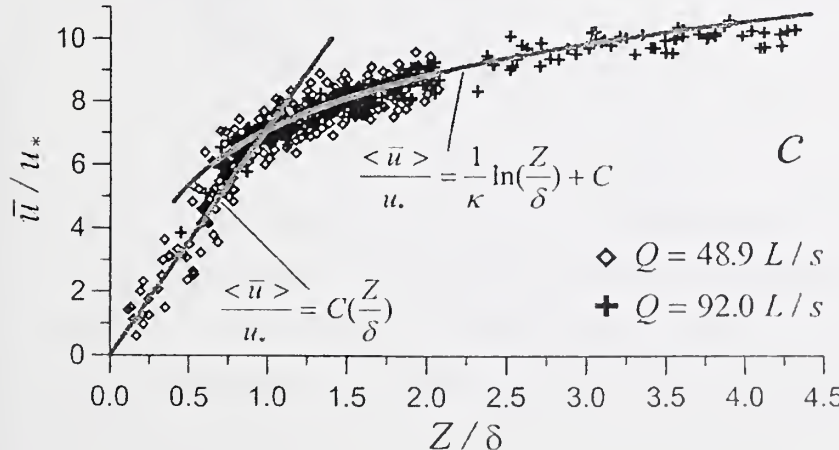
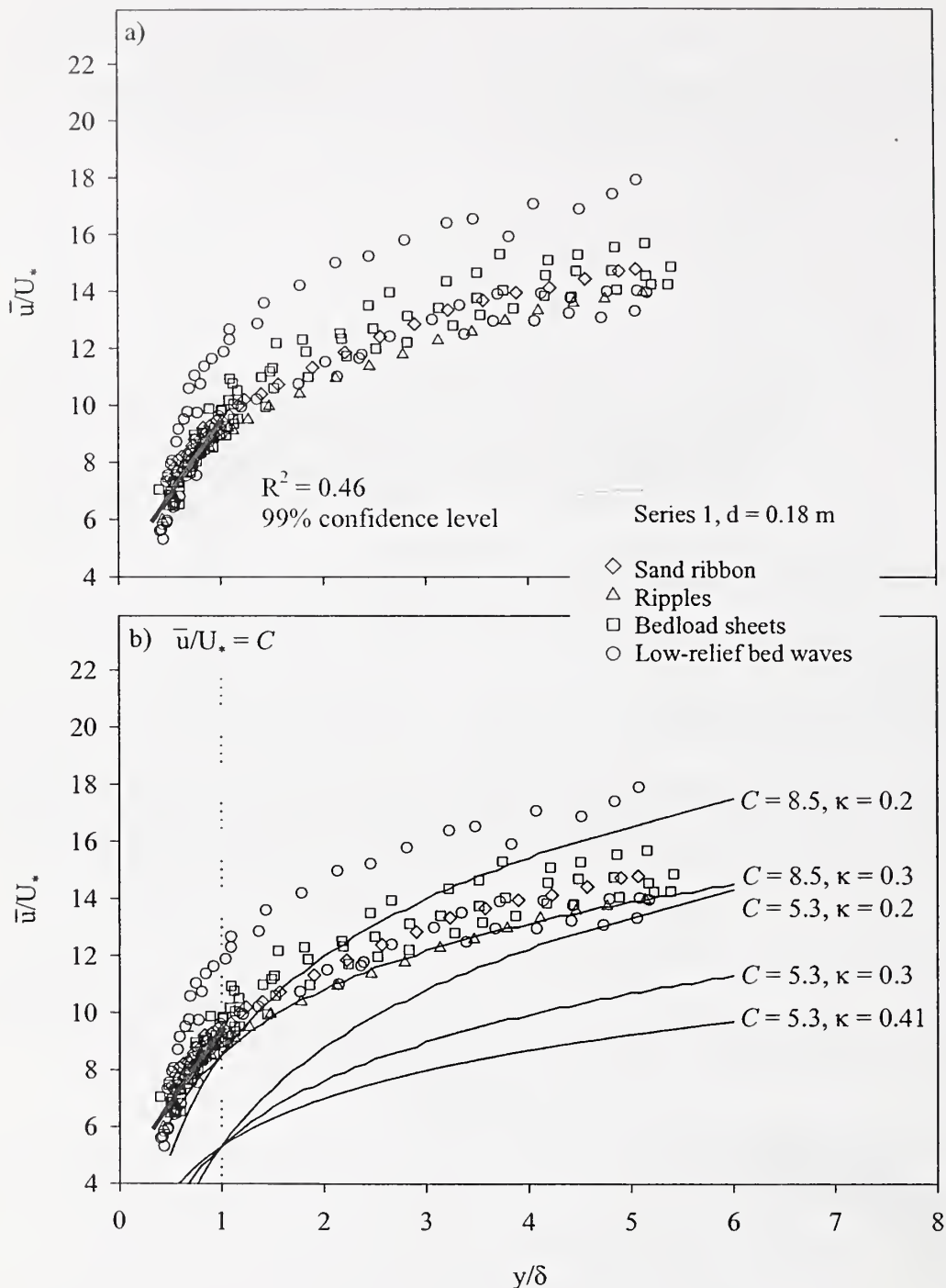
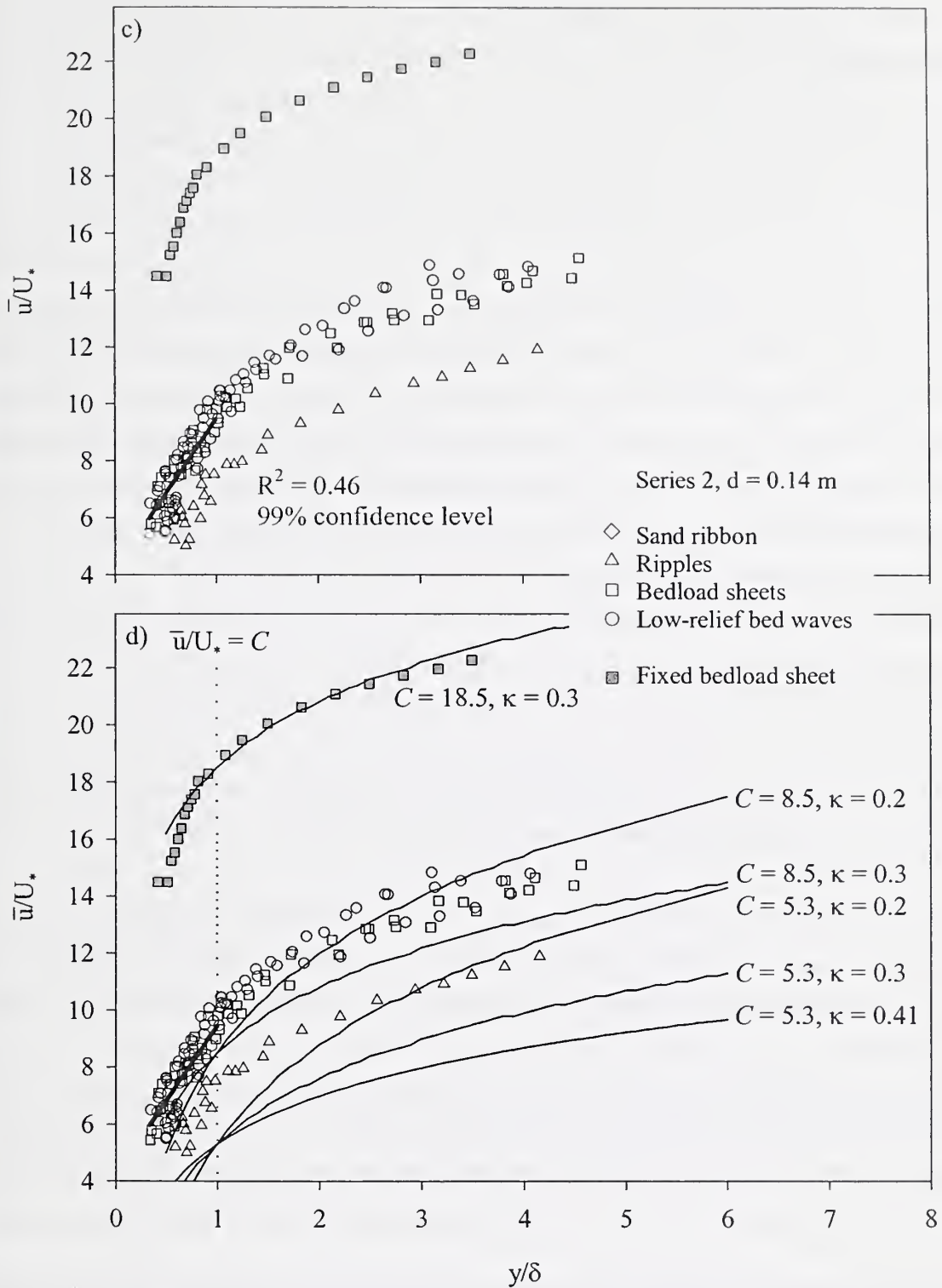


Figure 4.30: Comparison of the present experimental data with the theoretical spatio-temporally-averaged velocity distribution model of Nikora et al. (2001). The roughness layer and logarithmic layer equations are shown in red and blue respectively.





Since the roughness layer is approximately 30 mm and the maximum grain diameter is 32 mm, the bottom 20% of the flow (approximately 30 mm) can easily be envisaged as being influenced by roughness elements, and therefore no logarithmic region would be expected in the current experimental data. However, Nikora *et al.* (2001) demonstrated that the logarithmic curve fitted their experimental data for y/δ values up to 4.5 (Figure 4.29). Consequently, the logarithmic curve is compared in Figure 4.30b and d with the present data

using the C value (5.3) derived from the application of the roughness layer velocity distribution equation to all the spatially-averaged data, and the value of C over homogeneous sand roughness (8.5). The logarithmic velocity distribution plots well below the experimental data when $C = 5.3$ (Figure 4.30b and d). The upper and lower bounds of the mobile bed experimental measurements are associated with values of C around 11.5 and 8.5 respectively at a flow depth of 0.18 m, and 10.5 and 7 at a flow depth of 0.14 m. Therefore the value of C (8.5) for homogeneous sand roughness falls at the lower end of the spectrum of experimental values. The boundary conditions (e.g. spacing, morphology, packing and arrangement of large clasts and bedforms) vary between each experimental run, which influences the value of C and accounts for the data scatter observed in Figure 4.30. The fixed bedload sheet is associated with a C value of approximately 18.5, which is much greater than found over the mobile beds. The value of C appears to be positively related to the relative roughness of the bed, which is greatest for the fixed bedload sheet and lowest for the mobile rippled bed (Table 4.2 and Figure 4.30). Nikora *et al.* (2001) note that their model does not consider bedforms, however, the present analysis indicates that bedforms can be accommodated by altering the value of C for the logarithmic region. The gradient of the logarithmic curve is dependent on the value for κ . The present experimental data, both mobile and fixed, are described by $\kappa \sim 0.3$ (Figure 4.30), confirming that κ is reduced from the clear-water value of 0.41.

4.5 Conclusions

- 1) The profiles of downstream velocity measured in the present experiments over a bimodal sediment bed with bedforms are non-logarithmic, as indicated by the following:
 - a) Predictions of boundary shear stress from Reynolds stress projections and the depth-slope product were found to agree with $\pm 30\%$, whereas erroneous estimates were deduced from the law-of-the-wall, which assumes a logarithmic profile. Furthermore, estimates of the zero-velocity roughness height are high (i.e. typically > 1 mm)
 - b) The present experimental measurements were taken at values of $\frac{U_*y}{v} > 500$, where the velocity distribution is expected to diverge from the logarithmic law, whereas previous workers (Nezu and Rodi (1984) and Kirkgoz (1989)) have fitted the law-of-the-wall for $\frac{U_*y}{v} < 500$. The high values of $\frac{U_*y}{v}$ result from the higher shear velocities calculated for the present data set from measurements of Reynolds stress.
 - c) Nikora *et al.* (2001) note that roughness effects can distort the flow to a elevation of 2 to 5 times the height of the roughness elements ($\Delta \sim 10$ mm), which in this example coincides with the region in which the law-of-the-wall is potentially applicable (i.e. the bottom 20 % of the flow depth).

d) The law-of-the-wall was originally derived for flow over smooth beds, and was not explicitly formulated to describe the velocity distribution over a bed with any type of bed roughness (e.g. fixed or mobile sediment, uniform or mixed sized sediment and bedforms). However, the logarithmic law has been successfully applied in a variety of flow conditions. Kirkgoz (1989) applied the law-of-the-wall to measurements taken over fixed rough beds, forcing the gradient to equal that found over smooth beds in order for κ to equal 0.41, and imposing a linear fit to data displaying curvature.

2) When the law-of-the-wall is substituted by the velocity defect-wake law, κ values remain reduced from the clear water value of 0.41 (Nezu and Nakagawa (1993)), and Π coefficient results are predominately negative in contrast to previous studies. The empirical Π coefficient represents a variety of mechanisms which influence the entire velocity profile, and may amplify or negate each other. Over the fixed bedload sheet, κ exhibited a greater range, extending closer to the expected value of 0.41 compared with the mobile bed experiments, perhaps due to the lack of transported sediment which influences the fluid properties. This is supported by the fact that κ values are greater when determined from the whole flow profile, and not just the bottom 20 % where sediment concentration levels would be highest. Both κ and Π are elevated over the bedform crest. Once the flow is significantly modified by large clasts, the profile being integrated is no longer logarithmic near the bed, and consequently the value of κ may require adjustment, approaching 0.41 for low values of relative roughness. However, when reduced values for κ and Π are used, the velocity defect-wake law describes the experimental data reasonably well, with R^2 values greater than 0.93 at the 99% level of significance. Although, even when normalised, the velocity defect-wake distributions for all the experimental runs do not collapse to give a general trend due to the varying boundary conditions, in agreement with Kirkgoz (1989).

3) Time-averaged downstream velocity was found to be greatest over the bedform crest, where Reynolds stresses are at a minimum, reduced over the stoss, and lowest in the trough region where maximum values of Reynolds stress are located. Vertical profiles of downstream velocity in the separation and reattachment zones of the low-relief bed wave were observed to be slightly kinked, analogous to similarly located profiles over dunes which exhibited flow separation (Bennett and Best, 1995), suggesting the occurrence of flow separation downstream of the bed wave crest.

4) The average form related friction factor is 0.023, which is less than that attributed to the grain roughness (0.035), although estimates of form roughness using different methods exhibit great variability for the same experimental run (0.002-0.096). The average grain related equivalent sand roughness height (k_s') is approximated by $2-3D_{50}$. The presence of a bimodal sand-gravel mixture complicates the prediction of flow

resistance due to its complex relationship with the bedform dimensions, particle protrusion, sediment sorting and characteristic grain size.

5) The model of Wiberg and Smith (1991) overestimates the resistance to the flow provided by the coarse clasts, which causes the near bed ($y/d < 0.4$) velocities to be underestimated. Since the model compensates for the low near-bed velocities, by increasing the velocities in the outer flow ($y/d > 0.4$), the latter are overpredicted. The erroneous values predicted by the model of Wiberg and Smith (1991) may result from the fact that it does not take account of sediment sorting and bedform development. The velocity distribution model of Nikora *et al.* (2001) contains a parameter, C , which is dependent on the roughness geometry, as confirmed by the present experiments which indicate that C is positively related to the relative roughness. In the roughness layer C is equal to ~ 5.3 , in agreement with previous values obtained over gravel beds. However, C must be increased (and κ reduced) in order for the velocity distribution to be accurately described by the model in the logarithmic region.

Müller and Gyr (1996) note that complex interactions exist between the bed morphology, flow and sediment transport. The mean flow characteristics are important in order to characterise the overall flow conditions (e.g. boundary shear stress, depth-averaged downstream velocity), however sediment transport, which enables bedform development, is closely linked to fluctuations from the mean velocity (i.e. coherent turbulent structures) which are considered in detail in Chapter 5.

Chapter 5 : The turbulent flow structure over bimodal sand-gravel bedforms: implications for sediment transport and bedform development

5.1 Introduction

Flow turbulence exhibits a coherent structure, and is not random (Ashworth *et al.*, 1996; Massey, 1998). However, turbulence is associated with great complexity, which accounts for its theoretical intractability (Tritton, 1988). Consequently, laboratory experiments present one viable method of increasing our understanding of turbulence, in this case with reference to water flow over a deformable bimodal sand-gravel mixture. Advances in measuring techniques and computer power facilitate the collection of large quantities of high quality turbulence data.

Much insight into the structure of turbulent flow has been achieved by employing flumes with smooth boundaries (Nezu and Rodi, 1986, Cardoso *et al.*, 1989, Steffler *et al.*, 1989). Even in this most basic configuration, experimental scatter and uncertainties remain due to complexity of the turbulent flow. For instance, it is still difficult to determine the velocity gradient used to calculate turbulence production, mixing length and eddy viscosity. A roughened bed surface is usually accomplished by gluing down uniform spheres (Grass, 1971; Kirkgoz, 1989), whilst non-uniform mixtures have received little attention (Wang and Dong, 1996). To date, limited velocity and turbulence measurements have been conducted over mixed sand and gravel beds at shear stresses where sediment transport (Song *et al.*, 1994; Nikora and Smart, 1997; Nikora and Goring, 2000) or bedforms occur (Pitlick, 1992; Livesey, 1995; Bennett and Bridge, 1995a, Bennett *et al.*, 1998). However, detailed velocity and turbulence measurements are available for fixed bedforms developed in sand sized sediment, which can be related back to measurements collected during equivalent mobile conditions (Nelson *et al.*, 1993; McLean *et al.*, 1994; Bennett and Best, 1995, 1996; Robert and Uhlman, 2001; Best and Kostaschuk, in press). The presence or absence of mobile sediment (bed and suspended load), bedforms, and in the case of mixed sediments, grain size sorting, fractional transport and roughness discontinuities, have a significant, but poorly understood, impact on the turbulent structure of the flow.

In this chapter, various turbulent flow parameters (e.g. Reynolds stress, turbulence intensity, correlation coefficient, turbulence production, eddy viscosity and mixing length), averaged over space and/or time, are presented for both mobile and fixed bimodal sediment beds. Comparisons are made between locations over the bedforms observed, varying shear stresses and flow depths, and mobile and fixed

sediment beds. Furthermore, the present data set is compared with previous experimental and theoretical investigations in order to highlight and account for any similarities and contrasts. The implications of coherent turbulent flow structures for sediment transport and bedform development and stability are also considered.

5.2 Data analysis

5.2.1 Turbulence parameters

The mean flow equations and symbols are stated in Section 4.2.3 and expanded here in order to express various turbulence parameters. Kinematic eddy viscosity, ε , represents the influence of turbulence (i.e. large-scale coherent motions) on the mean flow, but is not a fluid property (Massey, 1998). When two neighbouring fluid layers move at a different velocity to each other, molecules, and therefore momentum, are exchanged between the layers. The result is a reduction in the velocity differential (i.e. the slower molecules are accelerated and the faster ones decelerated), the production of a shear stress at the boundary between the two fluid layers, and partial contributions to viscosity. Turbulent flow conditions involve the constant transfer of larger particles over greater distances in addition to the interchange of molecules. The larger particles transport either positive or negative momentum from one area of the flow to another, and a shear stress and effective viscosity (i.e. kinematic eddy viscosity) is generated wherever a relative motion exists, as also occurs with the interchange of molecules at a smaller spatial scale. Kinematic eddy viscosity is dependent on the degree of flow turbulence and, as illustrated in Equation 5.1, the flow location under consideration.

$$\tau_R = -\rho \overline{u'v'} = \rho \varepsilon \frac{\partial \bar{u}}{\partial y} \quad (5.1)$$

Using Equations 4.11 and 4.13, Equation 5.1 can be reworked to produce:

$$\varepsilon = \kappa y U_* \left(1 - \frac{y}{d} \right) \quad (5.2)$$

which is given in dimensionless form as:

$$\frac{\varepsilon}{U_* d} = \frac{\kappa y}{d} \left(1 - \frac{y}{d} \right) \quad (5.3)$$

Kinematic eddy viscosity can also be expressed in a dimensionless format which includes a wake coefficient by employing Equations 4.11, 4.13, 4.14, 4.21 and 5.1:

$$\frac{\varepsilon}{U_* \delta} = \kappa \left(1 - \frac{y}{\delta} \right) \left[\frac{\delta}{y} + \pi \Pi \sin \left(\frac{\pi y}{\delta} \right) \right]^{-1} \quad (5.4)$$

Mixing length, ℓ , (defined in Equation 5.5) is the average distance, perpendicular to the mean flow direction, over which a particle loses excess momentum and assumes the mean velocity of its

surroundings (Massey, 1998). In reality, the loss of momentum is gradual. The vertical variation in mixing length is described by Equation 5.5 (the dimensionless case is shown in Equation 4.18 and 5.6; the latter is based on Equations 4.11, 4.13, 4.14, 4.21 and 5.1 and includes a wake coefficient).

$$\ell = \kappa y \left(1 - \frac{y}{d}\right)^{0.5} \quad (5.5)$$

$$\frac{\ell}{\delta} = \kappa \left(1 - \frac{y}{\delta}\right)^{0.5} \left[\frac{\delta}{y} + \pi \Pi \sin\left(\frac{\pi y}{\delta}\right) \right]^{-1} \quad (5.6)$$

The production of turbulent energy extracts energy from the mean flow, due to the generation of turbulent fluctuations, which are typically associated with large scale coherent motions. The rate of turbulent generation, T , is expressed as:

$$T = -\overline{u'v'} \frac{\partial \bar{u}}{\partial y} \quad (5.7)$$

The correlation coefficient, R , of Reynolds stress (Equation 5.8), indicates the degree of similarity of turbulence, or in other words, the correlation between the Reynolds stress and the product of the rms values of both velocity components.

$$R = \frac{-\overline{u'v'}}{rmsu'.rmsv'} \quad (5.8)$$

5.2.2 Quadrant analysis

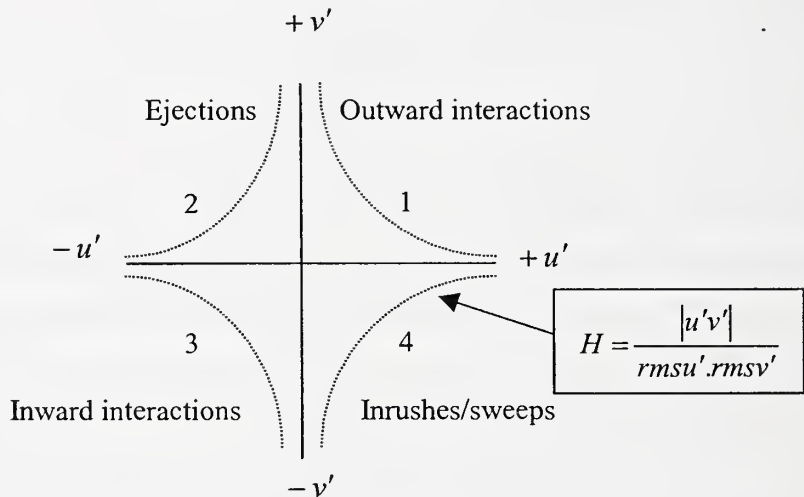
Conditional quadrant analysis of the instantaneous turbulent Reynolds stress ($u'v'$) allows quantitative understanding of the turbulence structure. The instantaneous downstream and vertical components of velocity are classified by this technique into four quadrants (Lu and Willmarth, 1973; Luchik and Tiederman, 1987). If the spanwise component of velocity (w) is also available, eight quadrants can be defined i.e. octant analysis. Quadrant analysis can be performed on the full instantaneous Reynolds stress signal, or just the values greater than a given threshold/hole size, H , which is expressed as:

$$H = \frac{|u'v'|}{rmsu'.rmsv'} \quad (5.9)$$

Thresholding enables the higher energy turbulent events to be selectively analysed, which contribute significantly to Reynolds stress and play an important role in the entrainment and transport of sediment. The threshold value is arbitrarily defined, since the number of turbulent events recorded diminishes as the threshold value increases. In both boundary layers and over bedforms, the detection of quadrant two events is typically associated with thresholds of 1-5, whereas for quadrant four events values of 2-3 have been employed (Lu and Willmarth, 1973; Luchik and Tiederman, 1987; Bennett and Best, 1995, 1996), although lower values down to zero have also been presented (Buffin-Bélanger and Roy, 1998; Buffin-Bélanger *et al.*, 2000).

Quadrant 2 (ejection) events are characterised by the ejection of low momentum fluid away from the boundary. Over smooth beds and closely packed, uniform grain roughness, quadrant 2 events are associated with the bursting process of classical boundary layer theory (Grass, 1971; Jackson, 1976). However, over bedforms and protruding large clasts, quadrant 2 events are linked to vortex shedding and Kelvin-Helmholtz instabilities along shear layers, which develop due to flow deceleration/separation (Bennett and Best, 1995). Along with quadrant 4 events, ejection events dominate turbulent energy and Reynolds stress production in turbulent boundary layers. Ejection events are important in the transfer of this turbulent energy away from the boundary, and the entrainment of sediment into the main region of the flow (i.e. sediment suspension, Kostaschuk and Church, 1993; Lapointe, 1996).

Figure 5.1: Classification of turbulent events into quadrants in the instantaneous $u'v'$ plane. A comparison of the instantaneous $u'v'$ product ($u' = u_i - \bar{u}$, $v' = v_i - \bar{v}$) with the rms u' .rms v' product determines the threshold value, H .



Inrushes of high momentum fluid from the outer-flow towards the boundary are termed quadrant 4 (sweep) events. Turbulent quadrant 4 events locally raise the bed shear stress on impact with the boundary, resulting in sediment entrainment (i.e. bedload transport, Drake *et al.*, 1988) in conjunction with quadrant 1 events (Williams, 1990).

Positive contributions to Reynolds stress are generated by quadrants 2 and 4, which cause energy to be extracted by the turbulence from the main flow. Conversely, quadrants 1 and 3 (outward and inward interactions) return energy to the main flow from the turbulence, and therefore are characterised by negative contributions to the Reynolds stress.

5.2.3 Time series analysis in the frequency domain: spectral analysis

Spectral analysis decomposes a record of fluctuations in time (in this case temporal variations in velocity) into a suite of waveforms using Fourier methods (Newland, 1975; Swan, 1995). A time series can be represented by a combination of sinusoidal functions (sine and cosine waves) with a given amplitude, frequency and phase. For each wave frequency, the amplitude and phase are determined by Fourier analysis, transforming the time series into the frequency domain. Waves with a significantly high amplitude (peaks) are identified, and can be related to periods of cyclicity in the time series (Kostaschuk, 2000). The frequency strength can be expressed by amplitude and power (i.e. the variance at that frequency). The maximum resolvable frequency is known as the Nyquist frequency, which is equal to half the length of the time series. Consequently, when data is uniformly sampled, the minimum resolvable wavelength is equal to twice the sampling interval, since in order to define a waveform, at least two observations are required to represent the crest and associated trough. However, the uniform sampling of higher frequencies can mimic lower frequency waveforms (i.e. an aliasing effect, which increases the noise at higher frequencies). The present spectral analysis is performed on LDA velocity measurements, which are sampled discontinuously through time. A Fourier spectrum can be generated for unevenly sampled data using the Lomb-Scargle periodogram (Press and Rybicki, 1989). This technique does not require the generation of an evenly spaced data set by resampling, which can cause some of the information (signal) to be lost. Waveforms with frequencies higher than the Nyquist frequency are not automatically aliased to lower frequencies when the data is unevenly sampled with respect to time, since some observations are temporally closer than the average sample interval.

Spikes in the spectra can result from random effects (i.e. noise). In order to identify peaks resulting from the signal, peak-based critical limit significance levels are employed. When the power is uniformly spread across the spectrum it is described as ‘white noise’, which can be used as a null hypothesis of randomness. A 99.9% critical limit is where only 1 in 1000 separate random noise events would generate the amplitude of the largest peak by purely random chance. The LDA records of downstream and vertical velocity over time were analysed using the following procedure:

- 1) Apply a tapering function (cosine with $\alpha = 0.1$) which smoothes the ends of the data record to zero. The series is assumed to be periodically continuous, and consequently any difference between the end points will cause a jump in the frequency spectrum. The time series is multiplied by the tapering function, which diminishes to zero at both ends, and causes the spectrum to be smoothed.
- 2) Remove the trend and mean of the time series by subtracting a linear least squares fit in order to spread energy to higher frequencies.

3) Generate a Lomb-Scargle periodogram, and detect significant spectral peaks by employing a local maxima identification algorithm and critical limits using the AutoSignal software package. A comparison was made with the results from another time series analysis software package (PITS), which requires resampling of the data to produce a regularly spaced series. The shape of the Fourier spectrum and the frequencies of the peaks were found to be consistent with those generated by the AutoSignal software package.

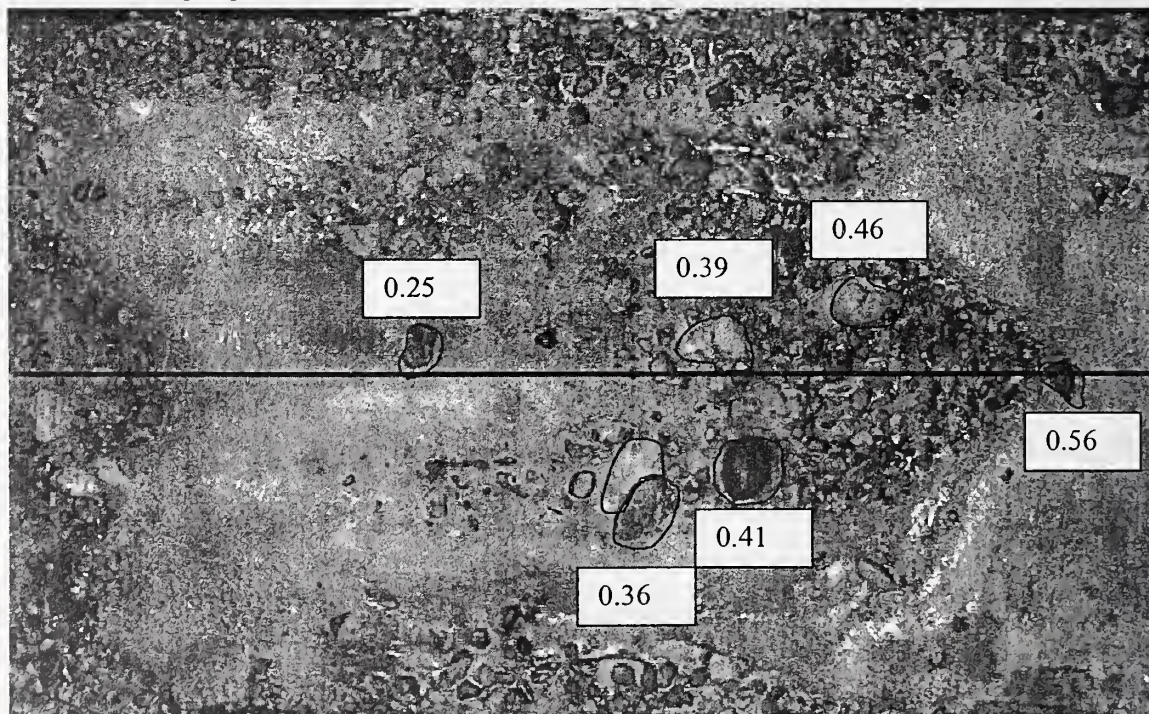
5.3 Results

5.3.1 Turbulence intensity and skewness

5.3.1.1 Bedload sheets

The rms of both the downstream (u') and vertical (v') velocity components (Figure 5.2a and b) increase towards the bed. At 0.02 m above the mean bed height, values of both rms u' and rms v' in the vicinity of the crest (located at 0.13 and 0.56 m along the flume) are lower (approximately 0.09 and 0.05 m s^{-1} respectively) than readings taken over the stoss and trough of the bedload sheet (around 0.11 and 0.06 m s^{-1} respectively).

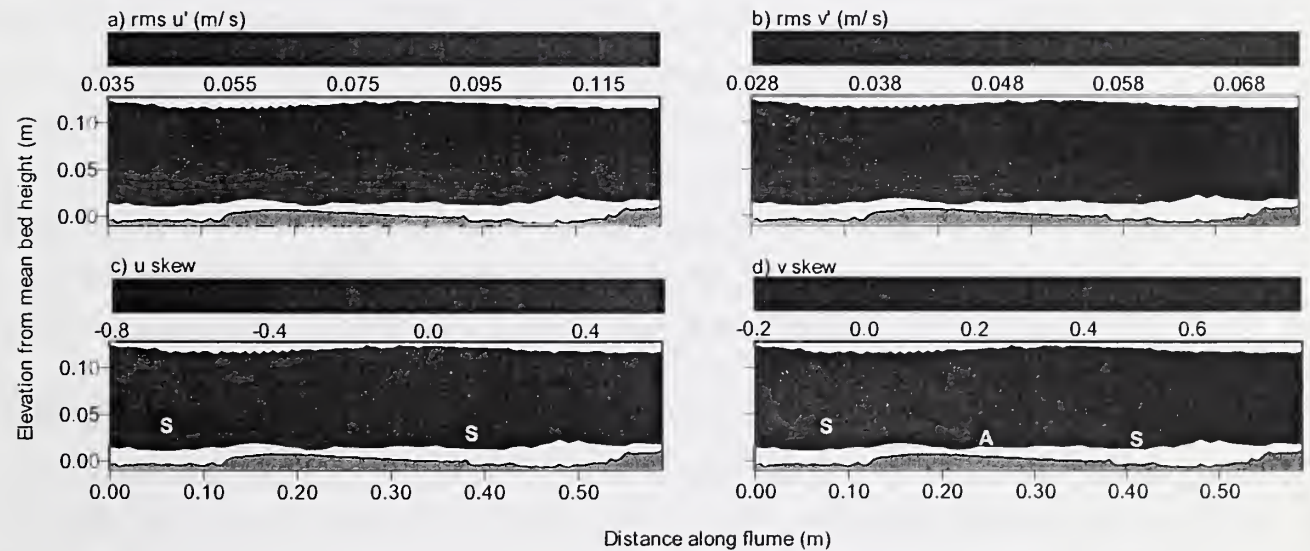
Plate 5.1: Fixed bedload sheet. Flow is from right to left. The straight red line indicates the transect along which velocity and turbulence measurements were taken. Protruding coarse clasts near the transect are highlighted in red, and their distance along the flume (m) is noted.



The spatial variation of skewness for both the downstream and vertical velocity components (Figure 5.2c

and d) illustrate that values of u_{skew} increase as the water surface is approached. Elongated zones of negative u_{skew} values (< 0.6) are highlighted in Figure 5.2c by the letter S, and are observed to extend downstream at approximately 0.04 m above the bed, coinciding with bands of maximum positive v_{skew} values (> 0.4 , represented by the letter S in Figure 5.2d). The zones identified in Figures 5.2c and d represent turbulent shear layers generated from coarse, exposed grains (e.g. the clast 0.25 m along the flume in Plate 5.1 is associated with turbulence production at position A in Figure 5.2d), and the crests of bedload sheets. Under the downstream shear layer (0.02 m above the bed, and 0.00-0.25 m along the flume) reduced v_{skew} values and increased u_{skew} values are recorded (approximately 0.2 and -0.2 respectively), reflecting the encroachment of the turbulent wake on the developing boundary layer (McLean *et al.*, 1994). Values of v_{skew} tend to fall towards the water surface.

Figure 5.2: Spatial distribution maps of time-averaged velocity moments. Flow is from right to left. The bedload sheets are shown in grey, and the white area indicates where measurements were not possible. Crests are located at 0.13 and 0.56 m along the flume. Shear layers are identified by the letter S. A shear layer is developed from a coarse grain at position A.



5.3.1.2 Low-relief bed waves

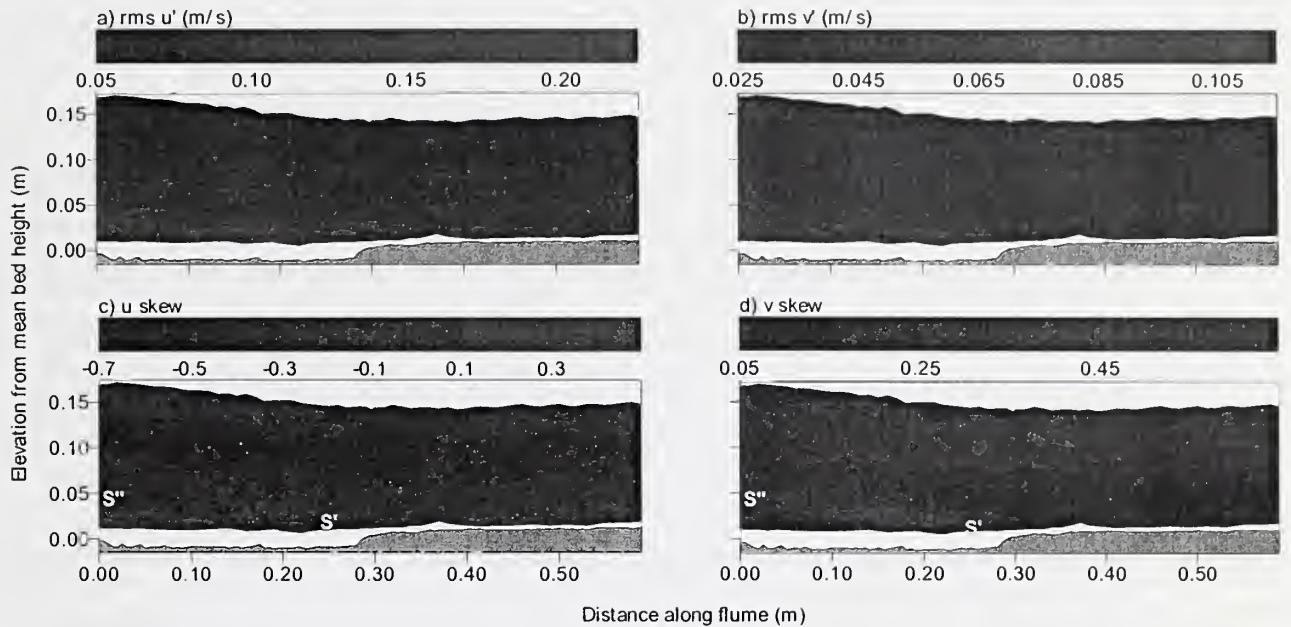
The rms of the downstream (u') and vertical (v') components (Figure 5.3a and b) reveal maximum values (> 0.15 and $> 0.085 \text{ m s}^{-1}$ respectively) in the bed wave trough (0.0-0.3 m along the flume, below 0.04 m above the bed). Both rms u' and rms v' values decrease as the water surface is approached.

The distribution of the downstream skewness (Figure 5.3c and d) exhibits maximum values (around zero) below 0.03 m from the bed along the whole of the section visible in Figure 5.3c. Values of u_{skew} around zero are also observed at the water surface. The largest negative skewness values (down to -0.7) for the downstream velocity component are located at approximately 0.1 m above the bed. Either side of this band of low values, the downstream skewness increases. Negative downstream velocity skewness values (down to -0.5) are also evident in a zone extending from 0.02 m above the bed, at 0.2 m along the flume, to 0.05 m above the bed, at a distance of 0 m along the flume (the region extending from S' to S'' in Figure 5.3c). Low negative u_{skew} values (down to -0.5) represent the turbulent shear layer, along which lower than average velocity fluid is ejected into the outer flow. However, the shear layer is picked out more clearly by the high positive values of v_{skew} (approximately 0.45, highlighted between S' and S'' in Figure 5.3d). Shearing is initiated at the bedform crest located at 0.3 m along the flume. High v_{skew} values (around 0.45) are also evident in a band at approximately 0.12 m above the bed. Low v_{skew} values (down to 0.05) are apparent above the crestal platform (0.02-0.07 m above the bed, 0.3-0.6 m along the flume) and below the shear layer generated from the crest (less than 0.025 m above the bed, 0-0.13 m along the flume). The latter reflects the infrequent movement of high velocity fluid into the deceleration zone (i.e. quadrant 4 events; McLean *et al.*, 1996).

5.3.1.3 Comparison of contour maps of turbulence intensity and skewness of velocity over fixed bedload sheets, low-relief bed waves, ripples and dunes (Bennett and Best, 1995, 1996).

Turbulence intensities over ripples, dunes and low-relief bed waves are elevated in the flow recirculation region and along the shear layer originating from the bedform crest. However, the situation is not so clear over the fixed bedload sheet due to the absence of velocity and turbulence measurements close to the bed and the occurrence of coarse clasts on the stoss (Plate 5.1).

Figure 5.3: Spatial distribution maps of time-averaged velocity moments. Flow is from right to left. The low-relief bed waves are shown in grey, and the white area indicates where measurements were not possible. The crest is located at 0.3 m along the flume. The shear layer developed from the crest of the low-relief bed wave is visible from S' to S'' .



The distribution of low skewness values of the downstream component of velocity, and high values of skewness of the vertical component of velocity, are similar over all the bedform types, highlighting the presence of turbulent shear layers originating at bedform crests. In the case of dunes and low-relief bed waves, there is also a zone of low downstream skewness and elevated vertical skewness higher in the flow, which parallels the water surface. The same shear layers can also be identified from the distribution of quadrant 2 (i.e. ejection) events, which will be considered in Section 5.3.4. Shear layers are formed at both the bedload sheet crest and from coarse particles protruding above the surface of the sheet. The shear layer generated on the mid-back of the downstream bedload sheet (Figure 5.2d, highlighted by the letter A) is associated with a coarse clast (Plate 5.1, 0.25 m along the flume). Turbulence generation by the coarse clast can merge with, and distort any evidence of, the shear layer generated at the downstream crest. Furthermore, if the bed were mobile, this coarse clast would be expected to quickly overpass the fine bedform stoss and not present a long term obstruction to the flow at this location. The fixed dunes and ripples studied by Bennett and Best (1995,1996) were uniformly covered in 0.22 mm diameter glass spheres, and therefore were not subject to variations in surface roughness. Both the fixed low-relief bed waves and bedload sheets in the present study exhibit grain size sorting, with a distinct change between the crest and trough, and a gradual transition elsewhere. Over the fixed bedload sheet the roughness changes are less distinct as they occur over a much smaller

spatial region. Furthermore, when bedload sheets are present, coarse, immobile sediment occurs at the side of the flume (top section of Plate 5.1), hindering LDA measurements close to the bed over the whole length of the bedload sheet. Conversely, the low-relief bed waves typically extend across the whole of the flume width, and velocity and turbulence measurements can be made very close to the bed over the finer areas of the bedform e.g. crest and stoss.

5.3.1.4 Normalised turbulence intensity

Figure 5.4 illustrates all the spatially averaged downstream and vertical turbulence intensities for the present experiments, made dimensionless by shear velocity, and the semi-theoretical exponential curves of Nezu and Nakagawa (1993, pg 53, $y = ae^{-bx}$ where $a_u = 2.30$, $a_v = 1.27$, $b = 1$). Turbulence intensity tends to decrease with distance from the bed. In the intermediate flow region ($0.3 < y/d < 0.9$), Nezu and Nakagawa (1993, pg 53) believe that the exponential laws provide a good balance between goodness of fit and simplicity. Different values for the coefficients in the equations have been proposed, but all fall within the range of experimental scatter (Table 5.1).

Table 5.1: Coefficients of the exponential laws for turbulence intensity, $y = ae^{-bx}$, where subscripts u and v refer to the downstream and vertical components respectively.

Reference	a_u	b_u	R_u^2	a_v	b_v	R_v^2	Conditions
Nezu and Nakagawa (1993)	2.30	1.00		1.27	1.00		Smooth bed
Nezu and Rodi (1986)	2.26	0.88		1.23	0.67		Smooth bed
Cardoso <i>et al.</i> (1989)	2.28	1.08	0.89				Smooth bed
Song and Graf (1994)	2.04	0.97		1.14	0.76		Uniform flow, fixed rough bed ($D_{50} = 12.3$, $D_{16} = 9.0$, $D_{84} = 16.5$ mm)
Present mobile bed experiments	1.76- 2.60	0.66- 1.01	0.87- 0.98	1.02- 1.44	0.40- 0.79	0.56- 0.95	Calculated for the intermediate region ($0.3 < y/d < 0.9$)
Present fixed bedload sheet	2.49	0.91	0.99	1.35	0.58	0.99	Calculated for the intermediate region ($0.3 < y/d < 0.9$)

The good agreement between the distribution of turbulence intensities in the intermediate region over a range of flow conditions highlights the rapid vertical ordering of flow over a rough boundary, resulting in the outer flow region being decoupled from the local influence of individual roughness elements. Previous measurements over smooth and rough beds, excluding those in the vicinity of the boundary (i.e. $y/d < 0.3$), support the ‘wall similarity hypothesis’ first suggested by Townsend (1976), which states that all the mean relative motions and energy containing components of turbulent motions are independent of bed roughness and viscous effects, except near the boundary. There is no distinct relationship between the value of the coefficients in the exponential laws for turbulence intensity and

the flow discharge, depth, relative roughness or bed state (i.e. mobile or fixed) in the present experiments. However, the coefficients in the exponential turbulence intensity curves have been shown by Song and Graf (1994) to be influenced by the occurrence of flow acceleration and deceleration, although in the present experiments all the runs were conducted under uniform flow conditions and therefore would not be expected to vary.

5.3.1.4.1 Downstream turbulence intensity

Agreement with the exponential curve ($a_u = 2.3$, $b_u = 1$) was found in the intermediate flow region ($0.3 < y/d < 0.9$) of the alluvial Missouri River (McQuivey, 1973), and gravel-bed rivers in New Zealand (Nikora and Smart, 1997). However, Nikora and Smart (1997) observed that the values of downstream turbulence intensity in the intermediate flow region plotted above the exponential curve when relative roughness was reduced. In the intermediate flow region ($0.3 < y/d < 0.9$), when $d = 0.14$ m (Figure 5.4b), the normalised downstream turbulence intensities for the low-relief bed waves and bedload sheets (both mobile and fixed, high relative roughness) plot above the exponential curve, whereas the ripple run (low relative roughness) plots below the curve, in contrast to Nikora and Smart (1997). However, in both cases the dependency of downstream turbulence intensity on relative roughness is inferred from the divergence of only one data set from the others. No variation in downstream turbulence intensity due to relative roughness is apparent in the intermediate flow region at a flow depth of 0.18 m (Figure 5.4a).

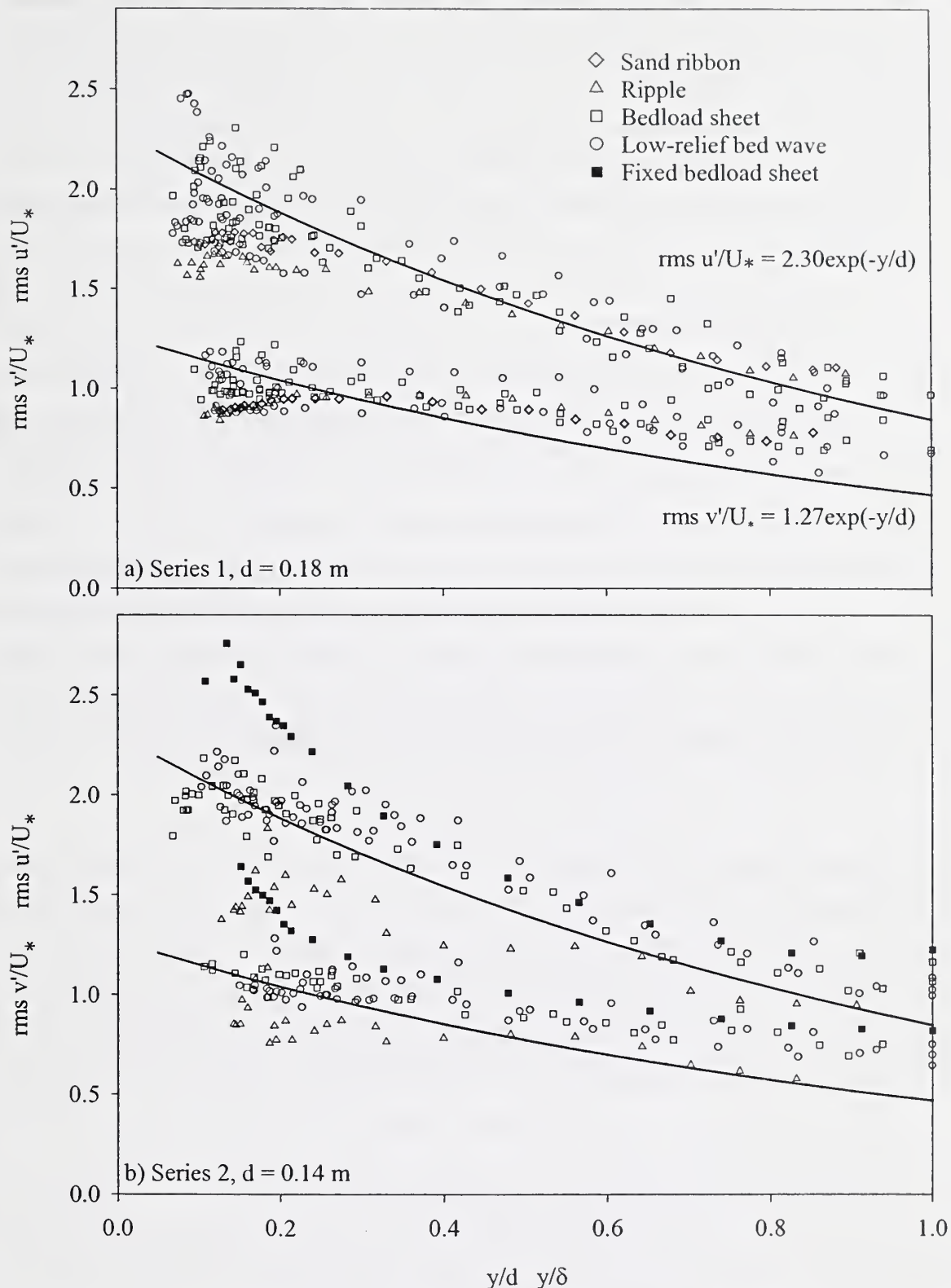
5.3.1.4.2 Vertical turbulence intensity

In the present mobile experiments, the measured vertical turbulence intensities are greater than predicted by the exponential curve of Nezu and Nakagawa (1993, $a_v = 1.27$, $b = 1$) when $y/d > 0.3$. Krogstad *et al.* (1992) found that the vertical turbulence intensity was elevated over a rough bed compared with a smooth boundary, and concluded that the effects of the boundary roughness extend into the outer flow, which is at variance with the 'wall similarity hypothesis' of Townsend (1976). Steffler *et al.* (1989) also found high values of vertical turbulence intensities, although Nezu and Rodi (1986) claim their vertical measurements were not accurate. Normalised vertical turbulence intensities could be reduced in order to coincide with the exponent curve by increasing the shear velocity, however this would also reduce the downstream turbulence component, which for series 1 (Figure 5.4a) presently collapses around the exponential curve. The presence of bedforms in the current study encourages the flow to move vertically by the generation of shear layers from the elevated crest, which transfer turbulent energy throughout the flow depth in the case of dunes. Furthermore, coarse clasts also hinder downstream motion, and can deflect and generate turbulent fluid vertically.

5.3.1.4.3 Divergence from the exponential turbulence intensity curves

The semi-theoretical curves provide an imperfect fit to the data, since it is assumed that the energy balance is locally in equilibrium (i.e. the amount of turbulence production and dissipation equate), which is only valid in the intermediate flow region ($0.3 < y/d < 0.9$). Divergence from the semi-theoretical curves occurs near the bed due to viscous and roughness effects (i.e. $y/d < 0.3$). Very close to the sediment bed (approximately $y/d < 0.1$), violent turbulent mixing causes downstream turbulence intensities to fall (Wang and Dong, 1996). In the present experiments, as the water surface is approached ($y/d > 0.9$) both the spatially-averaged turbulence intensities tend to diverge from the semi-theoretical equations of Nezu and Nakagawa (1993, Figure 5.4), giving higher values than predicted. Near the water surface ($y/d > 0.9$), turbulence intensities also rise at all locations over the fixed and mobile bedload sheet, but this trend is not evident at any specific location over the low-relief bed wave (Figure 5.5). Surface waves become influential as Froude numbers approach unity (Nezu and Rodi, 1986), causing values of both components of turbulence intensity to be greater than the curves shown in Figure 5.4 near the free surface ($y/d > 0.9$). In the present experiments, the Froude number ranged from 0.4-0.9, and therefore elevated values near the free surface are expected. The experiments of Cardoso *et al.* (1989) over a smooth bed also demonstrate an increase in streamwise turbulence intensity near the water surface despite lower Froude numbers of around 0.2. The influence of surface waves partly explains the large range of experimental scatter often observed near the water surface.

Figure 5.4: Spatially-averaged downstream and vertical turbulence intensities, normalised with shear velocity. The semi-theoretical curves of Nezu and Nakagawa (1993, pg 53) are given for comparison.



In the vicinity of the wall (i.e. $y/d < 0.3$) the influence of roughness is discernible i.e. the roughness layer. Various experimental research initiatives report that as relative roughness increases, the

normalised downstream turbulence intensity in the wall region decreases, and the vertical turbulence intensity rises (Grass, 1971; Nezu and Rodi, 1986). The reduction in streamwise turbulence intensity with increasing relative roughness is predominantly a result of the damping of large scale coherent eddies (Nezu and Nakagawa, 1993). The influence of relative roughness on turbulence intensity is seen to be greater (i.e. increased data range, Figure 5.4) for the downstream velocity component compared with the vertical velocity component, as confirmed by Nezu and Nakagawa (1993). They also note that the spanwise component of turbulence intensity is not significantly affected by relative roughness.

5.3.1.4.4 Peak turbulence intensities

Wang and Dong (1996) observed a peak rms u'/U_* of 2.0 at $y^+ = U_*y/\nu \approx 210$ ($y/d = 0.2$) over a fixed non-uniform gravel bed ($D_{50} = 10$ mm, Gaussian distribution), whereas Nezu and Nakagawa (1993) observed a peak value in rms u'/U_* of 2.8 at $y^+ \approx 10-20$ over a smooth flume bed. The maximum value of rms u'/U_* in the present experiments (occurring at $y/d \approx 0.1-0.2$, $y^+ \approx 1000-2000$) ranges from around 1.6 to 2.5 when the bed is mobile, and is about 2.8 for the fixed bedload sheet. Conversely, Nikora and Goring (2000, no bedforms present, $(D_{84}/D_{16})^{0.5} = 1.7$ (well sorted) compared with a value of 4.3 for the present experiments) found that near the bed ($y/d < 0.1$, $y^+ < 2000-7000$) turbulence intensities were greater when there was weak bedload, which was associated with a lower relative roughness (0.01) than the static bed (0.02) due to the greater water depth.

5.3.1.4.5 Influence of relative roughness on turbulence intensities

For the present data set, relative roughness was calculated for each run by a) dividing the average height of the largest bedform population by average flow depth, and b) dividing k_s (calculated from the law-of-the-wall) by the average flow depth (results are shown in Table 4.2). Both methods produce results that indicate a similar trend. The lowest downstream and vertical turbulence intensities near the wall ($y/d < 0.3$) are associated with ripples, which have small elevation and relative roughness. Bedload sheets and low-relief bed waves are similar in height and relative roughness, and no obvious distinction in terms of streamwise and vertical turbulence intensity is observed (Figure 5.4). Finally, the fixed bedload sheet demonstrates both the largest relative roughness and turbulence intensities. The present data therefore seems to contradict previous observations of relative roughness being inversely related to streamwise turbulence intensity near the bed ($y/d < 0.3$; Wang and Dong, 1996), and support the direct link between vertical turbulence intensity and relative roughness in this region (Grass, 1971).

Where just ripples are present, the sand fraction in gravel interstices is likely to be entrained, causing greater exposure of the large clasts constituting the extensive armour layer (up to 32 mm diameter), which may result in greater relative roughness than inferred from consideration of just the small (~ 5 mm high), spatially-limited ripples (about 120 mm wide and 700 mm long). However, entrainment of fine sediment from the gravel interstices also occurs when narrow (~ 60 mm wide) sand ribbons prevail (run A, $d = 0.18$ m). The sand ribbons, which have a lower relative roughness (~ 0.01), exhibit a higher downstream turbulence intensity near the bed ($y/d < 0.3$, Figure 5.4a) compared with the ripples. The sand ribbon and ripple bed configurations are most similar in nature to previous studies of turbulence intensity over flat smooth and rough beds (Grass, 1971, 1996; Wang and Dong, 1996), since the bedforms have minimal relief and spatial extent, and sorting of the original bimodal bulk mixture is limited. Consequently, a comparison of the sand ribbon and ripple runs supports the contention that relative roughness is inversely related to downstream turbulence intensity. However, if the ripple bed experimental run is compared with the bedload sheets and low-relief bed waves, relative roughness is found to be directly related to downstream turbulence intensity due to the presence of bedforms. Elevation changes over bedforms result in variations in flow velocity, for example in the lee of a bedform flow expands and decelerates, which increases the local velocity gradient, shearing and the production and intensity of turbulence. Previous experimental work concerning turbulence intensities has focused on smooth beds, and uniform or poorly sorted sediment with no bedforms being present. In these cases, the relative roughness term is applicable since the value for the equivalent sand roughness is fairly well defined. However, when the sediment has a bimodal distribution (size sorting effects), or bedforms are developed (form roughness), it is difficult to identify a single characteristic length scale.

The fixed bedload sheet exhibits greater turbulence intensity and relative roughness compared with the mobile bed equivalent (Figure 5.4b). The relative roughness is partly enhanced over the fixed bedforms due to the reduction in water depth (section 4.3.1). However, the value of relative roughness is also dependent on the method by which bed height is measured. Only two crests can be used to measure bedform height with a point gauge in the fixed bed run (average of 15 mm). In the equivalent mobile bed run (J), the height of 138 bedload sheets are measured (average of 12 mm) using an ultrasonic probe.

The decreased roughness (due to the absence of bedload, Nikora and Goring (2000)) and flow depth over the fixed bed compared with the mobile equivalent, cause higher flow velocities (i.e. $U = 0.77$ and 0.70 $m\ s^{-1}$ over the fixed and mobile bedload sheet respectively), and larger velocity gradients at location of rapid change in bed geometry e.g. downstream of the bedform crest and large, protruding clasts. Where stronger velocity gradients exist, shearing occurs and turbulence intensity is increased. Since the fixed bedforms and sediment did not move relative to the fluid, the velocity gradient over any

bed perturbations is maximised, resulting in strong turbulent fluctuations. However, the steeper the bedform (height/length), the greater the damping of turbulence intensity over the stoss due to enhanced topographic acceleration (Nelson *et al.*, 1993).

The method used to set the sediment bed critically influences the arrangement and density of roughness elements (Nowell and Church, 1979). In the present experiments, the bed is fixed by a coat of resin, which penetrates the sediment bed previously formed under mobile bed conditions. Where there is a low density of roughness elements, the individual roughness components and their associated wakes are isolated (limited interaction), causing downstream turbulence intensity to increase towards the bed when $y/d < 0.2$, e.g. the turbulent wakes generated from the crests of bedload sheets and low-relief bed waves. At the other end of the spectrum where roughness elements are closely packed, the origin of the turbulent flow is effectively shifted to the top of the roughness elements i.e. skimming flow, and downstream turbulence intensity decreases towards the bed in the region $y/d < 0.2$ (e.g. Wang and Dong, 1993; $D_{50} = 10$ mm). At intermediate densities of roughness elements, the downstream turbulence intensity remains approximately constant near the bed (Nowell and Church, 1979; e.g. ripple bed configuration, Figure 5.4), and the wakes generated from each individual roughness elements (e.g. bedforms and large clasts) are able to interact. The region between the inner and outer flow fields is most distinct (1-2 roughness heights above the elements) when there is interaction between the wakes of the roughness elements (Nowell and Church, 1979). The characteristics of the wakes are determined by the size of the formative roughness element and the Strouhal number (Levi, 1983a, b, 1991). The turbulent wakes mix into the outer flow and extend down towards the wall until the viscous effects become significant. Flow resistance is greatest in the region of wake interactions.

5.3.1.4.6 Spatial variations in turbulence intensity over a bedform

There is no obvious distinction in turbulence intensity over specific regions of the mobile bedload sheets (Figure 5.5ia and iia), due to the small spatial extent of each area of the sheet. However, the lowest values of turbulence intensity (below the spatial average) are located over the lower back of the fixed bedload sheet, whereas the highest values are recorded over the mid-stoss (red symbols in Figure 5.5iia). However, over the mobile low-relief bed wave, it is apparent that downstream turbulence intensities near the bed ($y/d < 0.2$) are greater than the spatial average in the trough region (region A on Figure 5.5ib). Furthermore, the downstream turbulence intensity is greatest over the fixed low-relief bed wave at flow reattachment and separation (which both occur in the trough region) when $y/d < 0.2$ (region B on Figure 5.5iib), and vertical turbulence intensities are elevated in the separation zone (region D on Figure 5.5iib). Moreover, turbulence intensities are reduced at location 'crest b' (region C and E on Figure 5.5iib) which is found on the crestral platform. However, at profile 'crest a' (located at

the change in slope over the crestral platform and associated with the start of flow expansion), turbulence intensities plot on the semi-theoretical curves of Nezu and Nakagawa (1993).

Over a uniformly roughened dune (Bennett and Best, 1995), both components of turbulence intensity are greatest near the bed ($y/d < 0.3$) in the trough region, with downstream turbulence intensity gradually decreasing over the dune stoss. Carling *et al.* (2000b) and Kostaschuk (2000) also observed turbulence intensity to be elevated in the wake zone of dunes. Bennett *et al.* (1998) confirm that near bed ($y/d < 0.3$) turbulence intensities are increased relative to the spatial average in the trough, but reduced over the crest of low-relief bed waves associated with upper-stage plane beds.

5.3.1.4.7 Discussion of the spatial distribution of turbulence intensity

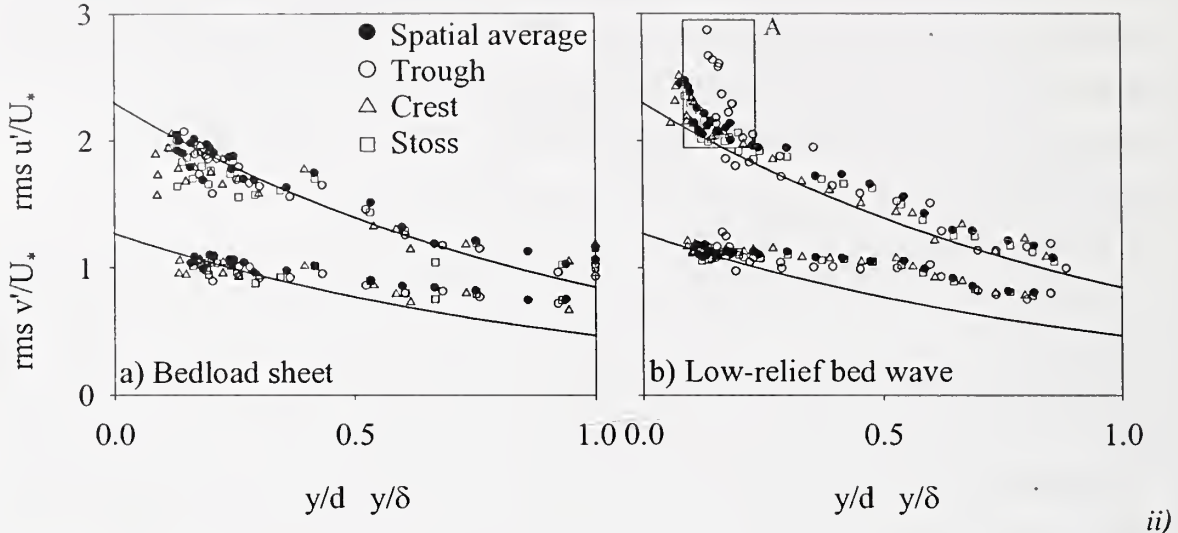
Downstream of the point of flow expansion, which occurs just upstream of the bedform crest, turbulent fluid from the free shear layer is transferred towards the bed by the advection of high turbulence intensity flow along the mean streamlines around the flow deceleration zone (Nelson *et al.*, 1993). In the trough of the low-relief bed wave, the elevated values of streamwise turbulence intensity that occur approximately 20-30 mm away from the bed coincide with the presence of a highly turbulent shear layer generated from the upstream crest. The shear layer is dissipated as it advects and disperses downstream from its crestral origin, and therefore its influence on near-bed flow gradually reduces over the length of the downstream bedform. Furthermore, flow is topographically accelerated over the bedform stoss side, damping turbulence, which produces reduced turbulence intensities at the crestral platform (regions C and E in Figure 5.5iib; Nelson and Smith, 1989; Nelson *et al.*, 1993). The presence of the shear layer also provides the main contribution to the elevated vertical turbulence intensities in the trough of the low-relief bed wave, in conjunction with the greater roughness associated with this region.

Over the bedload sheet, the morphological and textural changes are not as distinct as over the low-relief bed wave. Consequently, shear layer development is associated with both the crest of the bedload sheet and from protruding coarse clasts, which can occur in the trough and stoss, impacting any region immediately downstream. For example, in Plate 5.1 a coarse clast can be observed approximately 0.25 m along the flume, which coincides with the mid-back profile in Figure 5.5iia, which exhibits the highest turbulence intensity values (highlighted in red above the spatial average). The nearest upstream profile (lower back), demonstrates the lowest turbulence intensities observed (highlighted in red below the spatial average in Figure 5.5iia). Therefore, it can be concluded that the high turbulence intensities over the mid-back of the fixed bedload sheet result from a wake generated by the coarse clast rather than the upstream crest. Furthermore, due to the substantially shorter streamwise extent of the bedload

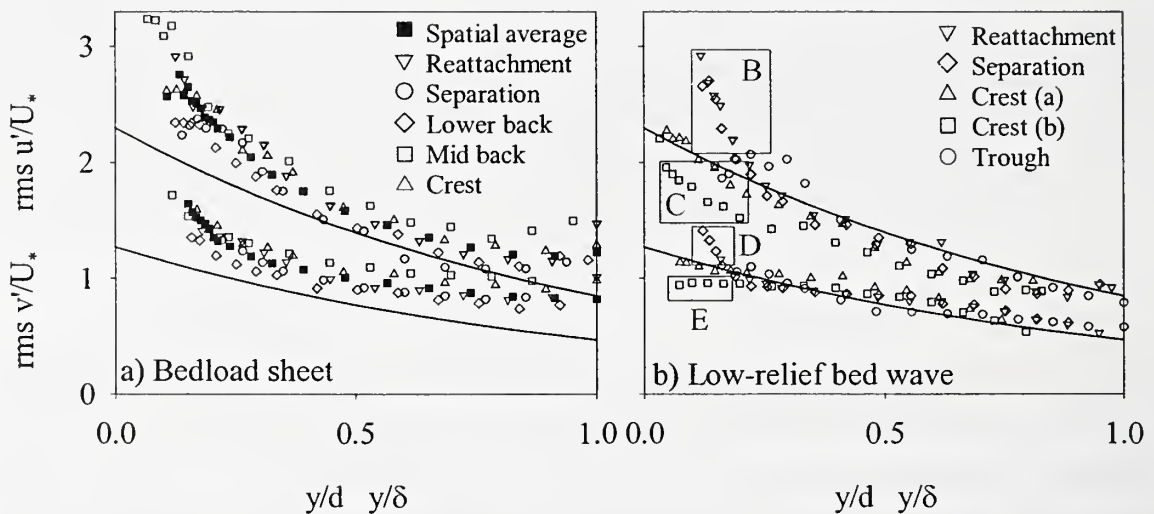
sheets compared with the low-relief bed waves, wherever the shear layer is generated it is likely to influence a significant proportion of the entire feature, reducing the contrast between regions.

Figure 5.5: Normalised turbulence intensity against dimensionless flow depth for specific bedform regions. The semi-theoretical curves of Nezu and Nakagawa (1993) are given for comparison (equations are given in Figure 5.4). The areas highlighted in red are discussed in the text.

i) Mobile bed conditions



Fixed bed conditions



Bedforms of greater height will experience a larger velocity gradient in their lee, creating more energetic Kelvin-Helmholtz instabilities, which interact more strongly with the outer flow. Over the bedform stoss, topographic acceleration is greatest between the reattachment point and the mid-back. Topographic acceleration causes the downstream decrease in turbulence intensity in the wake region to be intensified compared to the separated flow over a backward-facing step where downstream topographic acceleration is absent (Nelson *et al.*, 1993). Furthermore, the maximum value of turbulence intensity in the shear layer occurs further upstream over bedforms compared with backward

facing steps, due to the size of the separation zone being reduced by topographic acceleration (Nelson and Smith, 1989).

5.3.2 Reynolds stress

The determination of bed shear stress, which encompasses the horizontal and vertical variation of at-a-point Reynolds stress, is considered in Chapter 4 over both mobile and fixed beds. Reynolds stress decreases as the water surface is approached over fixed bedload sheets and low-relief bed waves (Figure 5.6), due to the influence of the free surface and the low velocity gradients in this area. Reynolds stress is at a maximum (> 7.5 Pa) in the trough of the low-relief bed wave (i.e. less than 0.02 m above the bed, and from 0.0 to 0.3 m along the flume), which is also true of the rms values of both the downstream and vertical velocity components (Figure 5.3). Reynolds stress is also maximised along the shear layer originating from the crests of fixed dunes and ripples (Bennett and Best, 1995, 1996). High stresses (> 1.4 Pa) are not confined to the trough region of bedload sheets, but occur along the entire bedform length within 40 mm of the bed. A minimal number ($< 2\%$) of negative Reynolds stress values were recorded near the water surface (minimum of -0.3), which indicates that precise equilibrium flow conditions were not attained over the fixed bedforms, as was also the case in the experiments of Nelson *et al.* (1993). Ideally Reynolds stress measurements (used in the calculation of quadrant analysis, turbulence production, eddy viscosity and mixing length) should be taken parallel to the streamlines. However, when bedforms are present, the streamlines diverge marginally from the bed morphology (Nelson *et al.*, 1993), which is used as a reference point. Negative values of Reynolds stress were omitted from any calculations.

Figure 5.7 and 5.8 illustrates the linear decrease in Reynolds stress in the outer flow region as the water surface is approached. The maximum Reynolds stress in each profile defines the top of the roughness layer ($y/d \approx 0.2-0.3$, $y \approx 30-50$ mm for the mobile experimental runs), in which Reynolds stresses are diminished due to drag and the interaction of mobile sediment with the fluid (Song *et al.*, 1994).

Near the bed ($y/d < 0.3$), values of Reynolds stress are elevated at all locations over the fixed bedload sheet, and for the spatially-averaged case (Figure 5.8iia; region A in Figure 5.7b), but this was not true for the equivalent mobile bedload sheet (Figure 5.8ia). However, measurements taken over the lower back of the fixed bedload sheet are below the spatial average (region B in Figure 5.8iia), as was also observed for turbulence intensity. Over the fixed low-relief bed wave, elevated Reynolds stress (and turbulence intensity) values below $y/d = 0.3$ were only apparent in the separation and reattachment zone (region C in Figure 5.8iib). Elevated Reynolds stresses (and turbulence intensities) were also noted in the trough region of the mobile low-relief bed wave at $y/d \approx 0.2$ (region A in Figure 5.8ib). Furthermore, Reynolds stresses (and turbulence intensities) are diminished for the profile taken over the

crestal platform of the fixed low-relief bed wave (e.g. crest b highlighted in area D of Figure 5.8ib), in accord with Bennett and Best's (1995) measurements over fixed dunes (Figure 5.9i). Whereas, at the profile recorded further downstream as the crestal platform begins to slope off (crest a), associated with flow expansion, Reynolds stress values collapse on to the line shown in Figure 5.8iib and 5.9i i.e. greater than on the crestal platform upstream. In the trough region i.e. in the separation zone and at reattachment, the Reynolds stress profiles follow a similar trend, with an upper linear section, and elevated stresses below approximately $y/d \sim 0.5, 0.4$ and 0.2 for the fixed dune (Bennett and Best, 1995), bedload sheet and low-relief bed wave respectively (Figure 5.9). Due to the significantly reduced roughness over the fixed dunes (0.22 mm glass spheres), measurements could be taken closer to the bed, and illustrate the decline in Reynolds stress due to roughness close to the bed ($y/d < 0.2$).

As the crest is approached over the stoss of a fixed dune, values of Reynolds stress increasingly diminish (Bennett and Best, 1995), diverging from the linear distribution of stress, in contrast to the data collected over the bedload sheet (Figure 5.9ii). Krogstad *et al.* (1992) also found that Reynolds stress is greater over a rough bed compared with a smooth boundary. Indeed, the presence of protruding coarse clasts on the fine stoss side of the fixed bedload sheet (e.g. the grain 0.25 m along the flume in Plate 5.1), and associated wake generation, accounts for the elevated near-bed ($y/d < 0.4$) Reynolds stress values observed at all locations over the fixed bedload sheet.

Bennett and Best (1998) also observed Reynolds stress to be greater than the spatial average in the trough region, and reduced over the crest of low-relief bed waves associated with upper stage plane beds. They suggest that when bedforms are present, causing the flow to be slightly non-uniform, it is inappropriate to linearly extrapolate Reynolds stress measurements down to the local bed level. Furthermore, Bennett *et al.* (1998) indicate that the Reynolds stress maxima in the trough region must occur above the bed and not at the bedform surface, with the exception of flow reattachment. Indeed, boundary shear stress is generally low in the deceleration zone due to the characteristic low velocities (Carling *et al.*, 2000b). Reynolds stresses are elevated over the trough region and at reattachment due to the turbulent shear layer generated from the upstream crest, which is caused by rapid flow expansion resulting from topographic variations. In the near-bed wake region zone of fixed dunes, Nelson *et al.* (1993) observed that Reynolds stress increases away from the bed, attaining a maximum in the centre of the turbulent shear layer, and falling to zero at the free surface. However, over the upper stoss of the fixed dunes, Reynolds stresses in the boundary layer, which developed downstream of reattachment, were greater than those in the wake region immediately above.

Figure 5.6: Maps of the spatial distribution of Reynolds stress over a) fixed bedload sheet, b) fixed low-relief bed wave. Flow is from right to left. Bedforms are highlighted in grey, while the white zone indicates no measurements were possible.

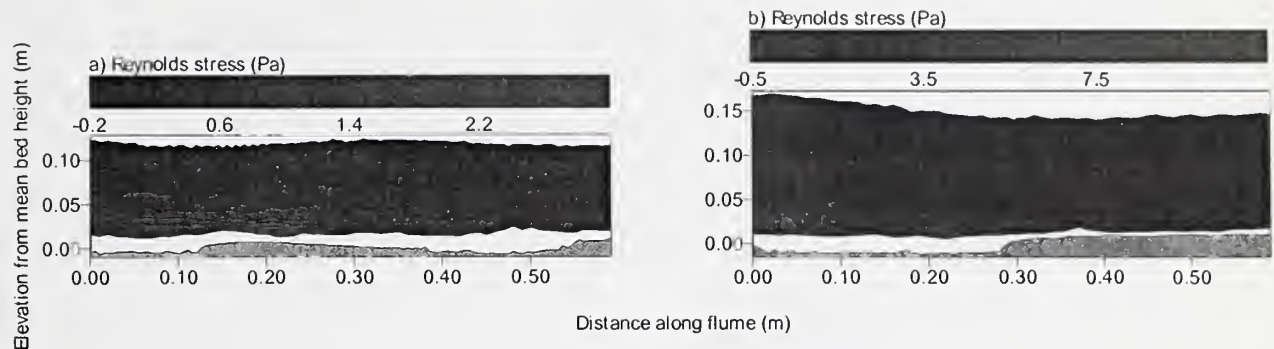


Figure 5.7: Spatially-averaged dimensionless Reynolds stress against normalised flow depth. Divergent points (highlighted area) are discussed in the text.

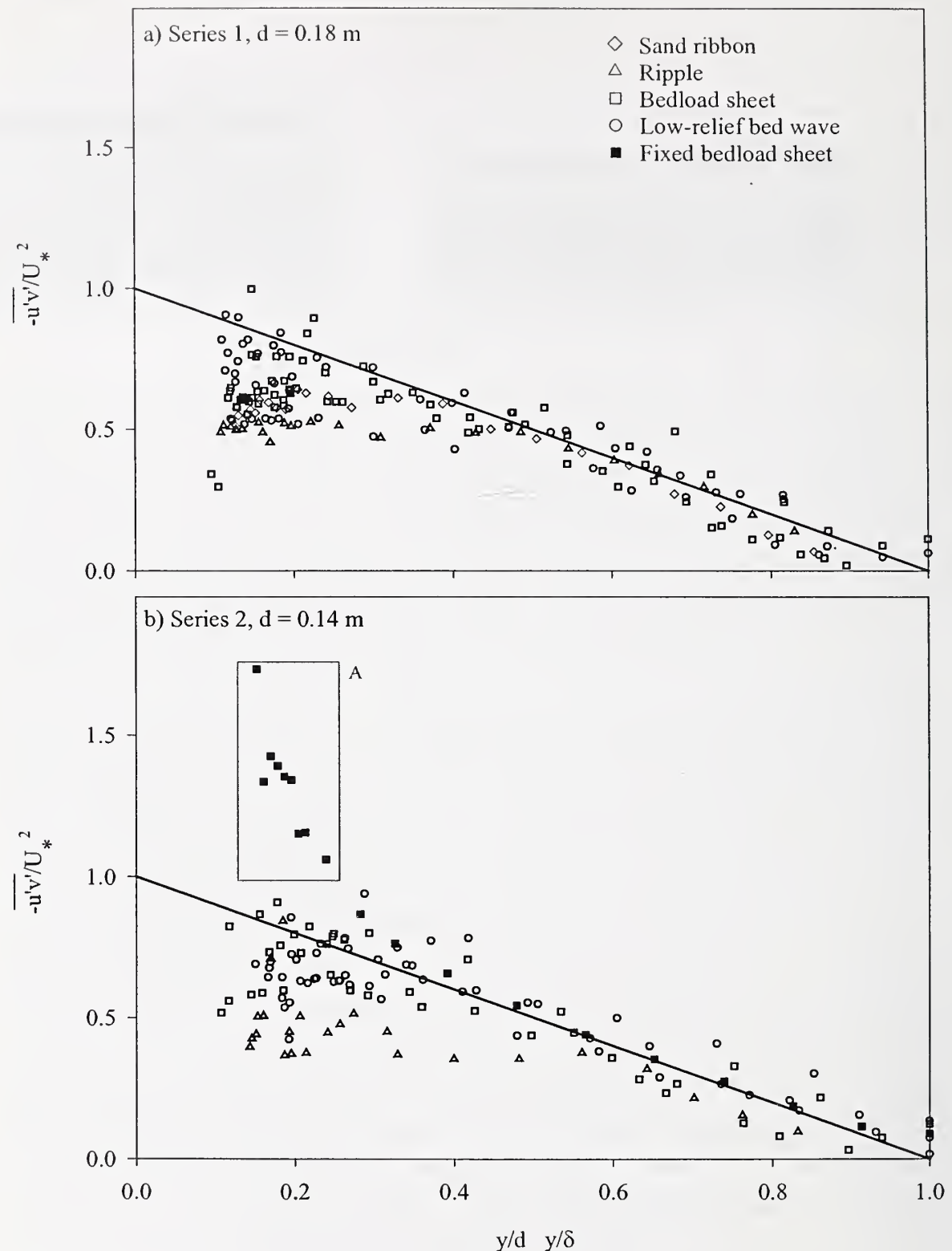
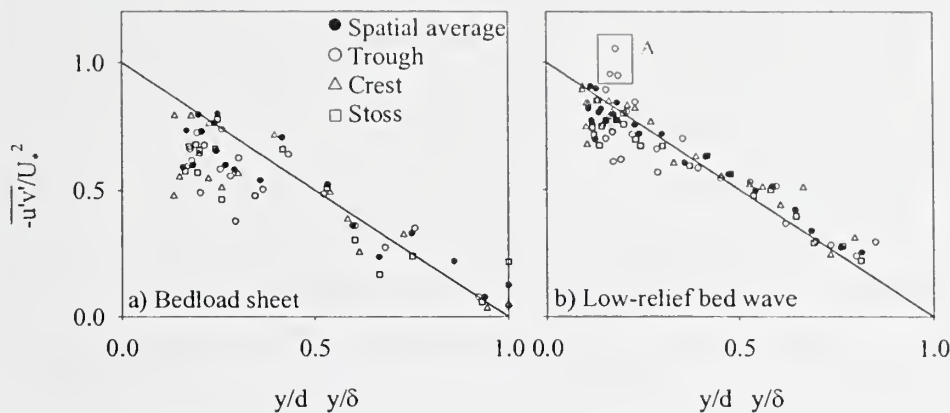


Figure 5.8: Normalised Reynolds stress against dimensionless flow depth for specific bedform regions. Highlighted areas are discussed in the text.

i) Mobile bed conditions



ii) Fixed bed conditions

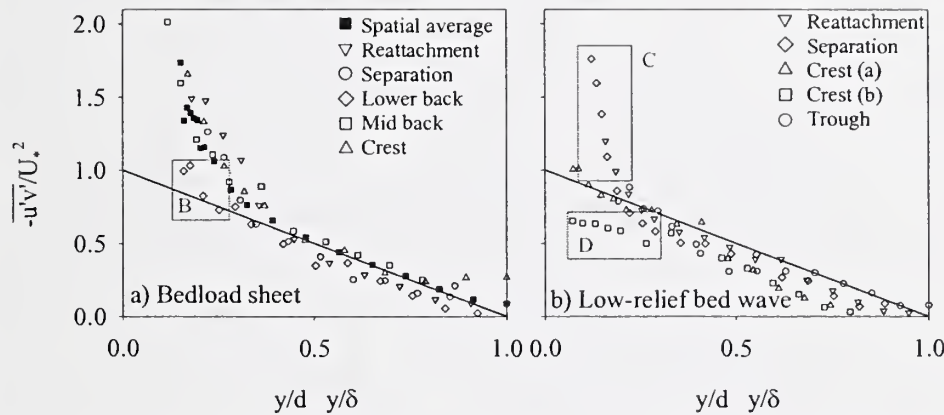
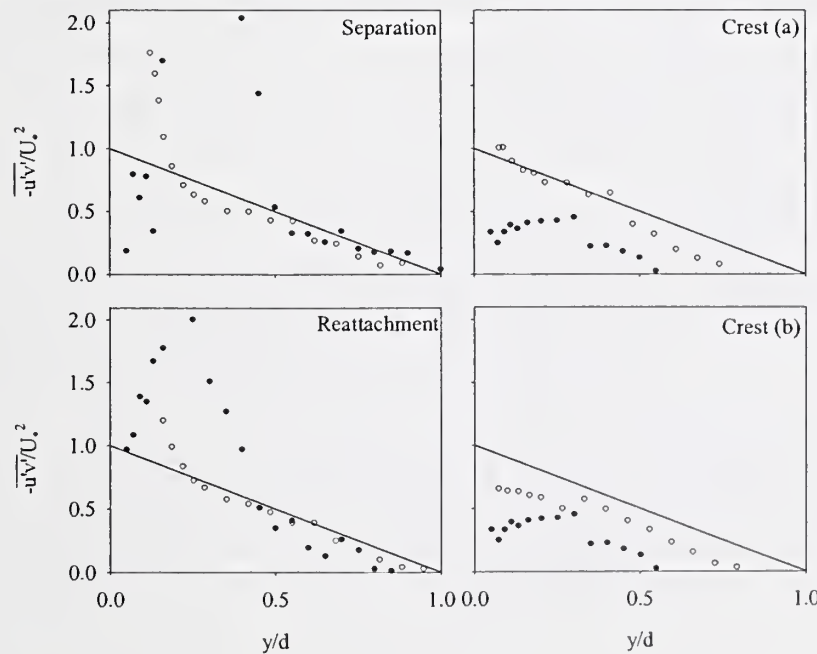
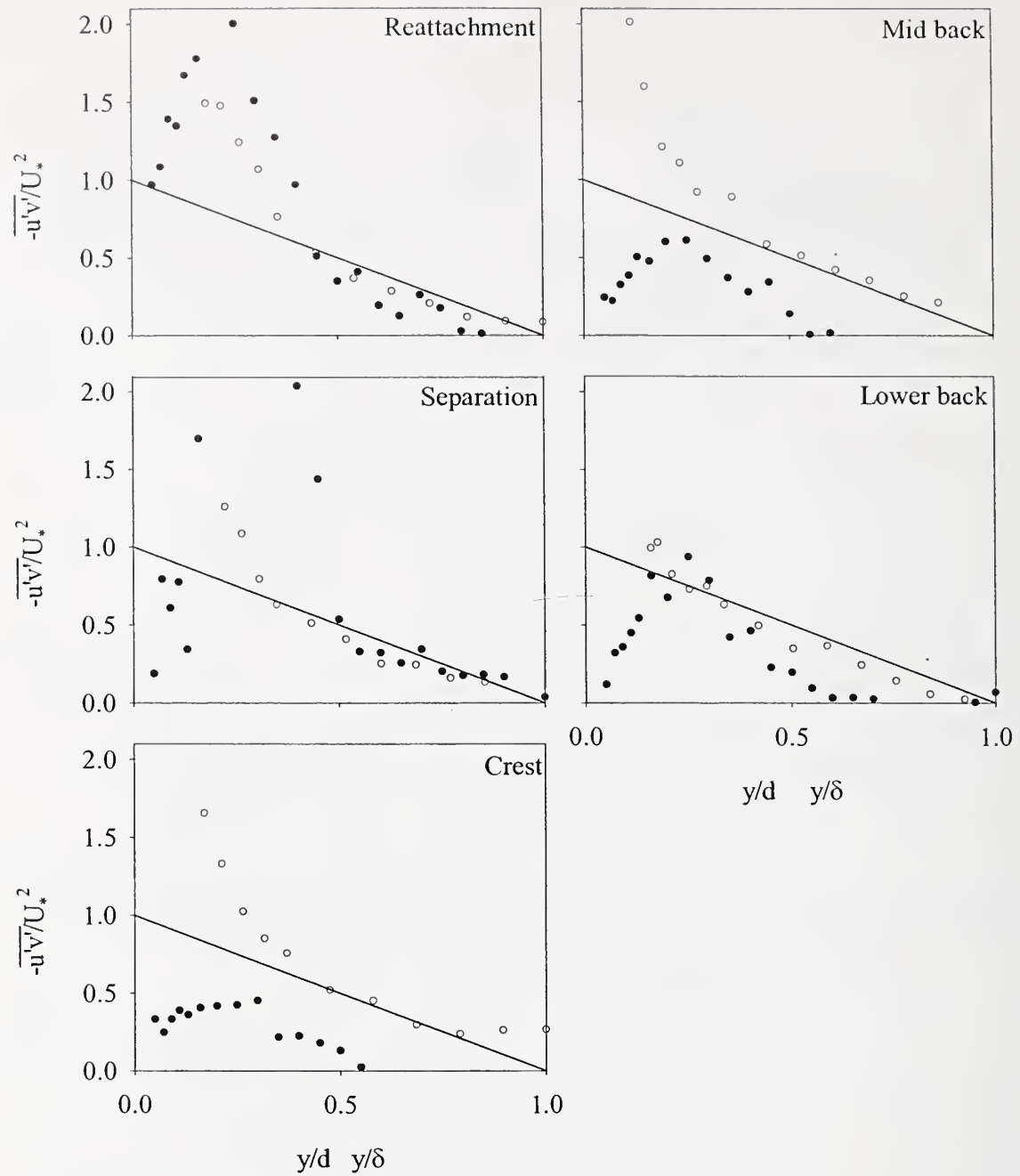


Figure 5.9: Normalised Reynolds stress measurements plotted against dimensionless flow depth.

i) Fixed low-relief bed wave (white symbols) and dune (black symbols, data from Bennett and Best (1995)).



ii) Fixed bedload sheet (white symbols) and dune (black symbols, data from Bennett and Best (1995)).



The fixed bedforms have a reduced drag due to the lack of bedload, the absence of the relative motion between fluid and sediment phases and the surface coat of resin. Consequently, the reduction in Reynolds stress due to bed roughness occurs lower in the flow over the fixed bed cases compared with the mobile examples, and below the region in which LDA measurements were possible. The reduced roughness over the fixed bedload sheets results in greater velocities compared with the mobile equivalent ($U = 0.77$ and 0.70 m s^{-1} for the fixed and mobile bedload sheets respectively), accentuating velocity gradients caused by any rapid changes in bed elevation (e.g. bedform crest and protruding coarse clasts).

5.3.3 Correlation coefficient of Reynolds stress, R

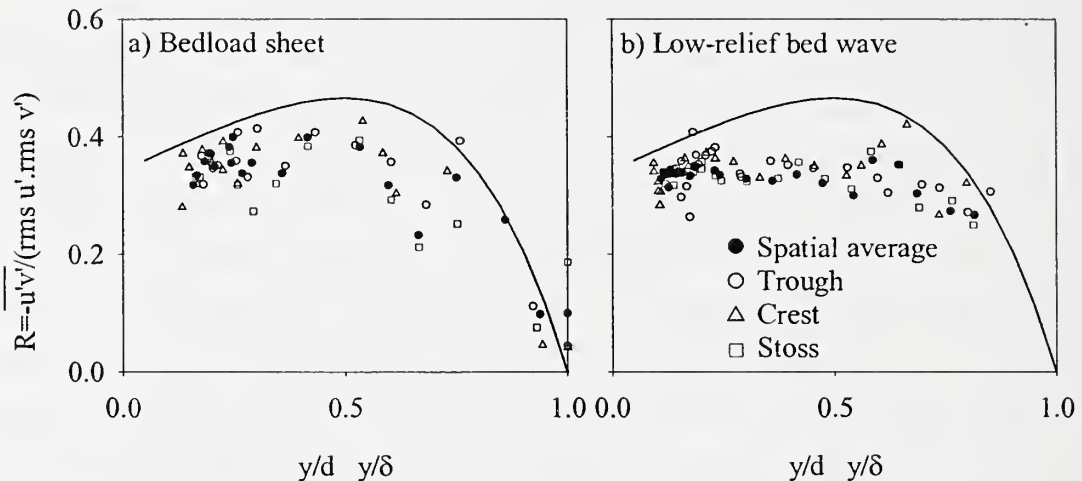
The correlation coefficient, R , is defined as the ratio of the Reynolds stress to the product of the downstream and vertical turbulence intensities. If the production of turbulent energy equals its dissipation, R is constant in the intermediate flow region ($0.2 > y/d > 0.6$, Figure 5.10 and 5.11), illustrating a good correlation between the downstream and vertical turbulent fluctuations. However, R decreases near the bed ($y/d < 0.2$) and free surface ($y/d > 0.6$) where turbulent energy production and dissipation are greater respectively. The reduction in the correlation coefficient observed near the bed ($y/d < 0.2$, Figure 5.10), results from the interaction between the internal boundary layer and the overlying turbulent wake region (Nelson *et al.*, 1993). Nezu and Nakagawa (1993) compared data from boundary layers, pipe flows and open-channels, and found the distribution of R to be universal regardless of mean flow parameters and boundary roughness. Furthermore, the present data demonstrates no apparent distinction in the correlation coefficient of Reynolds stress between different runs, mobile or fixed bedload sheets (Figure 5.11) or specific regions of the bedforms (Figure 5.10). Nezu and Nakagawa's (1993) calculated curve (for a Reynolds number, $Re = U_*d/\nu$, based on a shear velocity of 600) describes their compilation of data well, with the exception of the wall region ($y/d < 0.2$), and is plotted in Figure 5.10 and 5.11 for comparison with the present experimental results. The present data follows a similar trend to the curve proposed by Nezu and Nakagawa (1993), but plots below, with a roughly constant value of 0.35-0.4 in the intermediate region ($0.2 < y/d < 0.6$) rather than 0.4-0.5. The universality of R is therefore in question. The divergence from the curve of Nezu and Nakagawa (1993) could illustrate a dependency of R on Reynolds number, since the maximum Reynolds number of the data compiled by Nezu and Nakagawa is 90000, whereas for the present experiments the Reynolds number varied from 71421 to 147500. However, Reynolds number ranged from 350000 to 1300000 in the field measurements of Nikora and Goring (2000), and R varied from 0.3-0.5 in the intermediate flow region, with the lowest values being attributed to flows with weak sediment movement, but no bedforms, and the highest Reynolds numbers. Lower values of R can be attributed to sediment transport and the presence of bedforms, which were not considered in the data collated by Nezu and Nakagawa (1993). However, in the present data set, the fixed bedload sheet (no sediment transport) also has relatively low R values in comparison with the calculated curve in the intermediate flow region ($0.2 < y/d < 0.6$, Figure 5.11b).

Since sediment transport is absent over the fixed bed, the occurrence of bed features, which present topographic variations to the flow, must be influential in reducing the correlation coefficient, in addition to bedload movement (Nikora and Goring, 2000). Nelson *et al.* (1993) found that the correlation coefficient over the lower stoss of fixed dunes in the boundary layer and overlying wake were much lower (i.e. 0.1-0.2) and higher respectively than 0.4 (the value expected in a flat-bed boundary layer),

only converging to a value of 0.4 at the crest where the boundary layer is most fully developed. The correlation coefficient at $y/d < 0.3$ over the back, crest and separation/reattachment zone of the fixed bedload sheet were below, equivalent and above the spatial average respectively (box A in Figure 5.10iiia). Low correlation coefficients result from low frequency flow unsteadiness (e.g. 'flapping') of the turbulent shear layer and flow separation. However, near-bed ($y/d < 0.3$) values of the correlation coefficient do not fall below 0.3, indicating that flow separation is absent or intermittent, as was also found by Best and Kostaschuk (in press; $R = 0.3-0.5$ near the bed) for low-angle dunes. These low frequency events typically increase both components of turbulence intensity, without a similar rise in mean Reynolds stress (Nelson *et al.*, 1993), thereby reducing the correlation coefficient. Reynolds stress is not significantly affected by these low frequency events as enhanced downstream and vertical velocity fluctuations are poorly correlated. The boundary layer is greatly influenced by the presence of the overlying turbulent wake region.

Figure 5.10: The correlation coefficient of Reynolds stress, R , plotted against dimensionless flow depth for specific bedform regions. Highlighted area is discussed in the text.

i) Mobile bed conditions



ii) Fixed bed conditions

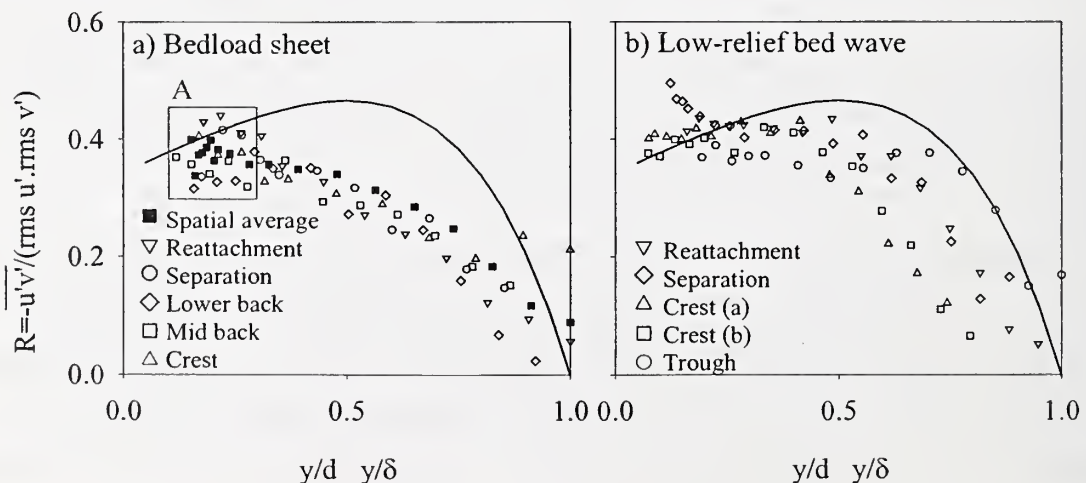
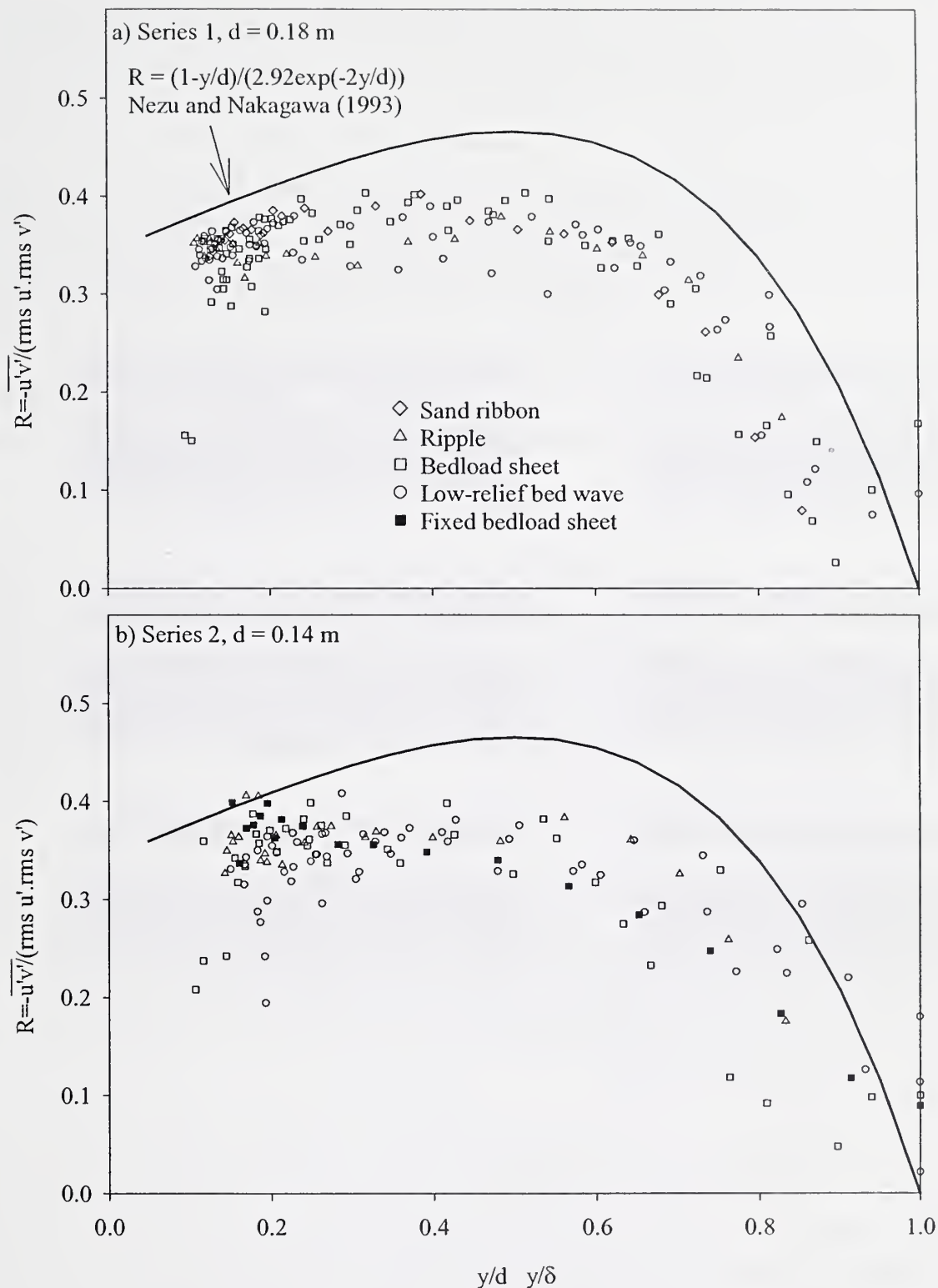


Figure 5.11: The spatially-averaged correlation coefficient of Reynolds stress against dimensionless flow depth.



5.3.4 Quadrant analysis

The salient features of quadrant analysis are considered separately for the fixed bedload sheet and fixed low-relief bed wave. Firstly, contour maps are presented in Figure 5.12 and 5.14, which illustrate the normalised number of quadrant events (i.e. the number of events in a given quadrant above a threshold value, expressed as a percentage of the total number of events). In this study, contour maps with a range of threshold values ($H = 0-6$) were produced and compared in order to identify the salient characteristics. The following discussion is based on a threshold of 2 for all quadrant events, and in addition a threshold of 5 and 3 for quadrant 2 and 4 events respectively, which incorporate all the main observations. The threshold value employed impacts upon the distribution of the normalised number of quadrant events. Furthermore, contour maps of the distribution of velocity and turbulence parameters are subject to uncertainty (e.g. method of interpolation, contour interval, distance between measurements and the period of measurement), and only broad time-averaged trends can be considered to be valid.

Figures 5.13 and 5.15 demonstrate the fractional contribution of each quadrant to $-\overline{u'v'}$ at different locations (highlighted in Figures 4.4 and 4.6) within the flow field over a range of thresholds. The points are selected to allow comparison of the turbulent flow structure in the shear layer, expansion zone and free stream. At a threshold value of 0, the fractional contributions are similar in magnitude to those previously obtained from flume experiments and field investigation of turbulent boundary layers (Bennett and Best, 1995).

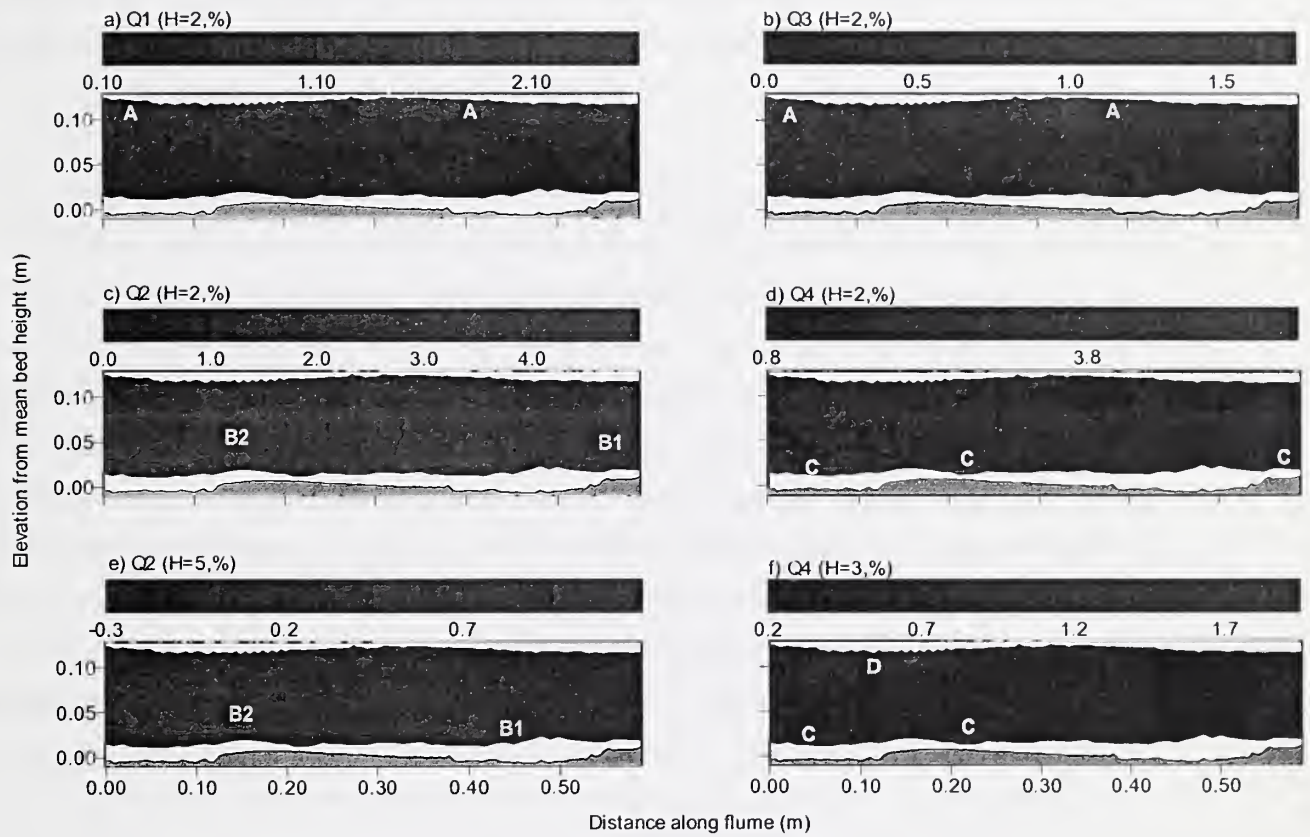
5.3.4.1 Bedload sheets

The percentage occurrence of quadrant 1 and 3 events increases towards the water surface (Figure 5.12a and b). Zones of maximum occurrence of quadrant 1 and 3 events are elevated (approximately 1.5 %) downstream of the crests (occurring at 0.13 and 0.56 m along the flume) near the flow surface (Figure 5.12a and b, highlighted by the letter A), as also found in the turbulence measurements taken over fixed dunes by Bennett and Best (1995).

The occurrence of quadrant 2 events is plotted at both a threshold of 2 and 5 in Figure 5.12c and e respectively. Elevated values ($> 4\%$ and 0.7% at a threshold of 2 and 5 respectively) form elongated bands of high occurrence in the flow field (highlighted by B1 and B2 in Figure 5.12), which are characteristic of turbulent shear layers. A high percentage occurrence of quadrant 2 events, attributed to shearing, has been previously identified from the crests of fixed ripples and dunes (Bennett and Best, 1995, 1996). Since it was not possible to take velocity and turbulence measurements within approximately 10 mm of the fixed bedload sheet surface, it is difficult to pinpoint the exact locations on

the bed where the turbulent shear layers are initiated. Furthermore, the bedload sheet in the test section was only ~ 0.4 m long, and the areal extent of the shear layer is dependent on the threshold and interpolation procedure employed. During the experimental program, flow separation was visually observed from the coarse gravel grains (up to 32 mm in diameter), which predominately rest in the trough region.

Figure 5.12: Maps of the spatial distribution of the normalised number (%) of quadrant events over fixed bedload sheets. Flow is from right to left. Q and H represent the quadrant and threshold respectively. The bedload sheets are shown in grey. No measurements were obtained in the white regions. Elevated values (highlighted by letters) are discussed in the text.



At a threshold of 5, elevated values ($> 0.7\%$) of the occurrence of quadrant 2 events are initially observed at approximately 0.02 m above the mean bed height and 0.45 m along the flume i.e. over the trough (B1 on Figure 5.12e). However, downstream, the shear layer is initiated over the crest (approximately 0.03 m above the mean bed height and 0.15 m along the flume i.e. B2 on Figure 5.12e). Furthermore, at a threshold of 2, high values ($> 4\%$) of the normalised number of quadrant 2 events first appear above the bedform crests (approximately 0.03 m above the mean bed height, and 0.13 and 0.56 m along the flume i.e. B1 and B2 on Figure 5.12c). The turbulent flow takes time to adjust to changes in roughness and morphology (Antonia and Luxton, 1971, 1972), and consequently upstream conditions affect the downstream turbulent flow structure, resulting in a complex turbulence signal even when the sediment is immobile. Furthermore, the location of turbulent structures varies over time (e.g. shear layer flapping; Roden, 1998), and their occurrence may be intermittent (Kostaschuk and Church, 1993; Lapointe, 1996).

The high normalised number of quadrant 4 events ($> 2.8\%$ at $H = 2$, $> 0.7\%$ at $H = 3$, represented by the letter C in Figure 5.12d and f) can be identified near the bed in the trough region (0.00-0.13 m along the flume), upper stoss (0.17-0.25 m along) and upstream crest (0.53-0.60 m). At a threshold of 3, values for the occurrence of quadrant 4 events also exceed 0.7% at the water surface in the vicinity of the downstream bedform crest (letter D in Figure 5.12f). Near the sediment boundary (< 0.03 m above the bed), elevated values of the normalised number of quadrant 4 events (C) are related to the shear layers identified in Figure 5.12c (B), and occur in-between the sediment bed and the shear layer (e.g. 0.00-0.13 m along the flume). Bennett and Best (1995, 1996) also observed that quadrant 4 events demonstrate the greatest percentage occurrence near the bed over fixed ripples and dunes, specifically in the flow separation region. The high normalised number of quadrant 4 events at around 0.17-0.25 m along the flume is associated with shearing from a coarse clast (previously identified from the skewness of the velocity components, Figure 5.2c and d) located approximately 0.25 m along the flume (Plate 5.1). However, the turbulent shear layer generated by the clast is not detected in the present contour maps of the distribution of the normalised number of quadrant 2 events at a threshold of 2 or 5. Quadrant 4 events highlight the transfer of high velocity fluid towards the bed from the shear layer, and consequently have been associated with entrainment and bedload transport (Williams *et al.*, 1989a, b; Nelson *et al.*, 1995).

Typically, quadrant 2 events dominate the fractional contribution to $-\overline{u'v'}$ at all thresholds (dark blue lines in Figure 5.13). At $H = 0$ quadrant 2 events contribute approximately 1, 0.8 and 0.7 to Reynolds stress in the free stream, shear layer and separation zone respectively. In the shear layer and free stream (Figure 5.13a-c and g-i) quadrant 2 events continue to make a contribution at higher thresholds (up to H

~ 10) compared with locations in the expansion/separation zone downstream of the bedform crest and coarse, isolated particles (Figure 5.13d-f, up to $H \sim 7$). Noise in the LDA signal may partially account for contributions to Reynolds stress at higher thresholds. However, Appendix I illustrates that the error is typically less than 1 % at a threshold of 2. The suspension of sediment and the production of Reynolds stress are thought to be significantly influenced by low frequency, high magnitude quadrant 2 events (i.e. $H > 6$). Lapointe (1996) notes that energetic quadrant 2 events occur for 1-5 % of the time, but account for 20-90 % of sand suspension episodes and exchange of turbulent momentum. Bennett and Best (1995) propose possible sources for these infrequent, energetic quadrant 2 events. Firstly, they may be produced by variations in the shear layer velocity gradient over time. Alternatively, their formation may relate to the interaction and pairing of vortices. Finally, 'flapping' of the shear layer at a reduced frequency was suggested as a possible origin for these rare, high energy quadrant 2 events. Furthermore, Lapointe (1996) determined that the greatest sand suspension events occurred more frequently under deeper flow conditions. The degree of flow separation, Reynolds stress and velocity differential across the shear layer, are influenced by bedform steepness and relative roughness (i.e. ratio of bedform height to flow depth), which in turn impacts on the intensity of shearing, and consequently both the intensity and frequency of vortex shedding (McLean *et al.*, 1994).

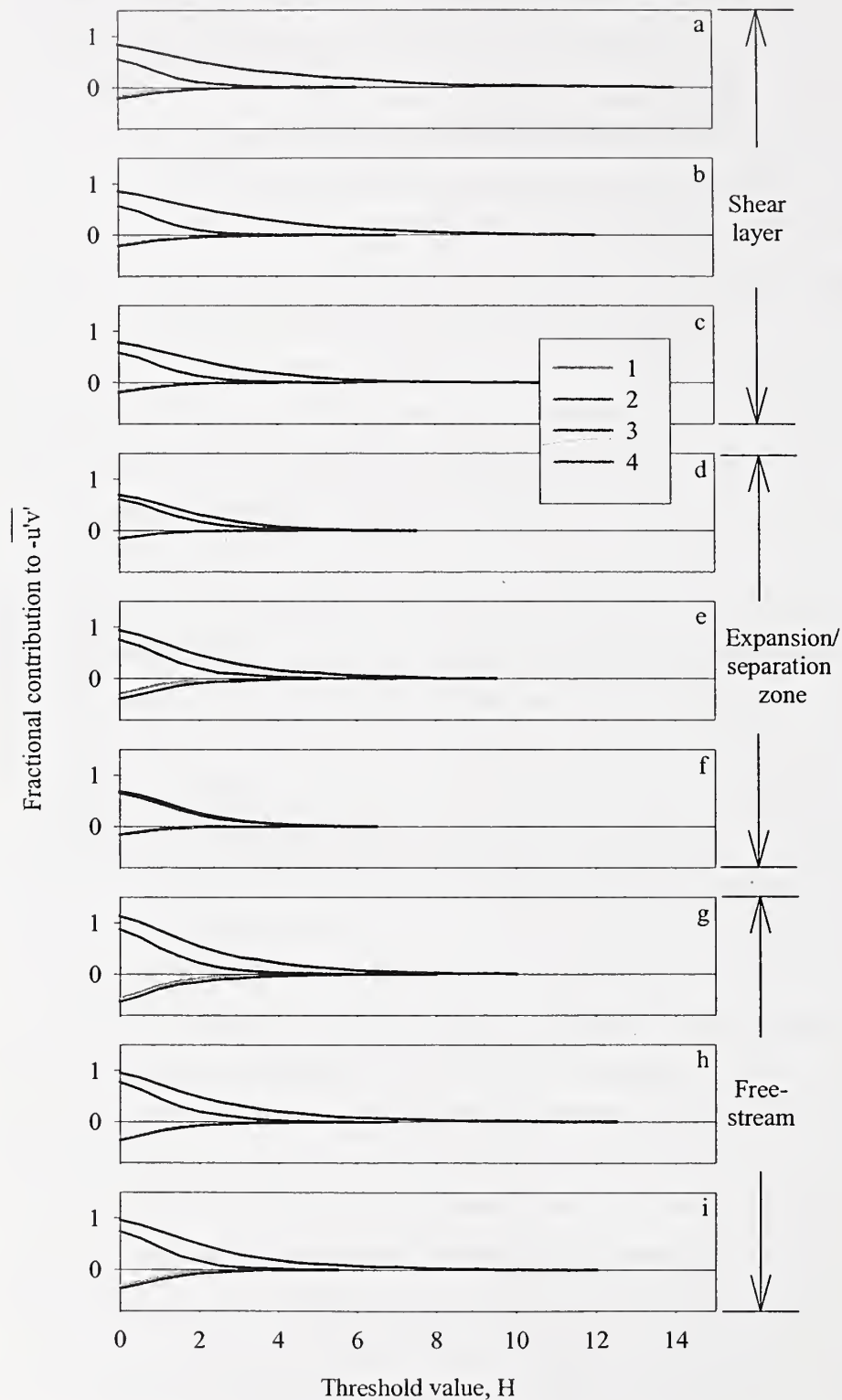
The fractional contribution to $-\overline{u'v'}$ from quadrant 4 events was most similar in magnitude to that from quadrant 2 events in the expansion/separation zones (located in the lee of bedform crests and isolated coarse particles; Figure 5.13d and f), due to the reduction in contributions from quadrant 2 events. The fractional contribution of quadrant 4 events is approximately 0.6 at $H = 0$ in the shear layer and expansion/separation zone, and rises to around 0.8 in the free stream. Similar contributions to $-\overline{u'v'}$ (> -0.2) are made by quadrant 1 and 3 events at all the 'characteristic' points shown in Figure 5.13, and above a threshold of 3 contributions are virtually zero.

5.3.4.2 Low-relief bed waves

The occurrence of quadrant 1 and 3 events rises towards the water surface, with peaks downstream of the bedform crest where the flow expands (Figure 5.14a and b, highlighted by the letter A). The same trend was found over fixed dunes in the experiments of Bennett and Best (1995). A band of high percentage occurrence of quadrant 2 events is apparent at both a threshold of 2 and 5 (Figure 5.14c and e, shown in red), which follows the curvature of the water surface, causing the values along the back of the bedform (0.4-0.6 m along the flume, $> 2.8\%$ at $H = 2$) to be elevated compared with those in the trough region (0.0-0.3 m along the flume, $< 2.8\%$ at $H = 2$). A similar mid-depth region dominated by high magnitude quadrant 2 events has been illustrated in flat bed flows (Willmarth and Lu, 1974). High magnitude quadrant 2 events can advect from the near-bed region into the outer flow, growing in

magnitude compared with the other quadrants due to the coalescence of vortices (Bennett and Best, 1996).

Figure 5.13: Fractional contribution of each quadrant to $\overline{-u'v'}$ over a range of thresholds. The location of each point over the bedload sheet is shown in Figure 4.4.



At a threshold of 5, a narrow zone of high occurrence can be identified ($> 0.4\%$, letter B in Figure 5.14e), which extends from the crest (0.3 m along the flume, B'), rising downstream and amalgamating with the main band of elevated values approximately 0.05 m along the flume and 0.05 m above the mean bed height i.e. B" in Figure 5.14e. This feature (B' to B" Figure 5.14e) confirms the development of a shear layer from the low-relief bed wave crest, which was earlier identified from the spatial distribution of skewness of the vertical velocity component (Figure 5.3d). Turbulent shear layers, identified by an elevated occurrence of quadrant 2 events, have also been observed to be developed from the crests of fixed ripples and dunes (Bennett and Best, 1995, 1996). A high normalised number of quadrant 4 events at a threshold of 2 and 3 (Figure 5.14d and f, > 3.5 at $H = 2$, > 1 at $H = 3$, represented by the letter C) extends from the change in slope in the crestal platform, and occurs throughout the trough region (i.e. 0.00-0.35 m along the flume), underlying the shear layer which develops from the crestal region of the low-relief bed wave. Elevated values of the normalised number of quadrant 4 events were also observed in the flow separation region over fixed ripples and dunes (Bennett and Best, 1995, 1996). The increased occurrence of quadrant 4 events highlights the transfer of relatively high velocity fluid along the shear layer towards the bed, associated with bedload entrainment and transport (Drake *et al.*, 1988; Williams *et al.*, 1989b; Nelson *et al.*, 1995). Fluid and momentum must be transferred to the area of flow separation and reattachment in order to counteract the effects of flow separation in the bedform lee and the removal of fluid by quadrant 2 events, thereby maintaining continuity.

Fractional contributions to $-\overline{u'v'}$ from quadrant 1 and 3 events are similar at all points in the flow (approximately -0.2 at $H = 0$), with little being added over a threshold of 3 (Figure 5.15). Similar findings were reported in Section 5.3.4.1 for the turbulent flow field over the fixed bedload sheets. The only exception occurs for points located within the high shear zone previously identified in the free stream (quadrant 2 occurrence $> 3.8\%$ at $H = 2$, Figure 5.14e), where fractional contributions from quadrant 1 and 3 are around -0.5 at $H = 0$ (Figure 5.15g and i).

At all locations and thresholds considered in the flow field over a low-relief bed wave, quadrant 2 events dominate the fractional contribution to $-\overline{u'v'}$ (Figure 5.15). However, quadrant 4 events almost equal quadrant 2 events with respect to fractional contributions to $-\overline{u'v'}$ (approximately 0.6 at $H = 0$) in the flow expansion zone downstream of the low-relief bed wave crest (Figure 5.15d and e). Quadrant 2 events contribute to $-\overline{u'v'}$ at higher threshold values in shear zones ($H \sim 12$, Figure 5.15a-c, g and i) compared with the expansion zone downstream of the bedform crest ($H \sim 6$, Figure 5.15d and e). In the free stream, points within the band of high percentage occurrence of quadrant 2 events ($> 3.8\%$ at $H = 2$, Figure 5.14c) also exhibit high fractional contributions (approximately 1.2 at $H = 0$, Figure 5.15g and

i), whereas outside this zone contributions from quadrant 2 events drop to around 0.8 at $H = 0$ (Figure 5.15a-f and h).

Figure 5.14: Maps of the spatial distribution of the normalised number (%) of quadrant events over a fixed low-relief bed wave. Flow is from right to left. Q and H represent the quadrant and threshold respectively. The bed wave is highlighted in grey. No measurements were possible in the white regions. Elevated values (highlighted by letters) are discussed in the text.

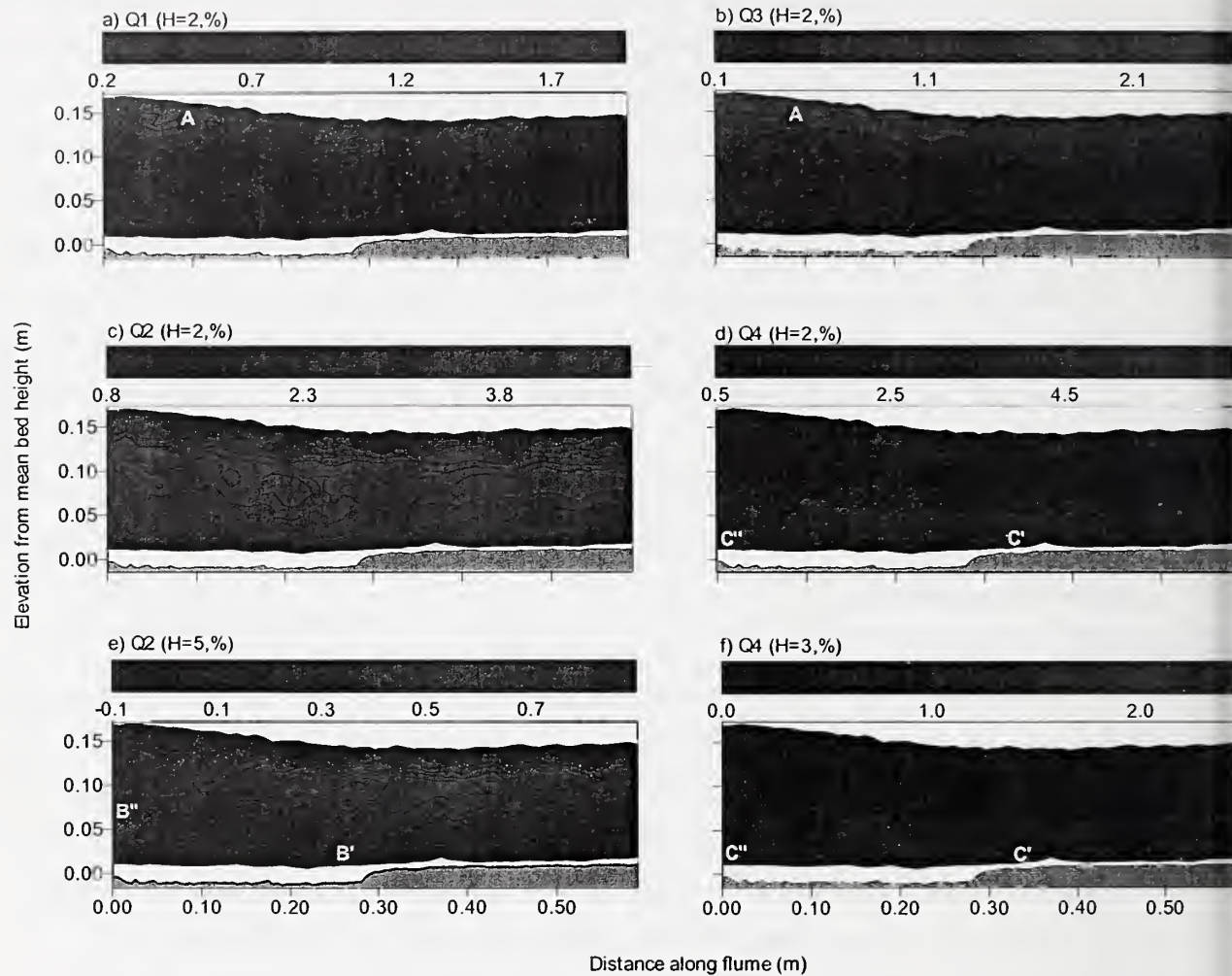
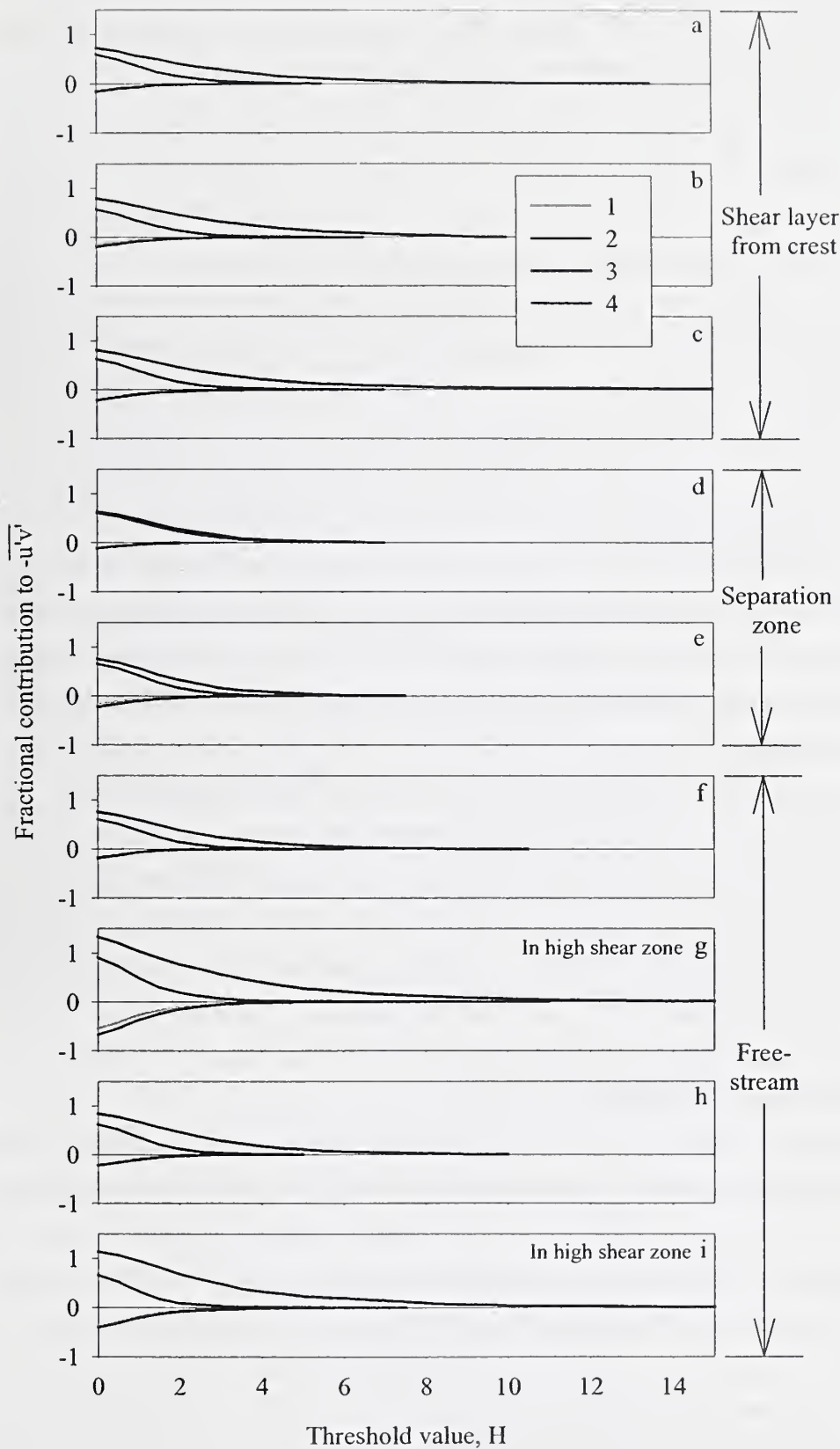


Figure 5.15: Fractional contribution of each quadrant to $-\overline{u'v'}$ over a range of thresholds. The location of each point over the low-relief bed wave is shown in Figure 4.6.



5.3.4.3 General trends for quadrant events

Quadrant 2 and 4 events dominate the production of turbulent energy and Reynolds stress over both smooth and rough beds (Grass, 1971), although over a rough boundary both events are stronger and more frequent. However, Reynolds stress production near the boundary over smooth beds is dominated by quadrant 2 events, whilst quadrant 4 events are most effective over rough boundaries (Nakagawa and Nezu, 1977; Krogstad *et al.*, 1992). Bennett *et al.* (1998) note that suspended sediment suppresses the magnitude of quadrant 2 events relative to quadrant 4 events near the bed where concentrations are highest. At a threshold of zero, Nikora and Goring (2000, gravel bed channel, $D_{50} = 12.5\text{-}16.2$ mm, no bedforms) found quadrant 2 and 4 events to persist for 60-70 % of the time in the lower flow region over a rough bed ($y/d < 0.6$). However, above $y/d > 0.6$ the duration of quadrant 2 and 4 events decreased, although their magnitude increased. The duration of quadrant 2 and 4 events were comparable near the rough bed, but since quadrant 4 exhibited a greater magnitude they dominate the contributions to turbulent energy and Reynolds stress in this region. Roy *et al.* (1996) also established that quadrant 4 events dominate shear stress production near a gravel-bed, and indicate that quadrant 2 events are most important in the outer flow region. In the present experiments measurements could not be taken very close to the bed, however, quadrant 2 events are confirmed to dominate the contribution to Reynolds stress in the outer flow (Figures 5.13 and 5.15). The measurements nearest to the rough bed were obtained in the flow separation/deceleration zone above the coarse bedform trough, where the contributions of quadrant 2 and 4 events were found to be comparable (Figures 5.13d-f and 5.15d and e). Williams *et al.* (1989a) took measurements of turbulence over a bimodal gravel sediment (with grain diameters ranging from 4-32 mm) which exhibited no bedforms. They found that contributions to Reynolds stress were intermittent, and that bedload (gravel) and suspended (sand) sediment transport were associated principally with quadrant 4 and 2 events respectively. McLean *et al.* (1994) suggest that bedload transport may also be influenced by large quadrant 1 events, despite their negative contribution to Reynolds stress.

5.3.5 Turbulence production

The energy spectrum of turbulence describes the distribution of energy among eddies of different sizes (Anwar and Atkins, 1982). Turbulence generation occurs in the productive spectral subrange (i.e. large scale eddies), and extracts energy from the mean flow, which can also be dissipated directly near the wall. The generation of turbulence produces fluctuations from the mean velocity, which are associated with large-scale coherent eddy structures. A cascade process transfers the turbulent energy from larger to smaller eddies in the inertial spectral subrange, which eventually dissipates into heat due to the molecular viscosity in the viscous spectral subrange. Increases in Reynolds number cause the inertial subrange to widen. Nowell and Church (1979) believe that in depth-limited flows over roughness

elements, a true inertial subrange is not present due to the systematic change in the shape of the energy spectrum over the flow profile. They also concluded that the rates of turbulent energy dissipation over roughness elements are very high in comparison with other common geophysical liquid flows, and yet correspond to the local rates of turbulent energy production in open channel flow. There is excess turbulent energy near the bed where production is concentrated, and a deficit near the free surface. However, with increasing distance from the boundary, turbulence becomes less anisotropic due to mixing (Roy *et al.*, 1996).

5.3.5.1 Classical boundary layer bursting (*hydraulically smooth bed*)

Over a smooth wall, turbulent energy and Reynolds stress are generated by the bursting cycle near the bed, consisting of multiple ejection and sweep events. The dynamic cycle of ejection and sweep events is directly associated with vortical structures which extend at 45° from the near-bed flow field, and are characterised by a horseshoe geometry, although this may be distorted and fragmented (Grass, 1971; Head and Bandyopadhyay, 1981; Falco, 1991; Grass *et al.*, 1991; Smith *et al.*, 1991). The footprints of these vortices are represented in the near-bed flow field by elongated, alternate high and low velocity streaks. These streaks reflect the scale of the vortices, and appear to have a universal spacing, λ^+ , of approximately 100 ($\lambda^+ = \lambda U_* / \nu \approx 100$, where λ is actual streak spacing, U_* is shear velocity and ν is viscosity; Grass, 1971; Defina, 1996). The transverse spacing between turbulent structures increases in a linear manner away from the bed (Defina, 1996), indicating that the longitudinal structures generating the streaks coalesce away from the boundary. Turbulent vortices entrain and transport fluid, momentum and sediment from near the bed into the outer flow. Within a vortex exist strong internal shear layers which can generate larger coherent turbulent flow structures downstream (Defina, 1996; Smith, 1996). The shedding of eddies from any shear layer enables the vortices to extract large amounts of energy from the mean flow, which is therefore retarded. Intense rotation in the vortices leads to the generation of secondary and subsidiary vortices, and the formation of vortex groups (Robinson, 1990; Smith, 1996). Accumulations of vortices enables the return flow from the sweep event to increase its magnitude and area of influence, which has important implications for sediment entrainment (e.g. patchy bedload movement, Drake *et al.*, 1988). Our understanding of vortex development and growth is complicated by their small scale and wide spectrum of morphologies.

Grass (1971, 1996) observed bursting over both smooth and rough (a layer of touching particles, with a thickness of one grain diameter (up to 12 mm)) boundaries. Over a rough bed, the low-speed streaks scale directly with the roughness element size, rather than the viscous length scale in the case of a smooth boundary. Low speed streaks have reduced coherence in the downstream direction over coarser beds. The structure of the turbulent boundary layer is critically influenced by relative roughness, the

ratio of clast size to viscous sublayer thickness and the density and arrangement of grains, although many questions remain regarding the actual effects of these interactions (Best, 1993).

5.3.5.2 Eddy shedding and flow separation (*hydraulically rough bed*)

Over a smooth bed, turbulence is generated in the lower part of the wall region ($y^+ = yU_* / \nu < 50$). However, this region is modified or destroyed by appreciable grain and form roughness (Grass, 1971; Leeder, 1980), which create their own flow field (Brayshaw *et al.*, 1983; Clifford *et al.*, 1992; Nelson *et al.*, 1993; McLean *et al.*, 1994; Best, 1996; Buffin-Bélanger and Roy, 1998), influencing the turbulent energy and pressure diffusion terms near the bed, and other nearby roughness elements (i.e. mutual interference). The turbulence structure is also modified by the presence of mobile sediment (Best, 1993; Best *et al.*, 1997; Carboneau and Bergeron, 2000). Discontinuities in the bed elevation cause the flow to either expand or contract, causing deceleration and acceleration in different flow regions, which modifies the velocity gradient. Consequently, additional methods of turbulence production need to be evoked for hydraulically rough flows e.g. flow separation and eddy shedding. Kelvin-Helmholtz instabilities develop along regions of strong shear, from which turbulent eddies can be shed (Tritton, 1988). Where flow separation occurs (e.g. over a coarse clast or bedform), a steep velocity gradient is formed between the retarded flow in the lee of the roughness element, and the accelerated flow above and around the obstacle. Turbulent energy is generated along this shear layer, and dissipation occurs mainly in the area of flow recirculation. However, the advection of low velocity fluid from the lee of obstacles can also generate turbulence (Kirkbride, 1994; Roy *et al.*, 1996). The generation of wakes is associated with excess turbulence production and the invalidity of the log defect law (Nowell and Church, 1979), the latter being demonstrated in Section 4.3.4. A second vortex system develops at the front and sides of protruding clasts, which involves the roll-down of the boundary layer in front of the grain (often associated with bed erosion), and generation of a horseshoe shaped vortex. Complex interactions occur between the upstream and flank vortices and eddy shedding from the shear layer (Acarlar and Smith, 1987a, b).

5.3.5.3 Turbulence production over bedforms developed in a bimodal sand-gravel mixture

Turbulence production is concentrated near the bed ($y/d < 0.3$), dropping off exponentially as the water surface is approached (Figure 5.16). As flow velocity increases, and the sediment bed transforms through the spectrum of bedforms from sand ribbons to low-relief bed waves, the level of turbulence generation at the bed rises in a non-linear fashion throughout the flow depth (Figure 5.16 and 5.17). For example, at a flow depth of 0.18 m (Figure 5.16a), and $y/d = 0.2$, a sand ribbon, ripple, bedload sheet and low-relief bed wave bed configuration are associated with a turbulence production of approximately 0.005, 0.0075, 0.01-0.025, 0.02-0.04 Pa s^{-1} respectively. The production of turbulence is greater when the flow depth is lowered e.g. at a flow depth of 0.14 m (Figure 5.16b) the turbulence production at y/d

$= 0.2$ for ripples, bedload sheets and low-relief bed waves is approximately 0.015, 0.02-0.03 and 0.025-0.16 Pa s^{-1} . Under lower flow depth conditions, the mean velocity is increased for a given discharge, enhancing velocity gradients over obstacles to the flow (e.g. coarse grains and bedforms) and increasing the magnitude of Kelvin-Helmholtz instabilities, which are a dominant source of turbulence. The mobile and fixed bedload sheet exhibit a very similar distribution of turbulence production, both with a value of 0.02 Pa s^{-1} at $y/d = 0.2$ ($y \approx 30 \text{ mm}$) in Figure 5.17 and 5.16b, resulting from wakes generated by grain and form roughness. However, higher in the flow column (i.e. $y/d = 0.3$ and 0.4, $y \approx 40$ and 55 mm; Figure 5.17) turbulence production is reduced over the fixed bedload sheet compared with the mobile example due to the lack of sediment in transport (e.g. overpassing coarse clasts), which generates additional turbulence at greater heights above the mobile bed (Wiberg and Rubin, 1989).

Figure 5.16: Spatially-averaged turbulence generation, T , plotted against normalised flow depth.

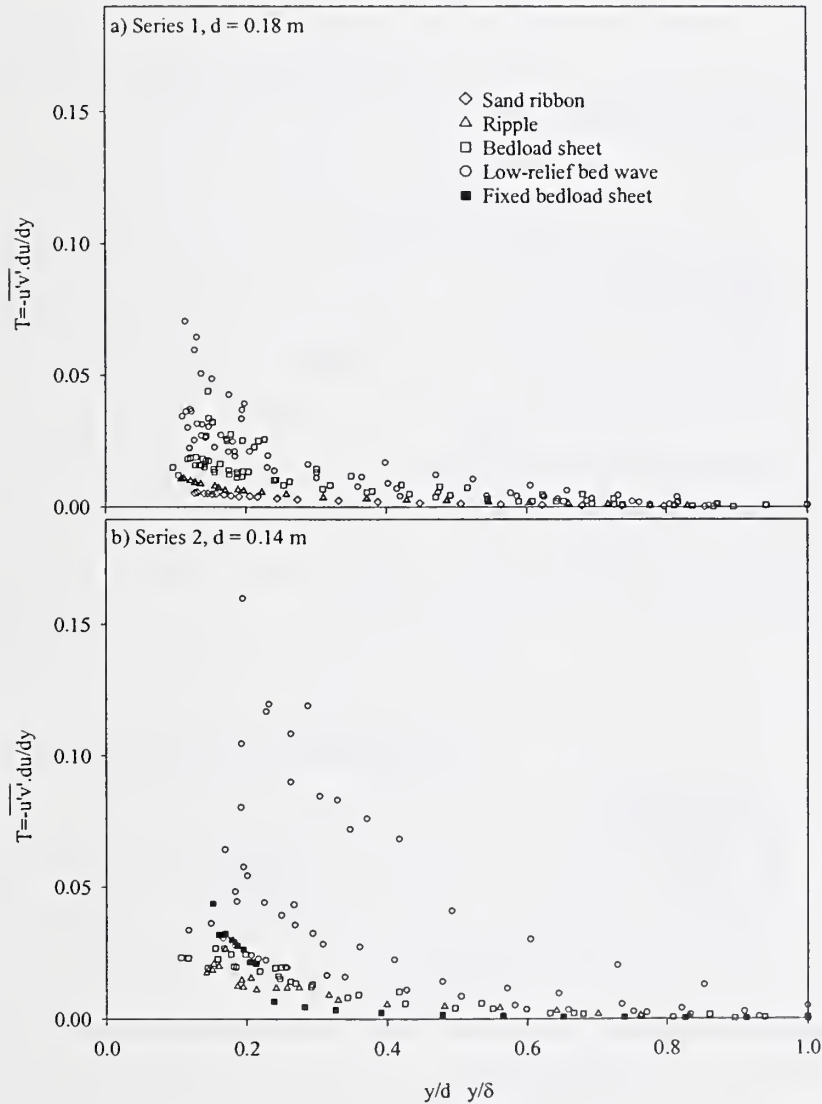


Figure 5.17: Spatially-averaged turbulence production plotted against depth averaged velocity.

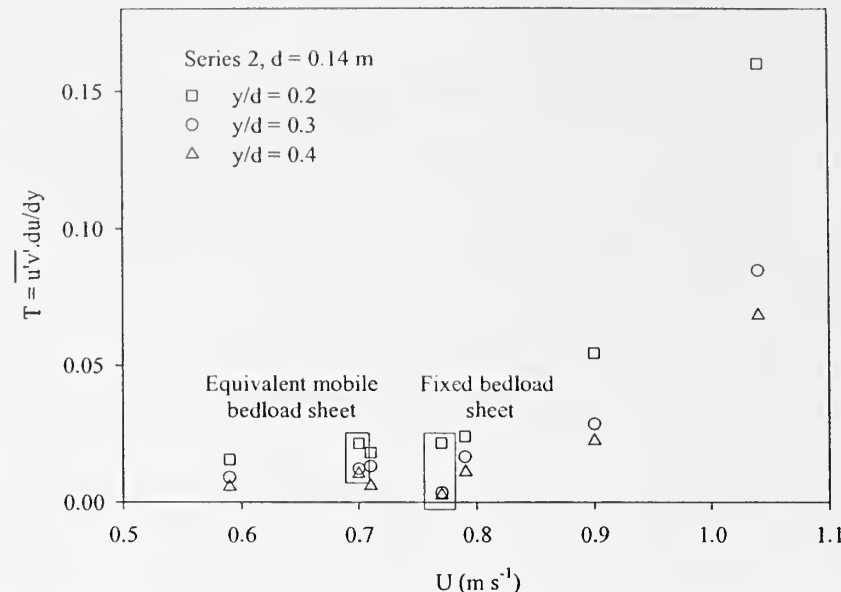
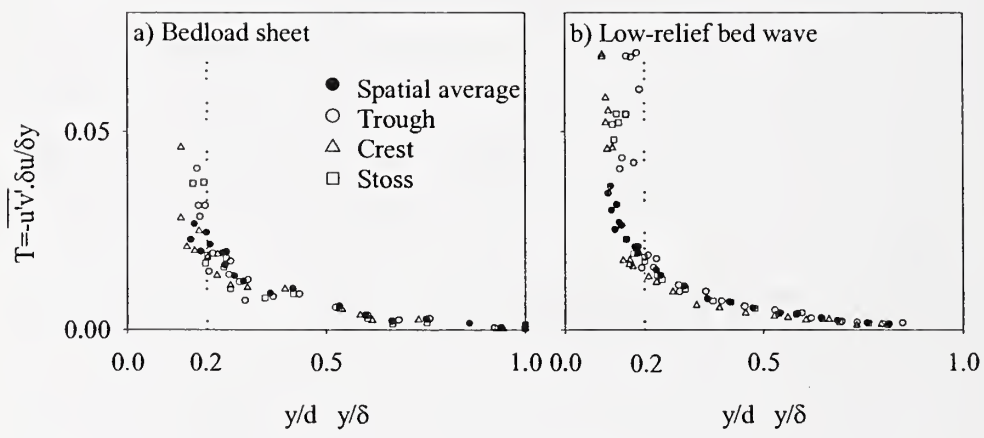


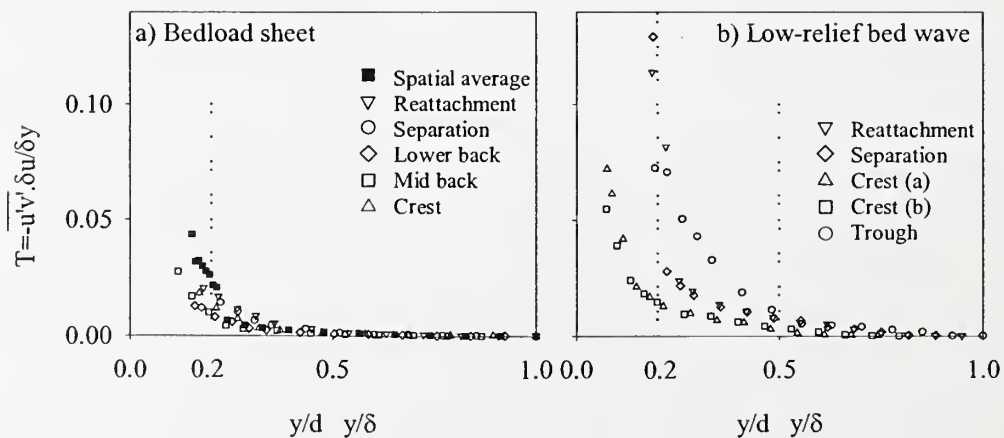
Figure 5.18: Turbulence production plotted against dimensionless flow depth for specific bedform regions. Dotted lines delimit areas discussed in the text.

i) Mobile bed conditions



ii) Fixed bed

conditions



Above $y/d = 0.2$ it is impossible to distinguish between the amount of turbulence production at specific regions over an individual bedform (Figure 5.18), with the exception of the fixed low-relief bed wave (Figure 5.18iib). Turbulence measurements were possible closer to the sediment bed over the finer grained crest and upper stoss; consequently, values are available for these regions at lower y/d values than for measurements over the coarser trough area, thus hindering any comparison of turbulence generation when $y/d < 0.2$. Furthermore, below $y/d = 0.2$ values of turbulence intensity increase rapidly towards the bed, impeding accurate comparisons. Moreover, in the calculation of y/d for the mobile bed runs, a spatially-averaged flow depth was employed. In the fixed low-relief bed wave example (Figure 5.18iib, $0.2 < y/d < 0.5$), the greatest turbulence production is evident in the trough ($\sim 0.07 \text{ Pa s}^{-1}$ at $y/d = 2$), reduced at separation and reattachment ($\sim 0.03 \text{ Pa s}^{-1}$), and the lowest over the crest ($\sim 0.01 \text{ Pa s}^{-1}$).

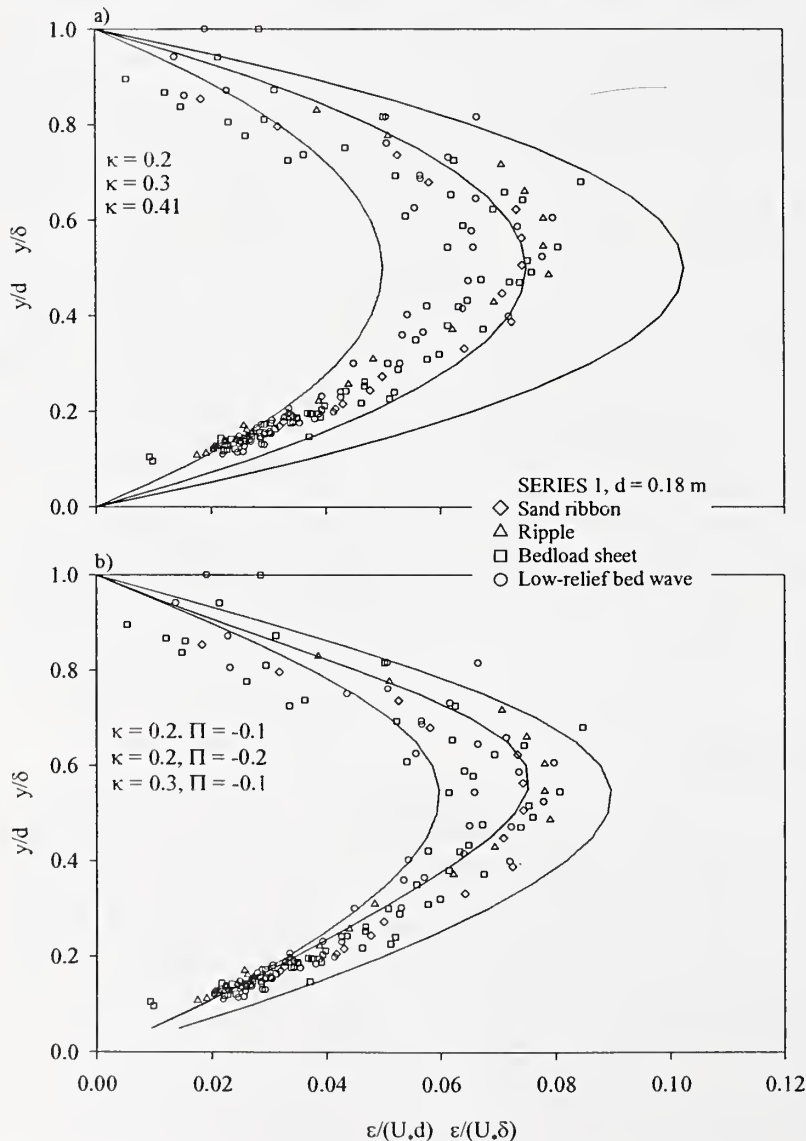
Turbulence production is greatest in the trough region due to the presence of coarse clasts capable of shedding eddies, and the dominant occurrence of a shear layer initiated from the upstream crest, which was previously identified from contour maps of the skewness of the velocity components and quadrant analysis (Figure 5.3 and 5.14). Since the magnitude of the wake is related to the size of the grain it is generated from (Nowell and Church, 1979), the tendency for the grain diameter to be greater in the trough will result in more turbulent energy being produced in this zone, although large grains may be temporarily be located elsewhere. The shear layer generated from the low-relief bed wave crest is damped in the streamwise direction due to topographic acceleration and turbulence dissipation. Furthermore, a boundary layer develops downstream of the reattachment point, causing turbulence production to be less effective over the stoss and crestral platform. The turbulence production measured by Carling *et al.*, (2000b) in the wake flow over sand dunes in the River Rhine, was one order of magnitude greater than over the stoss. Since the majority of turbulence is generated in the shear layer formed at the crest i.e. it is spatially specific, flow over bedforms cannot be considered to be identical to boundary layer flow (Nelson *et al.*, 1993).

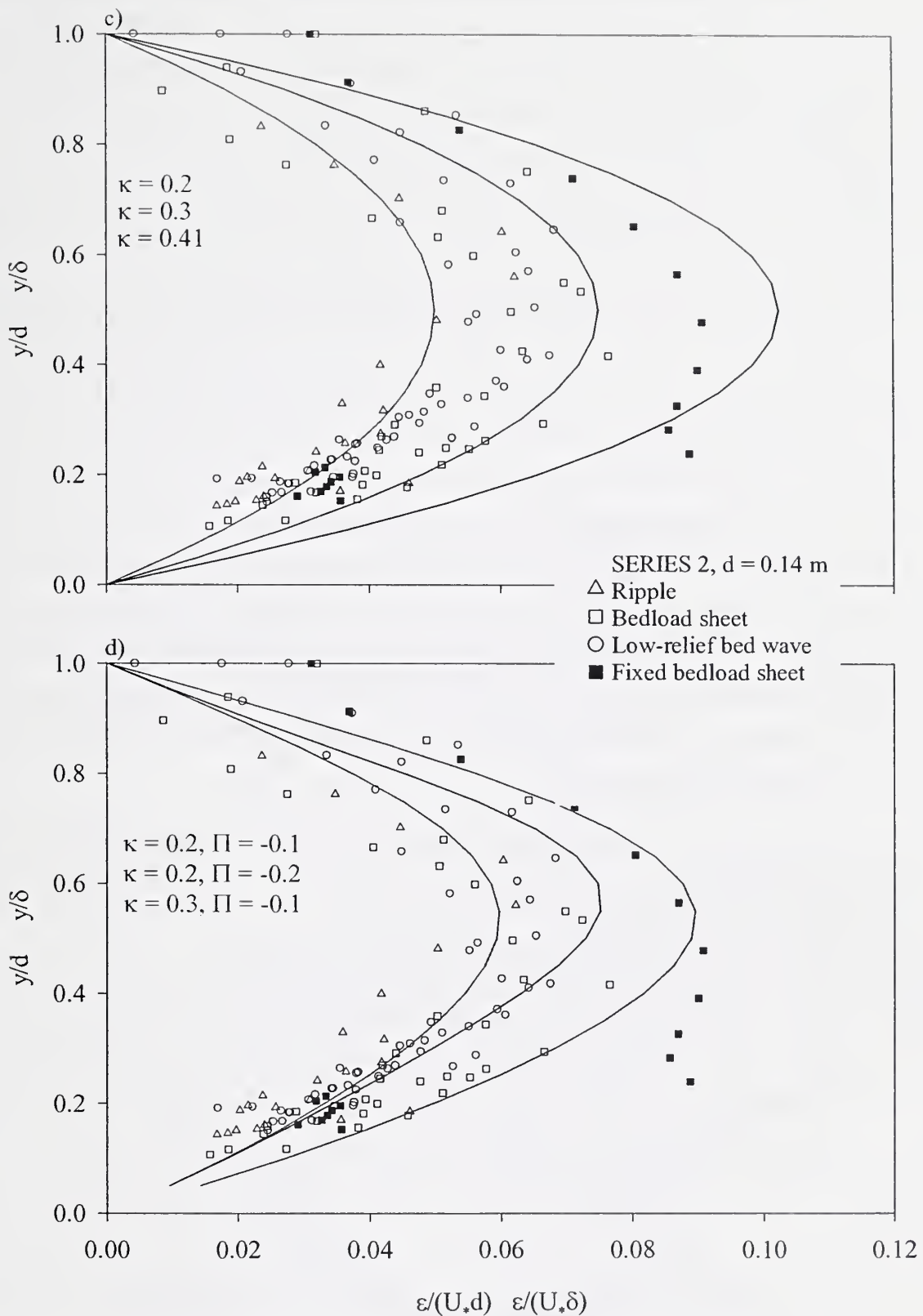
5.3.6 Kinematic eddy viscosity

In more basic models of turbulence, eddy viscosity is an important quantity used to determine the distribution of Reynolds stress (Nezu and Rodi, 1986). It is apparent from Figure 5.19 that dimensionless eddy viscosity increases away from the bed, reaching a maximum at $y/d \sim 0.55$ ($\varepsilon/(U_*d) = 0.06-0.085$ and $0.06-0.075$ when $d = 0.18$ and 0.14 m respectively) when the bed is mobile, and then diminishing towards the free surface which has a dampening effect on turbulent eddies. Large-scale turbulent structures are also damped (lower eddy viscosity) by the stretching of vortices resulting from topographic accelerations (Nelson *et al.*, 1993). Indeed, Song and Graf (1994), observed

a tendency for eddy viscosity to be reduced (damping of turbulence mixing) under accelerating flow conditions, and increased (amplified turbulence mixing) when flow decelerates. A lower flow depth enhances topographic accelerations (assuming bedform steepness remains relatively constant) and therefore accentuates turbulence dampening, reducing eddy viscosity values as noted above. The largest values of eddy viscosity (0.09 at $y/d \sim 0.5$, Figure 5.19c and d) are generated over the fixed bedload sheet, suggesting that sediment transport dampens turbulence, although it can also enhance turbulence (Vanoni, 1975; Best *et al.*, 1997). Nezu and Rodi (1986) found maximum dimensionless eddy viscosity values to range from 0.08-0.10 at $y/d \sim 0.5$ in open channel flows with smooth beds, supporting the idea that eddy viscosity is reduced by the occurrence of sediment transport.

Figure 5.19: Spatially-averaged eddy viscosity, normalised by the product of shear velocity and flow depth, plotted against dimensionless flow depth. The curves are calculated from Equation 5.3 (a and c) and Equation 5.4 (b and d) using the values of κ and Π stated.





There is considerable scatter in the values of dimensionless eddy viscosity (Figure 5.19), which increases with distance from the boundary. Near the water surface it is difficult to accurately determine

the velocity gradient, and therefore eddy viscosity. In the mid-depth region of the flow, eddy viscosity is dependent on the wake coefficient where a wake defect exists, and therefore in turn on the Reynolds number, which partly accounts for the scatter of experimental values. According to Nezu and Rodi (1986), the wake coefficient has a constant value of approximately 0.2 when the Reynolds number exceeds 100000. In the present experiments the Reynolds number varies from 71421 to 147500, and therefore the eddy viscosity is expected to show some dependence on the wake coefficient and Reynolds number. Furthermore, reduced values for the wake coefficient have been calculated for the present data set (Table 4.4). The example in Figure 5.20a demonstrates that the best fit by visual inspection for the smoothed spatially-averaged experimental data over a mobile bed (curve 1) is achieved when κ is derived from the law-of-the-wall over the whole profile, excluding any velocity defect (curve 5). The values of dimensionless eddy viscosity predicted by the defect wake law (curve 6) tend to be too large higher in the flow (i.e. $0.3 < y/d < 0.7$), in accord with the findings of Bennett *et al.* (1998) over an upper-stage plane bed. However, at specific regions over the mobile and fixed bedforms (i.e. crest, back and trough), the use of a wake coefficient (curve 6, κ and Π derived from the velocity defect-wake law for $y/d \leq 1$) can provide the best visual fit to the smoothed experimental data. The addition of a wake coefficient causes the maximum value to occur at a higher point in the flow (Nezu and Rodi, 1986) i.e. the distribution of eddy viscosity is not symmetrical about the mid-depth of the channel. The reduced κ and Π ($\kappa = 0.13-0.36$, $\Pi = -0.52$ to 0.10) values previously calculated from the velocity profiles are demonstrated to incorporate the range of eddy viscosity distributions for the present experimental runs (Figure 5.19).

Figure 5.20: Profiles of dimensionless a) eddy viscosity, ε , and b) mixing length, l , for run E (bedload sheet bed configuration).

Curve 1: Smoothed experimental data using equations 4.11 and 5.1(ε) or 4.15(l).

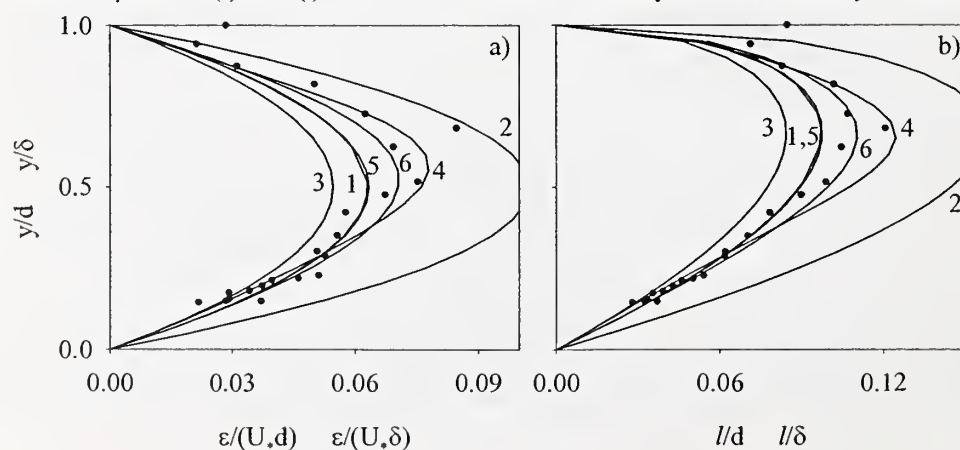
Curve 2: Equation 5.3 (ε) or 4.18 (l) with $\kappa = 0.41$.

Curve 3: Equation 5.3 (ε) or 4.18 (l) with κ derived from the law-of-the-wall for $y/d < 0.2$ using τ_R .

Curve 4: Equation 5.4 (ε) or 5.6 (l) with κ and Π derived from the velocity defect-wake law for $y/d < 0.2$ using τ_R .

Curve 5: Equation 5.3 (ε) or 4.18 (l) with κ derived from the law-of-the-wall for $y/d < 1$ using τ_R .

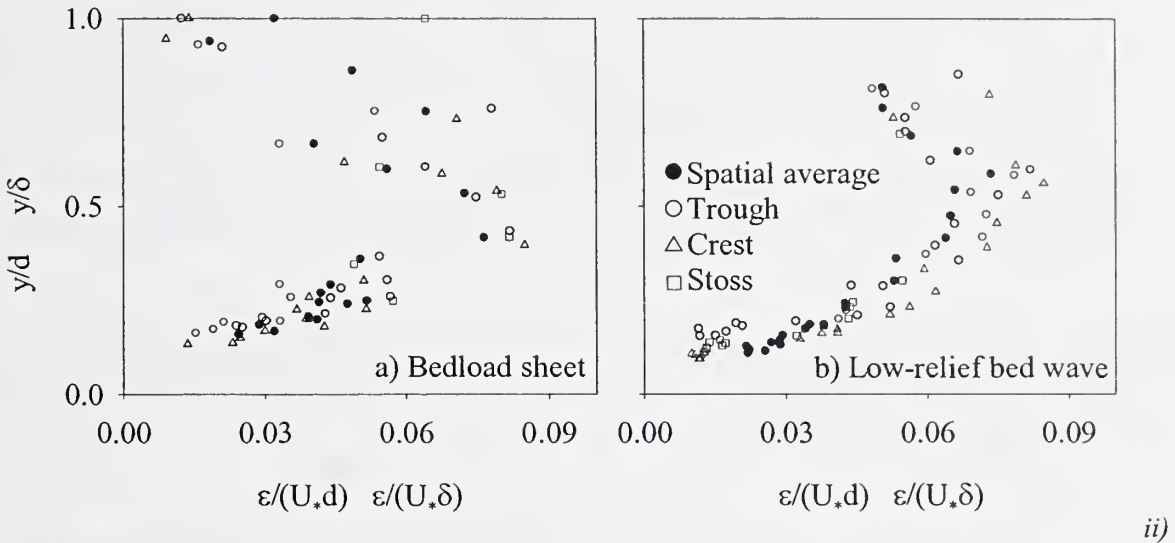
Curve 6: Equation 5.4 (ε) or 5.6 (l) with κ and Π derived from the velocity defect-wake law for $y/d < 1$ using τ_R .



It is difficult to accurately discern the changes in eddy viscosity between different locations over the bedforms due to experimental scatter, which results from the uncertainty in estimating the velocity gradient. However, in the case of the mobile and fixed low-relief bed waves, eddy viscosity is greatest over the crest (up to 0.14 and 0.085 for the fixed and mobile case respectively, as highlighted by the red symbols on Figure 5.21ib and iib (box B)). Furthermore, eddy viscosity at reattachment over the fixed bedload sheet (Figure 5.21iia, box A) falls below the spatial average. Carling *et al.* (2000b), observed eddy viscosity to be greatest in the turbulent wake over the trough of sand dunes in the River Rhine.

Figure 5.21: Normalised eddy viscosity plotted against dimensionless flow depth for specific bedform regions. The areas highlighted in red are discussed in the text.

i) Mobile bed conditions



Fixed bed conditions

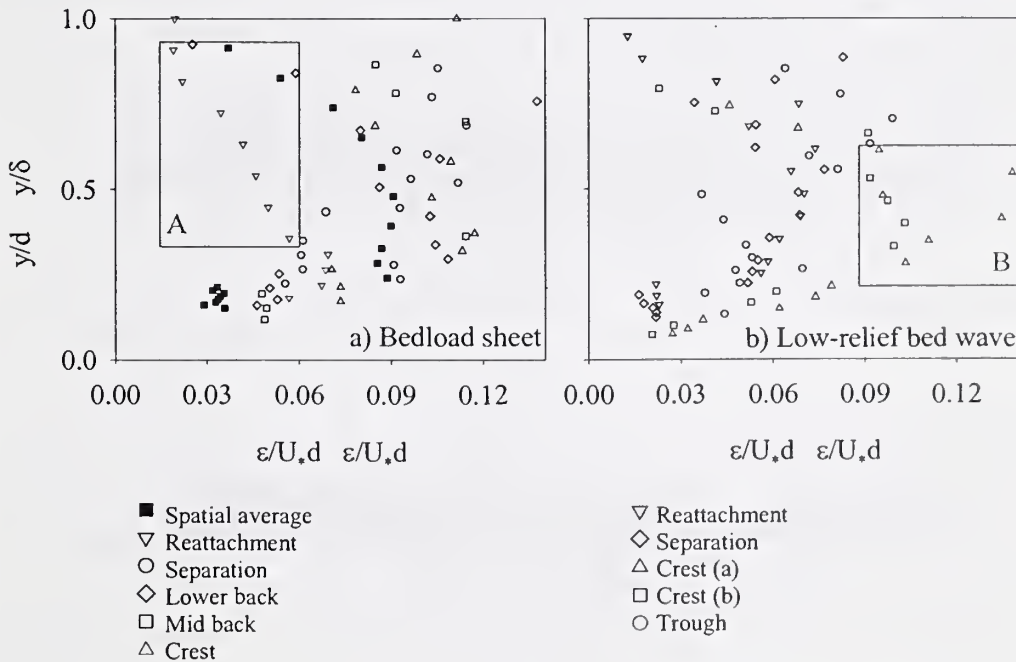
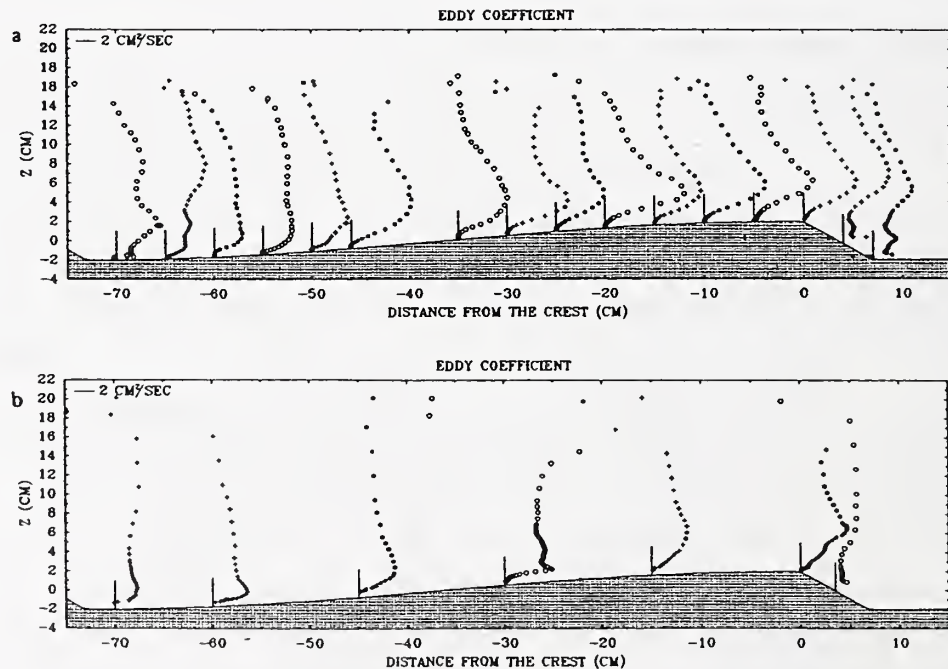


Figure 5.22 demonstrates the spatial evolution of eddy viscosity over a fixed two-dimensional bedform determined by Nelson *et al.* (1993). Eddy viscosity attains a maximum at the centre of the lowest wake region. Immediately downstream of the point of flow separation at the bedform crest, the high levels of turbulence generation cause eddy viscosity to increase (letter A in Figure 5.22a). A second maxima in eddy viscosity exists higher in the flow (letter B in Figure 5.22a), which is generated from the upstream crest, grows over the lower stoss, and then remains constant till the downstream crest, where it diminishes as the lower eddy viscosity maxima develops i.e. as soon as it overlies the shear layer generated from the downstream crest. A slight increase in shear velocity is associated with greater topographic flow deceleration near the bed, whilst Reynolds stress remains relatively constant, and accounts for the decline in the upper maximum of eddy viscosity (Nelson *et al.*, 1993). Over the upper stoss of the bedform, the eddy viscosity maxima is approximately constant since topographic acceleration is largest near the bed, reducing the shear, and Reynolds stress tends to decrease at a roughly equivalent rate. In the present experiments, flow separation typically occurs at the break in slope over the crestral platform of the low-relief bed waves i.e. upstream of the brinkpoint. Therefore, high eddy viscosities are expected over the downstream crestral region as observed in Figure 5.21 and 5.22.

Figure 5.22: The distribution of eddy viscosity over fixed two-dimensional bedforms (Nelson *et al.*, 1993). Z is the height above the mean bed level. Flow is left to right. Peaks in eddy viscosity are highlighted by points A and B.



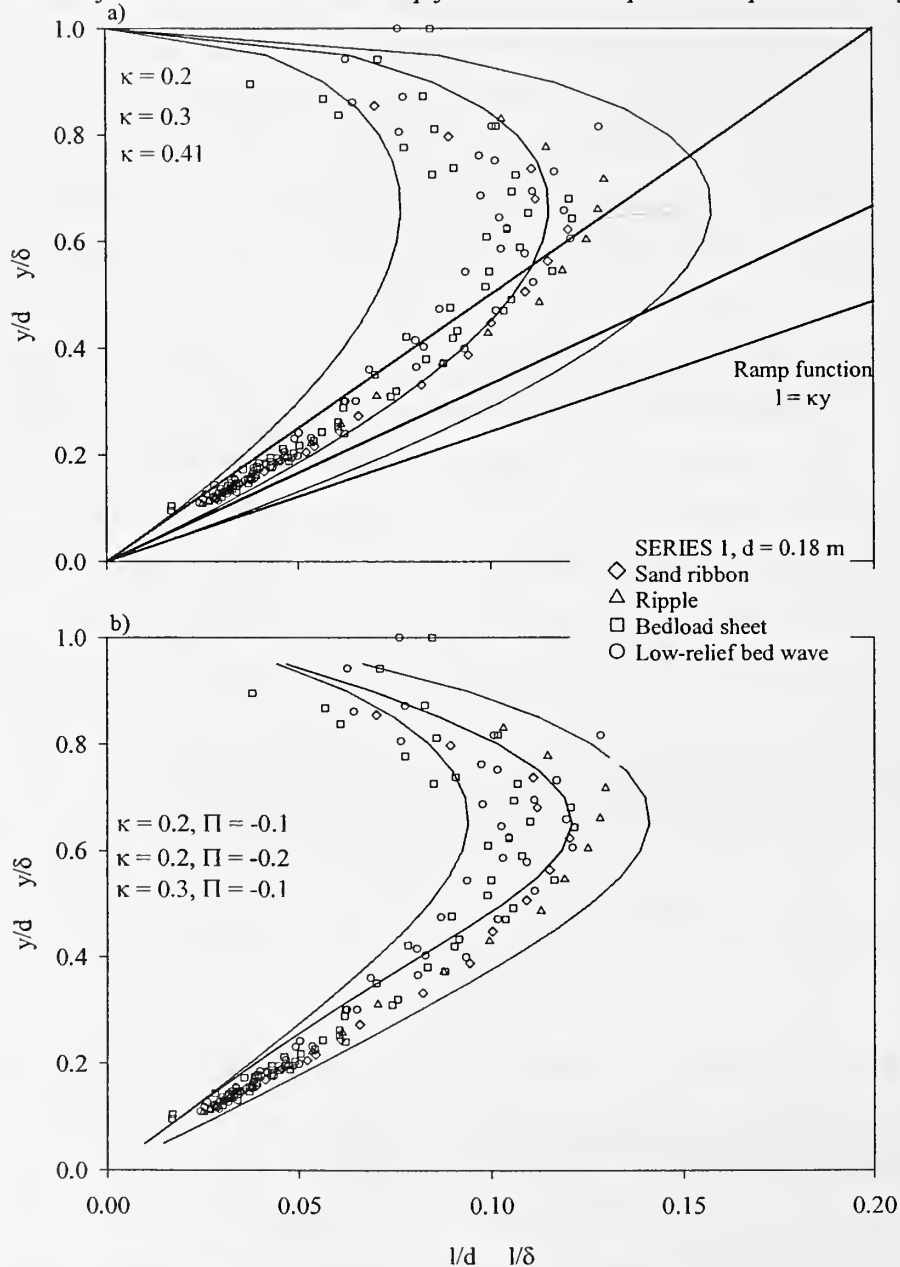
5.3.7 Mixing length

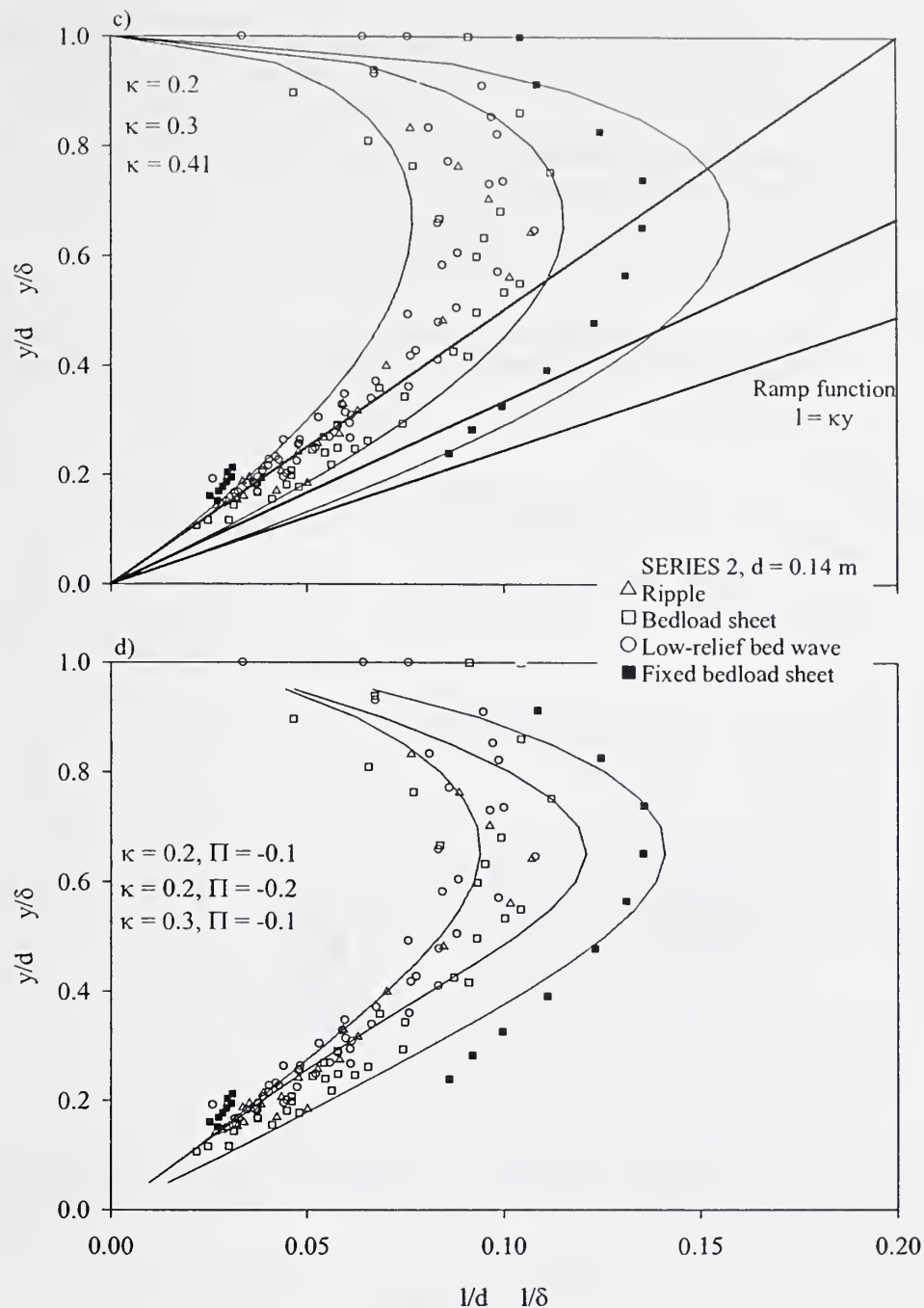
The vertical distribution of spatially-averaged mixing length, normalised by flow depth (Figure 5.23) exhibits an increase away from the boundary, reaching a maximum at approximately $y/d = 0.7$ ($l/d = 0.095-0.13$ and $0.08-0.11$ at $d = 0.18$ and 0.14 m). Mixing lengths are reduced when the flow depth is lowered since topographic acceleration is enhanced (assuming bedform steepness remains similar), accentuating vortex stretching which therefore dampens turbulent eddies (Tritton, 1988; Nelson *et al.*, 1993). In the vicinity of the free surface, mixing length is reduced since the vertical dimension of the eddies, and therefore turbulence scale, is restricted. The mixing lengths derived from the present data are of similar magnitude to past studies at $y/d = 0.7$ e.g. Kironoto and Graf (1994) $l/d = 0.1-0.2$ over a rough bed; Nezu and Rodi (1986) $l/d = 0.12-0.15$ over a smooth bed. Nowell and Church (1979) conclude that a simple characteristic length scale for turbulence, such as mixing length, is not possible in depth-limited flows over roughness elements. They state that the length scale of turbulence varies with flow depth (as demonstrated in Figure 5.23) and the density of roughness elements. Song *et al.* (1994) noted no distinct difference in the distribution of mixing length between gravel beds with and without bedload movement. However, the fixed bedload sheet exhibits the greatest value for dimensionless mixing length (~ 0.14 at $y/d \sim 0.7$) in the present experiments. When sediment is transported within turbulent eddies, the inertia of the grains causes a decline in eddy scale and therefore mixing length (Best *et al.*, 1997; Bennett *et al.*, 1998). However, the impact of sediment movement on turbulence (e.g. attenuation or enhancement) is complex and subject to continuing debate (Vanoni, 1975; Best *et al.*, 1997). A ramp function is shown in Figure 5.23, and provides a simple approximation in the lower part of the flow. The ramp function fits the data best when a κ value of 0.2 is employed, much less than the value of 0.41 normally stated (Nezu and Nakagawa, 1993). Nelson *et al.*, (1993) observed that the mixing length in the boundary layer was smaller than predicted by the ramp function, indicating a reduced value for κ . They noted that the greatest divergence from the linear trend coincided with the largest topographic acceleration at the mid-point of the bedform stoss. Large-scale turbulent structures are damped due to vortex stretching which result from topographic acceleration. Furthermore, Nelson *et al.* (1993) concluded that the boundary layer developed over the back of the bedform reduces mixing length in the lower section of the overlying wake flow, i.e. a transitional zone between the boundary layer and wake region.

Experimental data scatter is considerable, and increases away from the bed, resulting from the difficulties in obtaining accurate velocity gradients and retardation effects (Cardoso *et al.*, 1989; Kironoto and Graf, 1994). Furthermore, mixing length is influenced in the intermediate region by the wake coefficient when a wake defect is present, which is Reynolds number dependent. The smoothed profiles (curve 1) of normalised mixing length, when plotted separately for each spatially-averaged run

over a mobile bed (e.g. Figure 5.20b), demonstrates the best agreement with theoretical equations when a value of κ derived from the law-of-the-wall for the whole flow depth is used (curve 5), in accord with the dimensionless eddy viscosity results (Figure 5.20a). If the velocity wake-defect law is employed (curve 6) values are over-predicted for $0.3 < y/d < 0.8$. However, for specific regions over fixed and mobile bedforms (i.e. crest, stoss and trough), the smoothed mixing length data is often described best by the addition of a wake coefficient derived from the velocity defect-wake law over the whole flow depth.

Figure 5.23: Spatially-averaged mixing length, normalised by flow depth, plotted against dimensionless flow depth. The curves are calculated from Equation 5.5 (a and c) and Equation 5.6 (b and d) using the values of κ and Π stated. The ramp function is also plotted in part a and c for the stated κ values.



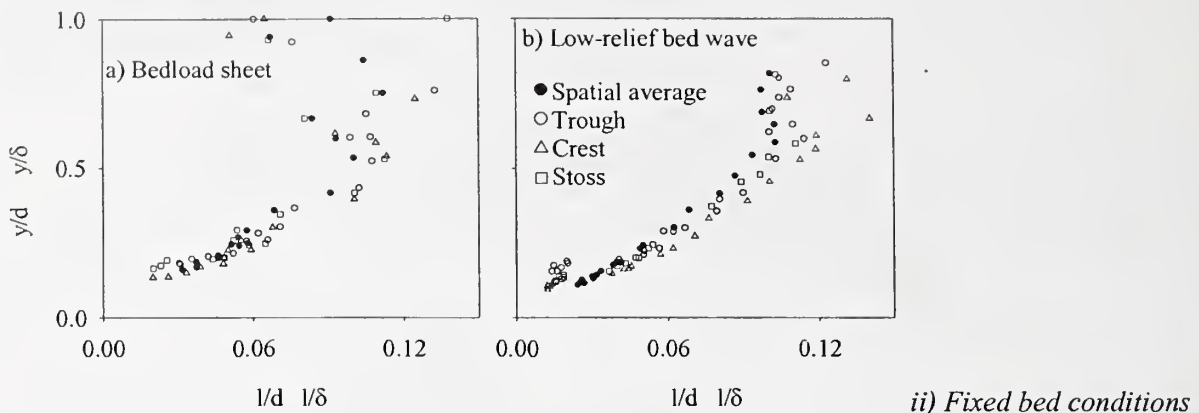


Mixing length is noted to be greatest over the crest of the fixed (up to $l/d = 0.25$) and mobile (up to $l/d = 0.14$) low-relief bed when $y/d < 0.8$ (red symbols on Figure 5.24ib and iib), as was also the case for eddy viscosity. In the case of the fixed bedload sheet, the values of mixing length in the separation and reattachment zone are demonstrated to be below the spatial average (red symbols in Figure 5.24iia), while the values recorded over the bedform stoss and crest were elevated above the spatial average. Carling *et al.* (2000b) noted the maximum mixing lengths occurred in the turbulent shear layer originating from the crest of sand dunes. Nelson *et al.* (1993) observed that the maximum value of mixing length increased over the lower bedform stoss side (i.e. -0.7 and -0.4 m downstream of the crest

in Figure 5.25), remaining constant over the upper stoss side. High values of mixing length are observed over the crest, as highlighted by the letter A in Figure 5.25, in accord with the present study.

Figure 5.24: Normalised mixing length plotted against dimensionless flow depth for specific bedform regions. The areas highlighted in red are discussed in the text.

i) Mobile bed conditions



ii) Fixed bed conditions

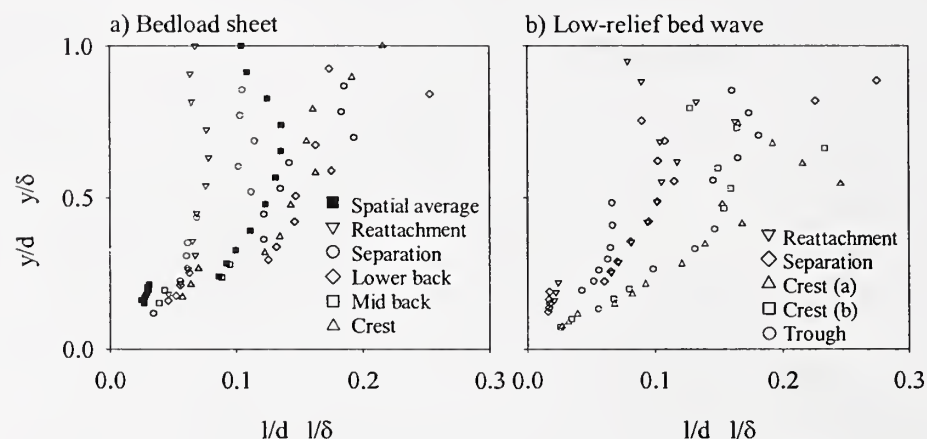
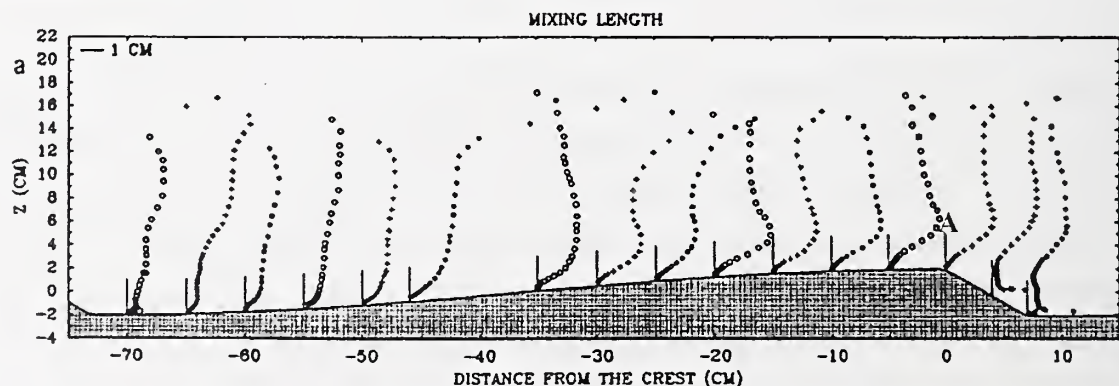


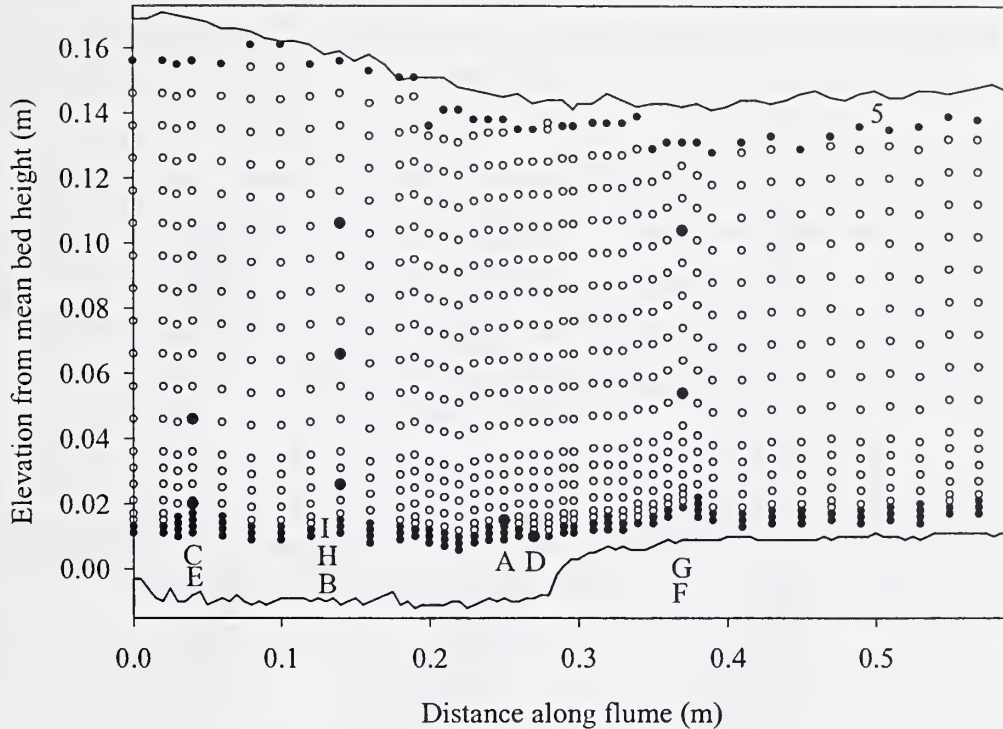
Figure 5.25: Spatial evolution of mixing length over a two-dimensional bedform (Nelson et al., 1993). Z is the height above the mean bed level. Flow is left to right. Peak values of mixing length are highlighted at point A.



5.3.8 Time series analysis in the frequency domain

Periodic variations in the downstream and vertical velocity time series at various locations in the flow over a fixed low-relief bed wave are identified in this section, and compared with predictions from theoretical and empirical equations. Furthermore, dominant statistically significant frequencies caused by eddy shedding and shear layer flapping will be distinguished and discussed.

Figure 5.26: Locations of selected LDA velocity time series (red circles). White and black circles represent two and one component velocity measurements respectively.



The resulting spectra taken at various locations over the fixed low-relief bed wave (Figure 5.26) are shown in Figure 5.27. Statistically significant peak frequencies which are dominant for both components of velocity are listed in Table 5.2. Simpson (1989) obtained frequency spectra downstream of a backward facing step, and observed two dominant frequencies in the separation zone. 1) A high frequency peak associated with the shedding of vortices from the separation point of the step and 2) a lower frequency is predominant outside the separation zone, which is attributed to flapping of the shear layer (Roden, 1998). Wake flapping is thought to result from the periodic transfer of the surrounding fluid into the separation region (Nezu and Nakagawa, 1993). Scale relations for the frequency of the vortex shedding (f_v) and wake flapping (f_w) have been proposed by Simpson (1989),

$$f_v \approx 0.8U_0 / x_r \quad (5.10)$$

$$f_w < 0.1U_0 / x_r \quad (5.11)$$

where U_0 is the mean velocity upstream of the point of separation and x_r is the average length of the separation zone, which is approximately 2-6 times the height of the obstacle i.e. bedform. The length of the separation zone (distance between the crest and reattachment, 120 mm) of the fixed low-relief bed wave is 6 times the bedform height (20 mm). The statistically significant frequency peaks at all points observed in the experimental flow fall in or below the range predicted by Equation 5.11 (Table 5.2 and 5.3) for wake flapping. Higher frequencies due to eddy shedding may be absent from the present spectra due to the lack of measurements below approximately 0.01 m above the mean bed level, where the influence of the separation/deceleration zone is greatest (Figure 5.26). Nezu and Nakagawa (1993) state that in the separation zone, eddy generation occurs over dune bedforms, and therefore the associated high frequency signal is strongest in this region. If flow separation is intermittent over the low-relief bed wave, as suspected, no particular frequency may dominate, and the spectral analysis method will be ineffectual. The height and shape of the bedform influence the strength and occurrence of flow separation (Kostaschuk and Church, 1993; Kostaschuk and Villard, 1996; Best and Kostaschuk, in press), which may also be caused by large clasts. Furthermore, turbulent events of differing magnitudes may occur at different frequencies, complicating the velocity spectral signal i.e. larger quadrant 2 events were found by Roden (1998) to be relatively infrequent.

Table 5.2: Statistically significant peak frequencies (Hz) observed for both velocity components at a given measuring point.

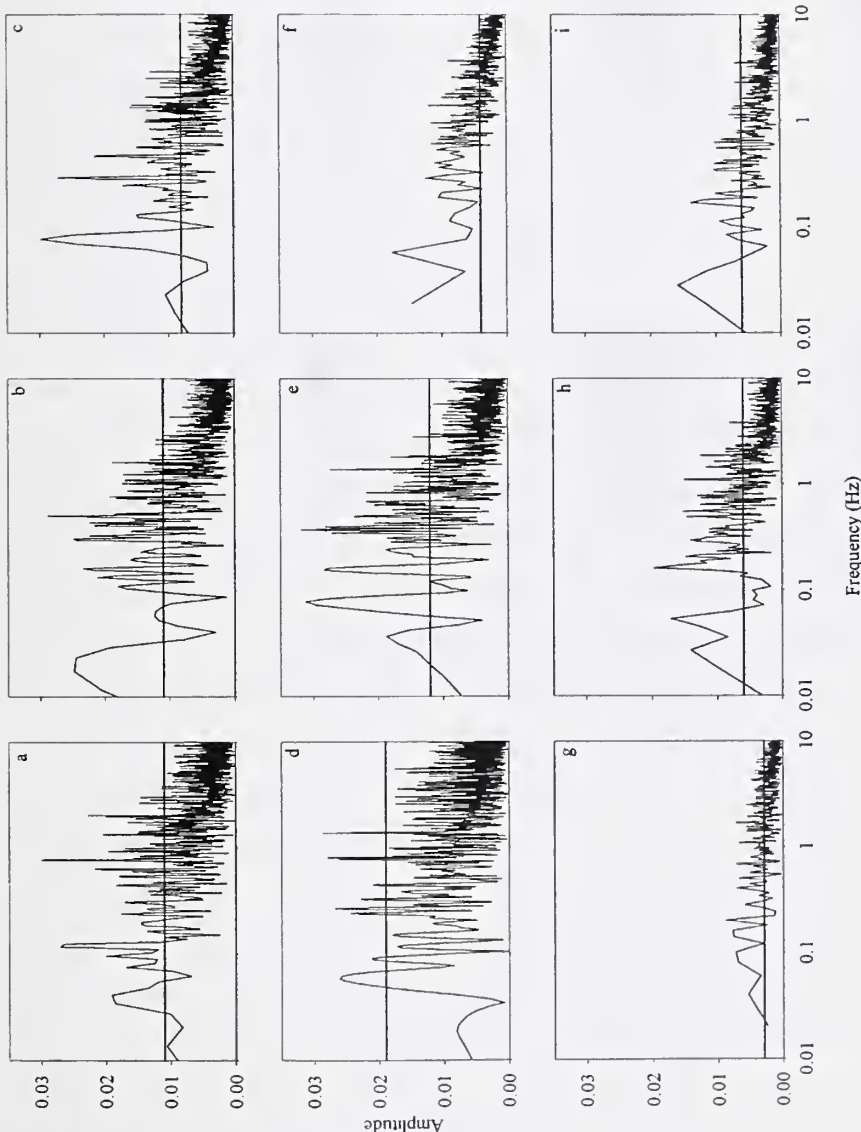
Measurement point (Figure 5.26)	Statistically significant (99.9 %) dominant frequencies (Hz) observed in both components of velocity
A	0.116 2.021
B	
C	0.290
D	
E	0.349
F	0.947
G	0.101 0.687
H	0.027
I	

Table 5.3: Predicted frequencies (Hz) for the recurrence of turbulence structures over a fixed low-relief bed wave, using a depth averaged velocity (U) of 0.87 m/s, flow depth (d) of 0.151 m and bedform height (h) of 0.02 m.

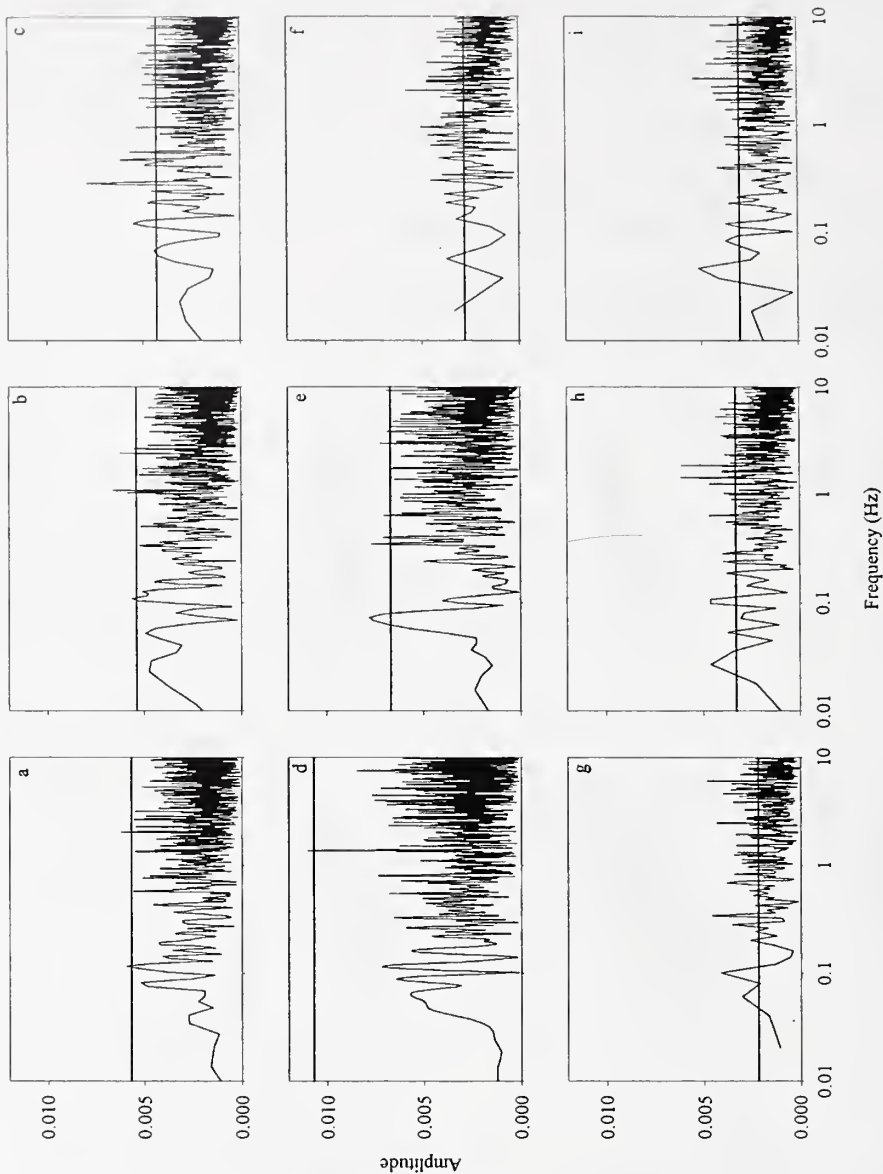
Predictive equation	Predicted frequencies (Hz)
Strouhal Law, Levi (1983b), depth-scale turbulent structures.	0.9
Itakura and Kishi (1980)	6.1
Simpson (1989): Vortex shedding	5.8-17.4
Wake flapping	0.7-2.2

Figure 5.27: Spectra of the time averaged a) downstream and b) vertical velocity at various locations over a low-relief bed wave. The 99.9 % significance level is shown.

a)



b)



The dominant frequencies associated with turbulent structures scaled on the entire flow depth can be predicted by the Strouhal law (Levi, 1983b, 1991) for both microturbulent and macroturbulent frequencies, f_s ,

$$f_s = U_s / 2\pi\delta \quad (5.12)$$

where U_s is the freestream velocity and δ is the boundary layer thickness (i.e. flow depth, d , where there is no velocity defect). Under comparable conditions, Jackson (1976) noted that the frequency of occurrence of boils was increased over a dune bed configuration compared with a flat bed. The frequency of turbulence structures produced by dunes, f_d , is predicted by the experimental and empirical equation of Itakura and Kishi (1980),

$$f_d = 0.14U / h \quad (5.13)$$

where U is the mean velocity over the bedform (dune), and h is bedform height. The predicted dominant frequency from the Strouhal law (0.9 Hz, Table 5.3) falls within the range of experimental values obtained (0.03-2.02 Hz, Table 5.2), whereas the empirical relation of Itakura and Kishi (1980) is at least 300 % greater (6.1 Hz, Table 5.3) than the statistically significant frequencies obtained from the frequency spectrums. The Strouhal law value (0.9 Hz) is within the range of frequencies associated with wake flapping by Simpson's (1989) relation (0.7-2.2 Hz), whereas the value predicted by the equation of Itakura and Kishi (6.1 Hz) falls within the range of frequencies linked to vortex shedding (5.8-17.4 Hz). Furthermore, Kostaschuk (2000) found that the equation of Itakura and Kishi (1980), despite being formulated specifically for dunes, did not agree as well as the Strouhal Law with his measurements taken over dunes in the Fraser River system, Canada. The greater frequencies predicted by the relation of Itakura and Kishi (1980) is attributed by Kostaschuk (2000) to the counting of shedded vortices in addition to eddies at the point of reattachment (associated with wake flapping) during flow visualisation experiments. However, at-a-point measurements are influenced by a variety of eddy sizes, vortex coalescence and wake effects, which tend to diminish the average eddy frequency. Clifford (1996) found a positive relationship between mean velocity and the period of turbulent structures, whereas the Strouhal law implies an inverse relationship exists (Equation 5.12). The Strouhal law is also problematic where eddy frequency varies with Reynolds number and particle size. Furthermore, one obstacle may shed eddies with a range of sizes, and therefore periods. At a particular point, the magnitude and frequency of eddies may be influenced by vortex pairing, shearing and coalescence. Indeed, Nowell and Church (1979) indicate that if a range of particles are present, the shedding of eddies and subsequent interactions will generate a complex distribution of frequencies. Therefore, despite successful applications (e.g. Clifford *et al.*, 1992; Robert *et al.*, 1993), the utility of the Strouhal law is subject to debate. In a depth-limited flow over coarse grains, Robert *et al.* (1993) observed dominant periods of 1-2 s, which decreased away from the bed.

Wavelet analysis (<http://paos.colorado.edu/research/wavelets/>) was implemented to try and identify any significant turbulence structures, which may be intermittent, varying in amplitude and frequency. Continuous wavelet analysis decomposes a regularly spaced time series a into time-frequency representation of the signal, which details the amplitude of any ‘periodic’ signals identified and how their amplitude varies with time i.e. pin points turbulent structures in both the time and frequency domain. In the present analysis, application of the continuous wavelet transform required that the LDA velocity time series be first resampled to produce regularly spaced measurements (100 and 25 Hz, using the PITSA software package), and any trend removed. At all measurement points, both the downstream and vertical velocity components demonstrate a significant spectral peak at a frequency of 1.26 Hz when the time series was resampled at 100 Hz, and 0.32 Hz when resampled at 25 Hz. The change in frequency observed should not occur when the sampling rate is altered, and may indicate the occurrence of aliasing. Furthermore, ADV velocity measurements recorded at 25 Hz in the flume, when empty of sediment, also exhibit a significant peak at a frequency of 0.32, and therefore this frequency may well be an artefact of the flume rather than related to turbulent flow structures. The velocity time series taken may also be too short (60 s) for the successful application of wavelet analysis (i.e. unable to identify low frequency signals). Furthermore, vortices generated from upstream bedforms have a significant impact on the turbulent flow structure downstream, adding increased complexity to the turbulent spectrum. The intermittent character of the turbulent structures leads to intermittency in the transport of sediment (Gyr and Müller, 1996).

5.4 Discussion and conclusions

5.4.1 Comparison of mobile and fixed beds

It is often assumed that the same flow structure and scaling laws apply to mobile and fixed beds (Nikora and Goring, 2000). However, in the outer flow ($y/d > 0.2$), values for eddy viscosity and mixing length were elevated over the fixed bed, while values for turbulence production were reduced, compared with the mobile run. Calculations of eddy viscosity, mixing length and turbulence production require a value for the velocity gradient, which is difficult to accurately evaluate and may be responsible for the differences observed between the mobile and fixed beds. Furthermore, greater values for the spatially-averaged turbulence intensity and Reynolds stress were measured near the fixed bed ($y/d < 0.3$) compared with the equivalent mobile bed due to the different flow resistance offered by the two boundaries. The influence of bedload on the flow is complex, and opposite effects can occur depending on bed roughness, and the relative magnitude of the flow (e.g. velocity, density and turbulence length scale) and sediment transport variables (e.g. grain size, density, velocity and concentration; Carbonneau and Bergeron, 2000). Bedload transport modifies the rate of dissipation of turbulent energy, although

the mechanisms responsible are unclear. The relative motion between the sediment (extracts momentum from the flow, reducing near bed velocity) and fluid phases generally causes the roughness length of the mobile beds to be greater than that of the fixed beds (Smith and McLean, 1977; Wiberg and Rubin, 1989; Best *et al.*, 1997; Bennett *et al.*, 1998), resulting in increased flow resistance (Song *et al.*, 1994). However, Heathershaw and Langhorne (1988), noted that during intense bedload transport over the sea floor, the roughness length fell, and was insensitive to lower rates of transport. Mobile sediment can cause the roughness of the bed to increase by 1-3 orders of magnitude compared with the roughness of a stationary bed (Wiberg and Rubin, 1989). The thickness of the bedload layer is thought to be directly proportional to the magnitude of the roughness. Resistance to the flow results from the generation of wakes from the sediment grains, which are accelerated by the flow as both bedload and suspended load (Carboneau and Bergeron, 2000). The magnitude of the roughness depends on the concentration of bedload and the vertical height over which a grain is accelerated before obtaining the same velocity as the surrounding fluid, which is approximately equal to the height of the bedload layer. In the experiments of Carboneau and Bergeron (2000), bedload transport was shown to both increase and decrease flow velocity over a rough bed. Turbulence modulation is influenced by the bed roughness, eddy shedding, grain inertial effects and interactions between grains, coherent flow structures and flow boundaries (Best *et al.*, 1997).

The non-permeable nature of the fixed bed causes reduced drag since there is no flow and dilation within the sediment bed (Zippe and Graf, 1983). Turbulent motions are not confined to the region above the porous bed, but instead extend into the particle interstices. Therefore, Mendoza and Zhou (1992) note that over a porous bed, the no-slip boundary condition is no longer strictly applicable, and an additional Reynolds stress exists. The decrease in drag due to the non-permeable bed further increases the difference in flow resistance between the fixed and mobile beds. Over rough permeable surfaces, the coefficient of resistance is influenced by Reynolds number (Mendoza and Zhou, 1992) and the relative thickness of the permeable layer. However, no difference between turbulent fluctuations over a permeable and non-permeable bed were distinguishable in the experiments of Zippe and Graf (1983).

The constantly changing bed morphology in the mobile bed runs adds to the complexity of the situation. When a mobile bed is fixed, it is not physically possible to maintain exactly the same hydraulic conditions. In the present experiments, when the bed was fixed the slope of the flume and the water discharge were maintained, while the water surface slope and flow depth altered marginally (Table 4.1). The reasons for the difference in water depth are explained in Section 4.3.1. The lower flow depths associated with the fixed experiments will increase their relative roughness.

5.4.2 The influence of roughness transitions on the turbulent flow field

Robert *et al.* (1996) obtained velocity and turbulence measurements in a gravel bed river along a transect which passed from an armoured bed upstream to large, superimposed, protruding clasts downstream. As was observed in the present study, coarse grains increase both the intensity and production of turbulence. Two distinct regions of flow were recognised by Robert *et al.* (1996), firstly a sublayer below the top of the coarse grains, characterised by flow towards the bed, intense eddy shedding and a correlation coefficient of approximately 0.4. Secondly, a wake zone exists above the coarse clasts, associated with positive vertical flow velocities, with reduced but highly variable values for the correlation coefficient, illustrating the varying impact of the protruding grains on the flow. Turbulence is produced by eddies with different origins i.e. vortices in front and at the flanks of the large clast, shedding from the shear layer associated with the separation zone and packets of low speed fluid from within the separation zone which are ejected into the outer flow (Acarlar and Smith, 1987a, b; Kirkbride 1994). However, turbulence production is dominated by vortex shedding in the lee of clasts, and therefore the spacing of coarse grains greatly influences the turbulent flow structure. Vortex interaction and stretching dominates the turbulent flow structure in depth-limited flows over coarse and irregular boundaries.

The most distinct roughness change in the current study occurs between the bedform crest (relatively smooth) and the downstream trough (coarse), although a decrease in elevation is also present, causing the effects of morphology and texture on the turbulent flow structure to be difficult to separate. The roughness transitions between the trough and stoss, and the stoss and crest are more gradual and complicated by the presence of superimposed bedforms. Antonia and Luxton (1971) observed the development of an internal layer at abrupt roughness transitions, which slowly approach an equilibrium state, and also noted greater turbulence in the vicinity of the rough wall compared with the smooth boundary. The latter observation is confirmed by the present experiments, where turbulence production and intensity are shown to be largest in the trough, which is the coarsest bedform region. However, most of the turbulent energy is contained within the shear layer generated from the elevated bedform crest. The flume experiments and numerical investigations of Nezu *et al.* (1993) illustrated that downstream of a smooth to rough boundary transition, the mean velocity near the bed diminished, which was partly compensated by an increase in the outer flow and vice versa. In Section 4.4.2 the velocity profile for the trough region of the bedload sheets and low-relief bed waves were shown to be reduced over the whole flow depth compared with the equivalent profile for the bedform crest located upstream. Furthermore, velocity profiles obtained at several locations in the trough of the fixed bedload sheets indicate that in the outer flow mean velocity is raised above the spatially-averaged value in accord with Nezu *et al.* (1993). The bed shear stress readjusts to its new value quite quickly following a

transition in bed roughness, being elevated (i.e. overshooting) and reduced (i.e. undershooting) immediately downstream of a smooth to rough and rough to smooth transition respectively (Nezu *et al.*, 1993). Downstream of a smooth to rough discontinuity, Nezu *et al.* (1993) observed that the contribution of quadrant 2 events to Reynolds stress fell and the ratio of quadrant 4 to quadrant 2 events increased. The same trends are illustrated in the zone of flow separation/retardance immediately downstream of the change in roughness from smooth (crest) to rough (trough) over a bedload sheet (Figure 5.13) low-relief bed wave (Figure 5.15).

The structure of the inner layer over a smooth and rough wall differ, and is dependent in the latter case on the roughness geometry. Over a smooth to rough discontinuity, the turbulence intensity within the internal boundary layer drives its development (flow is fully adjusted over a distance of less than 20 boundary layer thicknesses). However, downstream of a rough to smooth transition, the growth of the internal layer is relatively slow compared with a smooth to rough discontinuity since it is influenced by both the inner and outer layers, and the response of the turbulence parameters are less marked. In the present experiments, the variations in bed roughness and elevation occur frequently, hindering the full development of an internal boundary layer before another is initiated at a downstream transition in the wall conditions. Consequently, the multiple boundary layers interact (Livesey, 1995), resulting in a complex turbulent flow field.

5.4.3 Influence of turbulence on sediment transport

The movement of sediment is discontinuous (Raudkivi, 1966), with the largest grains being moved only sporadically at bed shear stresses greater than 7 Pa. Bedload transport is very sensitive to surface structures, grain size, relative roughness and small changes in flow conditions (Hassan and Church, 2000; Shvidchenko and Pender, 2000). The mean flow and sediment transport can be linked in steady, uniform flow, but accuracy decreases when applied to non-uniform conditions e.g. over bedforms (McLean *et al.*, 1994; Nelson *et al.*, 1995). The reduction in the correlation coefficient near the bed ($y/d < 0.3$; Figure 5.10), resulting from the interaction between the internal boundary layer and the overlying turbulent wake region, confirms the poor correlation between sediment transport and the local boundary shear stress (McLean *et al.*, 1996). Furthermore, greater sediment transport can be associated with increased turbulence intensity when bed shear stress remains constant (Nelson *et al.*, 1993). Higher turbulence intensity does not necessarily increase Reynolds stress since there is a poor correlation between the horizontal and vertical velocity fluctuations. The transport of sediment downstream can occur as a result of turbulence (e.g. quadrant 1 and 4 events) even where mean velocity, or bed shear stress, is zero (Thorne *et al.*, 1989; McLean *et al.*, 1996). The majority of bedload is moved by quadrant 4 events, although quadrant 1 events of comparable magnitude and duration move an equal quantity of sediment, but are less frequent (Thorne *et al.*, 1989; Nelson *et al.*, 1995). Both Drake *et al.*

(1988) and Williams (1989a, b) found that the transport of coarse sediment was relatively insensitive to fluctuations in vertical velocity, accounting for the dominance of quadrant 1 and 4 events in the transport of bedload. Drake *et al.* (1988) noted that the instantaneous shear stress associated with quadrant 4 events was three times the critical bed shear stress. In depth-limited flows the topographic acceleration alters the link between the mean flow and turbulence, whereas in much deeper flows, the bedforms behave as roughness elements. Carling *et al.*'s (2000b) measurements over sand dunes in the River Rhine (1.6-5.4 m flow stage, mean dune height 0.6 m), noted a broad positive relationship between bed shear stress and bedload transport, although there was much scatter. Bedload transport typically increased up the dune stoss, being lowest in the trough, and is attributed to the migration of superimposed bedforms. Buffin-Bélanger *et al.* (2000) have recently described high-speed wedge-like flow structures that are composed of quadrant 1 and 4 events, and extend throughout the whole flow depth. The relatively long duration of wedges (approximately 2 s) is more effective for sediment entrainment compared with several quadrant 1 and 4 events of shorter duration. However, the mechanism for the formation of high-speed wedges is unclear.

The predictions of a modified version of the sediment transport model of Meyer-Peter and Müller (1948), accounting for the fractional movement of coarse non-uniform sediment mixtures (van Rijn, 1993), are compared with measured mean bedload transport rates in Figure 5.28. The bedload transport rate, q_b , integrated over N grain size fractions is expressed as:

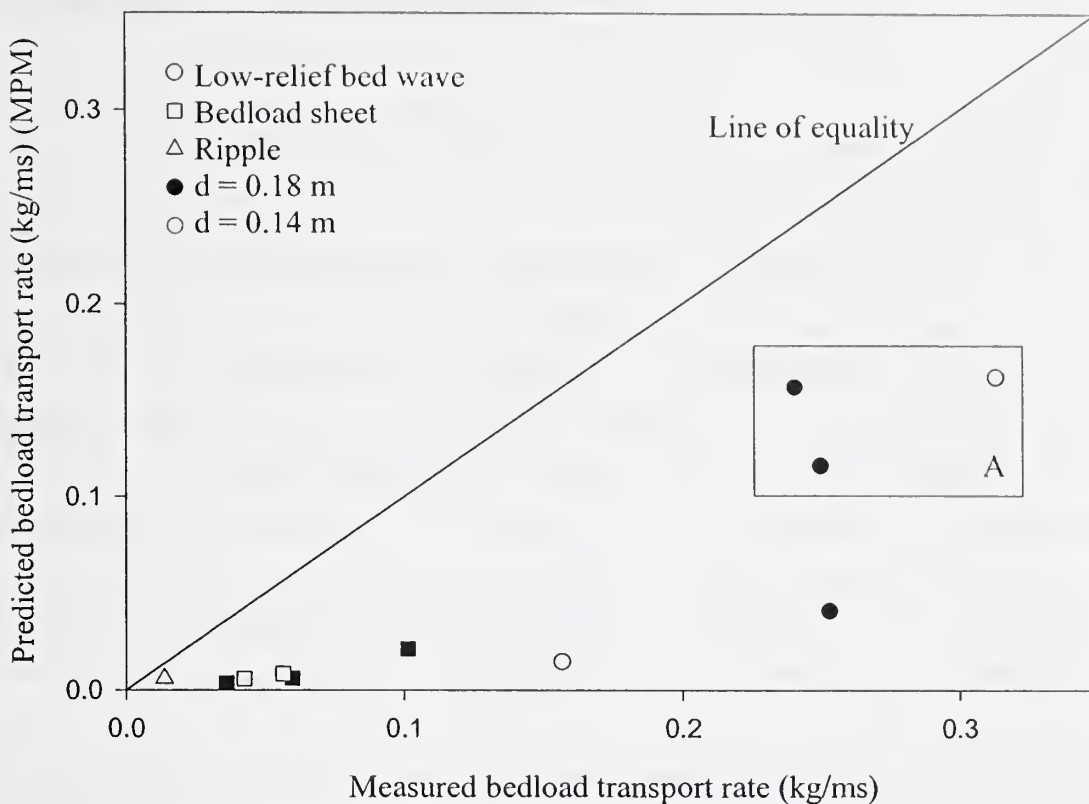
$$q_b = 8(s-1)^{0.5} g^{0.5} \sum_{i=1}^N p_i d_i^{1.5} (\mu \theta_i - \xi \theta_{cr})^{1.5} \quad (5.14)$$

where

p_i	Percentage of size class i of the bed material
d_i	Particle diameter of size class i
s	Specific density (= 2.65)
g	Acceleration due to gravity
μ	Bedform factor
θ_i	Mobility parameter of size class i
ξ_i	Correction factor of class size i
θ_{cr}	Critical mobility parameter based on the average diameter d_m (D_{50} used here)

The transport formula of Meyer-Peter and Müller (MPM) is based on laboratory experiments with uniform and graded (convex size distribution) sediment mixtures. The grain sizes employed ranged from 0.4-30 mm, with slopes of 0.0004-0.02 and depths of 0.1-1.2 m. The MPM equation is in widespread use, including sandy gravel-bed streams (Ashmore, 1988; Batalla, 1997).

Figure 5.28: Comparison of the predicted (MPM) and measured values of bedload transport rate. The best agreement is for the low-relief bed waves highlighted in Box A.



In all experimental runs the measured bedload transport rates are under-predicted (typically by 90-80 %) by the formula of MPM. The best percentage agreement (~ 50 %) is found for the low-relief bed waves highlighted in box A in Figure 5.28. Vertical and horizontal sorting of sediment, and the bimodal nature of the present experimental mixture, may partly contribute to the disagreement between measured and predicted bedload transport rates. In a sediment mixture, under conditions of selective entrainment a range of critical thresholds exist (Robert, 1993) due to the effects of relative protrusion, grain exposure, imbrication, clustering, and pivot and friction angle (Komar, 1987a, b). The bedload transport measurements made in the flume may be dependent on the width-depth ratio, flume system (feed or recirculating), and the number of bedforms included in each sample.

McLean *et al.* (1994) attributed the poor agreement of measured and predicted transport rates over a fixed dune to the occurrence of flow separation, and the inaccuracy in estimates of shear stress due to the thin boundary layer at reattachment. However, Nelson *et al.* (1995) stress that variations in the structure of turbulence not registered by bed shear stress should be expected in any developing boundary layer, even if flow separation is absent or intermittent e.g. the roughness transitions over bedload sheets (Antonia and Luxton, 1971, 1972), low-angle dunes (Best and Kostaschuk, in press). The higher than predicted rates of sediment transport downstream of reattachment over a fixed dune in

the experiments of McLean *et al.* (1994) are due to elevated turbulence intensities, greater occurrence of quadrant 1 events, and the reduced correlation coefficients, despite low mean velocities and bed shear stresses.

5.4.4 Comparison of the turbulent flow structure over bedload sheets, low-relief bed waves, ripples and dunes

Similar to the turbulent flow field over ripples and dunes formed in sand sized sediment, the turbulent flow over bedload sheets and low-relief bed waves exhibits free shear layers, which form the turbulent wake region that is distinguished by elevated turbulence intensities and Reynolds stress. The shear layer has been demonstrated to be characterised by positive vertical skewness values and frequent, high-magnitude quadrant 2 events, which are attributed to vortices being shed from the region of Kelvin-Helmholtz instabilities. Bennett and Best (1996) note that the length and thickness of the shear layers are equivalent to the length and height of the bedform in the case of fixed ripples and dunes in uniform sand roughness. The thickness of the shear layers generated from the bedload sheets and low-relief bed waves are similar to the their height (approximately 10-20 mm). It is not possible to document whether the length of the shear layer generated from the crest is equal to bedform length in the present experiments due to additional turbulent shear layers being generated from coarse clasts and superimposed bedforms, and the fact that the test section only covers the crestal region of the fixed low-relief bed wave.

Table 5.4 demonstrates the salient features of the turbulent flow field at various locations over different bedforms in order to highlight the contrasts and similarities in flow structure. Ripples are associated with essentially uniform flow conditions since the influence of the wakes generated from the crests is confined to the lower part of the flow, with complete mixing occurring in the bottom 20-40 % (Bennett and Best, 1996). The shear layer, and associated quadrant 2 events, generated from ripples extends parallel to the bed, whilst over the other bedforms it is topographically forced into the outer flow. Topographically induced flow acceleration and deceleration are apparent over bedload sheets, low-relief bed waves and dunes, causing non-uniform flow conditions and the stacking of individual wakes generated upstream (Nelson and Smith, 1989). The value of Reynolds stress at reattachment is dependent on the frequency and magnitude of quadrant 4 events, which are limited over ripples, but frequent and of high magnitude at dune reattachment. Over the fixed bedload sheet and low-relief bed wave, the presence of shear layers generated from coarse grains and superimposed bedforms on the stoss, cause elevated Reynolds stresses at multiple locations, and not just at reattachment downstream of the bedform crest, raising the spatially-averaged Reynolds stress value. Consequently, the presence of substantial grain and form roughness on a bedform stoss (not observed in the fixed bed experiments

of Nelson *et al.* (1993) and Bennett and Best (1995, 1996)) reduces the contrast between the spatially-averaged Reynolds stress and its value at reattachment downstream of the crest. The relatively low elevation of the bedload sheets and low-relief bed waves (~10 mm) also helps explain the reduced variation in Reynolds stress from the spatial average compared with larger dune bedforms (40 mm).

Table 5.4: Variations in flow parameters between different regions over the bedforms. Modified from Bennett and Best (1996).

Flow parameter	Bedload sheets	Low-relief bed	Ripples ¹	Dunes ²
	waves			
Uniformity	Non-uniform	Strongly non-uniform	Weakly uniform	Strongly non-uniform
Shear layer:				
Attitude	Parallel to stoss	Parallel to stoss	Parallel to bed	Parallel to stoss
Vertical extent	Extends to $0.5d$	Extends to $0.7d$	Limited to $0.2d$	Extends to water surface
Quadrant 2 events	Moderate vertical restriction and magnitude	Unrestricted vertically, high magnitude	Vertically restricted, low magnitude	Unrestricted vertically, very high magnitude
Velocity gradient	Moderate	Large	Small	Very large
Quadrant 4 events from outer region	Yes	Not detected in Figure 5.14	No	Yes
Reattachment:				
Quadrant 4 events	High percentage occurrence	High percentage occurrence	Infrequent, low magnitude	Frequent, high magnitude
Reynolds stress	$\sim \bar{\tau}_{R0}$	$2-3 \bar{\tau}_{R0}$	$2-3 \bar{\tau}_0$	$6-9 \bar{\tau}_0$
Turbulence intensity	Lowest over crest	Greatest in shear layer over trough	Greatest in shear layer over trough	Greatest in shear layer over trough
Correlation coefficient	Reduced over stoss, average over the crest and elevated in the deceleration zone	Spatial average is reduced from that expected in a uniform boundary layer		Over the stoss, increases and decreases in the developing boundary layer and wake respectively, towards a value similar to that expected in a uniform boundary layer at the crest
Turbulence production	Not possible to distinguish spatial variations	Greatest in shear layer over trough, lowest over crest		Greatest in shear layer
Mixing length and kinematic eddy viscosity	Below the spatial average at reattachment	Greatest over crest		Greatest in shear layer

¹ Wiberg and Nelson (1992); Bennett and Best (1996).

² Nelson *et al.* (1993); McLean *et al.* (1994); Bennett and Best (1995); Carling *et al.* (2000b).

The distinction between bedform types depends on a range of parameters, e.g. bedform geometry, water depth, channel width, sediment grain size distribution and flow strength (Carling, 1999). Furthermore, little quantitative data exists concerning the geometry, dynamics and associated turbulent flow structure of bedforms developed in coarse sediment (i.e. > 2 mm), and only relatively recently have some bedform types been recognised in poorly mixed sediments e.g. bedload sheets were first recorded by Whiting *et al.* (1988). Moreover, well-developed features are typically studied, with the critical transitional conditions between different bedform states being neglected. Consequently, some confusion exists in relation to bedform classification, and any bedform definitions may require revision in the light of future studies (Best, 1996). Therefore, accurate and detailed characterisation of the bedforms is viewed as the most important consideration in this study. Ripples are distinguished from the bedload sheets and low-relief bed waves by their much smaller height (3-5 mm compared with > 7 mm), and their influence on the turbulent flow structure being limited to the lowest 20 percent of the flow. It has been argued that bedload sheets and low-relief bed waves either represent distinct bedforms, transitional dunes, 2-D dunes or 3D dunes. Dune morphology can be very variable (e.g. angle of the slip face), leading to differences in their associated turbulent flow structure (e.g. magnitude and duration of flow separation; Kostaschuk and Villard, 1996). However, the reason for divergent morphologies is poorly understood (Best and Kostaschuk, in press). Furthermore, the geometry of bedforms varies between field and flume conditions (Carling, 1999). The similarities and contrasts between dunes and bedload sheets and low-relief bed waves are stated in Table 5.5.

Table 5.5: Contrasts and similarities between dunes, bedload sheets and low-relief bed waves.

Similarities	Contrasts
All experimental data plots in the dune stability field in Southard and Boguchwal's figures 2N, 2O and 2P (1990), which do not consider bedload sheets or low-relief bed waves. In Figure 3.17 (Best, 1996), the present data plots in the dune and bedload sheet regions. Most of the data for constructing stability diagrams is collected over fine, uniform sediment. The low-angle dunes recorded by Kostaschuk and Villard (1996) plotted in the stability fields for upper-stage plane beds or antidunes, highlighting the need to consider a range of factors when classifying bedforms.	Ashley (1990) defines dunes as having a wavelength of greater than 0.6 m, and a height over 0.075 m. The height of the bedload sheets and low-relief bed waves scale with the coarsest particles in transport (D_{90}), whereas dunes exhibit no scaling with grain size (Carling, 1999). The height of bedforms tends to decrease as the sediment becomes more poorly sorted and the D_{50} increases (Snishchenko <i>et al.</i> , 1989).
Permanent flow separation is not a prerequisite for dunes. Intermittent or no flow separation can occur over low-angled dunes (Best and Kostaschuk, in press). Shear layers are generated from the crest of dunes, bedload sheets and low-relief bed waves, as well as from coarse, protruding grains.	A poorly sorted sediment mixture is required for the formation of bedload sheets and low-relief bedwaves, which allows grain sorting by selective entrainment. Iseya and Ikeda (1987) and Dietrich <i>et al.</i> (1989) observed no bedload sheets when the sediment mixture contained gravel and no sand. Dunes can form in uniform sediment.
Low-relief bed waves and dunes scale with flow depth (Allen, 1984).	The velocity gradient is greater over dunes, increasing the magnitude, frequency and vertical extent of turbulence.
Coarse armour layers occur in the troughs of bedload sheets and low-relief bed waves. Immobile large grains are also present in the troughs of dunes when sediment transport rates are low.	The ratio of length to flow depth is approximately 5 for dunes (Allen, 1982), but ≤ 4 for bedload sheets and ≥ 18 for low-relief bed waves. The steepness (height/length) of equilibrium dunes is much greater (0.08; Carling, 1999) compared with bedload sheets (0.017) and low-relief bed waves (0.004).

5.4.5 Bedform development

5.4.5.1 Sand ribbons

At the lowest discharges, the sand fractions were selectively entrained in the present experiments, forming sand ribbons, which are narrow, elongated, flow-parallel features previously recorded by Iseya and Ikeda (1987), Ferguson *et al.* (1989) and Tsujimoto (1991, 1999). The development of these longitudinal forms is closely coupled to the development of secondary currents (Parker, 1992; Nezu and Nakagawa, 1993; Tsujimoto and Kitamura, 1996), which promote lateral bedload transport and sorting, and are facilitated by transverse variations in bed shear stress resulting from the alternate coarse and fine sediment stripes. However, secondary currents can develop in a sediment-free channel when the width-depth ratio is below five (Nezu and Nakagawa, 1985). Before conducting the present experiments, measurements of the lateral and downstream velocity components were taken using an ADV when the flume was filled with water and no sediment. The maximum lateral velocities were observed to be approximately 5 % of the downstream values, which occurred near the sidewall away from the bed. Downstream velocities and bed shear stresses have been found to be higher over the

coarse troughs compared with the ridges of finer sediment, amplifying and stabilising the streak geometry (Nezu and Nakagawa, 1993).

5.4.5.2 Ripples

As bed shear stress increases, the sandy elongated patches of sediment, which migrate over the static armour, grow in volume and become rippled (Allen, 1968; Leeder, 1980; Ikeda and Iseya, 1988; Baas, 1999). The development of bedforms from an initially flat bed occurs progressively (Southard and Dingler, 1971), rather than spontaneously (Bagnold, 1956). Raudkivi (1966) envisaged the growth of bedforms being initiated by a chance pile up of mobile sediment just above the threshold of motion, over which flow separation can occur. The accumulation of sediment may occur by 1) fast upstream particles sheltering downstream grains leading to grouping (e.g. kinematic waves), 2) intermittent turbulent coherent flow structures eroding excess sediment for the flow capacity (Williams and Kemp, 1971, 1972; Grass, 1983; Drake *et al.*, 1988, over fine gravel; Best, 1992), and 3) the presence of non-uniform sediment. The development of a downstream ripple occurs by erosion of sediment at the reattachment point of the shear layer generated from the initial bed defect, and its deposition downstream to form another disturbance to the sediment and flow fields. Liu (1957) suggested that ripples result from an instability at the sediment-fluid interface, and not by turbulent motions, surface waves and irregularities in the sediment bed. However, the instability mechanism does not account for the observed amplification and downstream propagation of ripples (Gyr and Müller, 1996).

Increases in bed shear stress caused larger clasts to be entrained and incorporated into the starved ripples (Chiew, 1991; Bennett, 1992; Wilcock, 1992), especially at the upstream end of the fine-grained stoss side where there is a roughness transition from the coarse grained trough. In uniform sediment, Leeder (1980) noted that ripples did not form in sediment with a diameter larger than 0.7 mm. The bimodal nature of the sediment enables clasts with a diameter greater than 0.7 mm to be transported by the ripple bedforms (e.g. overpassing of coarser sediment; Carling, 1996). Particle overpassing is promoted by the low friction angle and high relative protrusion of coarse clasts over the fine grained bedform back. Greater turbulent production occurs over the ripple forms compared with the sand ribbons due to the presence of shear layers originating from the ripple crests and overpassing coarse clasts (Table 5.6). Furthermore, ripples are distinguished by their traverse to flow morphology compared with the streamwise form exhibited by sand ribbons.

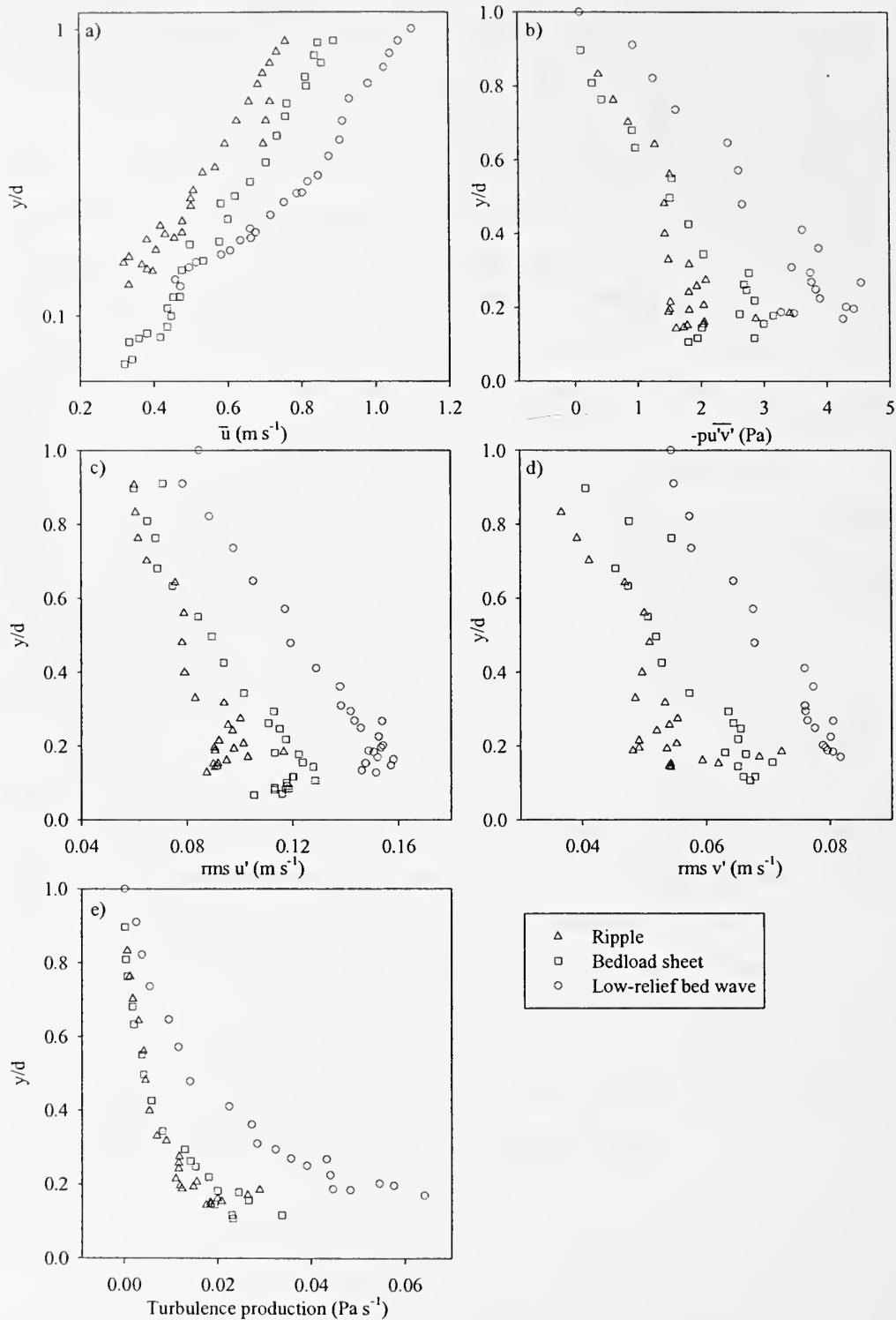
Table 5.6: Summary of the changing morphology, sediment transport, flow and turbulent structure between characteristic bed states in the present experiments. Arrows indicate the direction of increase for each parameter.

Bed state	Morphology			Sediment transport: quantity and size
	Height	Length	Topographic forcing	
Flat bed/ sand ribbon				
Ripple	↓			
Bedload sheet		↓		
Low-relief bed wave			↓	↓

Bed state	Turbulent flow structure			
	Turbulence production	Spatially-averaged ($y/d < 0.3$)		
		Normalised turbulence intensity	Normalised Reynolds stress	Spatial variability (horizontal and vertical)
Flat bed/ sand ribbon				
Ripple	↓			
Bedload sheet		↓		
Low-relief bed wave			↓	↓

Bed state	Turbulent flow structure			
	Velocity gradient	Flow uniformity	Water surface interactions	Vertical extent and magnitude of quadrant 2 events
Flat bed/ sand ribbon				
Ripple	↓	↑		
Bedload sheet			↓	
Low-relief bed wave				↓

Figure 5.29: Spatially-averaged mean flow (a, downstream velocity) and turbulence profiles (b, Reynolds stress; c, downstream turbulence intensity; d, vertical turbulence intensity; e, turbulence production). With the transition of the bed between ripples, bedload sheets and low-relief bed waves, the values of the mean flow and turbulence parameters increase, especially near the bed ($y/d < 0.3$) in the case of turbulence characteristics.



5.4.5.3 Bedload sheets

With increasing flow strength, ripples develop into bedload sheets ($\tau_{R0} > 3$), which are morphologically distinguished by their greater height (7-12 mm) compared with ripples (3-5 mm). Bedload sheets also transport a greater quantity and calibre of sediment, which increases grain roughness, turbulence production, turbulence intensity and Reynolds stress (Figure 5.29 and Table 5.6). The total sediment transport rate has been demonstrated to be directly related to the increase in bedform height using a modified version of Simons *et al.*'s (1965) formula (Equation 3.5, Figure 3.16), which was not originally derived for bedload sheets. The height of an individual ripple may become abnormally high (i.e. rogue ripple, Leeder, 1983) due to bedform amalgamations facilitated by the range of ripple migration rates (4-34 mm/s; Raudkivi and Witte, 1990; Ditchfield and Best, 1992; Coleman and Melville, 1994). Other suggestions for the production of a rogue ripple include small scale fluctuations in sediment transport e.g. the three-dimensionality of the ripple may cause transient increases in local bed shear stress. Furthermore, the shear layer originating at the ripple crest may 'flap' (Simpson, 1989), causing the point of reattachment, associated with high instantaneous Reynolds stresses, to vary and encompass a greater area, resulting in increased sediment erosion and transport. The greater height of the rogue ripple is associated with critical changes in the turbulent flow structure (e.g. magnitude of the velocity gradient, degree of flow separation/deceleration, intensity of shearing and magnitude and frequency of eddy shedding; McLean *et al.*, 1994), the influence of which propagates downstream. The turbulence intensity over bedload sheets is greater than that over the smaller ripple forms (Figure 5.29), which causes Reynolds stress, and therefore sediment entrainment, to increase at reattachment (Muller and Gyr, 1996). The greater erosion of sediment at the reattachment point is associated with increased deposition at the downstream bedform crest. The magnitude and frequency of quadrant 2 events caused by eddy shedding increases with the transition to bedload sheets. Quadrant 2 events originating from ripples are limited to the lowest 20 percent of the flow depth (Bennett and Best, 1996), whereas over bedload sheets quadrant 2 events are able to penetrate further into the outer flow, and are replaced by quadrant 4 events originating higher in the profile in order to maintain continuity.

5.4.5.4 Low-relief bed waves

Further increases in the amount and size of mobile sediment (due to increasing bed shear stress) are accommodated by the evolution of low-relief bed waves, which are associated with a substantial increase in wavelength (i.e. bedload sheets are up to 1 m long while low-relief bed waves range from 2.3-4.9 m long, Table 5.6; Wilcock and McArdell, 1993; Coleman and Melville, 1994). The low-relief bed waves developed in Series 1 ($d = 0.18$ m) are greater in height (13-15 mm) compared with the bedload sheets (7-12 mm), and therefore have reduced migration rates (up to 14 and 27 mm/s

respectively). Conversely, in series 2 ($d = 0.14$ m) the height and migration rate of the low-relief bed waves are similar to that of the bedload sheets due to the limitations imposed by the flow depth. The contraction of the flow over the crestral region causes bed shear stress to be elevated, inhibiting deposition and vertical growth, and resulting in the formation of a crestral platform. As low-relief bed waves develop (e.g. through bedform amalgamation), sediment transport rates rapidly increase (Table 5.6), and cannot be fully accounted for by the greater bedform dimensions. Consequently, the overpassing of coarse grains and the suspension of fine sediment must become increasing important components of total sediment transport. Since coarser particles are increasingly prone to transport as flow strength rises, the armoured trough eventually becomes mobile (bed shear stress > 7 Pa). The movement of a wider range of grain sizes, and the larger length of the low-relief bed waves, enables greater spatial grain size differentiation compared with the other bedforms, which is coupled with larger magnitude variations in turbulence production, turbulence intensity, Reynolds stress, mixing length and eddy viscosity between the different bedform regions. Furthermore, the spatially-averaged values of mean flow and turbulence parameters increase across the transition from bedload sheets to low-relief bed waves, especially near the bed ($y/d < 0.3$; Figure 5.29).

As mean shear stress increases, coarser clasts become incorporated and transported within the bedform, although a static armour remains in the trough until the bed shear stress exceeds approximately 7 Pa. The maximum grain size of the bedload associated with ripples, bedload sheets and low-relief bed waves was 13.2, 19.0 and 26.9 mm respectively. Bedform height therefore increases with the coarsest fractions found in the mobile sediment, and is approximately equal to half the size of the largest transported clast. The similar nature of the grain size distribution of the crest, stoss and bedload, for the bedload sheets, and the correspondence of the bedload, crest and bulk mixture when low-relief bed waves are present also supports this contention. Coarse clasts generate their own turbulent flow field (Brayshaw *et al.*, 1983), which influences adjacent grains through mutual particle interference. Since the height of the bedforms scales with the largest clasts in transport, shear layers originating from these large grains are important in the structure of the turbulent flow over these bedforms. However, the wakes generated from coarse grains are transient and occur at varying locations over the bedform. Furthermore, vortices can be shed from the crest of bedforms superimposed on the stoss side of bedload sheets and low-relief bed waves.

Although it was not possible to obtain velocity measurements in the lee of the fixed bedforms, flow separation was observed behind coarse clasts indicating that grain roughness effects remain important. The development of flow separation may be hindered by the close proximity of coarse clasts in the trough, causing wake interaction and impeding the crest generated shear layer from reaching the bed. The interaction of topographically-induced flow acceleration and coherent flow structures associated

with shear layers originating from bedform crests and coarse clasts are critical to the formation and migration of bedforms (McLean *et al.*, 1996; Muller and Gyr, 1996). Bedform stability is achieved when the maximum sediment transport rate is located at the crest (Nelson *et al.*, 1993). Increases in bedform height raise the velocity over the crest, enabling the greatest rates of sediment transport to locate at the crest. Furthermore, topographically-induced acceleration damps the intensity of turbulence, resulting in greater correlation of the bedload transport with mean values, facilitating the movement of the peak in transport to the crest. The degree of sediment sorting influences the formation and stability of bedforms (Wilcock and Southard, 1989; Chiew, 1991; Wilcock, 1992). For example, Wilcock (1992) observed that with increasing bed shear stress, dunes and bedload sheets developed from an lower-stage plane bed composed of a log-normal and a bimodal sediment mixture respectively. Furthermore, sediment sorting can result in variations in equilibrium morphology, even though the formative processes may be similar or identical e.g. bedload sheets and two-dimensional dunes (Best, 1996). Indeed, Wilcock (1992; $D_{50} = 1.83$) noted that as mixture sorting increased the height of dunes diminished, whilst their length increased. Whilst, Snishchenko *et al.* (1989) found that both dune height and length decreased with increasingly poorly sorted coarse sediment ($D_{50} = 1.55\text{--}8.5$ mm), and migration rate rose. If the sediment mixture contains a high proportion of sand sized fractions, sediment suspension may also be significant with regard to bedform stability (Best, 1996).

The present experiments highlight the spatial (both longitudinally and vertically) and temporal variability of turbulence over ripples, bedload sheets and low-relief bedwaves. With the transition to larger bedforms, the degree of spatial variability of turbulence increased, and the impact of the bedforms on the turbulent flow field extended further away from the bed. Spatio-temporal variations in turbulence parameters (e.g. Reynolds stress near the bed) are shown to have significant implications for local sediment transport rates, and consequently bedform development, migration and stability. The turbulent flow field over bedforms in a bimodal sand-gravel mixture is dominated by the generation of turbulent shear layers from bedform crests and coarse clasts, the occurrence of superimposed bedforms, topographic forcing and surface roughness.

Chapter 6 : Conclusions and opportunities for future research

6.1 Conclusions

Laboratory flume experiments have been conducted to characterise the hydraulic and sedimentological conditions associated with different flow depths and discharges over a bimodal sand-gravel mixture, and detail the morphology, texture, dynamics, sediment transport and associated turbulent flow structure of the bedforms developed.

6.1.1 Bedform morphology

With increasing bed shear stress, the following bedforms that are traverse to flow were documented:

Ripples	3-5 mm high, 0.03-0.80 m wavelength
Bedload sheets	7-12 mm high, 0.07-1.06 m wavelength
Low-relief bed waves	13-15 mm high (0.18 m flow depth) 8-10 mm high (0.14 m flow depth)
	2.30-4.85 m wavelength.

The different bedform populations were distinguished using the multivariate technique of cluster analysis on measurements of the height and period of individual bedforms. For each run, the dimensions of approximately 200 bedforms were studied. Every bedform population exhibits a range of values for each morphological and hydraulic characteristic under equilibrium conditions, and consequently there is a degree of overlap between bedform groups. The range of individual bedform characteristics (e.g. height and migration rate) within a group enables bedforms to evolve and develop. The dynamic nature of bedforms is illustrated by bed height records, which illustrate the superimposition and amalgamation of bedforms, facilitated by variations in migration rates and bed shear stress. Bedform amalgamation enables the development of 'rogue bedforms' (Leader, 1980) which share similarities with a bedform population different to that of the bedforms from which it was formed.

6.1.2 Bedform texture and sediment transport

Except for the Run N with the highest bed shear stress (7.9 Pa), the flow was unable to transport all the grain sizes present in the mixture, and consequently the starved bedforms migrated over a relatively coarse static armour, which composed the trough regions of the bedforms. In contrast, the bedform stoss sides were composed of the finest transported sediment, which coarsened towards the crest. Bedform migration accounts for the fluctuations in both total and fractional bedload transport rate, as is indicated by the similar grain size distributions of the bedload and bedform crest, which both coarsen with increasing bed shear stress, and the correspondence of bedload and bedform transport rates. Sediment contained within the

traverse bedforms is moved along a dune-like grain path (Wilcock and McArdell, 1993), with the exception of fine particles which are transported in suspension and the coarsest grains, which once entrained, can rapidly overpass several bedforms before being deposited. With increasing bed shear stress, these alternative transport mechanisms become more prevalent. The occurrence of different sediment transport mechanisms is one cause of variability in bedform wavelength.

Low-relief bed waves observed at a flow depth of 0.14 m, and bedload sheets, are approximately equivalent in height to the D_{90} (10.07 mm) of the bulk bimodal sediment mixture, whereas the low-relief bed waves observed at a flow depth of 0.18 m are equal in height to the D_{95} (14.55 mm). The grain size distribution of the crestal sediment and bedload correspond in the case of the bedload sheets, while the size distribution of the crest, bedload and bulk mixture are similar when low-relief bed waves are present (i.e. the larger fractions are transported in the bed waves). The maximum grain size of the bedload was 13.2, 19 and 26.9 mm for ripples, bedload sheets and low-relief bed waves respectively. Therefore, the coarsest fractions found in the bedload are directly proportional to the height of the bedform, which is approximately half the size of the largest clast in transport. However, the height of the low-relief bed waves is also directly dependent on the flow depth.

6.1.3 Mean flow characteristics

The vertical profiles of downstream velocity do not conform to the expected logarithmic shape. Estimations of the boundary shear stress obtained using the law-of-the-wall, which is based on a logarithmic profile, were found to be erroneous when compared with values calculated from Reynolds stress projections and the depth-slope product. Similarly, estimates of the zero-velocity roughness height from the law-of-the-wall are much higher than anticipated (i.e. typically > 1 mm). The measurements of downstream velocity were taken at $y^+ > 500$, where divergence from the logarithmic region is indicated by previous workers (Nezu and Rodi, 1984; Kirkgöz, 1989). Furthermore, Nikora *et al.* (2001) illustrate that the influence of roughness elements on the flow can extend to 2-5 times their height, which in the present case coincides with the lower 20 % of the flow depth where the law-of-the-wall is potentially applicable. Reduced values of the von Kármán constant, κ , from the clear water value of 0.41 (Nezu and Nakagawa, 1993) were calculated, and the values of the Coles' (1956) wake coefficient, Π , were predominantly negative in contrast to typical values of ~ 0.2 (Nezu and Rodi, 1986). The von Kármán and wake coefficients are dependent on the boundary conditions e.g. degree of sediment transport, morphology and texture. The measured downstream velocity profiles did not compare well with those predicted by the model of Wiberg and Smith (1991), which does not consider sediment sorting or the presence of bedforms. The present data indicate that the C parameter in the velocity distribution model of Nikora *et al.* (2001) is directly related to the relative roughness, and confirms the previous value of $C \sim 5.3$ obtained over gravel beds in the roughness layer. However, both the von Kármán

constant and C parameter require adjustment in the logarithmic region to attain agreement between the measured and predicted velocity distributions. Time-averaged downstream velocity is greatest over the bedform crest, where Reynolds stress is lowest, reduced over the stoss, and lowest in the trough where Reynolds stress is maximised.

6.1.4 Flow resistance

The average grain-related equivalent sand roughness height (k_s') is approximated by 2-3 D_{50} . The grain related friction factor has an average value of 0.035, which is greater than that attributed to the form roughness (0.023). However, the complex relationship of flow resistance with the bed morphology and texture causes different methods for calculating the magnitude of the resistance to vary substantially.

6.1.5 Turbulent flow structure

Ripples are characterised by fairly uniform flow conditions, with complete mixing of the shear layers originating from the crests within the bottom 20-40 % of the flow, since topographic forcing into the outer flow is weak due to the limited height of ripples. In contrast, bedload sheets and low-relief bed waves are approximately twice the height of ripples, and greater in length, causing significant topographically-induced flow acceleration and deceleration, leading to non-uniform flow conditions, a greater vertical extent and magnitude of quadrant 2 events and stacking of individual wakes generated upstream. Furthermore, the magnitude and frequency of quadrant 4 events is limited over ripples compared with bedload sheets and low-relief bed waves. With increasing bed shear stress, the level of turbulence production and intensity, the velocity gradient, spatial variability (both above and along the bedform), topographic forcing and the magnitude of quadrant 2 events are all shown to increase. The turbulent flow field is influenced by shearing from coarse clasts and bedform crests, and discontinuities in surface elevation and roughness.

6.1.6 A conceptual model of bedform development in a bimodal sand-gravel mixture

The results presented in this study, and synthesis with existing literature, can be used to propose a model for the evolution of bedforms in bimodal sand-gravel mixtures. At low shear stresses (approximately < 2 Pa), only the relatively fine sized sediment is selectively entrained, concentrating in longitudinal stripes (Run A; Iseya and Ikeda, 1987; Ferguson *et al.*, 1989; Robert *et al.*, 1992; Nezu and Nakagawa, 1993; Livesey, 1995; Tsujimoto, 1999). Small perturbations can develop on the surface of these elongated sandy regions due to the occurrence of a) turbulent flow structures (Best, 1992), b) non-uniform sediment and c) grouping by kinematic shock waves. Once the bed defect reaches a critical height, flow separation can occur, causing scour at reattachment and subsequent deposition downstream, facilitating the development and propagation of ripples (Runs B and I, shear stress of approximately 3 Pa; Williams and Kemp, 1971, 1972; Southard and

Dingler, 1971; Baas, 1999). The relatively fine surface texture of the ripple stoss side is associated with reduced drag and pivoting angle, enabling larger grains to be entrained from the surrounding coarse armour layer and either overpass the ripple or become incorporated within it. Consequently, the ripples may contain clasts larger than typically expected (i.e. > 0.7 mm; Leeder, 1980).

As bed shear increases above 3 Pa, bedload sheets are also observed in conjunction with ripples. Bedload sheets are approximately twice the height of ripples (~ 10 mm), although are comparable in length (< 1 m). With increasing bed shear stress, the quantity and calibre of the transported sediment increases, which is accommodated by the higher bedload sheets. The transport of larger clasts increases the grain roughness over the bedform, thus augmenting the magnitude and frequency of turbulent flow structures, facilitating greater bedload transport and therefore increasing bedform height. However, the coarse nature of the trough hinders erosion in the bedform trough, accounting for the lower relief of bedforms developed in mixed compared with unimodal sediments (Wilcock, 1992, Lanzoni, 2000), although the highest bed shear stress experienced (~ 8 Pa) was capable of transporting all the grain sizes available in the bed. Bedload sheets may develop from a 'rogue ripple' (Leeder, 1980), which can occur through bedform amalgamation, fluctuations in sediment transport and flapping of the shear layer. The greater height of the rogue ripple impacts on the turbulent flow structure, which in turn influences the ripples downstream e.g. it increases the magnitude of the velocity gradient, degree of flow deceleration, intensity of shearing, magnitude and frequency of eddy shedding, production of turbulence, turbulence intensities and Reynolds stress (Figure 5.29 and Table 5.6).

At bed shear stresses above approximately 4 Pa, low-relief bed waves are observed in conjunction with bedload sheets and ripples. Low-relief bed waves are substantially longer in length (2.3-4.9 m) compared with bedload sheets which are up to 1 m long. The bed waves developed in Series 1 ($d = 0.18$ m) are greater in height (13-15 mm) compared with the bedload sheets (7-12 mm), whereas in Series 2 ($d = 0.14$ m) the height and migration rate of the bed waves are similar to that of the bedload sheets due to limitations imposed by the flow depth. Flow contraction over the crest causes bed shear stress to increase, which inhibits deposition and vertical growth, leading to the formation of a crestral platform. During the transition from bedload sheets to low-relief bed waves, sediment transport rates (bedload and suspended), particle overpassing and the magnitude of turbulence parameters rapidly increase (Figure 5.29 and Table 5.6). The greater length of the bed waves and the wider range of grain sizes in transport, facilitate greater textural distinction between regions, which is coupled with larger variations in the turbulence parameters e.g. turbulence production and intensity, Reynolds stress, mixing length and eddy viscosity. The turbulent flow field and the development, migration and stability of bedforms developed in a bimodal mixture is dominated by shear layer generation from bedform crests and coarse clasts, topographic forcing and selective entrainment.

6.1.7 Comparison of low-relief bedforms with dunes

It is difficult to assign a characteristic grain size to the bedforms, and therefore plot them on a stability diagram. All of the experimental data plotted in the dune stability field of Southard and Boguchwal (1990), although, they did not have separate classifications for bedload sheets or low-relief bed waves. In Figure 3.17 (Best, 1996), the present bedforms plot in the dune and bedload sheet regions. It is a matter of debate whether bedload sheets and low-relief bed waves are equivalent to dunes, for which permanent flow separation is not a requirement (Best and Kostaschuk, in press). Profiles of downstream velocity in the trough region of the low-relief bed waves are slightly kinked, analogous to similarly located profiles over dunes experiencing flow separation (Bennett and Best, 1995), indicating the occurrence of weak flow separation downstream of the bed wave crest. Values for the correlation coefficient fall between 0.3 and the value over a flat-bed boundary layer (0.4), suggesting flow separation is absent or intermittent, as also found by (Best and Kostaschuk, in press) over low-angle dunes. In the case of bedload sheets and low-relief bed waves the contribution to total roughness is greater for the grain rather than form component, and flow separation was observed in the lee of coarse clasts. The presence of substantial grain and form roughness on the stoss of bedforms generated in bimodal sediment reduces the contrast between the spatially-averaged flow and turbulence parameters and their value at specific locations over the bedform e.g. at reattachment downstream of the crest.

Dune height scales with flow depth (Allen, 1984) and is much greater (> 0.075 m, Ashley, 1990) than that of the bedload sheets and low-relief bed waves (~ 0.01 m), which scale with coarsest particles in transport ($\sim D_{90}$), although the height of the low-relief bed waves is also dependent on flow depth. Since the height of the bedforms scales with the largest clast in transport, the shear layers originating from these coarse clasts, which are spatio-temporally variable, are a critical component of the turbulent flow structure. The reduced height of the low-relief bedforms causes flow separation/deceleration to occur on a smaller spatial scale compared with taller dunes, influencing the magnitude and frequency of turbulence structures generated along the shear layer, the amount of sediment transport and bedform spacing. The steepness (height/length) of equilibrium dunes is much greater (0.08; Carling, 1999) than bedload sheets (0.017) and low-relief bed waves (0.004). Furthermore, the ratio of length to flow depth is approximately 5 for dunes (Allen, 1982), but ≤ 4 for bedload sheets and ≥ 18 for low-relief bed waves. With increasing shear stress there is no clear trend for either an increase in height, or decrease in wavelength, of low-relief bed waves, as is associated with a transition to dune bedforms. However, low-relief bed waves may form a critical link between grain-scale features (e.g. pebble clusters and bedload sheets) and bedforms which scale with flow depth (e.g. dunes).

6.2 Opportunities for future research

The conclusions of this work indicate several profitable areas for further research, which would expand our understanding of the interactions between bedform development, bedload transport and turbulent flow over bimodal sediments.

- 1) Since velocity measurements were taken at-a-point using LDA, the evolution of individual vortices could not be tracked spatially, which is possible with recently developed flow visualisation techniques (e.g. particle imaging velocimetry, PIV). The two approaches complement each other, since flow visualisation gives an excellent overview of the turbulent flow field, whilst LDA data provides high spatial resolution in the areas of greatest interest e.g. in the area of flow deceleration.
- 2) The near-bed area downstream of the crest requires further investigation (detailed velocity measurements) in order to assess the relative importance of the velocity gradient and flow separation for the generation of macroturbulence. Furthermore, near-bed velocity measurements over the entire length of the bedforms are necessary to quantify the role of coarse clasts in the spatio-temporal generation of turbulence.
- 3) Only one bimodal sand-gravel sediment mixture was used in the present experiments. Comparison of the morphological and hydraulic characteristics of the bed with mixtures of different bimodality and sorting would help to assess if the trends established here are generally applicable to heterogeneous mixtures, and facilitate the development of bedform diagrams appropriate for mixed bed material. Furthermore, bed topology, turbulent flow structure and sediment transport can be measured over bimodal sediments in the field and compared with the flume situation.
- 4) The development of numerical models is needed to simulate the interactions between the generation of bedforms, sediment transport and turbulent flow structure in heterogeneous sediment. Selective entrainment, bedform amalgamation, grain roughness, topographic forcing and spatial variations in shear stress must be accounted for in these models.

Bibliography

Acarlar, M. S. & Smith, C. R. (1987a) A study of hairpin vortices in a laminar boundary layer. Part 1. Hairpin vortices generated by a hemisphere protuberance. *Journal of Fluid Mechanics*, **175**, 1-41.

Acarlar, M. S. & Smith, C. R. (1987b) A study of hairpin vortices in a laminar boundary layer. Part 2. Hairpin vortices generated by fluid injection. *Journal of Fluid Mechanics*, **175**, 43-83.

Adrian, R. J. (1996) Laser velocimetry. In: *Fluid mechanics measurements* (Ed. by R. J. Goldstein), pp. 175-293. Taylor and Francis, London.

Alexander, J. & Fielding, C. (1997) Gravel antidunes in the tropical Burdekin River, Queensland, Australia. *Sedimentology*, **44**, 327-337.

Allan, A. F. & Frostick, L. (1999) Framework dilation, winnowing, and matrix particle size: The behavior of some sand-gravel mixtures in a laboratory flume. *Journal of Sedimentary Research*, **69**(1), 21-26.

Allen, J. R. L. (1968) *Current ripples*. North Holland Publishing Company, Amsterdam, 433 pp.

Allen, J. R. L. (1982) *Sedimentary structures: Their character and physical basis, Volume 1*. Elsevier, Amsterdam, 593 pp.

Allen, J. R. L. (1983) A simplified cascade model for transverse stone-ribs in gravelly streams. *Proceedings of the Royal Society of London*, **A385**, 253-266.

Allen, J. R. L. (1984) *Sedimentary structures: their character and physical basis*. Elsevier, Holland, 663 pp.

Anderberg, M. R. (1973) *Cluster analysis for applications*. Academic Press, London, 359 pp.

Antonia, R. A. & Luxton, R. E. (1971) The response of a turbulent boundary layer to a step change in surface roughness. Part 1: Smooth to rough. *Journal of Fluid Mechanics*, **48**, 721-761.

Antonia, R. A. & Luxton, R. E. (1972) The response of a turbulent boundary layer to a step change in surface roughness. Part 2: Rough to smooth. *Journal of Fluid Mechanics*, **53**, 737-757.

Anwar, H. O. & Atkins, R. (1982) Turbulent structure in an open-channel flow. In: *Euromech 156: Mechanics of sediment transport* (Ed. by B. Mutlu Sumer and A. Muller), pp. 19-25, Istanbul.

Ashley, G. M. (1990) Classification of large-scale subaqueous bedforms: a new look at an old problem. *Journal of Sedimentary Petrology*, **60**(1), 160-172.

Ashmore, P. E. (1988) Bed load transport in braided gravel-bed stream models. *Earth Surface Processes and Landforms*, **13**, 677-695.

Ashworth, P. J., Bennett, S. J., Best, J. L. & McLlland, S. J. (1996) *Coherent flow structures in open channels*. John Wiley and Sons ltd., Chichester, 733 pp.

Ashworth, P. J. & Ferguson, R. I. (1989) Size-selective entrainment of bed load in gravel bed streams. *Water Resources Research*, **25**(4), 627-634.

Baas, J. H. (1993) Dimensional analysis of current ripples in recent and ancient depositional environments. Utrecht university.

Baas, J. H. (1999) An empirical model for the development and equilibrium morphology of current ripples in fine sand. *Sedimentology*, **46**(1), 123-138.

Bagnold, R. A. (1956) The flow of cohesionless grains in fluids. *Philosophical Transactions of the Royal Society of London*, **249**.

Batalla, R. J. (1997) Evaluating bed-material transport equations using field measurements in a sandy gravel-bed stream, Arbúcies River, NE Spain. *Earth Surface Processes and Landforms*, **22**, 121-130.

Bennett, S. J. (1992) A theoretical and experimental study of bedload transport of heterogeneous sediment. Ph.D., State University of New York.

Bennett, S. J. & Best, J. L. (1995) Mean flow and turbulence structure over fixed, two-dimensional dunes: implications for sediment transport and bedform stability. *Sedimentology*, **42**, 491-513.

Bennett, S. J. & Best, J. L. (1996) Mean flow and turbulence structure over fixed ripples and the ripple-dune transition. In: *Coherent flow structures in open channels* (Ed. by P. J. Ashworth, S. J. Bennett, J. L. Best and S. J. McLelland), pp. 281-304. John Wiley and Sons Ltd., Chichester.

Bennett, S. J. & Bridge, J. S. (1995a) The geometry and dynamics of low-relief bed forms in heterogeneous sediment in a laboratory channel, and their relationship to water flow and sediment transport. *Journal of Sedimentary Research*, **A65**(1), 29-39.

Bennett, S. J. & Bridge, J. S. (1995b) An experimental study of flow, bedload transport and bed topography under conditions of erosion and deposition and comparison with theoretical models. *Sedimentology*, **42**, 117-146.

Bennett, S. J., Bridge, J. S. & Best, J. L. (1998) Fluid and sediment dynamics of upper stage plane beds. *Journal of Geophysical Research*, **103**(C1), 1239-1274.

Bergeron, N. E. & Abrahams, A. D. (1992) Estimating shear velocity and roughness length from velocity profiles. *Water Resources Research*, **28**(8), 2155-2158.

Best, J. L. & Ashworth, P. J. (1994) A high-resolution ultrasonic bed profiler for use in laboratory flumes. *Journal of Sedimentary Research*, **A64**, 674-675.

Best, J. L., Bennett, S. J., Bridge, J. S. & Leader, M. R. (1997) Turbulence modulation and particle velocities over flat sand beds at low transport rates. *Journal of Hydraulic Engineering*, **123**(12), 1118-1129.

Best, J. L. & Kostaschuk, R. (in press) An experimental study of turbulent flow over a low-angle dune. *Journal of Geophysical Research*.

Best, J. L. (1992) On the entrainment of sediment and initiation of bed defects: insights from recent developments within turbulent boundary layer research. *Sedimentology*, **39**, 797-811.

Best, J. L. (1993) On the interactions between turbulent flow structure, sediment transport and bedform development: Some considerations from recent experimental research. In: *Turbulence: Perspectives on flow and sediment transport* (Ed. by N. J. Clifford, J. R. French and J. Hardisty), pp. 61-92. John Wiley and Sons, Chichester.

Best, J. L. (1996) The fluid dynamics of small-scale alluvial bedforms. In: *Advances in fluvial dynamics and stratigraphy*. (Ed. by P. A. Carling and M. R. Dawson), pp. 67-125. John Wiley and Sons Ltd., Chichester.

Biron, P. M., Roy, A. G. & Best, J. L. (1995) A scheme for resampling, filtering, and subsampling unevenly spaced laser Doppler anemometer data. *Mathematical Geology*, **27**(6), 731-748.

Biron, P. M., Lane, S. N., Roy, A. G., Bradbrook, K. F. & Richards, K. S. (1998) Sensitivity of bed shear stress estimated from vertical velocity profiles: The problem of sampling resolution. *Earth Surface Processes and Landforms*, **23**, 133-139.

Bluck, B. J. (1987) Bed forms and clast size changes in gravel-bed rivers. In: *River channels: environment and process* (Ed. by K. Richards), pp. 159-178. Blackwell, Oxford.

Boon, P. J. (1998) River restoration in five dimensions. *Aquatic Conservation - Marine and Freshwater Ecosystems*, **8**(1), 257-264.

Brayshaw, A. C. (1984) Characteristics and origin of cluster bedforms in coarse-grained alluvial channels. In: *Sedimentology of gravels and conglomerates, Vol. 10* (Ed. by E. H. Koster and R. J. Steel), pp. 77-85. Canadian Society of Petroleum Geologists Memoir.

Brayshaw, A. C., Frostick, L. E. & Reid, I. (1983) The hydrodynamics of particle clusters and sediment entrainment in coarse alluvial channels. *Sedimentology*, **30**, 137-143.

Buchhave, P. & George, W. K., Jr. (1979) The measurement of turbulence with the Laser-Doppler Anemometer. *Annual Review of Fluid Mechanics*, **11**, 443-503.

Buffin-Bélanger, T. & Roy, A. G. (1998) Effects of a pebble cluster on the turbulent structure of a depth-limited flow in a gravel-bed river. *Geomorphology*, **25**, 249-267.

Buffin-Bélanger, T., Roy, A. G. & Kirkbride, A. D. (2000) On large-scale flow structures in a gravel-bed river. *Geomorphology*, **32**, 417-435.

Byrd, T. C., Furbish, D. J. & Warburton, J. (2000) Estimating depth-averaged velocities in rough channels. *Earth Surface Processes and Landforms*, **25**, 167-173.

Carboneau, P. E. & Bergeron, N. E. (2000) The effect of bedload transport on mean and turbulent flow properties. *Geomorphology*, **35**, 267-278.

Cardoso, A. H., Graf, W. H. & Gust, G. (1989) Uniform flow in a smooth open channel. *Journal of Hydraulic Research*, **27**(5), 603-616.

Carling, P. A. (1996) Morphology, sedimentology and palaeohydraulic significance of large gravel dunes, Altai Mountains, Siberia. *Sedimentology*, **43**, 647-664.

Carling, P. A. (1999) Subaqueous gravel dunes. *Journal of Sedimentary Research*, **69**(3), 534-545.

Carling, P. A., Gölz, E., Orr, H. G. & Radecki-Pawlak, A. (2000a) The morphodynamics of fluvial sand dunes in the River Rhine, near Mainz, Germany. I. Sedimentology and morphology. *Sedimentology*, **47**, 227-252.

Carling, P. A. & Reader, N. A. (1982) Structure, composition and bulk properties of upland stream gravels. *Earth Surface Processes and Landforms*, **7**, 349-365.

Carling, P. A., Williams, J. J., Gölz, E. & Kelsey, A. D. (2000b) The morphodynamics of fluvial sand dunes in the River Rhine, near Mainz, Germany. II. Hydrodynamics and sediment transport. *Sedimentology*, **47**, 253-278.

Chiew, Y. M. (1991) Bed features in nonuniform sediments. *American Society of Civil Engineers, Journal of Hydraulic Engineers*, **117**(1), 116-120.

Church, M. A. & Jones, D. (1982) Channel bars in gravel-bed rivers. In: *Gravel-bed rivers* (Ed. by R. D. Hey, J. C. Bathurst and C. R. Thorne), pp. 291-324. John Wiley and Sons Ltd., Chichester.

Church, M. A., McLean, D. G. & Wolcott, J. F. (1987) River bed gravels: Sampling and analysis. In: *Sediment transport in gravel-bed rivers* (Ed. by C. R. Thorne, J. C. Bathurst and R. D. Hey), pp. 43-87. John Wiley and Sons Ltd., Chichester.

Clifford, N. J. (1993) Differential bed sedimentology and the maintenance of riffle pool sequences. *Catena*, **20**, 447-468.

Clifford, N. J. (1996) Morphology and stage-dependent flow structure in a gravel-bed river. In: *Coherent flow structures in open channels* (Ed. by P. J. Ashworth, S. J. Bennett, J. L. Best and S. J. McLelland), pp. 545-566. John Wiley and Sons Ltd., Chichester.

Clifford, N. J., Richards, K. S. & Robert, A. (1992) The influence of microform bed roughness elements on flow and sediment transport in gravel bed rivers: Comment on a paper by Marwis A. Hassan and Ian Reid. *Earth Surface Processes and Landforms*, **17**, 529-534.

Coleman, S. E. & Melville, B. W. (1994) Bed-form development. *American Society of Civil Engineers, Journal of Hydraulic Engineering*, **120**(4), 544-560.

Coles, D. F. (1956) The law of the wake in turbulent boundary layer. *Journal of Fluid Mechanics*, **1**, 191-226.

Costello, W. R. & Southard, J. B. (1980) Flume experiments on lower-flow-regime bed forms in coarse sand. *Journal of Sedimentary Petrology*, **51**(3), 849-864.

Crickmore, M. J. (1970) Effect of flume width on bed-form characteristics. *American Society of Civil Engineers, Journal of Hydraulic Engineers*, **96**(HY2), 473-496.

Dal Cin, R. (1968) "Pebble clusters": Their origin and utilization in the study of palaeocurrents. *Sedimentary Geology*, **2**, 233-241.

Dantec. (1996) BSA - Installation and user's guide, Denmark.

Dantec. (1998) BSA flow software - Installation and user's guide, Denmark.

Dantec. (2000) Dantec website (www.dantecmt.com).

de Jong, C. (1991) A reappraisal of the significance of obstacle clasts in cluster bedform dispersal. *Earth Surface Processes and Landforms*, **16**, 737-744.

Defina, A. (1996) Transverse spacing of low-speed streaks in a channel flow over a rough bed. In: *Coherent flow structures in open channels* (Ed. by P. J. Ashworth, S. J. Bennett, J. L. Best and S. J. McLelland), pp. 87-99. John Wiley and Sons Ltd., Winchester.

Derrow, R. W. (1993) SedBed Monitor, Model SM-2, User's manual. National Center for Physical Acoustics, University of Mississippi, Oxford.

Dietrich, W. E., Kirchner, J. W., Ikeda, H. & Iseya, F. (1989) Sediment supply and the development of the coarse surface layer in gravel-bedded rivers. *Nature*, **340**, 215-217.

Dinehart, R. L. (1989) Dune migration in a steep, coarse-bedded stream. *Water Resources Research*, **25**(5), 911-923.

Dinehart, R. L. (1992a) Evolution of coarse gravel bed forms: field measurements at flood stage. *Water Resources Research*, **28**(10), 2667-2689.

Dinehart, R. L. (1992b) Gravel-bed deposition and erosion by bedform migration observed ultrasonically during storm flow, North Fork Toutle River, Washington. *Journal of Hydrology*, **136**, 51-71.

Dinehart, R. L. (1999) Correlative velocity fluctuations over a gravel river bed. *Water Resources Research*, **35**(2), 569-582.

Diplas, P. & Fripp, J. B. (1992) Properties of various sediment sampling procedures. *Journal of Hydraulic Engineering*, **118**(7), 955-970.

Diplas, P. & Parker, G. (1992) Deposition and removal of fines in gravel-bed streams. In: *Dynamics of Gravel-Bed Rivers* (Ed. by P. Billi, R. D. Hey, C. R. Thorne and P. Tacconi), pp. 313-329. John Wiley and Sons, Chichester.

Ditchfield, R. & Best, J. (1992) Discussion: Development of bed features. *American Society of Civil Engineers, Journal of Hydraulic Engineering*, **118**, 647-655.

Dittrich, A. & Koll, K. (1997) Velocity field and resistance of flow over rough surface with large and small relative submergence. *International Journal of Sedimentary Research*, **12**(3), 21-33.

Drake, T. G., Shreve, R. L., Dietrich, W. E., Whiting, P. J. & Leopold, L. B. (1988) Bedload transport of fine gravel observed by motion picture photography. *Journal of Fluid Mechanics*, **192**, 193-217.

Durst, F., Melling, A. & Whitelaw, J. H. (1987) *Principles and practice of laser Doppler anemometry*. Braun, Kalsruhe, 405 pp.

Dyer, K. R. (1986) *Coastal and estuarine sediment dynamics*. John Wiley and Sons Ltd., Chichester, 342 pp.

Einstein, H. A. & Barbarossa, N. (1952) River channel roughness. *Transactions of the American Society of civil Engineers*, **117**, 1121-1146.

Engelund, F. (1977) Hydraulic resistance for flow over dunes. Institute of Hydrology and Hydraulic Engineering, Technical University of Denmark.

Engelund, F. & Fredsoe, J. (1982) Sediment ripples and dunes. *Annual Review of Fluid Mechanics*, **14**, 13-37.

Engelund, F. & Hansen, E. (1967) *A monograph on sediment transport*. Technisk Forlag, Copenhagen, Denmark.

Everitt, B. S. (1993) *Cluster analysis*. Edward Arnold, London, 170 pp.

Falco, R. E. (1991) A coherent structure model of the turbulent boundary layer and its ability to predict Reynolds number dependence. *Philosophical Transactions of the Royal Society of London, A* 336, 103-130.

Ferguson, R. I., Prestegaard, K. L. & Ashworth, P. J. (1989) Influence of sand on hydraulics and gravel transport in a braided gravel bed river. *Water Resources Research*, 25(4), 635-643.

Ferro, V. & Baiamonte, G. (1994) Flow velocity profiles in gravel-bed rivers. *American Society of Civil Engineers, Journal of the Hydraulics Division*, 120(1), 60-80.

Fredlund, M. D., Fredlund, D. G. & Ward Wilson, G. (2000) An equation to represent grain-size distribution. *Canadian Geotechnical Journal*, 37(4), 817-827.

Friedman, G. M. (1961) Distinction between dune, beach and river sands from their textural characteristics. *Journal of Sedimentary Petrology*, 31, 514-529.

Gabel, S. L. (1993) Geometry and kinematics of dunes during steady and unsteady flows in the Calamus River, Nebraska, USA. *Sedimentology*, 40, 237-269.

Gilvear, D. J. (1999) Fluvial geomorphology and river engineering: future roles utilizing a fluvial hydroystems framework. *Geomorphology*, 31, 229-245.

Gomez, B. (1983) Temporal variations in bedload transport rates: the effect of progressive bed armouring. *Earth Surface Processes and Landforms*, 8, 41-54.

Gomez, B. (1984) Typology of segregated (armoured/paved) surfaces: some comments. *Earth Surface Processes and Landforms*, 9, 19-24.

Gomez, B., Naff, R. L. & Hubbell, D. W. (1989) Temporal variations in bedload transport rates associated with the migration of bedforms. *Earth Surface Processes and Landforms*, 14, 135-156.

Grass, A. J. (1971) Structural features of turbulent flow over smooth and rough boundaries. *Journal of Fluid Mechanics*, 50(2), 233-255.

Grass, A. J. (1983) The influence of boundary layer turbulence on the mechanics of sediment transport. In: *Euromech 156: Mechanics of sediment transport* (Ed. by B. M. Sumer and A. Muller), pp. 3-17, Istanbul.

Grass, A. J. & Mansour-Tehrani, M. (1996) Generalized scaling of coherent bursting structures in the near-wall region of turbulent flow over smooth and rough boundaries. In: *Coherent flow structures in open channels* (Ed. by P. J. Ashworth, S. J. Bennett, J. L. Best and S. J. McLelland), pp. 41-61. John Wiley and Sons Ltd., Winchester.

Grass, A. J., Stuart, R. J. & Mansour-Tehrani, M. (1991) Vortical structures and coherent motion in turbulent flow over smooth and rough boundaries. *Philosophical Transactions of the Royal Society of London, A* **336**, 35-66.

Griffiths, G. A. (1989) Form resistance in gravel channels with mobile beds. *American Society of Civil Engineers, Journal of Hydraulic Engineering*, **115**(3), 340-355.

Gust, G. & Southard, J. B. (1983) Effects of weak bed load on the universal law of the wall. *Journal of Geophysical Research*, **88**(C10), 5939-5952.

Guy, H. P., Simons, D. B. & Richardson, E. V. (1966) Summary of alluvial channel data from flume experiments, 1956-61. *United States Geological Society Professional Paper 462-I*, 96.

Gyr, A. & Müller, A. (1996) The role of coherent structures in developing bedforms during sediment transport. In: *Coherent flow structures in open channels* (Ed. by P. J. Ashworth, S. J. Bennett, J. L. Best and S. J. McLelland), pp. 227-235. John Wiley and Sons, Chichester.

Gyr, A. & Schmid, A. (1989) The different ripple formation mechanism. *Journal of Hydraulic Research*, **27**(1), 61-74.

Hammond, F. D. C., Heathershaw, A. D. & Langhorne, D. N. (1984) A comparison between Shields' threshold criterion and the movement of loosely packed gravel in a tidal channel. *Sedimentology*, **31**, 51-62.

Harper, D. M., Ebrahimnezhad, M., Taylor, E., Dickinson, S., Decamp, O., Verniers, G. & Balbi, T. (1999) A catchment-scale approach to the physical restoration of lowland UK rivers. *Aquatic Conservation - Marine and Freshwater Ecosystems*, **9**(1), 141-157.

Hartigan, J. A. (1975) *Clustering algorithms*. John Wiley and Sons, London, 351 pp.

Hassan, M. A. & Church, M. (2000) Experiments on surface structure and partial sediment transport on a gravel bed. *Water Resources Research*, **36**(7), 1885-1895.

Hassan, M. A. & Reid, I. (1990) The influence of microform bed roughness elements on flow and sediment transport in gravel bed rivers. *Earth Surface Processes and Landforms*, **15**, 739-750.

Head, M. R. & Bandyopadhyay, P. (1981) New aspects of turbulent boundary-layer structure. *Journal of Fluid Mechanics*, **107**, 297-338.

Heathershaw, A. D. & Langhorne, D. N. (1988) Observations of near-bed velocity profiles and seabed roughness in tidal currents flowing over sandy gravels. *Estuarine, Coastal Shelf Science*, **26**, 459-482.

Hey, R. D. (1989) Bar form resistance in gravel-bed rivers. *Journal of Hydraulic Engineering*, **114**(12), 1498-1508.

Hey, R. D., Bathurst, J. C. & Thorne, C. R. (1982) *Gravel-bed rivers: fluvial processes, engineering and management*. John Wiley and Sons, Chichester, 376 pp.

Hoey, T. (1992) Temporal variations in bedload transport rates and sediment storage in gravel-bed rivers. *Progress in Physical Geography*, **16**(3), 319-338.

Hosel, W. & Rodi, W. (1977) New biasing elimination method for laser-Doppler velocimeter counter processing. *Review of Scientific Instruments*, **48**, 910-919.

Hubbell, D. W. (1964) Apparatus and techniques for measuring bedload. *Geological Survey Water-Supply Paper* **1748**, 74.

Hubbell, D. W., Stevens Jr, H. H., Skinner, J. V. & Beverage, J. P. (1987) Laboratory data on coarse-sediment transport for bedload-sampler calibrations. *United States Geological Survey Water Supply Paper* **2299**, 31.

Ikeda, H. & Iseya, F. (1988) Experimental study of heterogeneous sediment transport. Environmental Research Center, the University of Tsukuba, Tsukuba, 305 Japan.

Iseya, F. & Ikeda, H. (1987) Pulsations in bedload transport rates induced by a longitudinal sediment sorting: a flume study using sand and gravel mixtures. *Geografiska Annaler*, **69** A(1), 15-27.

Itakura, T. & Kishi, T. (1980) Open channel flow with suspended sediment on sand waves. In: *Third International Symposium on Stochastic Hydraulics* (Ed. by H. Kikkawa and Y. Isawa), pp. 599-609. Japanere Society of Civil Engineers and the International Association for Hydraulic Research, Tokyo.

Jackson, R. G. (1976) Sedimentological and fluid-dynamic implications of the turbulent bursting phenomenon in geophysical flows. *Journal of Fluid Mechanics*, **77**(3), 531-560.

James, C. S. (1993) Entrainment of spheres: an experimental study of relative size and clustering effects. In: *Alluvial sedimentation* (Ed. by M. Marzo and C. Puigdefabregas), pp. 3-10. Blackwell Scientific Publications, Oxford. *Special Publication*.

Julien, P. Y. & Klaassen, G. J. (1995) Sand-dune geometry of large rivers during floods. *American Society of Civil Engineers, Journal of Hydraulic Engineering*, **121**(9), 657-663.

Karahan, M. E. & Peterson, A. W. (1980) Visualisation of separation over sand waves. *Journal of Hydraulic Engineering*, **160**(HY8), 1345-1352.

Karim, F. (1995) Bed configuration and hydraulic resistance in alluvial-channel flows. *Journal of Hydraulic Engineering*, **121**(1), 15-25.

Kellerhals, R. & Bray, D. I. (1971) Sampling procedures for coarse fluvial sediments. *American Society of Civil Engineers, Journal of Hydraulic Engineering*, **97**(HY 8), 1165-1180.

Kennedy, J. F. (1963) The mechanics of dunes and antidunes in erodible-bed channels. *Journal of Fluid Mechanics*, **16**, 521-544.

Khadkikar, A. S. (1999) Trough cross-bedded conglomerate facies. *Sedimentary Geology*, **128**, 39-49.

Kirchner, J. W., Dietrich, W. E., Iseya, F. & Ikeda, H. (1990) The variability of critical shear stress, friction angle, and grain protrusion in water-worked sediments. *Sedimentology*, **37**, 647-672.

Kirkbride, A. D. (1993) Observations of the influence of bed roughness on turbulence structure in depth limited flows over gravel-beds. In: *Turbulence: Perspectives on flow and sediment transport* (Ed. by N. Clifford, J. French and J. Hardisty), pp. 185-196. John Wiley and Sons, Chichester.

Kirkbride, A. D. (1994) Turbulence structure in straight gravel-bed channels. Ph.D., University of Sheffield.

Kirkgöz, M. S. (1989) Turbulent velocity profiles for smooth and rough open channel flow. *Journal of Hydraulic Engineering*, **115**(11), 1543-1561.

Kironoto, B. A. & Graf, W. H. (1994) Turbulence characteristics in rough uniform open-channel flow. *Proceedings of the Institution of Civil Engineers, Water, Maritime and Energy*, **106**, 333-344.

Klaassen, G. J. (1992) Experiments on the effect of gradation and vertical sorting on sediment transport phenomena in the dune phase. In: *Proceedings of the International Grain Sorting Seminar*, pp. 127-145, Zurich, Switzerland.

Kline, S. J., Reynolds, W. C., Schraub, F. A. & Runstadler, P. W. (1967) The structure of turbulence in boundary layers. *Journal of Fluid Mechanics*, **30**, 741-773.

Klingeman, P. C. (1998) ASCE Sedimentation Committee examines river restoration. *Journal of Hydraulic Engineering*, **124**(6), 563-563.

Komar, P. D. (1987a) Selective grain entrainment by a current from a bed of mixed sizes: a reanalysis. *Journal of Sedimentary Petrology*, **57**(2), 203-211.

Komar, P. D. (1987b) Selective gravel entrainment and the empirical evaluation of flow competence. *Sedimentology*, **34**, 1165-1176.

Komar, P. D. & Li, Z. (1986) Pivoting analyses of the selective entrainment of sediments by shape and size with application to gravel threshold. *Sedimentology*, **33**, 425-436.

Kostaschuk, R. (2000) A field study of turbulence and sediment dynamics over subaqueous dunes with flow separation. *Sedimentology*, **47**, 519-531.

Kostaschuk, R. & Church, M. (1993) Macroturbulence generated by dunes: Fraser River, Canada. *Sedimentary Geology*, **85**, 25-37.

Kostaschuk, R. & Villard, P. (1996) Flow and sediment transport over large subaqueous dunes: Fraser River, Canada. *Sedimentology*, **43**, 849-863.

Kostaschuk, R. & Villard, P. (1998) Reply: Flow and sediment transport over large subaqueous dunes: Fraser River, Canada. *Sedimentology*, **45**, 219-221.

Koster, E. H. (1978) Transverse ribs: their characteristics, origin and paleohydraulic significance. In: *Fluvial sedimentology, Vol. Memoir 5* (Ed. by A. D. Miall), pp. 161-186. Canadian Society of Petroleum Geologists, Calgary, Canada.

Krogstad, P. A., Antonia, R. A. & Browne, L. W. (1992) Comparison between rough- and smooth-wall turbulent boundary layers. *Journal of Fluid Mechanics*, **245**, 599-617.

Kuhnle, R. A. (1986) Experimental studies of heavy-mineral transportation, segregation, and deposition in gravel-bed streams. Ph.D., Massachusetts Institute of Technology.

Kuhnle, R. A. (1992) Fractional transport rates of bedload on Goodwin Creek. In: *Dynamics of gravel-bed rivers* (Ed. by P. Billi, R. D. Hey, C. R. Thorne and P. Tacconi), pp. 141-155. John Wiley & Sons Ltd., Chichester.

Kuhnle, R. A. (1993a) Fluvial transport of sand and gravel mixtures with bimodal size distributions. *Sedimentary Geology*, **85**, 17-24.

Kuhnle, R. A. (1993b) Incipient motion of sand-gravel sediment mixtures. *American Society of Civil Engineers, Journal of Hydraulic Engineering*, **119**(12), 1400-1415.

Kuhnle, R. A. (1996) Unsteady transport of sand and gravel mixtures. In: *Advances in fluvial dynamics and stratigraphy* (Ed. by P. A. Carling and M. R. Dawson), pp. 183-201. John Wiley & Sons Ltd., Chichester.

Kuhnle, R. A. & Southard, J. B. (1988) Bed load transport fluctuations in a gravel bed laboratory channel. *Water Resources Research*, **24**(2), 247-260.

Langhorne, D. N., Heathershaw, A. D. & Read, A. A. (1986) Gravel bedforms in the West Solent, Southern England. *Geo-Marine Letters*, **5**, 225-230.

Lanzoni, S. (2000) Experiments on bar formation in a straight flume 2: Graded sediment. *Water Resources Research*, **36**(11), 3351-3363.

Lapointe, M. F. (1996) Frequency spectra and intermittency of the turbulent suspension process in a sand-bed river. *Sedimentology*, **43**, 439-449.

Laronne, J. B. & Carson, M. A. (1976) Interrelationships between bed morphology and bed-material transport for a small, gravel-bed channel. *Sedimentology*, **23**, 67-85.

Laronne, J. B., Garcia, C. & Reid, I. (2000) Mobility of patch sediment in gravel bed streams: patch character and its implications for bedload. In: *Gravel-bed Rivers 2000* (Ed. by P. Mosley), Christchurch, New Zealand.

Lawless, M. & Robert, A. (2001) Three-dimensional flow structure around small-scale bedforms in a simulated gravel-bed environment. *Earth Surface Processes and Landforms*, **26**, 507-522.

Lee, M. J., Kim, J. & Moin, P. (1990) Structure of turbulence at high shear rate. *Journal of Fluid Mechanics*, **216**, 561-583.

Leeder, M. R. (1999) *Sedimentology and sedimentary basins: From turbulence to tectonics*. Blackwell, Oxford, 592 pp.

Leeder, M. R. (1980) On the stability of lower stage plane beds and the absence of current ripples in coarse sand. *Journal of the Geological Society of London*, **137**, 423-429.

Leeder, M. R. (1982) *Sedimentology: Process and product*. Chapman and Hall, London, 344 pp.

Leeder, M. R. (1983) On the interactions between turbulent flow, sediment transport and bedform mechanics in channelized flows. In: *Modern and Ancient Fluvial Systems. Special Publication 6* (Ed. by J. D. Collinson and J. Lewin), pp. 5-18. International Association of Sedimentologists.

Levi, E. (1983a) Oscillatory model for wall-bounded turbulence. *American Society of Civil Engineers, Journal of Engineering Mechanics*, **109**(3), 728-740.

Levi, E. (1983b) A universal Strouhal law. *American Society of Civil Engineers, Journal of Engineering Mechanics*, **109**(3), 718-727.

Levi, E. (1991) Vortices in hydraulics. *American Society of Civil Engineers, Journal of Hydraulic Engineering*, **117**(4), 399-413.

Ligrani, P. M. & Moffat, R. J. (1986) Structure of transitionally rough and fully rough turbulent boundary layers. *Journal of Fluid Mechanics*, **162**, 69-98.

Liu, H. K. (1957) The mechanics of sediment ripple formation. *Journal of Hydraulic Engineering, Proceedings paper 1197*, **83**(2).

Livesey, J. (1995) Flow structure, bedform development and sediment transport in mixed sand and gravel. Unpublished Ph.D. Thesis, University of Leeds.

Livesey, J., Bennett, S. J., Ashworth, P. J. & Best, J. L. (1998) Flow, sediment transport and bedform dynamics in a bimodal sediment mixture. In: *Gravel-bed rivers in the environment* (Ed. by P. C. Klingeman, R. L. Beschta, P. D. Komar and J. B. Bradley), pp. 149-176. Water Resources Publications.

Lopez, F., Fernandez, R. & Best, J. L. (2000) Turbulence and coherent flow structures associated with bedform amalgamation: an experimental study of the ripple-dune transition. In: *Joint Conference on Water Resources Engineering and Water Resources Planning and Management* (Ed. by A. S. o. C. Engineers), Minneapolis, Minnesota.

Lu, S. S. & Willmarth, W. W. (1973) Measurement of the structure of the Reynolds stress in a turbulent boundary layer. *Journal of Fluid Mechanics*, **60**(3), 481-511.

Luchik, T. S. & Tiederman, W. G. (1987) Timescale and structure of ejections and bursts in turbulent channel flows. *Journal of Fluid Mechanics*, **174**, 529-552.

Lyn, D. A. (1993) Turbulence measurements in open-channel flows over artificial bed forms. *Journal of Hydraulic Engineering*, **119**(3), 306-326.

Marchand, J. P., Jarrett, R. D. & Jones, L. L. (1984) Velocity profile, water-surface slope, and bed-material size for selected streams in Colorado. USGS.

Massey, B. (1998) *Mechanics of fluids*. Stanley Thorne Ltd, Cheltenham, 722 pp.

Mazumder, R. (2000) Turbulence-particle interactions and their implications for sediment transport and bedform mechanics under unidirectional current: some recent developments. *Earth-Science Reviews*, **50**(1-2), 113-124.

McBride, E. F., Shepherd, R. G. & Crawley, R. A. (1975) Origin of parallel, near-horizontal laminae by migration of bed forms in a small flume. *Journal of Sedimentary Petrology*, **45**(1), 132-139.

McDonald, B. C. & Day, T. J. (1978) An experimental flume study on the formation of transverse ribs. *Geological Survey of Canada, Paper 78-1A*, 441-451.

McLaughlin, D. K. & Tiederman, W. G. (1973) Biasing correcting for individual realization of laser anemometer measurements in turbulent flows. *Physics of Fluids*, **16**, 2082-2088.

McLean, S. R. (1981) The role of nonuniform roughness in the formation of sand ribbons. *Marine Geology*, **42**, 49-74.

McLean, S. R., Nelson, J. M. & Shreve, R. L. (1996) Flow-sediment interactions in separating flows over bedforms. In: *Coherent flow structures in open channels* (Ed. by P. J. Ashworth, S. J. Bennett, J. L. Best and S. J. McLelland), pp. 203-225. John Wiley and Sons, Chichester.

McLean, S. R., Nelson, J. M. & Wolfe, S. R. (1994) Turbulence structure over two-dimensional bed forms: implications for sediment transport. *Journal of Geophysical Research*, **99**(C6), 12729-12747.

McLean, S. R., Wolfe, S. R. & Nelson, J. M. (1999a) Predicting boundary shear stress and sediment transport over bed forms. *Journal of Hydraulic Engineering*, **125**(7), 725-730.

McLean, S. R., Wolfe, S. R. & Nelson, J. M. (1999b) Spatially averaged flow over a wavy boundary revisited. *Journal of Geophysical Research*, **104**(C7), 15743-15753.

McQuivey, R. S. (1973) Summary of turbulence data from rivers, conveyance channels and laboratory flumes. *United States Geological Society Professional Paper 802-B*, 82.

Mehrotra, S. C. (1983) Antidune movement. *American Society of Civil Engineers, Journal of the Hydraulics Division*, **109**(HY2), 302-304.

Mendoza, C. & Shen, H. W. (1990) Investigation of turbulent flow over dunes. *American Society of Civil Engineers, Journal of Hydraulic Engineering*, **116**(4), 459-477.

Mendoza, C. & Zhou, D. (1992) Effects of a porous bed on turbulent stream flow above the bed. *Journal of Hydraulic Engineering*, **118**(9), 1222-1240.

Meyer-Peter, E. & Müller, R. (1948) Formulas for bed-load transport. In: *2nd Congress of the International Association of Hydraulic Research*, Stockholm.

Millar, R. G. (1999) Grain and form resistance in gravel-bed rivers. *Journal of Hydraulic Research*, **37**(3), 303-312.

Muhar, S., Schmutz, S. & Jungwirth, M. (1995) River restoration concepts - Goals and perspectives. *Hydrobiologia*, **303**(1-3), 183-194.

Müller, A. & Gyr, A. (1996) Geometrical analysis of the feedback between flow, bedforms and sediment transport. In: *Coherent flow structures in open channels* (Ed. by P. J. Ashworth, S. J. Bennett, J. L. Best and S. J. McLelland), pp. 237-247. John Wiley and Sons, Chichester.

Murphy, P. J. & Amin, M. I. (1979) Compartmented sediment trap. *American Society of Civil Engineers, Journal of Hydraulic Engineers*, **105**(HY 5), 489-500.

Naden, P. S. & Brayshaw, A. C. (1987) Small- and medium-scale bedforms in gravel-bed rivers. In: *River channels: environment and process* (Ed. by K. Richards), pp. 249-271. Blackwell, Oxford.

Nakagawa, H. & Nezu, I. (1977) Prediction of the contributions to the Reynolds stress from bursting events in open-channel flows. *Journal of Fluid Mechanics*, **80**(1), 99-128.

Nelson, J. M., McLean, S. R. & Wolfe, S. R. (1993) Mean flow and turbulence fields over two-dimensional bed forms. *Water Resources Research*, **29**(12), 3935-3953.

Nelson, J. M., Shreve, R. L., McLean, S. R. & Drake, T. G. (1995) Role of near-bed turbulence structure in bed load transport and bed form mechanics. *Water Resources Research*, **31**(8), 2071-2086.

Nelson, J. M. & Smith, J. D. (1989) Mechanics of flow over ripples and dunes. *Journal of Geophysical Research*, **94**(C6), 8146-8162.

Newland, D. E. (1975) *An introduction to random vibrations and spectral analysis*. Longman, London.

Nezu, I. & Nakagawa, H. (1993) *Turbulence in open-channel flows*. A.A. Balkema, Rotterdam, 281 pp.

Nezu, I., Nakagawa, H. & Tominaga, A. (1985) Secondary currents in a straight channel flow and the relation to its aspect ratio. In: *Turbulent shear flows 4*, pp. 246-260. Springer-Verlag.

Nezu, I. & Rodi, W. (1986) Open-channel flow measurements with a laser Doppler anemometer. *American Society of Civil Engineers, Journal of Hydraulic Engineering*, **112**(5), 335-355.

Nezu, I., Tominaga, A. & Nakagawa, H. (1993) Turbulent structures and bursting phenomena over roughness discontinuity in open channel flows. In: *Proceedings of the 5th International Symposium on Refined Flow Modelling and Turbulence measurements*, pp. 629-636, Paris.

Nienhuis, P. H. & Leuven, R. S. (2001) River restoration and flood protection. *Hydrobiologia*, **444**(1-3), 85-99.

Nikitin, I. K. (1980) Complex turbulent flows and heat and mass transfer processes. Ukraine Academy of Science, Ukraine.

Nikora, V. I. & Goring, D. G. (2000) Flow turbulence over fixed and weakly mobile gravel beds. *Journal of Hydraulic Engineering*, **126**(9), 679-690.

Nikora, V. I., Goring, D. G., McEwan, I. & Griffiths, G. (2001) Spatially-averaged open-channel flow over a rough bed. *Journal of Hydraulic Engineering*, **127**(2), 123-133.

Nikora, V. I., Goring, D. G. & Biggs, B. J. F. (1998) On gravel-bed roughness characterization. *Water Resources Research*, **34**(3), 517-527.

Nikora, V. I. & Shteinman, B. S. (1996) Turbulence in the Jordan River: A case study. In: *Flow modeling and turbulence measurements VI* (Ed. by Chen, Shih, Lienau and Kung), pp. 581-588. Balkema, Rotterdam.

Nikora, V. I. & Smart, G M. (1997) Turbulence characteristics of New Zealand gravel-bed rivers. *Journal of Hydraulic Engineering*, **123**(9), 764-773.

Nikuradse, J. (1933) Strömungsgesetze in rauhen Rohren. *Forschung auf dem Gebiete des Ingenieurwesens, Ausgabe B Band 4*.

Nowell, A. R. M. & Church, M. (1979) Turbulent flow in a depth-limited boundary layer. *Journal of Geophysical Research*, **84**(C8), 4816-4824.

Paola, C. & Seal, R. (1995) Grain size patchiness as a cause of selective deposition and downstream fining. *Water Resources Research*, **31**(5), 1395-1407.

Parker, G. (1991a) Selective sorting and abrasion of river gravel. I: Theory. *Journal of Hydraulic Engineering*, **117**(2), 131-149.

Parker, G. (1991b) Some random notes on grain sorting. In: *International grain sorting seminar, Vol. Mitteilungen 117*, pp. 1-58. ETH Zurich, Ascona, Switzerland.

Parker, G. (1992) Some random notes on grain sorting. In: *Grain Sorting Seminar, Vol. 117*, pp. 19-77. Mitteilungen, ETH-Zürich.

Parker, G., Dhamotharan, S. & Stefan, H. (1982a) Model experiments on mobile, paved gravel bed streams. *Water Resources Research*, **18**(5), 1395-1408.

Parker, G. & Klingeman, P. C. (1982) On why gravel bed streams are paved. *Water Resources Research*, **18**(5), 1409-1423.

Parker, G., Klingeman, P. C. & McLean, D. G. (1982b) Bedload and size distribution in paved gravel-bed streams. *American Society of Civil Engineers, Journal of the Hydraulics Division*, **108**(HY4), 544-571.

Parker, G. & Peterson, A. W. (1980) Bar resistance of gravel bed rivers. *Journal of the Hydraulics Division, American Society of Civil Engineers*, **106**(10), 1559-1575.

Parker, G. & Wilcock, P. (1993) Sediment feed and recirculating flumes: Fundamental differences. *Journal of Hydraulic Engineering*, **119**, 1192-1204.

Petts, G. & Calow, P. (1996) *River restoration: selected extracts from the Rivers handbook*. Blackwell, Oxford, 231 pp.

Pitlick, J. (1992) Flow resistance under conditions of intense gravel transport. *Water Resources Research*, **28**(3), 891-903.

Pollard, P., Devlin, M. & Holloway, D. (2001) Managing a complex river catchment: a case study on the River Almond. *Science of the total environment*, **265**, 343-357.

Poreh, M., Sagiv, A. & Seginer, I. (1970) Sediment sampling efficiency of slots. *American Society of Civil Engineers, Journal of Hydraulic Engineers*, **96**(HY 10), 2065-2078.

Press, W. H. & Rybicki, G. B. (1989) Fast algorithm for spectral-analysis of unevenly sampled data. *Astrophysical Journal*, **338**(1), 227-280.

Prestegaard, K. L. (1983) Bar resistance in gravel bed streams at bankfull discharge. *Water Resources Research*, **19**(2), 472-476.

Proffitt, G. T. & Sutherland, A. J. (1983) Transport of non-uniform sediments. *Journal of Hydraulic Research*, **21**(1), 33-43.

Pye, K. (1994) Properties of sediment particles. In: *Sediment transport and depositional processes* (Ed. by K. Pye), pp. 1-24. Blackwell Scientific Publications, Oxford.

Rashidi, M. & Banerjee, S. (1988) Turbulence structure in free-surface channel flows. *Physics of Fluids*, **31**(9), 2491-2503.

Raudkivi, A. J. (1966) Bedforms in alluvial channels. *Journal of Fluid Mechanics*, **26**(3), 507-514.

Raudkivi, A. J. (1997) Ripples on stream bed. *Journal of Hydraulic Engineering*, **123**(1), 58-64.

Raudkivi, A. J. & Witte, H. H. (1990) Development of bed features. *American Society of Civil Engineers, Journal of Hydraulic Engineering*, **116**(9), 1063-1079.

Reid, I., Braysahw, A. C. & Frostick, L. E. (1984) An electromagnetic device for automatic detection of bedload motion and its field applications. *Sedimentology*, **31**, 269-276.

Reid, I., Frostick, L. E. & Brayshaw, A. C. (1992) Microform roughness elements and the selective entrainment and entrapment of particles in gravel-bed rivers. In: *Dynamics of gravel-bed rivers* (Ed. by P. Billi, R. D. Hey, C. R. Thorne and P. Tacconi), pp. 253-275. John Wiley and Sons Ltd., Chichester.

Reid, I. & Hassan, M. A. (1992) The influence of microform bed roughness elements on flow and sediment transport in gravel bed rivers: A reply. *Earth Surface Processes and Landforms*, **17**, 535-538.

Richards, K. (1982) *Rivers: form and process in alluvial channels*. Methuen, London, 358 pp.

Richards, K. & Clifford, N. (1991) Fluvial geomorphology: structured beds in gravelly rivers. *Progress in Physical Geography*, **15**(4), 407-422.

Robert, A. (1993) Bed configuration and microscale processes in alluvial channels. *Progress in Physical Geography*, **17**(2), 123-136.

Robert, A., Roy, A. G. & De Serres, B. (1992) Changes in velocity profiles at roughness transitions in coarse grained channels. *Sedimentology*, **39**, 725-735.

Robert, A., Roy, A. G. & De Serres, B. (1993) Space-time correlations of velocity measurements at a roughness transition in a gravel-bed river. In: *Turbulence: Perspectives on flow and sediment transport* (Ed. by N. J. Clifford, J. R. French and J. Hardisty), pp. 165-183. John Wiley and Sons, Chichester.

Robert, A., Roy, A. G. & De Serres, B. (1996) Turbulence at a roughness transition in a depth limited flow over a gravel bed. *Geomorphology*, **16**, 175-187.

Robert, A. & Uhlman, W. (2001) An experimental study of the ripple-dune transition. *Earth Surface Processes and Landforms*, **26**, 615-629.

Robinson, S. K. (1990) Coherent motions in the turbulent boundary layer. *Annual Review of Fluid Mechanics*, **23**, 601-639.

Roden, J. E. (1998) The sedimentology and dynamics of mega-dunes, Jamuna River, Bangladesh. Ph.D., University of Leeds.

Roy, A. G., Buffin-Belanger, T. & Deland, S. (1996) Scales of turbulent coherent flow structures in a gravel-bed river. In: *Coherent flow structures in open channels* (Ed. by P. J. Ashworth, S. J. Bennett, J. L. Best and S. J. McLelland), pp. 147-164. John Wiley and Sons Ltd., Winchester.

Rust, B. R. & Gostin, V. A. (1981) Fossil transverse ribs in Holocene alluvial fan deposits, Depot Creek, South Australia. *Journal of Sedimentary Petrology*, **51**(2), 441-444.

Sambrook Smith, G. H. (1996) Bimodal fluvial bed sediments: origin, spatial extent and processes. *Progress in Physical Geography*, **20**(4), 402-417.

Sambrook Smith, G. H. & Ferguson, R. I. (1995) The gravel-sand transition along river channels. *Journal of Sedimentary Research*, **A65**(2), 423-430.

Sambrook Smith, G. H. & Ferguson, R. I. (1996) The gravel-sand transition: Flume study of channel response to reduced slope. *Geomorphology*, **16**(2), 147-157.

Sambrook Smith, G. H., Nicholas, A. P. & Ferguson, R. I. (1997) Measuring and defining bimodal sediments: problems and implications. *Water Resources Research*, **33**(5), 1179-1185.

Sear, D. A. (1994) River restoration and geomorphology. *Aquatic Conservation - Marine and Freshwater Ecosystems*, **4**(2), 169-177.

Seminara, G., Colombini, M. & Parker, G. (1996) Nearly pure sorting waves and formation of bedload sheets. *Journal of Fluid Mechanics*, **312**, 253-278.

Shaw, J. & Kellerhals, R. (1977) Paleohydraulic interpretation of antidune bedforms with applications to antidunes in gravel. *Journal of Sedimentary Petrology*, **47**(1), 257-266.

Shaw, J. & Kellerhals, R. (1982) The composition of recent alluvial gravels in Alberta River beds, Vol. 41, pp. 151. Bulletin of the Alberta Research Council.

Shimizu, Y., Tsujimoto, T. & Nakagawa, H. (1990) Experiment and macroscopic modelling of flow in highly permeable porous medium under free-surface flow. *Journal of Hydroscience and Hydraulic Engineering*, **8**(1), 69-78.

Shvidchenko, A. B. & Pender, G. (2000) Flume study of the effect of relative depth on the incipient motion of coarse uniform sediments. *Water Resources Research*, **36**(2), 619-628.

Simons, D. B., Richardson, E. V. & Nordin, C. F. (1965) Bedload equations for ripples and dunes. United States Geological Survey.

Simpson, R. L. (1989) Turbulent boundary layer separation. *Annual Reviews in Fluid Mechanics*, **21**, 205-234.

Smart, G. M. (1999) Turbulent velocity profiles and boundary shear in gravel bed rivers. *Journal of Hydraulic Engineering*, **125**(2), 106-116.

Smith, C. R. (1996) Coherent flow structures in smooth-wall boundary layers: facts, mechanisms and speculation. In: *Coherent flow structures in open channels* (Ed. by P. J. Ashworth, S. J. Bennett, J. L. Best and S. J. McLelland), pp. 1-39. John Wiley and Sons, Chichester.

Smith, C. R., Walker, J. D. A., Haidara, A. H. & Sobrun, U. (1991) On the dynamics of near-wall regime of turbulence. *Philosophical Transactions of the Royal Society of London: Series A*, **336**(1641), 131-175.

Smith, J. D. & McLean, S. R. (1977) Spatially averaged flow over a wavy surface. *Journal of Geophysical research*, **82**(12), 1735-1746.

Snishchenko, B. F., Muhamedov, A. M. & Mazhidov, T. S. (1989) Bedload composition effect on dune shape parameters and on flow characteristics. In: *Proceedings of the International Association for Hydraulic Research, 23rd Congress, Vol. B, Fluvial Hydraulics*, pp. B-105-B-112, Ottawa, Canada.

Song, T. & Graf, W. H. (1994) Non-uniform open-channel flow over a rough bed. *Journal of Hydroscience and Hydraulic Engineering*, **12**(1), 1-25.

Song, T., Graf, W. H. & Lemmin, U. (1994) Uniform flow in open channels with movable gravel bed. *Journal of Hydraulic Research*, **32**(6), 861-876.

Southard, J. B. & Boguchwal, L. A. (1990) Bed configuration in steady unidirectional water flows. Part 2. Synthesis of flume data. *Journal of Sedimentary Petrology*, **60**(5), 658-679.

Southard, J. B. & Dingler, J. R. (1971) Flume study of ripple propagation behind mounds on flat sand beds. *Sedimentology*, **16**, 251-263.

SPSS. (1998) Cluster analysis. In: *SPSS Base 8.0 Applications guide*, pp. 372. SPSS Inc, USA.

Steffler, P. M., Rajaratnam, N. & Peterson, A. W. (1985) LDA measurements in open channel. *Journal of Hydraulic Engineering*, **111**(1), 119-130.

Swan, A. R. H. & Sandilands, M. (1995) *Introduction to geological data analysis*. Blackwell Science, Oxford, 446 pp.

Teissyre, A. K. (1977) Pebble clusters as a directional structure in fluvial gravels: modern and ancient examples. *Geologica Sudetica*, **12**, 79-84.

Thorne, P. D., Williams, J. J. & Heathershaw, A. D. (1989) In situ acoustic measurements of marine gravel threshold and transport. *Sedimentology*, **36**, 61-74.

Townsend, A. A. (1976) *The structure of turbulent shear flow*. Cambridge University Press, Cambridge, 429 pp.

Tritton, D. J. (1988) *Physical fluid dynamics*. Clarendon Press, Oxford, 519 pp.

Tsujimoto, T. (1991) Fractional transport rate and fluvial sorting. In: *Proceedings of the International Grain Sorting Seminar, Vol. 117* (Ed. by D. Vischer), pp. 227-249. Mitteilungen, ETH Zurich, Ascona, Switzerland.

Tsujimoto, T. (1999) Sediment transport processes and channel incision: mixed size sediment transport, degradation and armouring. In: *Incised river channels: processes, forms, engineering, and management* (Ed. by S. E. Darby and A. Simon), pp. 37-66. John Wiley and Sons, Chichester.

Tsujimoto, T. & Kitamura, T. (1996) Interaction between cellular secondary currents and lateral alternate sorting. In: *Coherent flow structures in open channels* (Ed. by P. J. Ashworth, S. J. Bennett, J. L. Best and S. J. McLelland), pp. 359-374. John Wiley & Sons Ltd., Chichester.

Tunstall, S. M., Penning-Rowsell, E. C., Tapsell, S. M. & Eden, S. E. (2000) River restoration: Public attitudes and expectations. *Journal of the Chartered Institution of Water and Environmental Management*, **14**(5), 363-370.

van Rijn, L. C. (1984) Sediment transport, Part 1: Bed load transport. *Journal of Hydraulic Engineering*, **110**(10), 1431-1457.

van Rijn, L. C. (1993) *Principles in sediment transport in rivers, estuaries and coastal seas*. Aqua Publications, Amsterdam.

Vanoni, V. A. (1975) *Sedimentation Engineering*. American Society of Civil Engineers, New York, 745 pp.

Vanoni, V. A. & Hwang, L. S. (1967) Relation between bed forms and friction in streams. *Journal of Hydraulic Engineering*, **HY 3**(93), 121-145.

Wang, J. & Dong, Z. (1996) Open-channel turbulent flow over non-uniform gravel beds. *Applied Scientific Research*, **56**, 243-254.

Wang, J., Dong, Z., Chen, C. & Xia, Z. (1993) The effects of bed roughness on the distribution of turbulent intensities in open-channel flow. *Journal of Hydraulic Research*, **31**(1), 89-98.

Wathen, S. J., Ferguson, R. I., Hoey, T. B. & Werritty, A. (1995) Unequal mobility of gravel and sand in weakly bimodal river sediments equal patches fractional transport rates. *Water Resources Research*, **31**(8), 2087-2096.

Werner, B. T. & Kocurek, G. (1999) Bedform spacing from defect dynamics. *Geology*, **27**(8), 727-730.

Whiting, P. J. & Dietrich, W. E. (1990) Boundary shear stress and roughness over mobile alluvial beds. *Journal of Hydraulic Engineering*, **116**(12), 1495-1511.

Whiting, P. J., Dietrich, W. E., Leopold, L. B., Drake, T. G. & Shreve, R. L. (1988) Bedload sheets in heterogeneous sediment. *Geology*, **16**, 105-108.

Whittaker, J. G. & Jaeggi, M. N. R. (1982) Origin of step-pool systems in mountain streams. *American Society of Civil Engineers, Journal of the Hydraulics Division*, **108**(HY6), 758-773.

Wiberg, P. L. & Nelson, J. M. (1992) Unidirectional flow over asymmetric and symmetric ripples. *Journal of Geophysical Research*, **97**(C8), 12745-12761.

Wiberg, P. L. & Rubin, D. M. (1989) Bed roughness produced by saltating sediment. *Journal of Geophysics*, **94**, 5011-5016.

Wiberg, P. L. & Smith, J. D. (1991) Velocity distribution and bed roughness in high-gradient streams. *Water Resources Research*, **27**(5), 825-838.

Wilcock, P. R. (1992) Experimental investigation of the effect of mixture properties on transport dynamics. In: *Dynamics of gravel-bed rivers* (Ed. by P. Billi, R. D. Hey, C. r. Thorne and P. Tacconi), pp. 109-139. John Wiley and Sons Ltd., Chichester.

Wilcock, P. R. (1993) Critical shear stress of natural sediments. *American Society of Civil Engineers, Journal of Hydraulic Engineering*, **119**(4), 491-505.

Wilcock, P. R. (1998) Two-fraction model of initial sediment motion in gravel-bed rivers. *Science*, **280**, 410-412.

Wilcock, P. R. & McArdell, B. W. (1993) Surface-based fractional transport rates: mobilization thresholds and partial transport of a sand-gravel sediment. *Water Resources Research*, **29**(4), 1297-1312.

Wilcock, P. R. & Southard, J. B. (1988) Experimental study of incipient motion in mixed-size sediment. *Water Resources Research*, **24**(7), 1137-1151.

Wilcock, P. R. & Southard, J. B. (1989) Bed load transport of mixed size sediment: fractional transport rates, bed forms, and the development of a coarse bed surface layer. *Water Resources Research*, **25**(7), 1629-1641.

Wilkinson, R. H. (1984) A method for evaluating statistical errors associated with logarithmic velocity profiles. *Geo-Marine Letters*, **3**(49-52), 49-52.

Williams, G. P. (1967) Flume experiments of the transport of a coarse sand. *United States Geological Survey Professional Paper 562-B*, 31.

Williams, G. P. (1970) Flume width and water depth effects in sediment-transport experiments. *United States Geological Survey Professional Paper 562-H*, 37.

Williams, J. J. (1990) Video observations of marine gravel transport. *Geo-Marine Letters*, **10**, 157-164.

Williams, J. J., Thorne, P. D. & Heathershaw, A. D. (1989a) Measurements of turbulence in the benthic boundary layer. *Sedimentology*, **36**, 959-971.

Williams, J. J., Thorne, P. D. & Heathershaw, A. D. (1989b) Comparison between acoustic measurements and predictions of the bedload transport of marine gravels. *Sedimentology*, **36**, 973-979.

Williams, P. B. & Kemp, P. H. (1971) Initiation of ripples on flat sediment beds. *Journal of Hydraulic Engineering*, **97**(4), 505-522.

Williams, P. B. & Kemp, P. H. (1972) Initiation of ripples by artificial disturbances. *Journal of Hydraulic Engineering*, **98**(6), 1057-1070.

Willmarth, W. W. & Lu, S. S. (1974) Structure of the Reynolds stress and the occurrence of bursts in the turbulent boundary layer. In: *Turbulent diffusion in environmental pollution* (Ed. by F. N. Frenkiel and R. E. Munn), pp. 287-314. Academic Press, New York.

Wolcott, J. (1988) Non-fluvial control of bimodal grain size distributions in river bed gravels. *Journal of Sedimentary Petrology*, **58**, 655-663.

Yagishita, K. (1994) Antidunes and traction-carpet deposits in deep-water channel sandstones, Cretaceous, British Columbia, Canada. *Journal of Sedimentary Research*, **A64**(1), 34-41.

Yalin, M. S. (1992) *River mechanics*. Pergamon Press, Oxford, 219 pp.

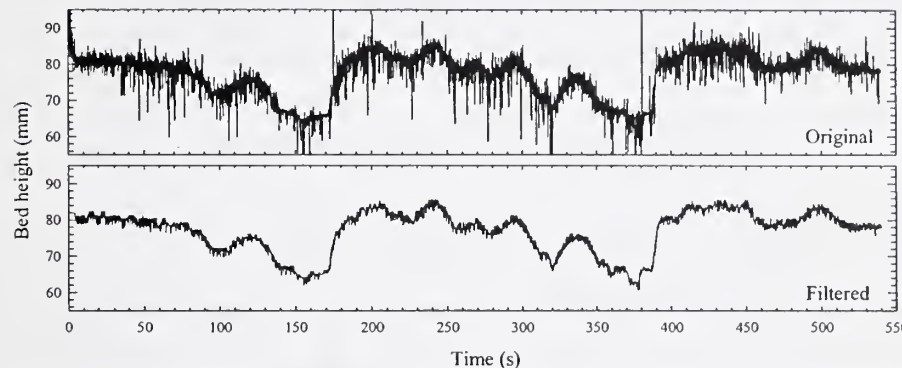
Zippe, H. J. & Graf, W. H. (1983) Turbulent boundary-layer flow over permeable and non-permeable rough surfaces. *Journal of Hydraulic Research*, **21**(1), 51-65.

Appendix I : Consideration of anomalous data values from ultrasonic and LDA time series

I.1 Ultrasonic probes

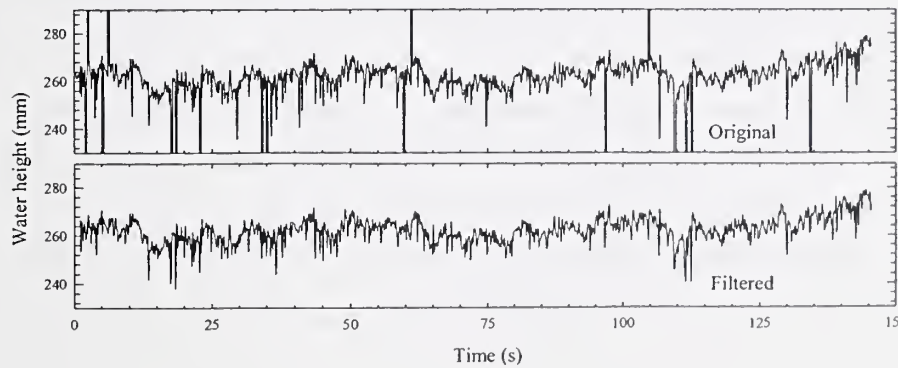
The bed height time series generated by the NCPA probe was filtered using a moving window filter. The mean value of each measurement and the 25 values either side is calculated, and any measurement greater than $\pm 2\%$ of the mean is rejected and not replaced. Examples of the original and filtered time series are shown in Figure I.1.

Figure I.1: Comparison of the filtered and original bed height record (Run F).



The profile of the water surface produced by the Contaq probe was also filtered (Figure I.2) using a moving window. In this case 40 points either side of the measurement are included in the mean calculation. If any measurement is greater than 15 % of the mean or less than 5 % it is replaced with the mean value. For both the NCPA and Contaq probe several values were tried for both the number of points included in the moving window and the rejection level. The combination which best eliminated spikes without removing valid points was selected by visual inspection of the filtered and unfiltered records.

Figure I.2: Comparison of the original and filtered record of water height (Run F).



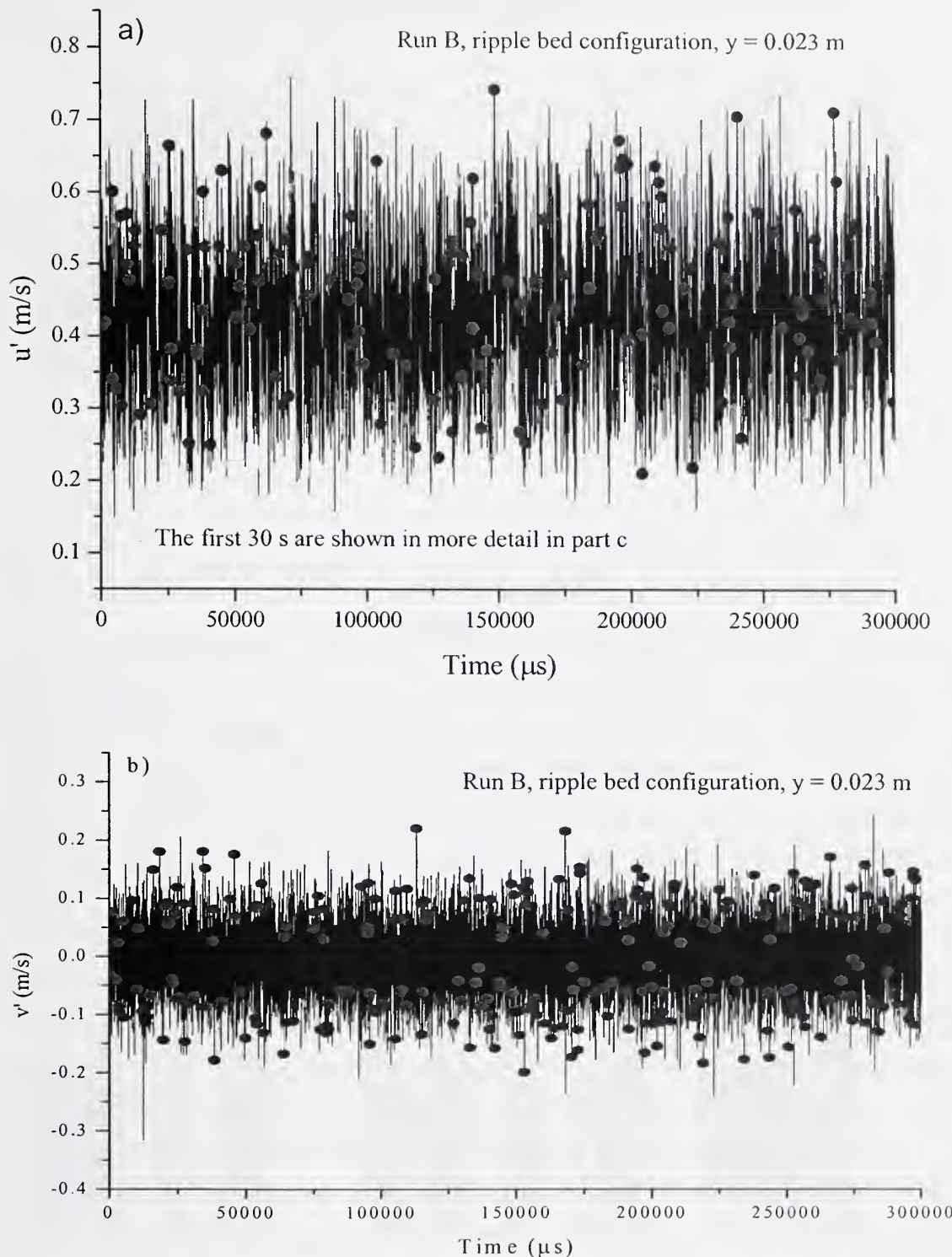
I.2 LDA

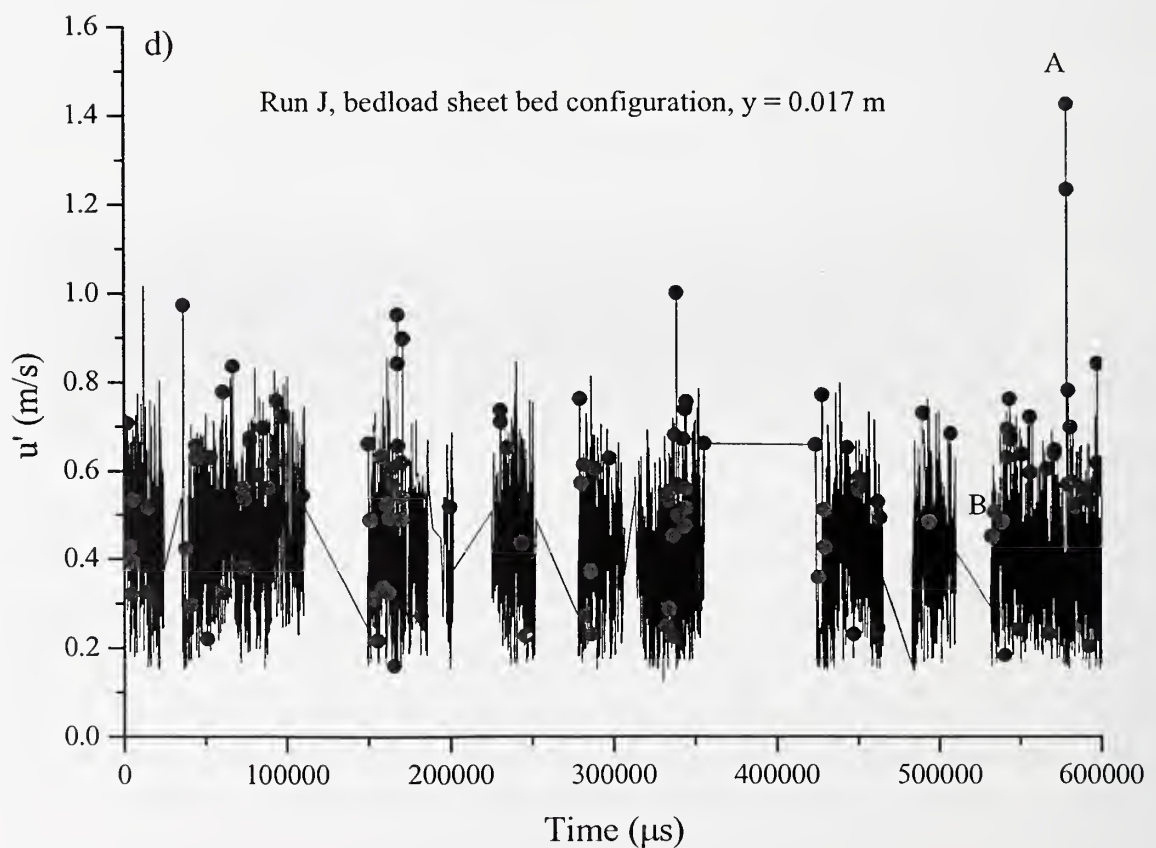
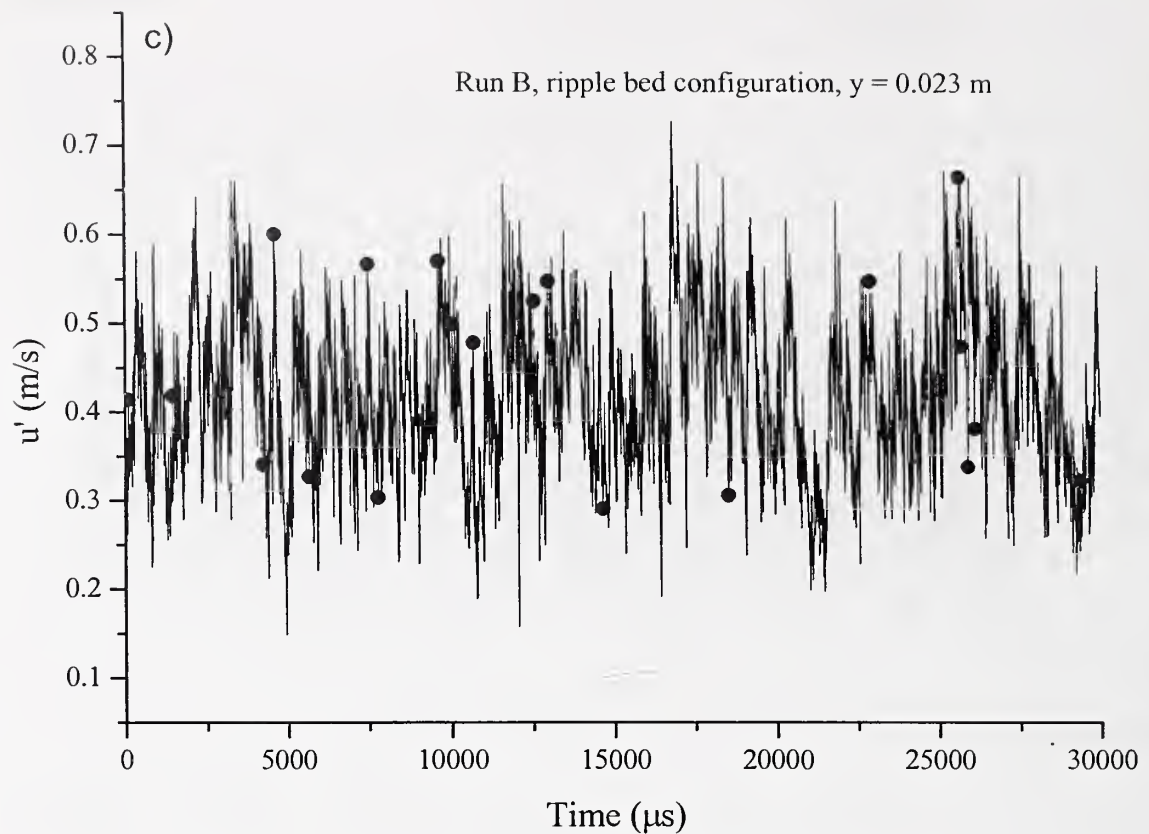
In the present experiments, velocity and turbulence parameters are calculated from the raw laser time series exported from the LDA processing software, in accord with the experimental procedure adopted by Nelson *et al.* (1993) and McLean *et al.* (1994). Many other studies which employ LDA measurements do not specify any additional post processing e.g. Nezu and Rodi (1986), Wang and Dong (1996). Post processing is not necessarily required for the calculation of velocity moments (Biron *et al.*, 1995), or for time series analysis with the development of software and techniques which can accommodate randomly sampled data. Furthermore, various validation operations are conducted in the LDA experimental arrangement, which optimise the velocity signal and minimise the level of noise. In the current study, validation rates were typically between 80-100 % for both the mobile and fixed bed experiments. Stages within the LDA procedure which assess whether a given velocity measurement is valid or not include:

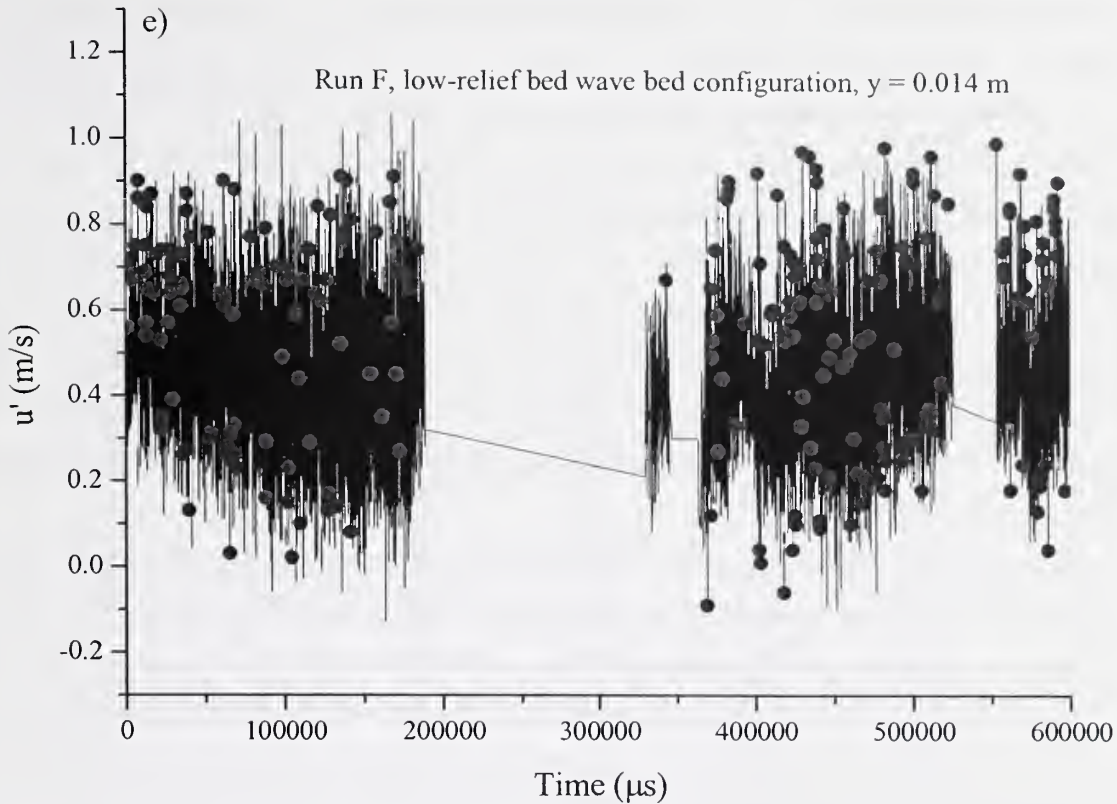
- 1) The user can set divergence limits for various signal quality parameters, which determine whether an individual Doppler burst signal is accepted. The criteria that have to be met by a valid burst signal include the signal-to-noise-ratio, the number of fringes to be intersected by the particle, and the measured velocity range.
- 2) A high pass filter is applied to the output of the photomultipliers in order to remove the low frequency component (i.e. pedestal or envelope), caused by the particle traversing the measuring volume. The high frequency component remains, which represents the movement of the particle through the interference fringes and contains the velocity information.
- 3) The system is operated in coincidence rather than random mode. In random mode a signal is validated if a Doppler burst of sufficient magnitude is recorded for either velocity component, whereas in coincidence mode, both velocity components have to register a genuine Doppler burst simultaneously in order for the measurement to be considered valid.

Visual observation of typical laser time series collected in the present study illustrate the extremely low occurrence of large anomalous data spikes (e.g. point A on Figure I.3d). These isolated, extreme values are thought to be an artefact of the optics and internal electronics of the LDA equipment (Biron *et al.*, 1995). Consequently, such anomalous points are not considered to constitute part of the real velocity signal, or relate to turbulent structures within the flow. A spike in one component of velocity is typically not correlated with an extreme measurement in the other concurrently measured velocity component. Indeed, in the present examples of laser time series, measurements which are identified by the filter for removal largely cannot be related to similar events in the other component of velocity. On the time series, red symbols represent points to be removed by the filter associated with just one velocity component, whereas blue symbols signify that both components are affected (one point in Figure I.3a and b).

Figure I.3: Examples of the original LDA time series. Red and blue symbols indicate the points which are removed by the filter.







Although anomalous data points could be removed by hand, this is a subjective, time consuming and labour intensive process. Alternatively, a filter can be applied to each time series, which is objective in that the removed data points can be defined mathematically and the process is repeatable. However, some subjectivity remains in the definition of what represents the real signal and what is erroneous. Livesey (1995), Bennett and Best (1995, 1996) and Bennett *et al.* (1998) employ a simple band filter to remove any spikes, which has a limited effect on the data. Livesey (1995) adopted a scheme where abnormal values from electromagnetic current meters and LDA time series were classified as being greater than three standard deviations from the mean of the whole record. However, it is felt that due to the movement and development of sediment, bedforms and coherent flow structures relative to the laser measuring volume (e.g. Figure I.3c), that it is more appropriate to use a moving window filter in the present study. In order to validate a velocity measurement, the mean and standard deviation are calculated from the measurement point and ten data points either side. If the measured velocity is greater than three standard deviations from the average of the selected points it is rejected. The impact of filtering LDA time series is illustrated using a moving window of 11 points due to the rapidly varying nature of the turbulent flow. The number of points included in the moving window was optimised by trying different values. If the number of points included in the moving window is reduced, fewer measurements tend to be eliminated. However, if more points are incorporated into the moving window high magnitude, high frequency velocity fluctuations may be removed by the filter. The temporal resolution of the filtering technique is dependent on the data rate, which is in turn

determined by the density of light scattering particles, the sensitivity of the photomultipliers and the validation levels employed in extracting the Doppler frequencies (Nelson *et al.*, 1993). It is apparent from examination of the laser time series shown in Figure I.3 that the application of a filter involves a trade off between the benefits (i.e. removal of spikes e.g. at position A, Figure I.3d) and drawbacks (i.e. removal of real components of the signal e.g. at position b). The velocity and turbulence measurements calculated from the raw and filtered laser time series are compared in Table I.1, for the mobile bed runs B (ripple bed configuration), J (bedload sheets) and F (low-relief bed waves) in order to quantify the effect of using the original, rather than filtered, signal. The filter removes less than 1 % of the data points from the time series, and the vast majority of velocity and turbulence parameters exhibit a variation of less than 1% between the original and filtered values. The main contrasts between the filtered and raw data are:

- 1) The percentage difference in time-averaged downstream velocity calculated from the original and raw data files varied by nearly 17 % at isolated points near the bed in runs J and F. However, this region is important for the implementation of the law-of-the-wall. Consequently, a further comparison was made concerning the application of the law-of-the-wall to the original and filtered signal, and no significant difference was identified (Table I.1f and Figure I.4). Furthermore, the law-of-the-wall remains erroneous.
- 2) Occasional high percentage differences were observed between the time-averaged vertical velocity calculated from the raw and filtered data. However, the impact upon the Reynolds stress was minimal (up to 6.5 %), probably due to the filter removing both positive and negative vertical velocity measurements.
- 3) High percentage differences (up to 42 %) between filtered and original time-averaged downstream turbulence intensities are evident for isolated time series near the bed e.g. Figure I.3d and e. However, within the obvious exception of the major peak at A in Figure I.3d, the many of the measurements which are filtered out appear valid when visually assessed.
- 4) The percentage differences for quadrant results (particularly quadrant 1 events) at a threshold of 2 are sporadically high in the fixed bed examples (up to 22 %). The normalised number of quadrant events are plotted on contour maps, and any erroneous values will be smoothed out by the interpolation process.

Table I.1: Differences between the original and filtered LDA time series shown as an absolute percentage of the original values.

a) Run B, ripple bed configuration.

y (m)	% of filtered points	\bar{u} (m s^{-1})	\bar{v} (m s^{-1})	$rmsu'$ (m s^{-1})	$rmsv'$ (m s^{-1})	$-\rho\bar{uv}$ (Pa)
0.013	0.32	0.88		6.47		
0.015	0.18	0.00		0.12		
0.016	0.11	0.00		0.00		
0.018	0.14	0.00		0.13		
0.018	0.13	0.00		0.00		
0.019	0.41	0.03	0.00	0.00	0.23	0.23
0.019	0.45	0.00	1.64	0.12	0.45	0.04
0.022	0.45	0.00	0.00	0.00	0.47	0.22
0.022	0.46	0.00	14.29	0.12	0.45	0.05
0.023 (Figure 1.3a-c)	0.49	0.00	0.00	0.00	0.22	0.13
0.021	0.38	0.02	0.00	0.00	0.22	0.13
0.027	0.46	0.00	0.00	0.12	0.43	0.05
0.028	0.53	0.00	0.00	0.12	0.43	0.04
0.029	0.49	0.00	0.00	0.12	0.43	0.01
0.032	0.45	0.00	0.00	0.00	0.21	0.07
0.034	0.44	0.00	0.00	0.12	0.21	0.00
0.038	0.51	0.00	0.00	0.00	0.20	0.01
0.044	0.51	0.02	0.58	0.00	0.20	0.15
0.053	0.45	0.00	0.50	0.00	0.20	0.03
0.064	0.43	0.00	0.00	0.00	0.00	0.04
0.074	0.43	0.00	0.65	0.00	0.20	0.04
0.084	0.49	0.00	0.00	0.00	0.00	0.07
0.094	0.48	0.00	0.00	0.15	0.22	0.02
0.104	0.51	0.00	0.00	0.00	0.00	0.05
0.114	0.50	0.00	1.43	0.16	0.00	0.03
0.123	0.51	0.00	0.00	0.00	0.00	0.10
0.134	0.59	0.00	0.00	0.18	0.25	0.10
0.143	0.60	0.00	0.00	0.00	0.00	0.05
0.154	0.32	0.11		0.18		

b) Run J, bedload sheet bed configuration.

y (m)	% of filtered points	\bar{u} (m s^{-1})	\bar{v} (m s^{-1})	$rmsu'$ (m s^{-1})	$rmsv'$ (m s^{-1})	$-\rho\bar{uv}$ (Pa)
0.013	0.15	0.00		0.12		
0.016	0.21	0.06		1.79		
0.016	0.22	2.66		3.45		
0.017	0.31	16.78		41.99		
0.020	0.20	0.02		0.17		
0.017 (Figure 1.3d)	0.29	13.37		10.26		
0.024	0.15	0.02		0.09		
0.021	0.68	1.37	19.57	1.80	2.53	6.46
0.020	0.69	0.09	5.00	0.29	1.16	1.47
0.024	0.38	0.00	5.56	0.00	0.78	0.20
0.026	0.43	0.02	0.00	0.09	0.31	0.16
0.023	0.48	0.00	0.00	0.00	0.52	0.08
0.030	0.43	0.00	0.00	0.09	0.16	0.06
0.030	0.46	0.00	0.00	0.10	0.17	0.01
0.031	0.44	0.00	0.00	0.00	0.32	0.01
0.033	0.44	0.00	0.00	0.10	0.17	0.09
0.036	0.49	0.00	3.70	0.00	0.18	0.06
0.044	0.48	0.00	2.63	0.11	0.18	0.01
0.051	0.41	0.00	0.00	0.00	0.17	0.06
0.066	0.45	0.00	0.00	0.11	0.19	0.15
0.074	0.47	0.00	0.00	0.13	0.00	0.01
0.082	0.43	0.00	0.00	0.00	0.00	0.04
0.093	0.42	0.00	0.00	0.00	0.21	0.03
0.106	0.44	0.01	0.00	0.00	0.23	0.15
0.116	0.48	0.00	0.00	0.00	0.00	0.31
0.123	0.49	0.00	0.00	0.00	0.00	0.24
0.133	0.35	0.00		0.16		

c) Run F, low-relief bed wave bed configuration.

y (m)	% of filtered points	\bar{u}	\bar{v}	$rmsu'$	$rmsv'$	$-\rho\bar{uv}$
		(m s ⁻¹)	(Pa)			
0.018	0.29	1.44		9.39		
0.017	0.32	16.01		11.21		
0.016	0.34	0.02		0.21		
0.016	0.43	0.26		29.92		
0.014 (Figure 1.3e)	0.41	11.54		26.78		
0.019	0.81	2.06	262.50	3.51	3.37	2.15
0.020	0.94	0.07	4.76	0.23	1.01	1.32
0.023	0.93	0.09	0.00	0.39	1.16	1.88
0.021	0.74	0.05	8.00	0.33	1.08	1.89
0.024	0.50	0.02	93.55	2.26	0.30	3.52
0.023	0.50	0.02	1.92	0.08	0.63	0.09
0.025	0.54	0.00	0.00	0.08	0.45	0.12
0.028	0.42	0.13	0.00	0.00	0.31	0.12
0.031	0.36	0.00	0.00	0.08	0.30	0.13
0.033	0.38	0.01	1.01	0.08	0.30	0.01
0.033	0.34	0.00	0.93	0.09	0.31	0.18
0.041	0.34	0.00	0.60	0.09	0.30	0.17
0.043	0.31	0.00	0.00	0.00	0.31	0.02
0.054	0.28	0.00	0.00	0.00	0.30	0.08
0.064	0.29	0.00	0.00	0.10	0.47	0.17
0.074	0.31	0.01	0.00	0.00	0.32	0.07
0.084	0.28	0.00	0.44	0.10	0.33	0.36
0.097	0.27	0.00	0.80	0.11	0.49	0.69
0.104	0.33	0.01	0.83	0.12	0.52	0.81
0.115	0.32	0.00	20.00	0.00	0.19	0.02
0.122	0.32	0.00	0.00	0.00	0.20	0.04
0.136	0.26	0.01	0.00	0.00	0.00	0.09
0.145	0.26	0.00	0.86	0.14	0.21	0.10
0.152	0.14	0.00		0.00		

d) Fixed run 1, bedload sheet bed configuration. A threshold of 2 is employed.

Point	% of filtered points	Fractional contribution				Normalised number (%) of events			
		Q1	Q2	Q3	Q4	Q1	Q2	Q3	Q4
A	0.93	15.00	0.24	3.09	1.14	21.86	0.36	4.91	1.85
B	0.38	6.37	0.23	1.71	0.71	7.82	0.38	0.66	0.06
C	0.26	5.00	0.21	0.40	0.16	6.97	0.47	0.25	0.05
D	0.33	0.00	0.39	5.73	0.17	1.28	0.71	4.81	0.33
E	0.62	2.58	0.68	2.27	1.14	0.62	0.07	2.11	2.57
F	0.31	3.72	0.08	4.81	0.18	2.81	0.07	4.96	0.16
G	0.49	1.72	0.11	0.07	0.47	2.56	0.12	0.03	0.42
H	0.41	1.06	0.13	0.99	0.21	1.38	0.41	1.41	0.01
I	0.79	4.58	0.32	0.26	0.18	13.88	1.35	0.80	0.31

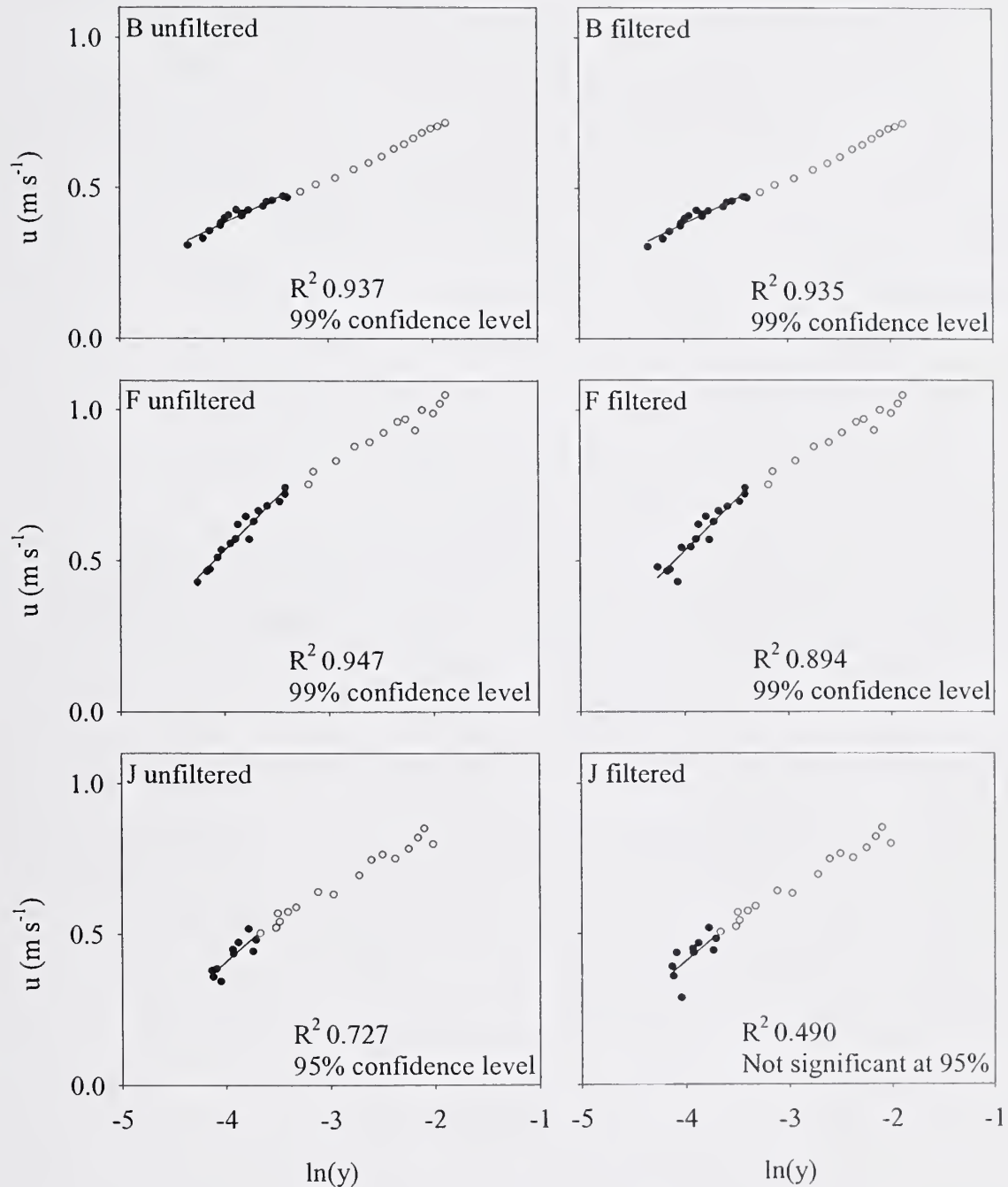
e) Fixed run 2, low-relief bed wave bed configuration. A threshold of 2 is employed.

Point	% of filtered points	Fractional contribution				Normalised number (%) of events			
		Q1	Q2	Q3	Q4	Q1	Q2	Q3	Q4
A	0.40	2.23	0.49	2.63	1.42	7.31	0.64	3.98	1.87
B	0.37	10.91	0.67	1.61	0.44	13.94	0.93	2.49	0.05
C	0.32	6.70	0.20	0.46	0.19	6.35	0.08	2.02	0.08
D	0.69	3.07	1.84	0.00	0.49	7.35	0.71	0.73	1.22
E	0.47	2.44	0.90	4.33	0.76	1.41	0.80	2.39	0.11
F	0.24	0.00	0.16	0.55	0.72	0.58	0.43	1.71	0.72
G	0.22	0.78	0.21	0.19	0.16	1.36	0.36	0.28	0.31
H	0.23	0.48	0.48	0.00	0.26	1.38	0.67	1.25	0.41
I	0.22	0.56	0.56	0.22	4.14	1.26	1.03	0.57	5.14

f) Law-of-the-wall.

Run	U_* (m s ⁻¹)	τ_0 (Pa)	κ	y_0
B	0.71	1.43	0.71	1.86
J	5.29	10.29	5.58	7.28
F	0.69	1.37	0.69	0.51

Figure I.4: Application of the law-of-the-wall to filtered and unfiltered LDA time series.





NATIONAL AGRICULTURAL LIBRARY



1022606250